EPFL

Novel Insights into Thin Film Instabilities:
From Fundamentals to Metamaterial Applications

Présentée le 12 avril 2021

Faculté des sciences et techniques de l'ingénieur
Laboratoire des fibres et matériaux photoniques
Programme doctoral en science et génie des matériaux

pour l'obtention du grade de Docteur ès Sciences

par

Louis Marie Philippe MARTIN-MONIER

Acceptée sur proposition du jury

Prof. F. Stellacci, président du jury
Prof. F. Sorin, directeur de thèse
Prof. T. Gacoin, rapporteur
Prof. M. Dickey, rapporteur
Prof. F. Gallaire, rapporteur

École
polytechnique
fédérale
de Lausanne

2021

Acknowledgements

I would like to first express my sincere gratitude to my advisor Prof. Fabien Sorin for having given me the opportunity to carry out my research works in his group. I have deeply appreciated the research freedom and trust he provided throughout the Ph.D. Thanks to his patience, motivation, and extended knowledge, Fabien's guidance helped me throughout the PhD journey, providing feedback on research and largely helping to shape this thesis.

I would like to further thank my thesis committee: Prof. Francesco Stellaci, Prof. Michael Dickey, Prof. Thierry Gacoin, as well as Prof. Francois Gallaire. I would like to thank them for the time they took to review this PhD dissertation, their insightful comments and encouragements.

No man is an island. This statement rings particularly true during the PhD journey, and I therefore thank my fellow labmates for the great time past together in the past four years. With this, I would like to thank my closest collaborators in the past four years: Tapajyoti Dasgupta, Pierre-Luc Piveteau and William Esposito, whose enthusiasm, hard work, and continuous exchanges have largely contributed to the present thesis. Of course, my thanks also goes to the whole FIMAP team throughout the years: Tung Nguyen-Dang, Federica Sordo, Wei Yan, Yuanyuan Guo, Alexis Page Marco Volpi, Ines Richard, Bastien Schyrr, Rajasundar Chandran, Sharzhad Shadman, Andreas Leber, Chaoqun Dong, Nicola Bartolomei. The PhD experience would have been very different without all of you, thanks for being part of the journey.

I am indebted to my collaborators throughout the campus at EPFL, whose help also proved essential to this thesis. Given the highly interdisciplinary nature of the present work, collarboration has been key to sucess, and I am deeply grateful to have met and worked with multiple very gifted and friendly collaborators: Prof. Gallaire, Prof. Lacour, Prof. Altug, Pier Giuseppe Ledda, Filiz Yesilkoy, Aurelian John-Herpin, Laurent Dejace, Karim Achouri, Kuang-Yu Yang, Hsiang-Chu Wang among many others. In many ways, research is like a puzzle where every collaborator brings in his own invaluable piece, and without which the whole image remains elusive. Thank you to all those who contributed to shape the present work.

I would like to thank my friends from the extended EPFL community as well, whose company I have dearly enjoyed over these four years, whether it be for mountain sports, swimming, traveling, or social outings: Gianluca Prandini, Lukas Riemer, Sergio Hernandez-Charpak, Tanja Thompsen, Alice Comberlato, Lea Ghisalberti, Gabriele Berutto, Anna Pogrebna, Ivan Madan, Florian Durrafourg, Arnaud Gelb, Andreana Daniil, Riccardo Ravasio, Timo Rey, Ozgun Kocabiyik, Rebekah Wells, Cecilia Giovanazzo, Baris Caglar, Natasha Lopanitsyna… It is difficult to be fair and cite everyone here and would like to extend my thanks to all the wonderful people I have met during my time at EPFL. I would also like to thank the team of PolyDoc, with whom we have created a fantastic PhD community across doctoral schools from scratch in two years, and take this occasion to wish all the best to the future team.

My deep thanks for the very professional and helpful teams at CMi and CIME: Cyril Hibert, Joffrey Pernollet, Rémy Juttin, Julien Dorsaz, Fabienne Bobard, Gegroire Barroz, Daniele Laub, Colette Valloton and the many more fantastic scientific staff who have taught me so much. Their dedication have enabled me to carry out challenging projects at

an incredible pace. Their professionalism and availability brings a considerable added value to an institution such as EPFL.

Teaching constituted a significant part of my learning experience at EPFL. I have tremendously learned both as teaching assistant for Materials Science courses and as a supervisor for several semester project. Motivating students, retaining their attention, generating their enthusiasm has been for me a source of motivation as well as a source of reward. Teaching is about transmitting, and this entails a set of very specific skills that do not necessarily overlap with those skills learned in research. I am grateful to the many students I have met who have taught me to teach: Niloofar Khornian, Tiphaine Matthieu-Pennober, Pierre-Luc Piveteau, Govind Krishnamani, Xueyan Zhang, as well as the multiple generations of EPFL bachelor students throughout the years.

Last but not the least, I would like to thank my family: my parents and to my brothers for supporting me throughout this journey, and who have helped me grow in several dimensions during these past four years.

Abstract

The advent of metamaterials, e.g. artificially structured materials with physical properties significantly distinct from their bulk counterparts, has ushered in new perspectives in materials science and photonics, and constitutes today a new research frontier. Tailored order at the micro- or nanoscale has unlocked a host of novel opportunities in fields such as harmonic generation, wavefront shaping, and biochemical detection and analysis. Recent progress in dynamic tuning of metamaterial properties ("active" metamaterials) further promise to demultiply their impact, radically redefining functionality in modern optical devices. This progress has heavily relied on thin films, which constitutes fundamental building blocks for many micro- and nanoscale devices today. As dimensions of devices has shrunk, the question of thin film stability has become critical in numerous systems, given that their intrinsic high surface-to-volume ratio makes them particularly subject to instabilities. Such instabilities are potentially responsible for loss of percolation and disordered geometries, hence threatening both metamaterial integrity and functionality. In this thesis, we propose to investigate the stability of thin optically functional films for application in passive and active 2D-metamaterials (metasurfaces) along two complementary persepectives. In a first perspective, we investigate the possibility to guide pre-defined or "template" instabilities in thin chalcogenide films to induce prescribed order at the micro and nanoscale through a diverse set of original processes, effectively providing a novel frame for scalable yet high performance optical devices. In a second perspective, thin film instabilities are supressed in highly unstable liquid metal thin films, opening up novel perspectives for electronic and optical nanostructures.

Keywords

Résumé

Dans ce projet de thèse, nous proposons (i) de prédire la stabilité des couches minces et la dynamique des réarrangements dans divers systèmes et (ii) de déterminer et d'exploiter les propriétés optiques et / ou électroniques découlant des structures résultantes. Dans un premier temps, nous étudions les diverses instabilités des verres de chalcogénure à haut indice pour le développement de métamatériaux par de nouvelles techniques de fabrication, combinant la mécanique des fluides avec l'optique d'une manière nouvelle. Compte tenu que les performances de nombreux dispositifs optiques avancés peuvent être sensibles à des changements des paramètres géométriques de même quelques nanomètres, des modèles théoriques basés sur l'équation d'écoulement des films minces ou directement à partir des équations de Navier-Stokes sont développés pour prédire la réorganisation du matériau à l'échelle nanométrique. S'appuyant sur cette compréhension, un certain nombre de méta-dispositifs photoniques permettant soit un contrôle de phase ou bien supportant des résonances à haut facteur de qualité sont proposées. Ces méta-dispositifs illustrent l'étendu du champ des possibles avec ces méthodes, comprenant entre autre la génération de deuxième harmonique améliorée par résonance, ou bien des bio-capteurs basés sur la détection de l'indice de réfraction. Dans un deuxième temps, nous nous concentrons sur le développement de métamatériaux actifs basés sur l'actionnement mécanique, qui sont actuellement limités par la fragilité de leurs méta-atomes constitutifs. Contrairement aux verres de chalcogénure fragiles, les métaux liquides représentent une classe intéressante de matériaux plasmonique intrinsèquement extensibles, mais qui restent difficile à modéliser à des échelles réduites en raison de leur énergie de surface libre élevée. En controllant finement les dynamiques d'oxydation et de démouillage, un nouveau schéma de fabrication pour des couches minces de métal liquide est mis au point, tandis que la physique derrière le procédé est présentée en détail. Dans un troisième temps, les résultats des métamatériaux et les opportunités sophistiquées offertes par la texturation en photonique sont exploités pour développer de nouvelles stratégies de conception pour les systèmes électriques extensibles avec un comportement électromécanique sur mesure. Cette thèse de doctorat ouvre la voie à des applications dans de nombreux domaines, notamment l'électronique extensible, les cristaux photoniques, les métasurfaces, l'optique non linéaire et l'optoélectronique.

Summary

In this thesis project, we propose (i) to predict thin film stability and rearrangement dynamics in various systems and (ii) to determine and exploit optical and/or electronic properties arising from resulting structures. In a first axis. we investigate and exploit the various instabilities of high index chalcogenide glasses for development of metamaterials through novel fabrication schemes, combining fluid mechanics with optics in novel ways. Given that the performance of many advanced optical devices can be sensitive to changes of even a few nanometers either in size or spacing, theoretical models based on the either on the thin film equation or directly on the Navier-Stokes equations are developed to predict material re-arrangement at the nanoscale. Relying on this process, a number of photonic meta-devices achieving phase control or supporting high Q.F resonances are proposed, with a broad applicative scope including resonantly-enhanced second harmonic generation (SHG), refractive index sensing-based biosensors and magnetic mirrors. In a second axis, we focus on the development of active metamaterials based on mechanical actuation, which are currently limited by the brittleness of their constituent meta-atoms. In opposition to brittle chalcogenide glasses, liquid metals represent an interesting class of intrinsically stretchable plasmonic materials, but that remain challenging to pattern and shape at reduced length scales due to their high free-surface energy. A novel fabrication scheme for thin liquid metal thin films is developed, and the rationale behind the process is investigated. The findings from metamaterials and the sophisticated opportunities offered by simple texturing in photonics are leveraged in a third axis of this research to develop novel design strategies for stretchable electrical systems with tailored electromechnical behavior. This PhD thesis paves the way for application in many fields, including stretchable electronics, photonic crystals, metasurfaces, non-linear optics and opto-electronics.

Outline

This thesis is structured around seven chapters:

In Chapter 1, an introduction to static and dynamic thin film concepts is provided. Thin film instabilities and their morphological consequences are introduced. Finally, the consequence of order is discussed in photonic and electronic materials.

In Chapter 2, the concept of template instability is discussed and two distincts processes based on templated instabilities are presented: in-air templated instabilities (gas - viscous film - solid substrate, also known as dewetting) and in-fiber templated instabilities (viscous film and cladding). Achievable architectures with both processes are presented. The work on in-air template instabilities has already been published in Nature Nanotechnology, and is the result of a collaboration with Tapajyoti Das Gupta and the BIOS laboratory of Prof. H. Altug (EPFL). The engineered wicking work presented in this chapter is not yet published, and will be further developed in collaboration with Pierre-Luc Piveteau. Finally, the work on in-fiber template instabilities is not yet published, and is the result of a collaboration with William Esposito.

In Chapter 3, the physics behind in-air templated instabilities is studied, and two distinct models are presented to understand their evolution. A first linearized model based on comparison between reflow and spinodal time scales is presented to predict the dominant re-arrangement mechanism. In a second stage, we introduce a full non-linear model that can model the evolution of a thin film over a templated substrate during all the stages of the process. The first linearized model has been included in the previous Nature Nanotechnology article. The non-linear modelling work is the result of a fruitful collaboration with the LFMI laboratory led by Prof. Francois Gallaire (EPFL), and is not yet published.

In Chapter 4, we develop a model to understand the dynamics behind in-fiber template instabilities. Relying on a time-discretized Langrangian approach, a numerical scheme simulating the evolution of a corrugated thin film undergoing down scaling by several orders of magnitude is introduced. The derived model provides a basis for a stability criterion of corrugated thin films during thermal drawing. The model was established in collaboration with William Esposito, and has yet to be published.

In Chapter 5, photonic meta-devices exploiting architectures obtained through in-air template instabilities of chalcogenide glasses are investigated. These architecture show the ability to either support high quality factor resonances or achieve fine phase control through tailored interferences, which is harnessed for a number of applications including sensing or second harmonic generation. The combination of works presented in this chapter is largely the product of collaborative work with Tapajyoti Das Gupta and Pierre-Luc Piveteau. Only the work on selenium-based index sensing is published in Nature Nanotechnology, while the work on Arsenic triselenide index sensing, meta-reflectors, and 2π phase control will be published as separate works. The work on second harmonic generation is under review in Nanoscale.

In Chapter 6, the focus is placed on liquid metals, another class of materials which bears potential for mechanically-actuated meta-devices. A novel process to suppress thin film instabilities during thermal evaporation of liquid metals

is introduced, and a stretchable meta-device relying on liquid metals is demonstrated. This work was published in Advanced Functional Materials, and was developed in collaboration with Tapajoyti Das Gupta.

In Chapter 7, the understanding developed in previous works around texturing and photonic metamaterials is leveraged to propose a new approach to tailor electromechanical response in stretchable materials. Relying on an effective medium approach, a numerical scheme is introduced to reversibly associate periodic multi-conductive architectures with electromechanical response. This work is under review in Science Advances.

Table of Contents

List of Figures

List of Tables

Chapter 1   Introduction

1.1   Thin film stability

1.1.1   The thermodynamic limit

1.1.1.1   *Spreading Parameter vs. Hamaker constant*

The study of thin film stability involves the study of interactions between two (or more) immiscible liquids. The interfaces between these liquids is deformable provided the materials have sufficient mobility (e.g. sufficiently low viscosity), and evolve to minimize overall interfacial energy. In the simpler case involving two immiscible viscous fluids, this is equivalent to minimizing the surface-to-volume ratio of the thinner film, yielding spherical interfaces. However, when minimizing interfacial energy between three interfacing media (solid-liquid-air system for instance), the resulting shapes can be significantly more complex.

The surface tension of a single material taken alone in vaccum is characterized by its free surface energy, more commonly referred to as surface tension γ. This surface tension relates a cost associated to the creation of an elementary surface. Surface tension finds its orgin in the imbalance of Van der Waals forces at the interface between the material and vaccum. Let us consider a molecule placed at the interface between a fluid and vacuum, which is pulled away from the surface by an elementary distance δr. Dispersive forces based on induced dipole-induced dipole interaction generate an attractive Van der Waals-type interaction between this molecule and its neighbors. These attractive interactions arise from only a single side of the interface, yielding a resulting force normal to the interface pulling the molecule back towards the liquid phase (see Figure 1.1(a)). Surface tension hence arises from an imbalance in Van der Waals interactions at the interface.

Let us now turn to a thin film configuration involving multiple interfaced materials. The stability of the system can be estimated by resorting to the so-called spreading parameter P, which is combination of the various free surface energies associated to each individual material in vaccum. We consider here a solid substrate S, on top of which is placed a liquid film L and a surrounding atmospheric environment G. The expression of the spreading parameter P reads:

$$P = [E_{substrate}]_{dry} - [E_{substrate}]_{wet} \tag{1.1}$$

$$P = \gamma_{SG} - (\gamma_{SL} + \gamma_{LG}) \tag{1.2}$$

Where $[E_{substrate}]_{dry}$ (respectively $[E_{substrate}]_{wet}$) is the total energy associated to the dry (respectively wet) substrate, and $\gamma_{SG}, \gamma_{SL}, \gamma_{LG}$ are the surface tensions associated respectively to the solid-gas, solid-liquid and liquid-gas interfaces. If the spreading parameter P is positive, the film spontaneously spreads over the substrate (total wetting, net energy minimization for the substrate). In the opposite case where the spreading parameter P is negative, the film forms isolated agglomerates spreading over the substrate (partial wetting, net energy gain for the substrate, see Figure 1.1(b)). To minimize overall system energy in the partial wetting situation, the resulting droplets adopt a specific equilibrium contact
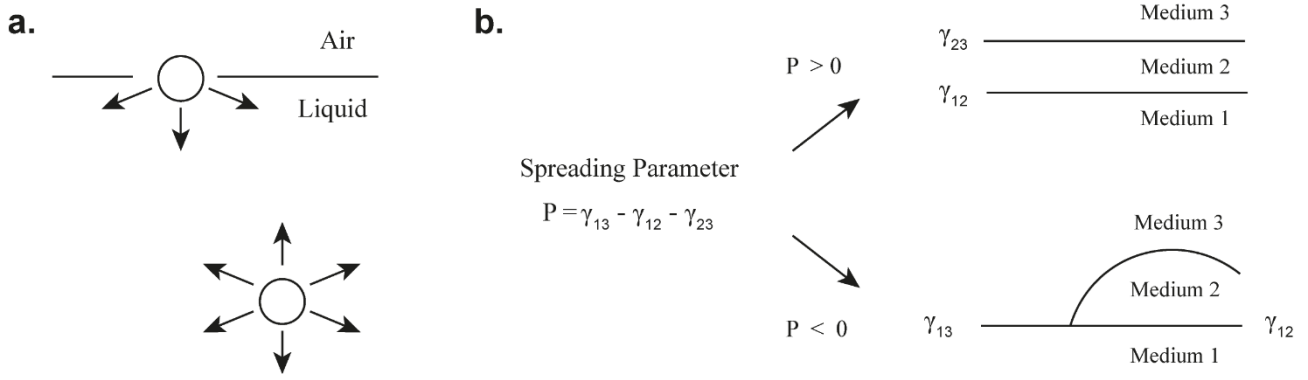
Figure 1.1 – Van der Waals origin of surface tension and spreading parameter. (a) At the interface, a molecule experiences an imbalance in attractive Van der Waals forces with neighborhooding molecules. (b) Illustration of the spreading parameter P: a negative spreading parameter yields a partial wetting situation, while a positive spreading parameter yields complete wetting. Figures inspired from reference 1.

angle with the substrate, written θ_E. This equilibrium contact angle is defined by the balance between three forces acting at the contact line, defined as the interface between all three media. These three forces are associated to each of the three individual surface tension components γ_{SG}, γ_{SL}, and γ_{LG} (denoting respectively solid-gas, solid-liquid and liquid gas interactions). Explicitly writing this equilibrium condition projected along the substrate yields the Thomas-Young equation:

$$\gamma_{SG} - \gamma_{SL} - \gamma_{LG}.\cos\theta_C = 0 \tag{1.3}$$

The Thomas-Young equation is fundamental in all capillary-related effects, in that it relates the contact angle, an observable, with the various energetical parameters of a given system. This allow to re-express the spreading parameter P:

$$P = \gamma_{LG}.(cos(\theta) - 1) \tag{1.4}$$

Let us now consider the idealistic case where the interactions between the various molecules are purely of dispersive nature (e.g. induced dipole-induced dipole interactions). In this particular case, the spreading parameter is intrinsically linked to the polarizability of the liquid and solid materials, given by[1]:

$$P = k\,(\alpha_S - \alpha_L)(\alpha_L) \tag{1.5}$$

An interesting feature of this expression is that it provides immediately a physical criterion for spreading. If the liquid is more polarizable than the substrate, then the liquid partially wets the substrate, otherwise the liquid fully wets the substrate. This bears particular importance in the present thesis: optical materials with large polarizabilities (e.g. high permittivities) constitute the bulk of thin films considered later on. From equation (1.5), it appears that higher relative dielectric constant (and hence refractive index) are associated to higher polarizabilities. Since the high-index optical materials considered in this work (e.g. chalcogenide glasses and liquid metals) have significantly higher refractive indices than the considered substrates (polymers, elastomers or silica glass mostly), they always remain in the partial wetting regime.

The spreading parameter focuses on the evolution of the substrate energy (c.f. equation (1.1)). By taking only the energetic perspective of the substrate, only the liquid-solid interface is considered. This fundamentally neglects the another important interface, namely that between the liquid and the surrounding gas. To account for this second interface, one must turn to a 3D intensive quantity, namely the disjoining pressure (which can equivalently be seen as a volumetric energy). Bringing two interfaces initially situated at infinity from each other to a finite distance d induces an imbalance in Van der Waals interaction and gives rise to the so-called disjoining pressure Π. In the case of two parrallel interfaces:

$$\Pi = \frac{A_{SLV}}{6.\pi.d^3} \tag{1.6}$$

The Hamaker constant A_{SLV} represents the component of the disjoining pressure that is solely dependent on the system materials, while the dependence with respect to d is determined by the system geometry. Contrarily to the spreading parameter P, the Hamaker constant encompasses the whole system energy (both liquid-gas and liquid-solid interfaces), and depends on the distance d between the interfaces. From this first introduction, the Hamaker constant appears as a fundamental constant determining how a three body system evolves. Similarly to the spreading parameter, the Hamaker constant is proportional to the constituent materials' polarizability:

$$A_{i,j} = \pi^2 \rho^i \rho^j C_{i,j} = k\alpha_i\alpha_j \tag{1.7}$$

Where ρ^i (resp. ρ^j) is the atomic densities, α_i (resp. α_j) is the polarizability of material i (resp. j), and $C_{i,j}$ is the particle-particle pair interaction coefficient, and k is a constant coefficient. The Hamaker constant for two bodies S and G interacting through a phase L can be further re-expressed:

$$A_{SLV} = A_{SV} + A_{LL} - A_{SL} - A_{LV} \tag{1.8}$$

$$A_{SLV} \propto (\alpha_S - \alpha_L)(\alpha_L - \alpha_V) \tag{1.9}$$

Depending on the sign of the Hamaker constant, one can, in a very similar way to the spreading parameter, gain an idea of film stability through the comparative values of material polarizability. If $A>0$, bringing the two interfaces close to each other stabilizes the overall system, and the thin film is hence stable. In the opposite configuration where $A<0$, bringing the two interfaces together has a destabilizing effect, and the film is unstable. In the next section, methods to accurately predict the Hamaker constant value will be discussed.

1.1.1.2 *Hamaker constant calculation: the Lifshitz approach*

To correctly quantify the Hamaker constant, it is necessary to develop the resulting force arising from London-van der Waals interactions. The London-Van der Waals force between two atoms in free space (simply referred to as Van der Waals force in the rest of this work) stems from the interaction between the electronic shells of interacting molecules, which reciprocally create induced dipoles. The associated force is completely determined by the frequency-dependent electric polarizabilities of the individual atoms (e.g. the ability to deform the electronic cloud) and by the properties of the medium through which electromagnetic interactions propagate. In the classical Van der Waals approach, one calculates the total resulting force by simply adding the various pairwise intermolecular potential, implicitly assuming pairwise additivity (so-called Hamaker procedure[2]). This assumption is valid for materials with sufficiently low densities (e.g. gases), but is not accurate for the vast majority of condensed materials. To address this issue and provide a correct estimation of Van der Waals forces in condensed media, a theory has been developed by Lifschitz[3] (and further developed by Dzyaloshinskii[7], Ninham and Parsegian[4]), which includes many-body forces by treating the bodies as a continuous medium with intensive parameters (e.g. intensive permittivites and polarizabilities). Lifschitz theory is not based on the assumption of pairwise additivity, and takes into account the influence of neighbors on each pair intermolecular force. All local electromagnetic fluctuations are treated as a global electromagnetic field varying over the whole system. Relying on the material frequency-dependent permittivities ε, the potential w between two spheres 1 and 2 (radii a_1 and a_2) interacting through a medium 3 can be calculated by taking all absprotion frequencies into account[5,6,7,8]:

$$w(r) = -\frac{C_{VDW}}{r^6} = -\frac{3kTa_1{}^3a_2{}^3}{r^6}\frac{\varepsilon_1(0) - \varepsilon_3(0)}{\varepsilon_1(0) + \varepsilon_3(0)} \cdot \frac{\varepsilon_2(0) - \varepsilon_3(0)}{\varepsilon_2(0) + \varepsilon_3(0)} - \frac{3ha_1{}^3a_2{}^3}{\pi r^6}\int_{\nu=0}^{\infty}\frac{\varepsilon_1(i\xi) - \varepsilon_3(i\xi)}{\varepsilon_1(i\xi) + \varepsilon_3(i\xi)} \cdot \frac{\varepsilon_2(i\xi) - \varepsilon_3(i\xi)}{\varepsilon_2(i\xi) + \varepsilon_3(i\xi)}d\nu \quad (1.10)$$

where $\varepsilon_1(i\nu_n)$, $\varepsilon_2(i\nu_n)$ and $\varepsilon_3(i\nu_n)$ are the (real) dielectric constants associated to media 1 and 2, and 3. A particularly interesting case is when all three materials have one single dominant absorption frequency ν_e, typically in the UV-visible region. In this case, the dielectric permittivities can be re-expressed[8]:

$$\varepsilon(i\nu) = 1 + \frac{n^2 - 1}{1 + (\nu/\nu_e)^2} \quad (1.11)$$

Further developments enable to identify a Hamaker constant $A_{\nu>0}$ associated to all positive frequencies (pure dispersive contributions) and another Hamaker constant $A_{\nu=0}$ associated to the zero-frequency (pure dipolar contributions):

$$A = A_{\nu-0} + A_{\nu>0} \approx \frac{3kT}{4}\left(\frac{\varepsilon_1(0) - \varepsilon_3(0)}{\varepsilon_1(0) + \varepsilon_3(0)}\right)\left(\frac{\varepsilon_2(0) - \varepsilon_3(0)}{\varepsilon_2(0) + \varepsilon_3(0)}\right) + \frac{3h\nu_e}{8\sqrt{2}}\frac{(n_1^2 - n_3^2)(n_2^2 - n_3^2)}{(n_1^2 + n_3^2)^{\frac{1}{2}}(n_2^2 + n_3^2)^{\frac{1}{2}}\left((n_1^2 + n_3^2)^{\frac{1}{2}} + (n_2^2 + n_3^2)^{\frac{1}{2}}\right)} \quad (1.12)$$

The previous derivation of the Hamaker Constant above has been done in the case of two dielectric spheres embedded in a medium 3. It has however been shown that this relationship holds actually for arbitrary geometries[9], and thus also in particular for thin film configurations. The hypothesis of a single peak absorption frequency for the various materials considered is particularly adapted for chalcogenide glasses studied in this thesis, since they are commonly associated to large transparency window beyond ~ 600 nm, and show strong absorption in the UV. A particularly important and useful feature of the Lifschitz approach is that it can provide an effective Hamaker constant which can simply be re-injected in the classical Hamaker procedure (e.g. direct summation based on pairwise additivity of element unit volumes). This feature of the Lifschitz approach will be further exploited in this thesis work.

The above result provides an interesting and especially useful relationship relating the refractive indices and static dielectric constants of the three materials (n_1, n_2, n_3, $\varepsilon_1(0)$, $\varepsilon_2(0)$, $\varepsilon_3(0)$) with the Hamaker constant, which fundamentally determines the surface interactions between the various materials. From a broader perspective, the relationship above enables to link the material's optical properties with their surface properties. This thesis work will be dealing with both properties: (i) surface properties to tailor adhesion and self-assembly processes and (ii) optical properties to investigate photonic applications.

1.1.2   Hydrodynamics of thin films

Provided an unstable thin film (A<0) gains enough mobility to rearrange, different elements may drive its flow. In this section, the two main drivers for flow as well as the master equation for thin fluid flow are introduced.

1.1.2.1   *Driving Forces for flow*

A first drive for thin fluid flow is associated to the Laplace pressure, which arises from the curvature of the free interface(s). Considering the air-liquid interface, corrugations increase the overall surface area and hence the system's global surface energy. The Laplace pressure will consistenly smoothen the film to reduce local curvature. To understand the origins of this pressure, let us consider a molecule placed at a local height minimum. This molecule will experience

attractive interactions with its neighbors, giving rise to a resulting elementary force dF₁ normal to the interface. An identical molecule placed at a local height maximum will feel a reduced resulting elementary force dF₂ from the interaction with its distinct surrounding. The difference dF = dF₁-dF₂ gives rises to an interfacial pressure P_L (see Figure 1.2). This pressure can be directly linked to the curvature κ of the interface:

$$P_L = \gamma\kappa \tag{1.13}$$

Where γ is the interfacial tension between liquid and air. This pressure can be either positive or negative depending on the sign of curvature, driving the flow in either direction of the interface. As an important note, Laplace pressure arises solely from the considerations of a single interface.
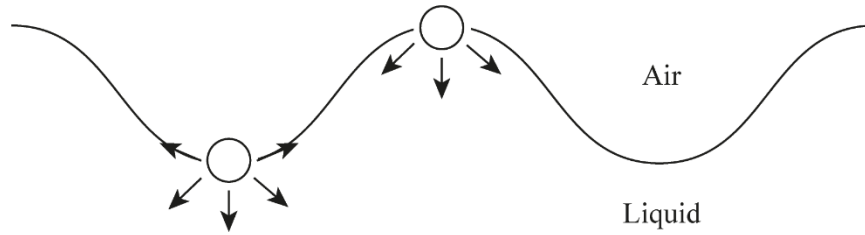
Figure 1.2 – Microscopic origin of Laplace pressure. A molecule at a film crest will experience a stronger pull back towards the film than a molecule place at a film through. The resulting difference in local force is at the origin of Laplace pressure.

The second drive for thin film flow stems from the imbalance in Van der Waals interactions when bringing two interfaces close to each other. When the Hamaker constant is negative, this imbalance gives rise to a disjoining pressure Π, which may also drive film re-arrangement to minimize the overall system energy. The disjoining pressure drives local film thinning and potential breakup for sufficienty high viscosities. In the case of a flat thin film[10]:

$$\Pi(d) = -\frac{A_{SLV}}{6.\pi.d^3} \tag{1.14}$$

1.1.2.2 *Deriving the thin film equation*

Let us now turn to the evolution of a thin viscous film on a plane substrate. The flow dynamics are guided by the Navier-Stokes equation:

$$\frac{\partial(\rho\boldsymbol{V})}{\partial t} + \rho(\boldsymbol{\nabla}.\boldsymbol{V})\boldsymbol{V} = \boldsymbol{\nabla}.(\eta(\boldsymbol{\nabla}\,\boldsymbol{V} + (\boldsymbol{\nabla}\,\boldsymbol{V})^{\mathrm{T}}) - p\boldsymbol{I}) + \rho\boldsymbol{g} \tag{1.15}$$

Where ρ is the volumetric mass, $\boldsymbol{V}$ is the velocity, p is the pressure, $\boldsymbol{I}$ the identity tensor, $\boldsymbol{g}$ the gravitational field. For thin films, gravity is typically neglected given the capillary lengths $L = \sqrt{\gamma/\rho g}$ involved, which are considerably larger than the film thicknesses (t) considered in this work ($t < 1\ \mu m$). Considering a typical polymeric viscous fluid with $\gamma \sim 30$ mN/m and $\rho \sim 10^3$ kg.m⁻³, the capillary length amounts to $L \sim 2.10^{-3}\ m >> t \sim 1\ \mu m$. The pressure gradient term includes multiple contributions, namely the Laplace pressure P_L and the disjoining pressure Π.

The "brute" Navier-Stokes equation is considerably problematic to solve, as it admits no general solution. The thin film equation is a reformulation and simplification of the Navier-Stokes equation in the case of a thin viscous Newtonian, incompressible film on a flat substrate. The thin film equation relies on the lubrication approximation: the length scales along the surface L_x, L_y are considered much larger than those normal to the surface L_z. The following boundary

conditions are usually considered: (i) absence of slip at the interface between the liquid and the substrate; (ii) no shear at the liquid-air interface; (iii) independence of pressure gradient on the z-coordinate (normal to the flat film). The derivation of the thin film combines the Navier –Stokes equation with the mass conservation equation in stationary state under the previously stated conditions:

$$\nabla \cdot (\rho \boldsymbol{V}) = 0 \tag{1.16}$$
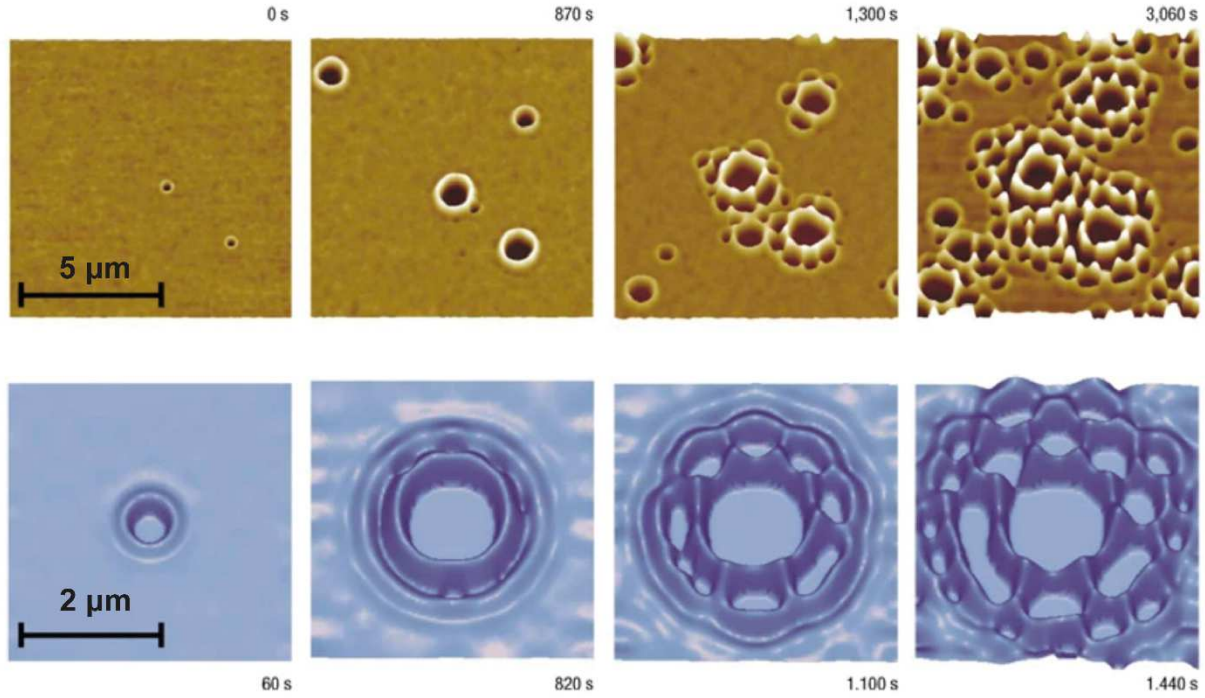
Figure 1.3 – Simulation of dewetting on flat substrate based on precursor film approach. Experimental (top) and simulated (bottom) thickness profile of a PS film over a Si wafer as a function of time. Simulations are based on precursor film approach, implementing a Lennard-Jones type potential with a residual thickness layer to avoid any divergence of φ, φ''. Adapted from reference 11.

Developments yield the (scalar) thin film equation linking pressure p, film height h, and film viscosity μ:

$$\frac{\partial h}{\partial t} = -\frac{1}{3\mu} \nabla \cdot (h^3 \nabla p) \tag{1.17}$$

The thin film equation is derived in the 2D case in the next section in more details. Simulating full dynamics of thin film evolution based on the thin film equation have proved particularly challenging, for a number of reasons: (i) there is no guarantee that non-negative solutions to the equations exists; (ii) numerical schemes to preserve the non-negativity of solutions are challenging to develop in multiple dimensions; (iii) 3D implementations are particularly costly in computational terms. Recently, numerical schemes based on the Lennard-Jones potential have demonstrated the possibility to qualitatively reproduce dynamic evolution and final patterns observed by dewetting[11]. Until now, investigations into the dynamics of dewetting have essentially focused on flat solid substrates, with a free interface between the film and the superstrate. One of the objectives of the present work will be to adapt the current framework to less conventional systems where dewetting takes place, such as systems with (i) a templated substrate, (ii) a viscous superstrate instead of air, and (iii) a system with modulated thickness undergoing continuous down-scaling.

1.1.2.3 *Linear stability analysis on a textured substrate*

Let us start by considering a film of initial thickness h_0 on top of a substrate with a slowly varying texture, as depicted in Figure 1.4. Two types of forces are exerted on this film: the disjoining pressure ϕ, which represents an effective molecular interaction between the film and the substrate, and the Laplace pressure p_L, which arises from curvature gradients on the film surface profile.
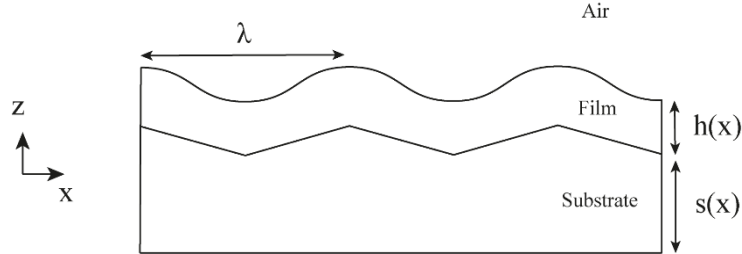
Figure 1.4 – Schematic of a film undergoing spinodal instability over a flat substrate. The film has a thickness height h(x), and is placed over a substrate with spatially varying height s(x). We consider the evolution of perturbations of wavelength λ at thefilm's free surface.

Let z be the vertical coordinate, $s(x) = S_0$ be the local height of the substrate, $h(x)$ the film thickness, with:

$$z_x = z - s(x) \tag{1.18}$$

We can start the analysis by laying down various hypotheses.[12,13,14,15,16] Firstly, the hypotheses made in Section 1.1.2.2 are enforced, yielding a simplified expression of the Laplace pressure p_L and specific boundary conditions:

$$p_L(x) = \gamma \kappa = -\gamma \partial_{z_x z_x}(h + s) \tag{1.19}$$

$$v_z(z_i = 0) = 0 \tag{1.20}$$

$$\partial_{z_x} v_x(z_x = h) = 0 \tag{1.21}$$

$$\partial_{z_x} P = 0 \tag{1.22}$$

These assumptions are completed by two additional hypotheses; namely that (i) the film material is considered Newtonian and incompressible and (ii) that inertia is neglected, as supported by the film's high viscosity during the annealing step around the glass transition temperature. The total pressure P in the film amounts to:

$$P = p_L + \phi(z) - \phi(h(x)) \tag{1.23}$$

Using the assumption (1.22) above, the projection of the Navier-Stokes equation along the x-axis reads:[12,13,14,15]

$$\partial_x P = \eta . \partial_{zz} v_x \tag{1.24}$$

By integration, we can calculate the classic Poiseuille flow velocity profile v_x. With the boundary conditions (1.20) and (1.21), a integration over the film height yields the flux J:

$$J(x, t) = \int_0^{h(x)} v_x(z_i) \, dz_i = -\frac{1}{3\eta} . \partial_{xx} P . h^3(x) \tag{1.25}$$

The incompressibility of the fluid yields the time-evolution equation of the film along the x-axis[12,13,14,15,16]:

$$\partial_t h + \partial_x \left(\frac{h^3}{3\eta} . \partial_x (\gamma . \partial_{xx} \zeta + \phi(h)) \right) = 0 \tag{1.26}$$

The equation (1.26) is the thin film equation in 2D. It is interesting to note that this equation is highly similar to the Cahn-Hillard equation, which describes concentration in binary mixtures as a function of time. In the Cahn-Hillard equation,

binary mixture may phase separate based on the free enthalply of mixing, a phenomenon commonly referred to as spinodal decomposition. Similarly to the binary process, the propagation of instabilities at the surface of a film are referred to as spinodal instabilities.

Let us now study the evolution of a small perturbation ($\varepsilon \ll h_0$) evolving at the fluid surface with a wavenumber $k = 2\pi/\lambda$ and amplitude $\varepsilon(t)$ over a flat substrate ($s(x) = s_0$):

$$h(t) = h_0 + \varepsilon(t).sin(kx) \tag{1.27}$$

At the initial stage of the flow, when $h(x)$ is still comparable with h_0, we can linearize the equation (1.26) to obtain[14,15]:

$$\partial_t \varepsilon = \frac{h_0^3}{3\eta}k^2\big(-\gamma k^2 + \partial_x \phi(h_0)\big)\varepsilon(t) + O(\varepsilon^2) \tag{1.28}$$

As apparent from equation (1.28), the stability of the film essentially depends on the sign of the Van der Waals potential. If $\partial_x \phi(h_0) \le 0$, then the perturbation is damped for all wavevectors k and the film is stable. However, if $\partial_x \phi(h_0) > 0$, there can exist a range of wavevectors $0 < k < k_c$ for which a perturbation is amplified. We can identify the time scale associated with the initial stage of spinodal dewetting[14,15]:

$$\tau_{sp} = \frac{3\eta}{\gamma h_0^3 k^2(k_c^2 - k^2)} \tag{1.29}$$

With

$$k_c = \sqrt{\frac{1}{\gamma}\frac{\partial \phi}{\partial x}(h_0)} \tag{1.30}$$

Instead of estimating its effect analytically[17,154,155], we will rely in this work on experimental results to quantify directly τ_{sp}. In the case where spinodal dewetting is favored (e.g. $0 < k < k_c$ and $\partial_x \phi(h_0) > 0$), pinch-off is due to the growth of a particular wavelength λ_m that grows fastest, ultimately defining a characteristic distance in dewetted patterns. The wavelength λ_m of the fastest growing perturbation ε verifies:

$$\frac{\lambda_m}{\sqrt{2}} = \lambda_c = \frac{2\pi}{k_c} \tag{1.31}$$

The spinodal instability time scale associated to this characteristic wavelength λ_m may thus be rewritten :

$$\tau_{sp}(k_m) = \frac{3\eta}{\gamma h_0^3 k_m^4} \tag{1.32}$$

Equation (1.32) established an interesting linear dependence between time scale τ_{sp} and viscosity η, which will be exploited later on in this work. Introducing ε_0, the initial perturbation amplitude, the solution to equation (1.28) reads:

$$\varepsilon(t) = \varepsilon_0 e^{\frac{t}{\tau_{sp}}} \tag{1.33}$$

It is important to note that the growth of spinodal instabilities arises in this case from molecular interactions and not curvature gradients. To conclude, we have hence identified conditions for which a flat film may be unstable on its substrate based on linear stability analysis.

1.1.3 Dewetting patterns: the rise of disorder

1.1.3.1 *On the role of the Van der Waals Potential in dewetting of amorphous materials*

We have previously introduced in section 1.1.1 the concept of Hamaker constant and further detailed in section 1.1.2.1 that the imbalance in Van der Waals interactions induces a disjoining pressure. The disjoining pressure, akin to the Van der Waals potential Φ_{VdW} , may drive spinodal instabilities in thin liquid films. The Van der Waals potential is fundamental in several ways, since it determines both dynamic parameters (e.g. which dewetting mechanism unfolds preferentially) and equilibrium parameters (e.g. contact angle as well as final dewetting patterns).

The Van der Waals potential is at heart associated to the dispersive mutual interaction between electronic shells, as discussed in Section 1.1.1.2. In the simplifying frame of the Lennard-Jones potential, the interaction potential $w_{i,j}$, between two atoms i and j spaced by a distance r can classically be understood as a balance between long-range attractive forces proportional to r^{-6}, and short range repulsive interactions (known as Born Repulsion), proportional to r^{-12}. The balance between these two terms defines an equilibrium radius r_{eq}, assimilated to the atomic sphere radius in the hard shells model. The resulting forces between two atoms is given by:

$$w_{i,j}(r) = \frac{B_{i,j}}{r^{12}} - \frac{C_{i,j}}{r^6} \tag{1.34}$$

Where $B_{i,j}$ and $C_{i,j}$ are constant coefficients solely dependent on the nature of i and j. Assuming the medium is isotropic and homogeneous, one can determine the potential $F_{i,j}$ associated to the interaction between an elementary volume of specie i and a plane P of elementary thickness ds of specie j situated a distance s apart by simply integrating the potential $w_{i,j}$ in three dimensions using cylindrical coordinates:

$$F_{i,j}(s) = \rho^i \rho^j \int_{r=s}^{\infty} \int_{\theta=0}^{2\pi} w_{i,j}(r) r\, dr\, d\theta \tag{1.35}$$

$$F_{i,j}(s) = \rho^i \rho^j \int_{s}^{\infty} 2\pi r w_{i,j}(r) dr = -\frac{\rho^i \rho^j C_{i,j} 2\pi}{4s^4} + \frac{\rho^i \rho^j B_{i,j} 2\pi}{10 s^{10}} \tag{1.36}$$

Where ρ^i and ρ^j are the densities associated to species i and j respectively. The term in s^{-10} is commonly neglected at distances significantly larger that the equilibrium radius, but is kept here for the sake of generality. Now integrating the contributions of all planes from a distance $s = R$ to infinity, we obtain the overall interaction potential $W_{i,j}$:

$$W_{i,j}(s) = \int_{s=R}^{\infty} F_{i,j}(s) ds \tag{1.37}$$

$$W_{i,j}(s) = -\frac{\rho^i \rho^j C_{i,j} 2\pi}{4} \int_{s=R}^{\infty} \frac{ds}{s^4} + \frac{\rho^i \rho^j B_{i,j} 2\pi}{10} \int_{s=R}^{\infty} \frac{ds}{s^{10}} \tag{1.38}$$

$$W_{i,j}(s) = -\frac{\rho^i \rho^j C_{i,j} 2\pi}{12 R^3} + \frac{\rho^i \rho^j B_{i,j} 2\pi}{90 R^9} = \frac{B}{R^9} - \frac{A}{6\pi R^3} \tag{1.39}$$

We have identified the Hamaker constant $A = \rho^i \rho^j C_{i,j} \pi^2$ as well as the Born repulsion energy $B = \rho^i \rho^j B_{i,j} 2\pi/90$. When neglecting the R^{-9} term, we now recognize the form of the potential introduced in Section 1.1.2.1. This modelling of interaction between two atoms is largely simplified, as it does not address properly the multi-body problem as soon as more than two atoms are involved. However, as discussed in section 1.1.1.2, the multi-body problem can simply be taken into account using a modified effective Hamaker constant and treating the interacting medium as continuous, which is assumed in the rest of this work. The calculation procedure above is known as the Hamaker procedure, and can be applied to continuous media using the effective Hamaker constant, e.g. the medium's intensive properties. When the Hamaker constant is negative, the film can reduce its energy by thinning, ultimately leading to dewetting. Depending on the comparative influence of the constants A and B, different interface potential arise, which give rise to different dewetting scenerios[18] (See Figure 1.5).

In the first case where the interface potential is continuously increasing from its minimum to a distance at infinity, film thinning is always favoured and the film is systematically unstable. This corresponds to a situation where the second derivative of the Van der Waals potential is negative for the initial film thickness h_0 considered: $\Phi_{VdW}''(h = h_0) < 0$. In this situation, dewetting may lead to the spinodal instabilities discussed in section 1.1.2.3. In this case, all surface waves are amplified. However, similarly to the Rayleigh Plateau instability, a characteristic wavelength grows fastest which becomes dominant during the dewetting process. While this bi-continuous pattern arises essentially at the onset of dewetting, it has been shown that the most commonly observed mechanism in this situation corresponds to the re-arrangement of this initial bi-dimensional wavy pattern into a set on circular holes and rims. In particular cases only, the characteristic order may be present in the final microstructure. In this thesis, we report the observation of several patterns with a characteristic order in the final microstructure. This constitutes a likely indication that the system undergoes spinodal dewetting, followed by a re-arrangment of the wavy pattern into holes and rims with a very characteristic spacing, that we assimilate in first approximation to the spinodal wavelength[18].

In a second case, the interface potential has a local maxima at finite thickness. In energetic terms, this implies that the film is unstable for small thicknesses only. For thicknesses beyond this local maxima, an energy barrier has to be overcome for spontaneous film thinning. Local defects are required to induce dewetting, which can occur for instance due to the presence of a dust particle. This regime is commonly referred to as "heterogeneous nucleation". Contrarily to
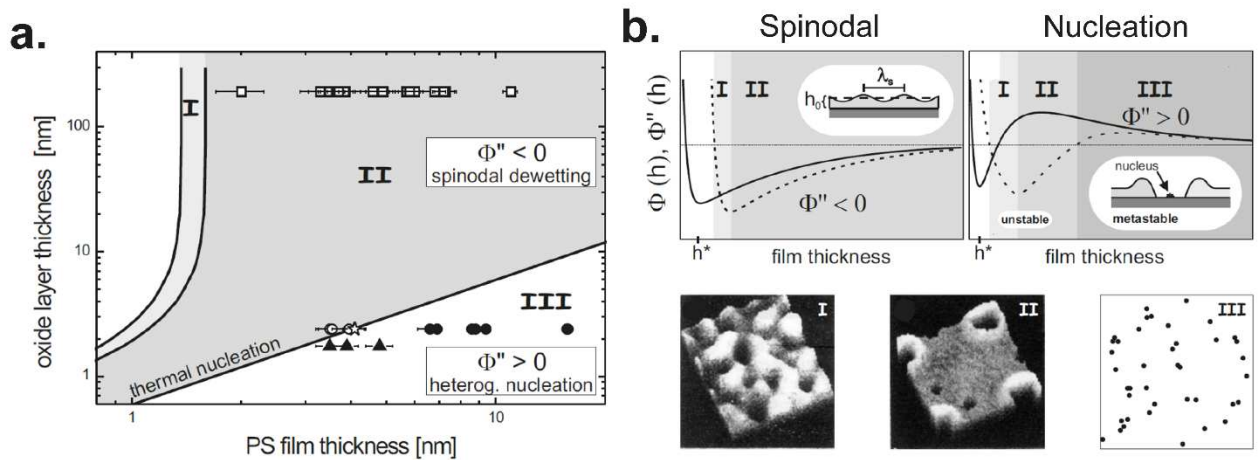
Figure 1.5 – Influence of Van der Waals potential on dewetting patterns. (a) Stability graph of polystyrene (PS) films on Si wafers, as Si wafer oxide layer thickness and PS film thickness. The potential curvature defines the stability criterion. Adapted from ref. 10. (b) Representation of the potential φ and its corresponding curvature φ'' as a function of PS thickness. Three regimes can be identified based on the value of φ'': spinodal regime (bttom left image), Thermal nucleation (bottom middle image) and (c) heterogeneous nucleation of holes (bottom right image). Adapted from ref. 10.

1.1. Thin film stability

spinodal dewetting, nucleation of holes is a random process, and there is a priori no correlation between position of holes. In the case where the initial film thickness yields a Van der Waals potential close to its local maximum, providing a slight additional energy (e.g. thermal energy) is enough for the film to overcome the energy barrier and lead to nucleation. This peculiar situation is referred to as thermal dewetting. It gives rise to holes which appear gradually with time (e.g. different size of holes are apparent in the final microstructure). This is in stark contrast with the case of spinodal dewetting, where the surface waves are amplified over the whole film, and hence holes nucleate within a short time span. Similarly, heterogeneous nucleation gives rise to film nucleation within a restrained time span. It is thus the shape of the potential which dictates the morphological evolution and the resulting patterns (i.e. isolated holes and formation of droplets in polygonal networks, or bicontinuous ridges leading to spinodal dewetting). Therefore, on a chemically heterogeneous substrate, both types of pattern can coexist, which is observed in this work.

When a film dewets, it is important to note that its corresponding Van der Waals potential does not diverge, essentially thanks to the presence of the Born repulsion term. The films thins down to an equilibrium thickness h_{eq} in the holes, which implies consequently that dewetting "holes" are still filled with film material of very reduced thickness (typically a few Angströms). This is a particularly important element for dewetting simulations, which have thus far heavily relied on this peculiarity to avoid divergence issues.

When two atoms or molecules dispersively interact over an increased distance L orders of magnitude larger than the characterisitic atomic spacing, electromagnetic retardation effects may arise. Dispersive interactions are based on an induced dipole-induced dipole interaction, which takes a finite amount of time to travel between both elements. If the time for electromagnetic interaction to travel between both elements is significantly larger than the period of the fluctuating dipole itself, then the attractive interaction may be significantly reduced. The Van der Waals potential presented in (1.34) assumes a non-retarded Van der Waals interaction. Considering a revolution frequency of 3.10^{15} Hz (c.f. Section 1.1.1.2), the characteristic distance associated to retardation effects corresponds to d~3.10^8/3.10^{15}~10^{-7} m. Since thin films considered in this work are essentially initially thicker than 10 nm, retardation effects arise in all thin films considered in this work. However, given the weak effect of Van der Waals forces above thickness of order d, these retardation effects are not considered for the sake of simplicity.

1.1.3.2 *On the role of materials in dewetting patterns*

The interplay between Laplace pressure and destabilizing Van der Waals interactions in thin films evolving on over flat substrates give rise to a wide variety of characteristic patterns. Dewetting has been previously studied in the frame of polycrystalline and single crystalline films (solid-state dewetting), as well as in the frame of amorphous films (viscous dewetting). In a general manner, dewetting occurs in three stages: (i) nucleation of holes; (ii) growth of holes; (iii) pinch off into droplet arrays. However, the characteristic patterns obtained in the final dewetting stage are starkly dependent on the thin film's microstructure (e.g. single crystal, polycrystalline, amorphous) and dewetting mechanism.

In the case of single crystal dewetting, peculiar dewetting patterns arise due to the anisotropic surface energies involved.[19,20,21,22,23,24] Systems studied include Ni single crystal on MgO[21,24], silicon on insulator[22], or Si-Ge alloys on Si substrates[23]. Anisotropic free surface energies yields an intrinsic anisotropy in the dewetting patterns, and brings about a unique set of novel instabilities such as corner or faceting instabilities. This can be exploited to drive the dewetting along

specific directions (see Figure 1.6(a)). Dewetting in the single crystal state is essentially driven by surface diffusion[19,22] with a flux J along the surfaces given by equation (1.40):

$$J = -\left(\frac{D_s \gamma_f N_s \Omega}{kT}\right) \vec{\nabla}_s \kappa \qquad (1.40)$$

where D_s is the surface diffusivity, γ_f is the surface energy, N_s is the number of surface atoms per area, Ω is the atomic volume, k is Boltzmann's constant, T is temperature, and κ is the local surface curvature. Equation (1.41) ensues for the evolution of film height h:

$$\frac{\partial h}{\partial t} = -\left(\frac{D_s \gamma_f N_s \Omega}{kT}\right) \left(\vec{\nabla}_s^2\right)^2 h \qquad (1.41)$$

This equation of motion constitutes a marked difference with the re-arrangement of amorphous materials, which are driven by viscous flow (c.f. equation (1.17)) rather than surface diffusion. Another important difference is that the influence of Van der Waals forces are commonly neglected for single-crystal dewetting: the anisotropy in surface energy largely drives the re-arrangement process, even at reduced thicknesses[19]. Nucleation in single crystals remains however poorly understood[25], which explains why a large focus has been placed on studying the evolution of pre-patterned single-crystal films. These studies have demonstrated interesting (although limited) perspectives to control the final dewetting pattern. In the polycrystalline case, dewetting dynamics follow a similar equation of motion. The resulting patterns change markedly, as diffusion can happen along the grain boundaries.[19,26,27,28] Grain boundaries play a particular role in the hole formation process, acting as preferential channels for flow. Given that grain boundaries are associated to varying interfacial energies, there is an intrinsically random component to polycrystalline dewetting (see Figure 1.6(b)). Some studies have for instance demonstrated that fingering instability was influenced by the grain boundaries. Film pre-patterning into patches (based on Au or Ag for instance) also demonstrated final patterns which where largely influenced by grain size, inducing irregularity in the final dewetting patterns.

Dewetting of amorphous thin films[29,30,31,32,33,34,35] unfold according to a distinct process, e.g. viscous flow rather than surface diffusion. Surface energy in thin viscous films is isotropic, which constitutes a marked difference with polycrystalline metal films. Dewetting thin film studies have largely focused on the development and evolution of instabilities at their surface, mostly relying on polymeric systems such as polystyrene (PS)[29,31,33], polydimethylsiloxane (PDMS)[32], but also metal melts such as gold or copper.[34] The presence or absence of slip is an important element to take into account when modelling amorphous dewetting, as it has been shown to lead to marked differences in dewetting behavior and final microstructure[29].

Two main type of characteristic patterns arise in dewetting of amorphous materials[29,30,33,34,35]: (i) spinodal dewetting patterns, characterized by a single characteristic spacing (see Figure 1.6(c)) and (ii) tessellation patterns which consist of nanoparticle arrays arranged in random polygonal shapes (see Figure 1.6(c)-(d)). The rise of either of these dewetting regimes is essentially dependent on film thickness and curvature of the Van der Waals potential, as discussed in the previous section. It is important to note that destabilizing Van der Waals forces are relatively weak until thicknesses <10 nm. To illustrate this point let us consider a film thickness of 50 nm with a typical Hamaker Constant A~10^{-19} J. Based on expression (1.14), the disjoining pressure Π amounts to ~ 40 Pa, a considerably small pressure in absolute value. In the case of spinodal dewetting patterns, the characteristic wavelength observed upon dewetting is directly linked (although not identical) to the growth of unstable small perturbations over the whole substrate. In contrast, the more common tessellation figures observed at larger film thicknesses are the consequence of random local nucleation and growth of

holes spurred by local defects. As these holes grow, the material accumulates in "fingers" along the polygonal edge, giving rise to Rayleigh instability and ultimate formation of droplets.
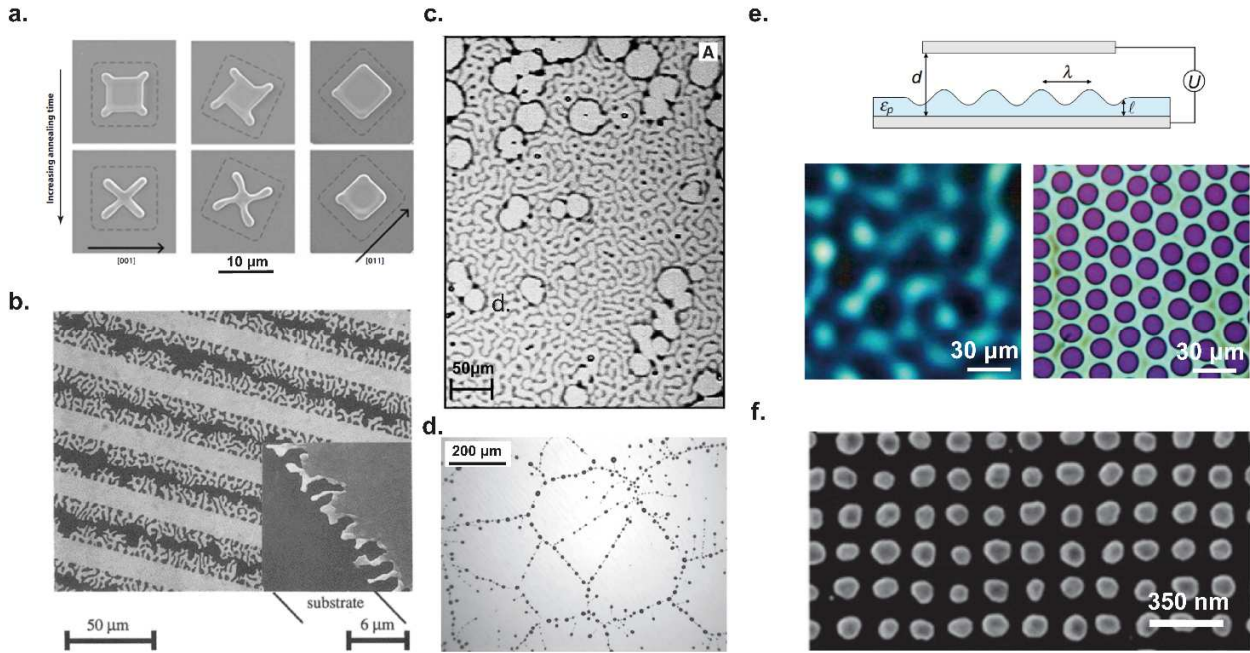
Figure 1.6 – Variety of dewetting patterns. (a) Time evolution of 120 nm –thick Ni single crystal square patches with three different crystal orientations. Adapted from ref 24. (b) Optical microscope image of 80nm polycrystalline Au films pre-patterned into 25 μm wide stripes during dewetting. Adapted from ref 26. (c) Dewetting of liquid crystal films undergoing combined nucleation/growth of holes, indetified by the large circular patterns, and spinodal dewetting, identified by the shorth range undulative modes. Adapted from ref 35. (d) Equilibrium dewetting patterns of 110 nm –thick Polystyrene (PS) film on a hydrophobic Si wafer. Adapted from ref 29. (e) Experimental demonstration of Electrohydrodnyamic instabilities, inducing a controlled characteristic wavelength in dewetting patterns. (Top) schematic of the experimental setup and (bottom) optical microscopy images of PS film dewetting under an electric field E=U/d. The thickness and applied potential is increased from the bottom left to the bottom right figure, so that PS columns touching joining the two electrodes form in the bottom right micrograph. Adapted from ref. 32. (f) 21 nm polycrystalline gold film dewetted on Si wafer patterned with periodic inverted pyramids. Adpated from ref. 28.

Is it possible to induce order from such re-arrangement mechanisms? This question has been a longstanding question in the field, and has been the object of numerous studies. An interesting recent development has been in the field of electro-hydrodynamic instabilities[32]. Applying an intense spatially patterned electric field between the interfaces of a thin dielectric film, one can polarize its constituent material and induce instabilities with well-defined spacings (see Figure 1.6(e)). Other interesting endeavors include dewetting of thin polycrystalline metal films onto pre-patterned substrates, which can yield (within a specific thickness range, determined by the pattern geometrical parameters) a relatively well-ordered arrangement of particles, both in terms of position and spacings[28] (see Figure 1.6(f)). Nevertheless, the polycrystalline nature of the dewetted material implies a poor reproducibility, significant particle size distributions. The overall limited control observed in polycrystalline dewetting has inhibited further investigations with alternative parameters and materials.

1.1.3.3 *On the role of contact angles*

The contact angle between the film and the substrate in the case of a substrate-film-air system is a central parameter that links microscopic (e.g. Van der Waals Potential) with macroscopic properties (e.g. contact angle). The contact angle value is key to determine both the dynamics as well as the equilibrium structures that arise upon film dewetting. [1,10,19] Let us consider a dewetted film at equilibrium composed of droplets on a surface. While the droplets may appear isolated, a thin film of thickness $h_{eq} \ll R$ (where R is the droplet characteristic size) links the various droplets

together, effectively defining a single film with height modulations that remain strictly positive over the whole film. This film, also known as the precursor film, has a thickness typically in the angstrom range, as measured in several dewetted systems.[10,18] This precursor film is particularly relevant for several reasons, First, this film enables the coarsening of droplets with time, an important phenomenon also known as Oswald ripening. Secondly, the precursor film enables to establish a relationship between contact angle and the Van der Waals potential $\varphi(h)$. Assuming that the disjoining pressure arises from a Lennard-Jones potential, one can write:

$$\varphi(h) = \frac{B}{h^8} - \frac{A}{12\pi h^2} \tag{1.42}$$

where $A = A_{123}$ is the Hamaker constant of the system substrate (1) - film (2) - air (3) and B is the Born coefficient, that embed respectively the long range attractive and short range repulsive forces. It should be noted that many approaches exist to express the intermolecular potential ϕ combining the influence of long and short range forces[36]. The previously introduced Lennard-Jones potential is linked to the disjoining pressure Π through:

$$\Pi = -\frac{\partial \varphi}{\partial h} = \frac{8B}{h^9} - \frac{A}{6\pi h^3} \tag{1.44}$$

A positive Hamaker constant induces destabilizing negative pressure for films larger than the equilibrium thickness $h_{eq} = (48\pi B/A)^{1/6}$, obtained by imposing $\varphi'(h_{eq}) = 0$. When regions of the film reach the precursor film thickness h_{eq}, the local equilibrium at the interface between the precursor film and the thicker regions defines an apparent contact angle θ given by:[10]

$$1 + tan^2\,\theta = \left(\frac{\varphi(h_{eq})}{\gamma} + 1\right)^{-2} \tag{1.45}$$

Considering solely angles between 0° to 90°, relation (1.45) provides a bijective relationship between the contact angle and the precursor film h_{eq}. This relationship hence sets an important link between microscopic interactions, characterized by the Hamaker constant, and macroscopic observables such as the contact angle. The precursor film is also particularly useful for dewetting simulations, ensuring the positivity of solutions to the thick film equation over the whole substrate simply based on the use of a tailored potential.

The reasoning presented above is valid assuming complete equilibrium between the precursor film and droplet. When considering a dynamic situation such as ridge retraction during dewetting, the equilibrium condition may not necessarily be satisfied. The presence of surface roughness or chemical inhomogeneities, even residual, may contribute to local pinning of the triple line (interface between liquid, gas and solid). Given the intrinsic triple line elasticity, this commonly gives rise to contact angle hysteresis. Macroscopically, this translates in the observation of receding or advancing contact angles associated to a contact line pinned away from its equilibrium position. To ensure quasi-static equilibrium during dewetting and hence identify the contact angle during dewetting, one must employ particularly smooth and chemically homogeneous substrate to insure that the contact angle observed is constantly equal to its equilibrium value.

1.2   On the role of order in material properties

In Section 1.1, thin film stability and re-arrangement mechanisms of unstable films have been discussed. These phenomena can yield structures with a particular order, which may or may not be associated with peculiar optical or electrical properties. The following section aims at providing a brief introduction (and/or reminder) of the consequences of order on material properties, with a particular focus on 2D metamaterials and their applications.

1.2.1   Photonic materials

1.2.1.1   *Photonic Crystals vs. Metamaterials*

The propagation of electromagnetic waves through an arbitrary medium can be expressed in a general manner by the Maxwell Equations:

$$\nabla \cdot \boldsymbol{E} = \frac{\rho_v}{\varepsilon} \tag{1.47}$$

$$\nabla \cdot \boldsymbol{H} = 0 \tag{1.48}$$

$$\nabla \times \boldsymbol{E} = -\mu \frac{\partial \boldsymbol{H}}{\partial t} \tag{1.49}$$

$$\nabla \times \boldsymbol{H} = \boldsymbol{J} + \varepsilon \frac{\partial \boldsymbol{E}}{\partial t} \tag{1.50}$$

Where $\boldsymbol{E}$ is the electric field, $\boldsymbol{H}$ the magnetic field, μ_0 is the magnetic permittivity in vaccum and ε_0 is the dielectric permittivity in vaccum, ρ_v is the charge carrier density and $\boldsymbol{J}$ is the current flow density. It is important to note that these equations are fundamentally scale-invariant: they are independent of length scale, and phenomena that arise from these equations can be observed at arbitrary length scales that are solely determined by the structure imparted to the material, as well as its permittivity and permeability values. Another important property that arises from these equations is the time reversal-invariance: the physics of wave propagation through a material can be inverted with respect to time.

Two distinct types of materials have attracted particular attention in photonics. The first type involves so-called "photonic crystal" structures. The physics behind these structures resembles that underpininning semiconductor physics. Just like for semiconductors, properties arising from photonic crytals stem from symmetry considerations in 1D, 2D, or 3D. This gives rises to photonic band gaps, e.g. frequencies for which any wave with arbitrary wavevector cannot propagate through the considered medium, in direct analogy with the conduction bandgap in semiconductor physics. The field of photonic crystals has largely been established by seminal works from both John[37] and Yablonovitch[38]. Popular examples of photonic crystals include distributed Bragg reflectors[39] (1D) or photonic crystal fibers[40] (2D). 3D photonic crystals take more exotic shapes, such as Yablovonite[41] or spheres in diamond lattice[42]. The photonic bandgap can be understood as a result of constructive/destructive interference of diffracted waves scattered by the artificially structured medium. For diffraction to occur, photonic crystal require the incident wavelength λ to be of the order of the dimensions of artificial

scattering sites (e.g. unit cells), written a. Photonic crystals are hence based on diffractive effects, and thus cannot be approximated as homogeneous materials.

Metamaterials represent a second class of composite materials whose properties are not observed in their constituent materials. The main difference with photonic crystal lies in the characteristic size of the meta-atoms, written a, which are in this case considerably smaller than the incident wavelength: $a \ll \lambda$. This implies a significant difference with photonic crystals, namely that meta-materials do not induce diffraction in the far-field. The light passing through metamaterial only sees an effective medium, with averaged properties. In the case of dielectric materials, the resonant response is the result of specific Mie-type scattering from each sub-wavelength meta-atom. The total meta-atom scattering cross-section (C_s) can be expanded into a sum of spherical electric and magnetic multipolar terms (Mie expansion):

$$C_s = \frac{2\pi}{k^2} \sum_{m}^{\infty} (2m + 1)(|a_m|^2 + |b_m|^2) \tag{1.51}$$

where a_m and b_m are Mie coefficients of the mth-order electric and magnetic multipolar modes, respectively. Through tailored Mie scaterring, one can engineer an effective dielectric constant $\varepsilon = \varepsilon' + i\,\varepsilon''$ and effective permeability $\mu = \mu' + i\,\mu''$. These parameters define the material's effective refractive index $n^2 = \varepsilon\,\mu$. Like their photonic crystal counterparts, metamaterials bear a number of interesting and counterintuitive properties. Veselago[43] first noted that propagation through a medium for a monochromatic ray is only allowed if $\varepsilon\,\mu > 0$, that is if μ and ε are either both positive or both negative. In the case where permittivity and permeability are both negative, the refractive index n is both real and negative, which has intriguing consequences on the flow of light, such as reversed refraction (direct consequence of Snell-Descartes' law with a negative index). This peculiar property has offered several opportunities, among which the possibility to focus the rays of a nearby source beyond the diffraction limit[44] or also cloaking[45] (e.g. deflection of a beam around an object). To fully tap into the potential of meta-materials, there has been a strong focus on the development of meta-materials in 3D, such as the first prisms with negative index[46] to illustrate the existence of reversed refraction. Nevertheless, manufacturing of 3D metamaterials poses considerable fabrication challenges, and the potential to scale up their fabrication remain limited.

The decription above provides a "thumb rule" to distinguish metamaterials from photonic crystals. In the (very common) intermediate case, a more precise criterion distinguishing metamaterials from photonic crystals has been recently established.[47] This condition relies on the comparison between the Bragg wavelength λ_{Bragg} in photonic crystals, identified by the first order of diffraction, with the Mie scattering wavelength λ_{Mie}, associated to the multipole of highest resonant wavelength. Based on this criterion, one can identify precisely identify the role of geometrical parameters and material permittivity on the transition from metamaterial to photonic crystals. In the case of infinite dielectric rods of permittivity ε and radius r arranged in a periodic lattice of period a, an increase in rod permittivity contributed to increase the ratio $\lambda_{Mie}/\lambda_{Bragg}$. Similarly, an increase in the radius to period ratio r/a also increases the ratio $\lambda_{Mie}/\lambda_{Bragg}$, providing a more quantifiable definition of metamaterials.

1.2.1.2 *Introduction to metasurfaces*

Considerable research efforts have been recently dedicated to the novel field of metasurfaces (e.g. 2D meta-materials), whose fabrication process is considerably more accessible using established lithographic processes than 3D

metamaterials. Athough restricted to 2D, these artificial sheets with sub-wavelength thickness offer extended possibilites to manipulate impinging electromagnetic waves. This field has largely been established by the seminal works of both P. Lalanne[48] and F. Capasso[49]. In conventional optical elements such as lenses or waveplates, a propagation over a distance much larger that the wavelength is required to induce significant changes in either amplitude, phase or polarization of the light, which makes these elements inevitably bulky. Metasurfaces demonstrated by P. Lalanne and F. Capasso[48,49] have demonstrated the potential to induce controlled phase jumps with controlled spatial variation from nano-resonating elements (dubbed "meta-atoms"). This control was demonstrated over distances much smaller than the incident wavelength, leading to unprecedented size, weight, and cost benefits. Based on this framework, a generalized form of Snell's law for metasurfaces has been proposed[49]:

$$\text{Generalized law of refraction} \begin{cases} n_t sin(\theta_t) - n_i sin(\theta_i) = \dfrac{1}{k_o}\dfrac{d\Phi}{dx} & (1.52) \\[2em] cos(\theta_t)sin(\varphi_t) = \dfrac{1}{n_t k_o}\dfrac{d\Phi}{dy} & (1.53) \end{cases}$$

$$\text{Generalized law of reflection} \begin{cases} sin(\theta_r) - sin(\theta_i) = \dfrac{1}{n_i k_o}\dfrac{d\Phi}{dx} & (1.54) \\[2em] cos(\theta_r)sin(\varphi_r) = \dfrac{1}{n_i k_o}\dfrac{d\Phi}{dy} & (1.55) \end{cases}$$

Where $\frac{d\Phi}{dx}$ and $\frac{d\Phi}{dy}$ are the components of the phase gradient induced by the meta-atoms along the in-plane x- and y-directions respectively, k_0 is the amplitude of the freespace wavevector, n_i and n_t are the indicies of the incident and transmitting media, θ_i, θ_r, θ_t, are the angles of the incident, reflect and transmitted rays. The two phase-gradient terms in these equations highlight the possibility to controllably tune the amplitude, phase and polarization of outbound rays by engineering the phase gradient between the sub-wavelength meta-atoms in the metasurface plane. Tailoring phase imparted by meta-atoms largely relies on geometrical parametrization of the sub-wavelength resonators. To insure high efficiency, impedance matching requirements with free space must be met for either high transmission or reflexion. A number of strategies have been suggested to improve impedance matching such as Huygens metalens or reflect-arrays which are discussed in more details below.

1.2.1.3 *Metasurfaces for wavefront shaping*

A first axis of reaserch in the field has been centered on the development of arbitrarily-shaped wavefronts. Arbitrary wavefront control can be achieved in two ways. A first possibility is to use antenna dispersion. Since a single resonance can only provide phase coverage from 0 to π, this methodology requires the combination of multiple resonances to cover the complete 0-2π phase range required for arbitrary wavefront shaping. Using plasmonic materials, this is commonly done using so-called reflect-arrays (or transmit-arrays), which consist in metallic resonators placed on top of a continuous reflecting layer. In this structure, the scattering element resonance combines with its image in the back plane to cumulate phase jump and yield a controllable phase shift. Based on this phenomenon, anomalous refraction and reflection have been among the first demonstrations of tailored wavefronts.[50,51] An alternative strategy consists in using V-shaped plasmonic antennas to engineer the emergence of tailored magnetic modes based on the angle of the V-shaped antenna. The combination of phase induced by the engineered magnetic and electric cumulate in the outbound beam. V-

shape antennas and reflect-arrays have been used to demonstrate anomalous refraction[52], meta-lenses[53], as well as vortex beam generation[54,55]. Other demonstrated applications include controlled optical activity (i.e rotation of linearly polarized light), such as for instance in waveplates[56,55,57]. An increasingly popular method to easily control the phase based on antenna dispersion capitalizes on the simulteaneous excitation of electric and magnetic modes of equal amplitude. The controlled overlap between these two modes can also provide a phase coverage that spans the full 0-2π spectrum (known as First Kerker condition), while ensuring unitary transmission. This has given rise to so-called Huygens meta-lenses based on various dielectric materials.[58,59] However, as all dispersion-based antennas, its operation range is limited to a small range of wavelength where the two electric and magnetic dipole modes interfere.
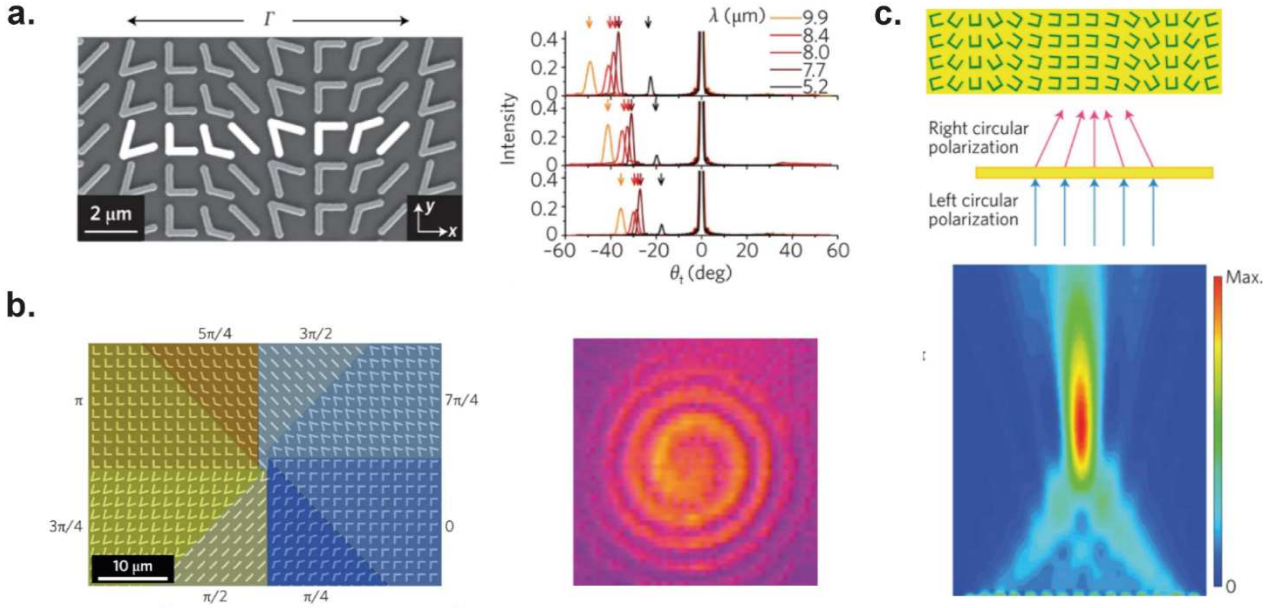
Figure 1.7 – Phase-gradient metasurfaces. (a) Au-based V-shape antennas on Si wafer. (Left) Scannning electron microscopy image and (right) experimental far-field intensity profile showing the ordinary and anomalous refraction fro three distinct periods: Γ= 13, 15, 17 μm. Adapted from ref. 41. (b) (Right) Similar metasurface concept as presented in (a), but imparting a different phase profile. (Left) The phase profile produces vortex beams in the far field. (c) Illustration of the Panchratnam-Berry phase metasurface concept. The top schematic shows a array of identical apertures with different in-plane orientations. The bottom graph shows the intensity profile of an outbound beam with right circular polarization, in a plane perpendicular to the metasurface. The inbound beam has left circular polarization.

Another way to impart a tailored phase shift to an incident beam is by resorting to the geometrical phase, also known as Pancharatnam-Berry phase.[60,61] This is commonly implemented by creating identical anisotropic scatterers with spatially varying orientation (in-plane orientation). Such scatterers induce both a local polarization shift and a local phase shift dictated by the scatterer orientation. In a general manner, the incident beam orientation can be decomposed according to right and left-handed polarized waves to analyze the phase imparted by the anisotropic scatterer:

$$E_T^{R/L} = \frac{t_o + t_e}{2} E_I^{R/L} + \frac{t_o - t_e}{2} e^{\pm i2\alpha} E_I^{L/R} \tag{1.56}$$

Where t_o and t_e are, the scattering coefficients for incident light linearly polarized along each principal axis 1 and 2 of the anisotropic scatterer, $E_I^{R/L}$ is the emitted field with the same handedness as the incident ray and $E_I^{L/R}$ is the emitted field with opposite handedness as the incident ray, and α is the Pancharatnam-Berry phase. Filtering out the first emitted component with unchanged handedness provides an emitted electromagnetic wave with a tailored phase jump. Relying on this principle, vortex beams[62] and meta-lenses[63,64] were implemented using U-shaped apertures or identical rod resonating elements with spatially varying orientation. One of the considerable advantages of the Pancharatnam-Berry phase

is that it is intrinsically broadband. This methodology is however limited at high wavelengths by decreased scattering efficiency and by the diffraction limit at low wavelengths.

1.2.1.4 *High Q.F Metasurfaces for Sensing and Non-Linear Processes*

Metasurfaces are particularly interesting not only for their ability to control phase, but also for their ability to sustain high quality factor (Q.F.) resonances. As such, they can strongly confine the electromagnetic energy in highly localized regions. A number of resonances have drawn interest to trap photons over extended times in localized regions, among which Surface Plasmon Polaritons (SPP) and Fano resonances. This finds applications in a number of fields, including non-linear metasurfaces and index sensing, both of which are presented here in greater details.

An important field of applications for high Q.F. metasurfaces is sensing. Surface-enhaced Raman Scattering (SERS) is a first sensing technique based on metamaterials that has gained widespread popularity recently.[65,66,67,68] The method consists in enhanced exicitation of specific molecular vibrational modes (Raman modes) through an engineered resonance near the metasurface. The measurement of scattered signal (Raman scaterring) allow to simultaneously detect multiple molecular signatures, potentially with high specificity, high accuracy and high reproducibility[69]. Metasurfaces bring significant improvements to SERS as they can create resonant field enhancement over the relevant spectral range in a reproducible manner. Another important application lies in refractive index sensing. In this method, strong resonances are engineered, typically producing sharp signatures either in the transmission or reflection spectrum. As a superstrate of specific index n_{sup} is placed above the metasurface, the sharp signature shifts and provides an estimation of the change in refractive index. Sophisticated methods grafting receptors that target specific analytes have enabled to make this method chemical-specific[70]. Demonstrations using either plasmonics[71], dielectrics[72,73] (see Figure 1.8(a)) or hybrid structures[74] have demonstrated significant sensitivities, which commonly depend on the spatial extension and magnitude of the field enhancement caused by the resonance. Metasurfaces offer a novel paradigm for accurate point-of-care diagnostics, which would certainly meet widespread industrial interest, provided simpler and more scalable manufacturing processes are developed.

Non-linear metasurfaces aim at generating with high efficiency given harmonics of an incident monochromatic signal of frequency ω. The focus could be placed either on the enhancement of the second harmonic (SHG: ω →2 ω), third harmonic (THG: ω →3 ω) or four-wave mixing (FWM: $\omega_1 + \omega_2 \rightarrow \omega_3 + \omega_4$). Before focusing on the role of metasurfaces in non-linear optics, a brief introduction/reminder of the physics behind non-linear optics is provided, based on reference 75. To begin with, let us consider a very general polarizable medium. Applying an external electric field E onto this medium generates a polarization vector P, expressed as:

$$\begin{aligned} P &= \varepsilon_0 \big(\chi^{(1)} E + \chi^{(2)} E^2 + \chi^{(3)} E^3 + \cdots \big) \\ &= P_{\text{Linear}} + P_{\text{non-linear}} \end{aligned} \tag{1.57}$$

where $\chi^{(i)}$ is the material's i-th order susceptibility, linked to the material's refractive index by the relationship $n = \sqrt{1 + \chi}$. Let us now consider a plane wave of the form $\vec{E} = E\vec{e_x} = E_0 e^{i(wt-kz)} \vec{e_x}$ propagating through this medium, associated to a scalar electrical potential $V = V_0 e^{i(wt-kz)}$. Rewriting the Maxwell equations provides the well-known propagation equation (up to the second harmonic, solely for illustration):[75]

$$\frac{\partial^2 E}{\partial x^2} - \frac{n^2}{c^2}\frac{\partial^2 E}{\partial t^2} = \varepsilon_0 \mu_0 \chi^{(2)} \frac{\partial^2}{dt^2}(E^2) \tag{1.58}$$

Looking for harmonic solutions, one can develop equation (1.58) to identify the intensity $I_{2\omega}$ of the output signal at the second harmonic and show that:

$$I_{2\omega} \propto {I_\omega}^2 \tag{1.59}$$

As apparent in equation (1.59), the intensity of the non-linear output signal is directly proportional to the square of the input signal. This is a fundamental element in non-linear optics: high-power sources are usually required to extract a significant amount power in the form of harmonics. This is explains why high Q.F. resonances are a particularly interesting platform in the field of non-linear optics. They offer the possibility to significantly enhance locally the electromagnetic field, and hence locally provide strong intensities at the fundamental frequency. Strategies combining resonant enhancement of both the fundamental and the harmonic (SH or TH for instance) can improve significantly the overall SH/TH signal.
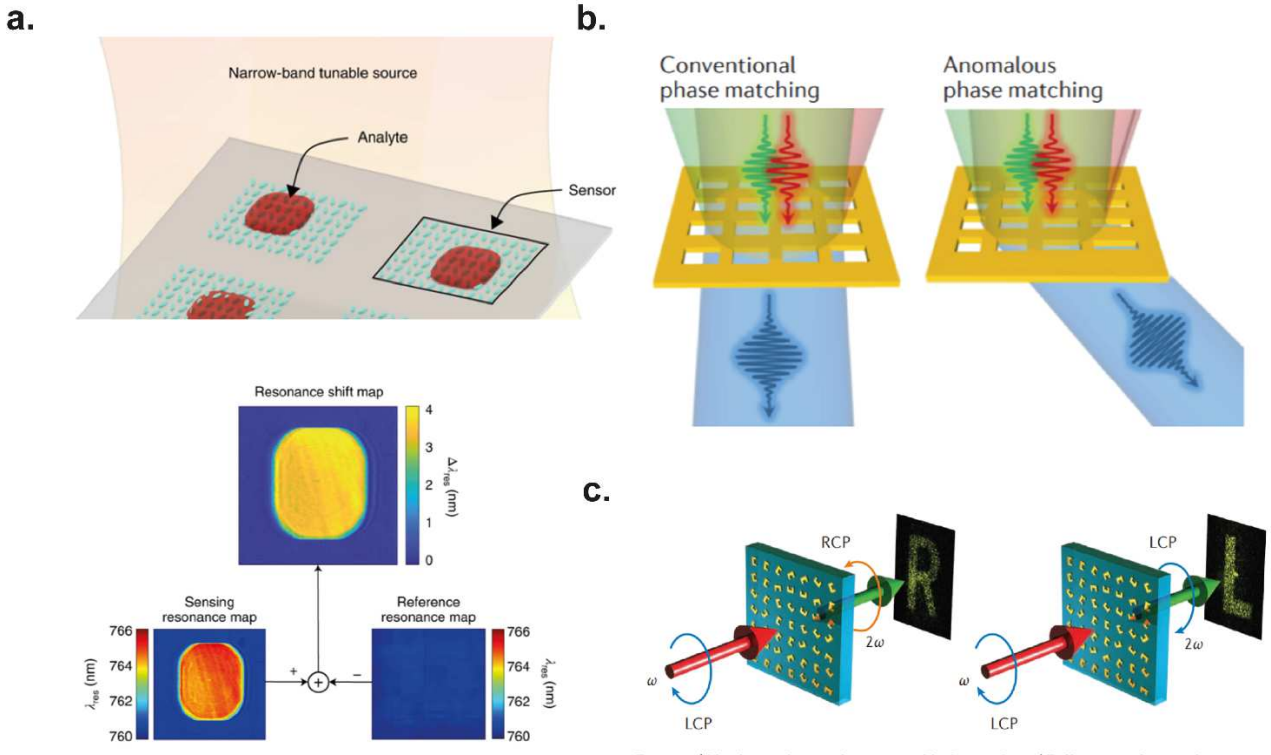
Figure 1.8 – High Q.F. metasurfaces for sensing and non-linear processes. (a) (Top) Schematic of a hyperspectral imaging device, where each sensor square supports a sharp Fano-type resonant mode at a precise wavelength. (Bottom) Shining a narrow band source onto the multiple sensor squares provides a resonant shift map, which detects the analyte concentration. Adapted from ref. 72. (b) Schematic illustrating phase control in multiple wave mixing process: dependiong on the metasurface phase profile, the outbound beam can be either normally transmitted or anomalously refracted. Adapted from ref. 77. (c) Non-linear metasurface hologram for circularly polarized light baed on the Pancharanam-berry phase concept. Two distinct images may be encoded in the output beam based on the output polarization. Adapted from ref. 81.

Symmetry plays an important role in non-linear optics. In non-linear crystals, centro-symmetricity at the atomic scale is critical to ensure emission of non-linear signal. To illustrate the role of symmetry on harmonic generation, let us investigate second harmonic generation under specific symmetry conditions. One can assimilate the physics of light propagation at the atomic scale by a forced oscillator equation of the charge e, which yields a polarization $p = e.x(t)$. This charge e evolves inside a medium with potential $V(x)$ representative of the non-linear medium. Considering the one-dimensional case, one can write the Taylor development of $V(x)$ for small perturbations:[75]

$$V(x) = m\left(\frac{1}{2}\omega_0{}^2 x^2 + \frac{1}{3}\beta x^3 + \frac{1}{4}\gamma x^4 + \cdots\right) \tag{1.60}$$

The associated retracting force reads:

$$\vec{F}(x) = m(\omega_0{}^2 x + \beta x^2 + \gamma x^3 + \cdots) \tag{1.61}$$

Including such a retracting force in the charge oscillator model provides the following equation of movement for the electron position $x(t)$[75]:

$$\frac{d^2 x}{dt^2} + \Gamma \frac{dx}{dt} + \omega_0{}^2 x + \beta x^2 + \gamma x^3 = \frac{e}{m} Re\left[E_\omega e^{i(kz-\omega t)}\right] \tag{1.62}$$

Where the development is limited to the third order for simplification purposes, the first order derivative term represents dampening effects, and $E_\omega e^{i(kz-\omega t)}$ is the incident electric field. Considering centro-symmetric structures, we obtain $V(x) = V(-x)$, which implies thait odd powers (resp. even powers) will disappear in equation (1.60) (resp. equation (1.61)). A direct consequence is the disappearance of even-power terms in the forced harmonic oscillator model, which forbids SH generation. To control symmetry conditions within materials, scientists have typically resorted to high purity large single crystals, which are challenging to produce. Using metasurfaces, adjustment of both meta-atom and lattice symmetry is sufficient to ensure (non) centro-symmetric requirements for either SHG or THG, independently of the material's intrinsic crystalline structure[76]. This is particularly interesting, as it allows for non-linear signal enhancement even from materials who would not give rise to non-linear effects in their bulk state.

Phase matching is another important additional requirement for efficient non-linear signal emission, ensuring that all non-linear processes occur coherently in SHG. This requires for instance an identical refractive index at the fundamental and at the second harmonic. This does not occur naturally due to dispersion effect, and commonly requires the use of birefringent materials. Requirements for phase matching between the various non-linear emission processes unfolding simultaneously are significantly simpler to meet in metasurfaces, given that emitting meta-atoms are deeply subwavelength in nature. Phase can be further continuously fine-tuned for each meta-atom if required by using anisotropic geometries with spatially varying orientation (Pancharatnam Berry phase, see previous section).

An interesting aspect of non-linear metasurface platform is that they can either be used solely for various frequency conversions such as SHG, THG, or FWM, or can be deployed in combination with wavefront engineering. This demultiplies the capabilities of such meta-devices. Based on these concepts, previous works have demonstrated the possibility to implement simultaneously harmonic generation/FWM and tailored phase profiles suh as beam steering (FWM, see Figure 1.8(b))[77], non-linear Airy beams[78] (three waves mixing), vortex beam generation[79](THG), or conversion of a single frequency incident beam into multiple images (e.g. multiple phase profiles, see Figure 1.8(c)) with a single metasurface[80,81]. Other applications for non-linear applications include optical frequency combs[82] and ultrafast all-optical switches.[83,84]

1.2.1.5 *Active metasurfaces*

Active metasurfaces have attracted considerable recent attention for their ability to provide a dynamic modulation of light, contrarily to their passive counterparts whose static optical response is fixed at the design stage. As such, active metasurfaces provide a novel integrated pathway to dynamic switching between multiple phase profiles. A number

of key measures characterize the potential of active metasurfaces, among which (i) the dynamic range over which response can be tuned, (ii) their optical efficiency and (iii) the degree of accuracy over resulting optical properties. Multiple methods have been proposed to actively tune metasurface response. By adjusting inter meta-atom spacing or orientation, mechanical deformation[85,86,87] has been demonstrated as an efficient lever for collective dynamic actuation over extended dynamic ranges. The lack of deformable photonic materials however commonly restricts the range over which signal can be tuned. Turning to non-mechanical tuning methods can prove beneficial on other aspects such as response time, power consumption and actuation accuracy. Moreover, such methods afford more degrees of freedom for design. Alternatives involving thermo-optic[88,89], all-optical[90,91] or electro-optical[92.93] effects have been investigated using rigid materials, but still induce relatively limited change in refractive index. Resorting to free carrier injection[94] has helped alleviate this issue, but at the expense of significant optical losses. The use of non-volatile rigid phase-change materials such as $Ge_2Sb_2Te_5$ or derivated compounds[95,96] represent an alternative given their significant index contrast ($\Delta n > 1$) between amorphous and crystalline states. Capitalizing on the capabilities of phase change materials, previous works have demonstrated active wavefront control, effectively allowing for controlled switching between various phase profiles.[97,98,99,100,101] Reseach on active metasurfaces is a dynamic topic of research, with still much work to be done to substantiate the promises of integrated yet dynamic optical devices. From this brief overview of active metasurfaces, it clearly appears that the choice of materials is key to ensure a high degree of functionality and reliable operation, particularly for mechanically-actuated metasurfaces.

1.2.1.6 *Which materials for metasurfaces?*

Meta-atom material composition constitutes an important choice in metasurface design. Typical requirements include low loss materials to allow for high metasurface efficiency and high refractive index to ensure strong confinement of light. The first demonstrations of metasurfaces have largely relied on plasmonic materials such as gold mainly due to the strong responses they provide. By relying on antenna dispersion in plasmonic meta-atoms, oscillatory surface plasmons are excited as the light impinges on the element, which can induce strong tunable phase jumps based on the nanoresonator size and/or shape. Resonant modes associated to plasmonic metasurfaces are traditionally associated with strong field confinement, notably for instance with graphene[102]. Plasmonic antenna are also commonly associated with very thin form factors, much smaller than the incident wavelength. Nevertheless, using plasmonic materials entails a number of drawbacks. Firstly, these materials exhibit significant absorption, which inevitably reduces the optical efficiency of the meta-device. Losses can also be an issue in bio-sensing device, as Joule effect induces local heating and potential destruction of surrounding biochemical analytes. Secondly, plasmonic material intrinsically show negligible magnetic response at optical and infrared frequencies, and require engineered geometries such as V-shapes or split resonators to induce strong magnetic response, which is essential for a number of applicatoins such as negative index materials based on tailored permittivity and permeability (see Section 1.2.1.1 above). All-Dielectric metasurfaces have emerged as a viable alternative to traditional plasmonic metasurfaces. These materials show a number of advantages over their plasmonic counterparts, such as extremely low optical absorption. All-dielectric resonators based on simple shapes such as spheres or cylinders can intrinsically support both electric and magnetic modes, based on the relatively strong polarization current that arise inside the resonator structure. This constitutes a significant advantage compared to metallic structures.

Whether plasmonic or dielectric, materials used until now in meta-assemblies have largely relied on rigid materials. Plasmonic materials have involved the use of metals, which can be compliant thanks to their ductility, but which cannot undergo extended mechanical deformation. Dielectric materials commonly used are even more restrictive in terms

of mechanical properties: materials such as chalcogenides, silicon dioxide, or titanium dioxide glasses are well known to be highly brittle. Some strategies have been proposed to withstand extended deformation[103], but soft photonic materials has thus far remained elusive.

1.2.2 Electrical implications of order

As discussed in Section 1.2.1, materials with a particular ordering at the wavelength or sub-wavelength scale have attracted considerable interest in the past decades for photonic applications. Material order and symmetry considerations at the atomisitic scale have also driven essential progress in semiconductor materials. The extended use of silicon, nowadays the workhorse of the microelectronics industry, is a particular case in point. However, materials developed thus far have essentially been of rigid nature, a necessity to ensure stable microstructural parameters and advanced electronic/photonic properties. Providing a material with the ability to deform by either bending or stretching could however endow it with unique abilities and functionalities. For instance, the integration of deformable yet conductive materials have paved the way for a new generation of truly conformable devices than can be seamlessly integrated over biological tissues. The applications of such stretchable conductive materials and structures include sensing[104,105,106], but also actuation in soft robotics[107,108,109] and stretchable optics.[105]
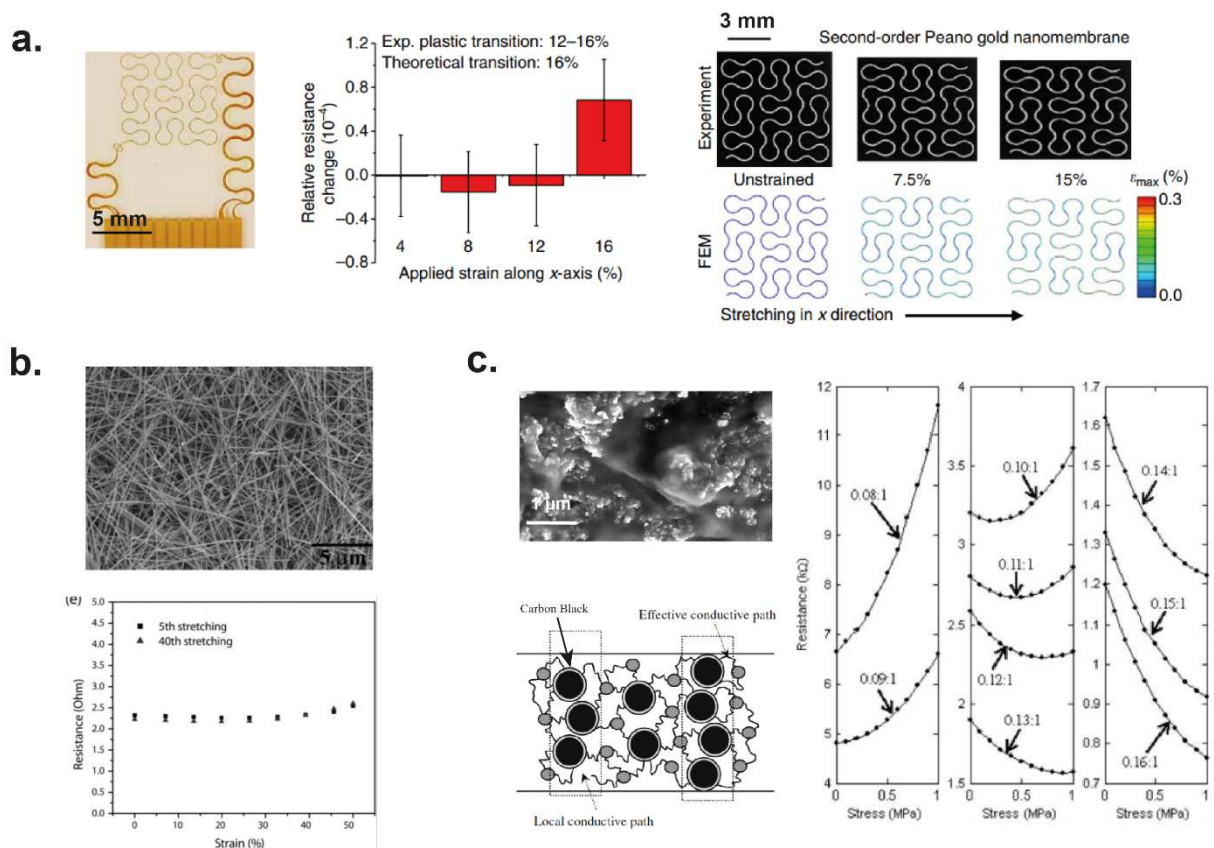
Figure 1.9 – Influence of order on properties of stretchable conducting materials. (a) Fractal Peano-type layouts : (left) experimental layout with metal wires. (middle) Resistance response of layout to strain. (right) Finite element modelling of strain evolution within the wire as a function of maximal reversible strain, as a function of elongation. Adapted from ref 113. (b) Silver Nanowire networks used as conducting electrode embedded inside elastomers: (top) Scanning electron microscopy image of the Ag nanowire network and (bottom) evolution of resistance with strain of the nanowire network. Adapted from ref 108. (c) Electrical response of carbon black composites: (top left) SEM image of the carbon balck embedded in rubber. (bottom left) Schematic of the equivalent resistor network for current flow. (right) Resistance vs. strain curves corresponding to increasing carbon black filler: rubber weight ratio. Adapted from ref 106.

Although much attention has already been placed on the development of stretchable materials, the microstructure and associated order within stretchable materials has largely played a secondary role in the field of stretchable materials. Microstructure offers the possibility to tailor the response in resistance with strain beyond classical deformation theory of homogeneous materials. Atypical resistive behavior with strain has been observed in various near-percolation composite systems, such as carbon-nanotube[110, 111] or silver nanowire-based[112,113] composites (see Figure 1.9(b)-(c)). Until now however, works investigating such systems have remained focused on randomly distributed networks[114], while the leverage over resistance-strain behavior has remained limited to composite loading (see Figure 1.9(c)). The lack of order at the meso- or macroscopic scale inevitably limits the variety of resistance response. Responses with negative Gauge factor have also been observed in micro or nano-structured liquid metal thin films, but the inherent randomness of the structure limits again tuning possibilities[115,116]. Recent works using deterministic geometries of folded lines of a single rigid metal, semiconductors, or rigid composite[117,118] (see Figure 1.9(a)) have achieved constant resistance-strain relationships. However, such an approach provides no tunability and remains fragile, thus limited in strain. Moreover, it induces inevitable challenges to rigorously identify the elastic and plastic mechanics of these composite materials. While recent studies have pointed to the role of orientation in 1D nanomaterials to explain complex resistance response with strain[114], no analytical approach has been proposed to understand the link between microstructure and resistance-strain behavior in ordered 2D-systems. Providing new degrees of freedom in design could open up several applications that simply offer new functionality to the material. Maximized resistance change with strain has already attracted considerable research efforts, with direct applications in highly sensitive soft deformation sensors for instance. Nevertheless, other interesting applicative opportunities remain largely uninvestigated, such as: (i) Constant-current stretchable electrode: a considerable amount of electrical components such as LEDs require either constant current or constant voltage sources to function. Stretchable interconnects interfacing these components need to maintain stable resistance under extended elongation to maintain such constant current/voltage signal and avoid the need for additional constant current/voltage regulators directly inside rigid chips. (ii) Switches: providing a constant response followed by a sharp increase beyond an elongation threshold could be instrumental in the design of switches, which would enable interesting possibilities in sensing, monitoring, or drug delivery. (iii) Periodic signal modulation: allowing for a system to come back through a given state (e.g. resistance value) with multiple input values (e.g. multiple strain values) simply relying on the microstructural behavior. This could open up novel perspectives in soft robotics and actuation. Cyclically stretching such an assembly could for instance provide a periodic electrical signal with a well-defined increased frequency, effectively acting as an electro-mechanical frequency converter. This could also act as a multiple strain level sensor, whose level density and sensitivity could be tuned using the proposed framework.

Chapter 2   Templated instabilities: a novel platform for fabrication of advanced photonic devices

2.1   Introduction to advanced fabrication techniques

Micro- and nanoscale photonic devices are currently at the forefront of research. Manufacturing such advanced devices today often relies heavily on complex processes to provide the required fabrication resolution and accuracy. However, these processes offer limited scalability and remain restricted to conventional rigid substrates. The success of silicon-based technology, the workhorse of microelectronics industry for over five decades, is a particular case in point. However, efficient large-scale manufacturing of advanced photonic or electronic functionalities on unconventional non-rigid substrates remains up to now a considerable challenge[119].

The first and most straightforward method for nanostructure fabrication involves well-established lithographic process. It provides high repeatability and very high resolutions, down to 10 nm for electron beam lithography tools and 1 nm for the most advanced techniques.[120,121,122] Nonetheless, complexity and high cost of equipment motivate researchers to look for novel fabrication methods. Additionally, some geometries like spheroids cannot be manufactured by this process[123].

Chemical methods represent high-throughput and simple alternatives to fabricate ordered nanoarrays of dielectric particles. Chemical vapor deposition by decomposition of silanes can be used to generate silicon sphere arrays. Fabrication of a size-tunable monodispersed silicon colloids was for instance achieved via decomposition of Si_3H_8 at high temperature in supercritical n-hexane, which can naturally self-assemble into hexagonal 2D structures[124]. Upon nanoparticle synthesis, there are various ways to pattern these nanostructures into regular arrays. It has been shown that relatively optically transparent polymer/nanoparticle composite could be patterned using a hot pressing-based approach with a soft textured mould[125]. Other researchers have also achieved self-assembly of nanoparticles into lines using a solution-based approach[126]. There are inherent disadvantages to these methods such as chemical waste, possible contamination of nano-materials fabricated, as well as additional steps required for the generation of ordered nanostructures. High-pressure chemical vapor deposition[127] (HPCVD) inside microstructured optical fibers has shown considerable potential to produce continuous nanowire arrays with tailored architectures, allowing for successive deposition of various concentric layers within such fibers of arbitrary geometry. Interestingly, this method allows to achieve deposition within channels down to several hundred of nanometers over lengths up to a few centimeters. The deposition time in this process however scales as the square of its length, thereby limiting applicability.

Lasers can also be used to generate sub-micron resolution particle arrays, often based on direct material ablation[128]. The advantages here include material selectivity, high energy density, and good resolution, with resolutions down to 100 nm in diameter. Chemical waste is not generated, and particle purity remains excellent. Examples of materials used in this technique include single crystalline ZnO, CdSe, ZnSe, and CeO_2.[123] However, lack of control over generated particle position and size impedes applications in nanophotonics. Laser-induced transfer methods represent another attractive approach to nanoparticle fabrication[129]. In this method, laser radiation is focused on the interface between the printed

material and transparent donor substrate which transfers material onto another receiver substrate placed in intimate contact with the donor sample. Highly ordered arrays can be obtained, with spacings ranging from 5 to 375 nm. The associated drawback to laser-based methods are mostly related to the high quality of the laser radiation needed, which should be at the same time very stable, accurately focused and positioned, and possess a precise beam shape[119]. Nevertheless, laser-assisted methods show high repeatability and throughput with a single-step process.

While classic lithographic methods require excellent film stability during the fabrication process, some others to the contrary directly exploit intrinsic instability arising in thin film configurations. This is the particular case of dewetting, the final self-assembly process discussed here. It consists in exploiting the high surface to volume ratios of thin films to induce rearrangement. By thermal annealing, solid materials can be softened either when nearing the glass transition temperature or the melting point.[19] When atom mobility is high enough, capillary forces force the film to rearrange into an array of particles. Texture can then guide dewetting to produce ordered arrays of particles by modulating local chemical potential, or inducing a Laplace pressure-driven velocity field in a viscous fluid. Textured dewetting of various polymer, metal or silicon films has been already investigated to some extent.[19,24,28,32] Dewetting has been used for a broad application spectrum, ranging from microlensing[130] to field effect transistor manufacturing[131] for polymers or 2D high-density magnetic data storage manufacturing[132] for metals. While the template dewetting of metals has a great potential, their optical properties are affected by their polycrystalline microstructure and high roughness. Polymers can dewet into complex nano-scale and smooth architectures but their reduced refractive indices do not allow for advanced optical designs. Thus far, while some glasses are well suited for fluid-based processes such as thermal drawing[133,134], liquid depositions[135], thermal imprinting or molding techniques[136], the template dewetting of optical glass thin films have not been exploited as a simple and scalable approach to realize advanced nanophotonic structures. Fluid instabilities of glasses at the nanoscale remain to be studied and subtly controlled.

In this chapter, we introduce two separate process to self-assemble materials at the nanoscale based on controlled evolution of template instabilities to realize state-of-the-art nanophotonic structures over large areas, soft and rigid substrates. We apply our methods to chalcogenide glasses because they exhibit the proper thermo-mechanical, rheological and surface properties for template dewetting. They are also widely used in photonics for their high index of refraction and high transmission in the infrared, as well as for their non-linear optical[137], phase change[138] and optoelectronic properties.[139] In the first system, we present a self-assembly process of thin chalcogenide films based on in-air template instabilities and demonstrate their applicability in metasurfaces. By engineering the interplay between texture reflow, spinodal instabilities and capillary break-up, we demonstrate the self-assembly of a variety of optical nanostructures with feature sizes down to ~100 nm and inter-particle distance down to 10 nm. In the second system, we introduce a novel process to achieve meter-long periodic arrays of chalcogenide nanowires in a single thermal drawing step. We combine angle deposition on nanoimprinted polymer substrate with thermal drawing to obtain large-scale periodic nanowire arrays. Based on this process, we demonstrate the ability to independently tune nanowire diameter and spacing, providing an unprecedented control over in-plane geometrical parameters.

2.2   In-air templated instabilities

In the first system, we present a self-assembly process of thin chalcogenide films and demonstrate their applicability in metasurfaces. Most of the work presented in this section has made the object of a publication in Nature Nanotechnology.[140]

2.2.1 Presentation of the process

The concept of in-air template instabilities and its practical implementation is presented in Figure 2.1(a). Soft
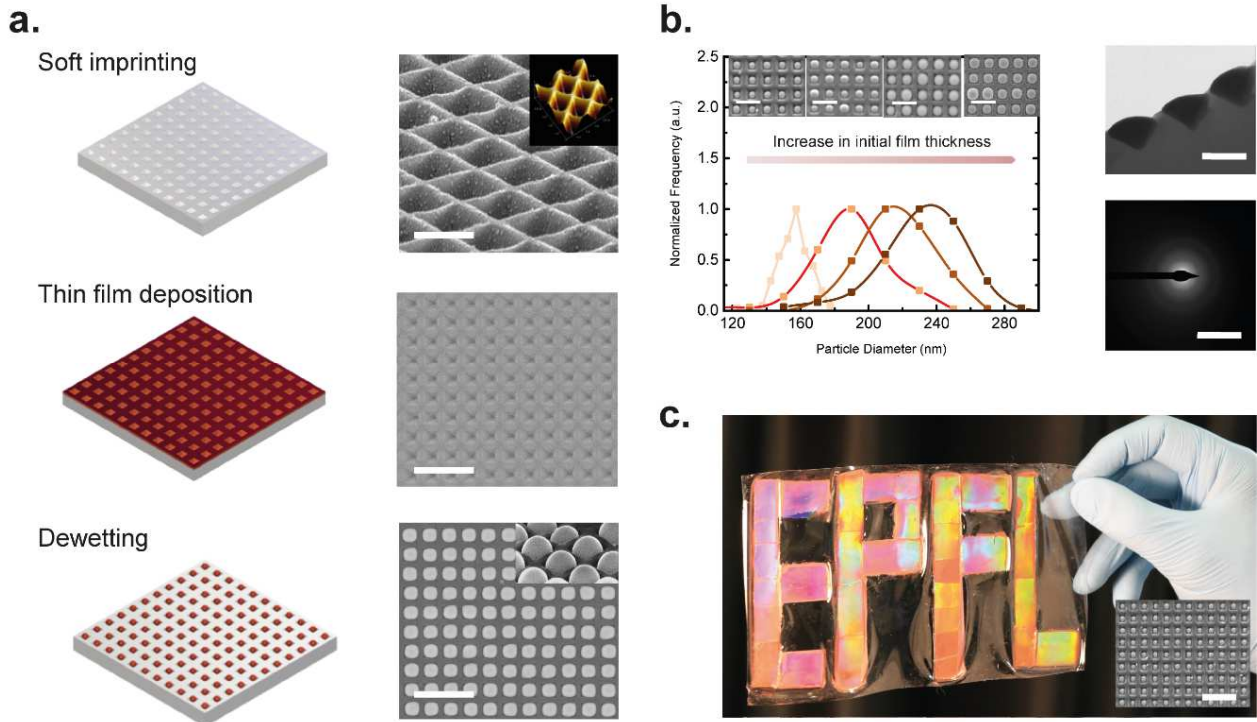
Figure 2.1 – Fabrication process for optical metasurfaces. (a) Schematic (left) and SEM image (right) of the process with an optical glass ($Ge_6Se_{82}Te_{12}$). (Top) The fabrication starts with thermal or ultraviolet nanoimprinting of the required pattern on a substrate. An atomic force microscopy (AFM) profile of the texture is shown in the inset of the SEM image. Scale bar, 400 nm. (Middle) The next stage is thin-film deposition of high-index optical glass. Scale bar, 1 μm. (Bottom) Annealing is then carried out to induce the dewetting process. Scale bar, 1 μm. Bottom inset, A tilted view for a 350 nm square lattice with Se nanoparticles. (b) Left, Particle size distribution obtained with single-step dewetting, showing the tunability of particle size. Inset, Corresponding SEM images for different film thicknesses. Scale bars, 350 nm. Right, Cross-sectional TEM analysis showing a bright-field image of the Se nanoarray (top) and the associated diffraction pattern (bottom). Bright-field image scale bar, 200 nm. Dark-field image scale bar, 5 nm−1 . (c) Optical photograph showing a largearea (20×11 cm^2) EPFL logo-shaped metasurface on a polymer substrate. Inset, SEM image of the corresponding nanostructure. Scale bar, 1 μm.

lithography is first used to replicate a silicon master mould onto a thermoplastic or sol-gel layer via thermal or ultraviolet (UV) nano-imprinting (Figure 2.1(a)(top)) using a PDMS negative mould. A thin layer of chalcogenide glass is then deposited by thermal evaporation or other approaches[141] (Figure 2.1(a)(middle)), before annealing is performed in ambient air at different temperatures and for different times (Figure 2.1(a)(bottom)). Annealing induces dewetting of the glass layer, which breaks up into an array of well-dispersed and self-ordered nano-objects, as apparent on the Scanning Electron Microscope (SEM) images of Figure 2.1(a) showing an array of $Ge_6Se_{82}Te_{12}$ nanoparticles. This self-assembly occurs for different initial film thicknesses as shown in Figure 2.1(b), where the particle size distribution is plotted for four different initial thicknesses of pure Se films. It appears that the underlying pattern imposes the periodicity and position of the particles, while the amount of material deposited dictates the particle size. The nano-objects adopt the shape and occupy the convex regions of the underlying texture, as shown in the Transmission Electron Microscope (TEM) image of Figure 2.1(b). Also, the diffraction pattern from the TEM sample shows that the glass remains amorphous during the whole process. This approach is simple and scalable, as highlighted in Figure 2.1(c) where an EPFL logo is fabricated via the embossing of a 20x11 cm^2 polycarbonate sheet with nanostructured assembled PDMS molds. The inset of Figure 2.1(c) shows a SEM view of the patterned area with a nearly perfect array of high dielectric constant nano-objects. Chalcogenides are well-known for their propensity to oxidize in ambient conditions, and we hence also investigated their
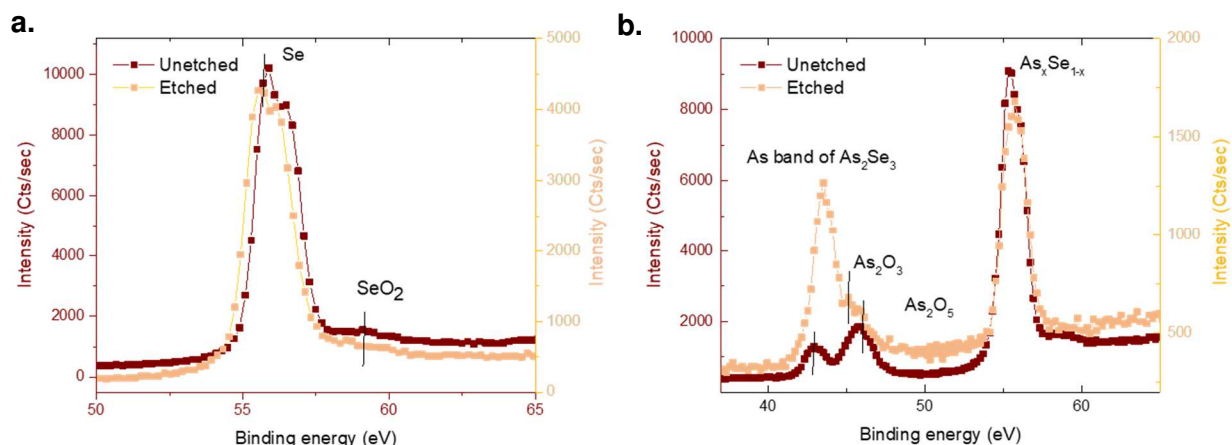
Figure 2.2 – Oxidation of Chalcogenide glass upon dewetting. (a) XPS spectrum of Se after dewetting at 80°C for 2 minutes under ambient condition. Presence of selenium oxide traces is confirmed by the bump observed around 59-60eV. XPS spectrum after etching a ~10 nm thick layer of material reveals that the oxide is mostly present on the surface (b) XPS spectrum of As_2Se_3 after dewetting at 200°C for 10 minutes under ambient condition. Presence of arsenic oxide traces is confirmed by the bump observed around 46-47eV. XPS spectrum associated to arsenic oxides dramatically decreases after etching a ~10 nm thick layer of material, revealing only surface oxidation.

oxidation upon dewetting. X-ray photoelectron spectroscopy (XPS) measurements reveal only traces of oxides at the surface (Figure 2.2), which do not induce significant deviations in terms of optical responses.

While the use of templated dewetting is in itself not new, two elements make this process stand out. Firstly, the use of high index chalcogenides provide unprecedented functionality compared with the previous use of low index polymer materials. While polycrystalline metallic materials had already been considered, their polycrystallinity proved detrimental for the final architectures, which showed significant randomness due to diffusion along the grain boundaires. In this process, the glassy nature of the film is fundamental to provide the highest possible regularity in the final architecture. Chalcogenide glass are therefore ideal candidates in terms of processing, with a large temperature separation between the glass transition temperature and the cristallisation temperature, a second important element in this process. Moreover, we take advantage here of the nanometric feature sizes to help delay crystallization, as observed in other works with for instance metallic glasses.[142] The novelty of the process therefore lies in stretegic choice of material and scope of applications.

2.2.2   Process flexibility

In Figure 2.3(a)-(d), we show how this process can be adapted to particle arrays with different feature sizes, lattices, material compositions and substrates, parameters that can all be tuned to tailor the optical attributes of the result-ing metasurfaces. We demonstrate arrays with particle sizes down to around 100 nm (Figure 2.3(a)), and different lattice arrangements such as a hexagonal structure shown in Figure 2.3(b). The material composition can also be engineered, provided that the glass can keep its stoichiometry when processed into a thin film, and can resist crystallization during annealing. Germanium-based composition ($Ge_6Se_{82}Te_{12}$), investigated for its phase-changing characteristics for optical memories[143] (Figure 2.3(c)), is a good example. Low processing temperatures enable the use of less conventional flexible and stretchable substrates such as thermoplastic sheets or elastomers (Polydimethylsiloxane (PDMS) in this case) as shown in Figure 2.3(d). It is important to note however that the soft nature of the substrate may influence the dynamics of dewetting.[144] Also, the optical properties of hard and soft substrates can be further tailored through porosity or by adding fillers to polymers or sol-gels.[145,146,147]

Template dewetting also allows to go further in the complexity of the architectures that can be designed. For example, increasing the distance between the pyramid (the "mesa") will leave in this region material that has not reflowed around their edges. As illustrated in the schematics of Figure 2.3(e), the remaining film will reflow into its equilibrium shape governed by the contact angle between the glass and the substrate. These engineered fluid instabilities produce particles both within pits and on top of mesas, yielding quasi-3D arrays of particles (SEM image shown in Figure 2.3(f) along with size distribution in Figure 2.3(g)) with interesting optical properties discussed in Chapter 5.

Another interesting feature in many nanostructures is the ability to reach nanometer scale inter-particle distance. Achieving this by single-step dewetting would require either too fine textures or too thick films that no longer rearrange according to the texture. We propose instead a successive dewetting scheme where the film is deposited in several steps with systematic intermediate annealing, as shown schematically in Figure 2.3(h). After the first annealing, the film has fully dewetted in the inverted pyramid structure (Figure 2.3(i)). The successive deposition and annealing steps serve the same purpose and grow step-by-step the nano-objects, reducing the inter-particle distance in a controlled way down to 10 nanometers (Figure 2.3(i)). This simple self-assembly approach hence achieves resolutions on par with those provided by electron beam lithography, without the burden of cost and complex equipment, onto rigid and soft substrates.
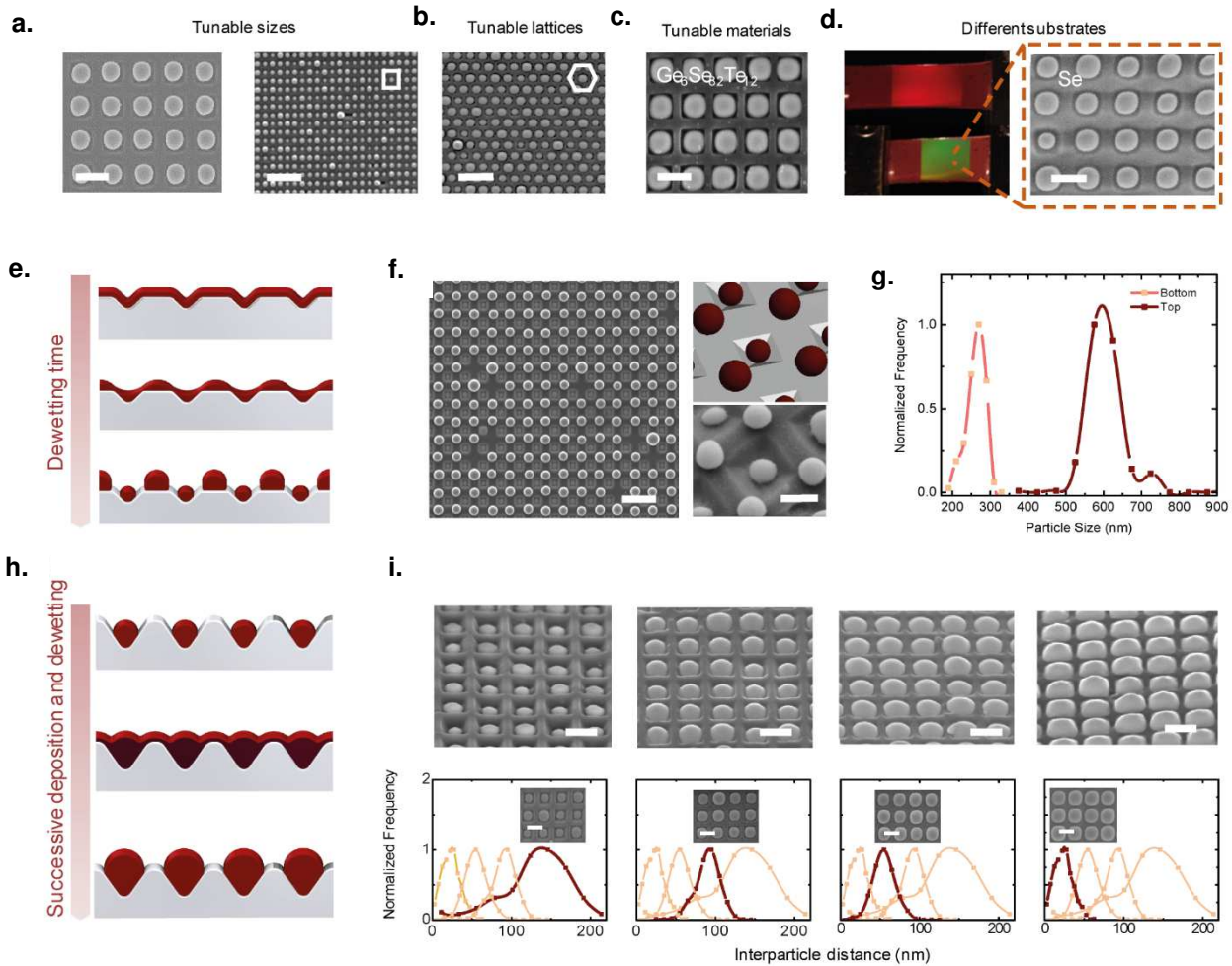
Figure 2.3 – In-air templated instability versatility. (a–d), Scalability of the fabrication method: dewetting of optical glass on a 1 µm square lattice (scale bar, 1 µm) and a 200 nm square lattice (scale bar, 1 µm) (a), and a 350 nm triangular lattice (scale bar, 1 µm) (b). The method applies to different material compositions such as $Ge_6Se_{82}Te_{12}$ (scale bar, 350 nm) (c) and Se (scale bar, 350 nm) (d). The process applies to different substrates: thermoplastic polycarbonate (a–c) and elastomeric PDMS (d). Structures are obtained by engineering the pattern parameters and deposition cycles. By widening the inter-pit distance ('mesa'), quasi-3D structures can be obtained. (e) Cross-sectional schematics show the dewetting process for large mesas. (f) Left, SEM image showing a top view of the quasi-3D structures experimentally observed. Scale bar, 2 µm. Bottom right, 30° tilted SEM image of the quasi-3D structure. Scale bar, 500 nm. Top right, Corresponding 3D schematic. (g) Size distribution of particles on mesas ('Top') and within pits ('Bottom'). By engineering the deposition cycles, a small interparticle distance can be obtained. h, Schematics illustrating the successive deposition process. (i) (Top) SEM images. (Bottom) Corresponding particle size distributions of successive optical glass deposition (here Se) and dewetting. Scale bars, 350 nm.

Finally, we demonstrate that continuous lines of optical glasses with sub-micrometer feature sizes can be obtained. To produce such structures, we take advantage of the difference in time scale between template-induced reflow, that reshapes the film into linear structures, and Rayleigh-Plateau instability, which leads to capillary break-up of lines into particles. If the time scale associated to template reflow is shorter than the one associated to Rayleigh-Plateau instabilities, the system can be frozen into linear structures. In Figure 2.4(a) and (b), we show a schematic of this principle and the SEM micrographs that show the dewetting process resulting in continuous glass lines.

With this understanding, it is then possible to make shapes with a variety of in-plane aspect ratios. In Figure 2.4(c), we show different examples such as cross arrays (top left) and a triangular metasurface (top right). More isolated structures can be fabricated by delaminating interline regions mechanically upon dewetting. With this method, we demonstrate continuous honeycomb lattice (Figure 2.4(c), bottom left) and an isolated EPFL logo, highlighting the possibility to realize photonic circuit designs. To further emphasize on the potential of our approach, we realized in Figure 2.4(d) a well-known V-antenna metasurface architecture.
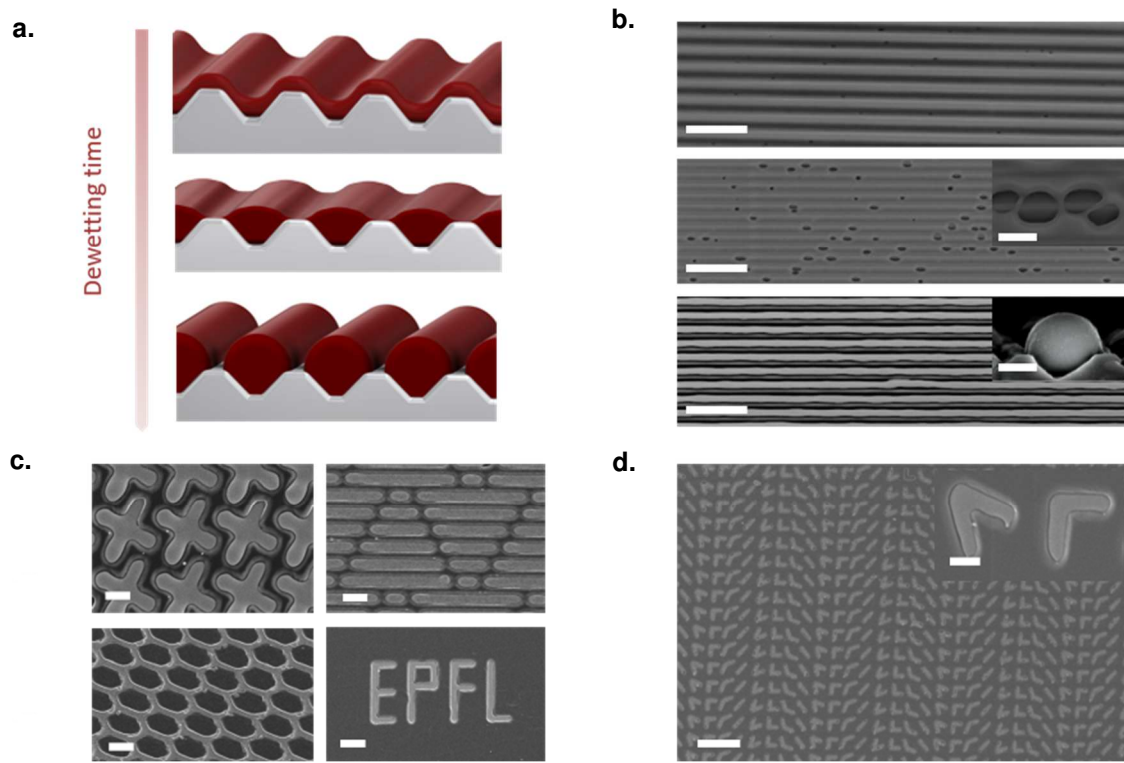
Figure 2.4 – Linear features by dewetting. (a) Schematic illustration of continuous line formation process involving an interplay between reflow, spinodal and Rayleigh-plateau instabilities. (b) Top-view SEM images illustrating the process. Top, Initial thin continuous film on a 350 nm periodic 1D texture. Scale bar, 1 μm. Middle, Reflow induces thinning of the film above the concave regions of the pattern, favouring growth of spinodal instabilities parallel to the lines. This ultimately leads to hole formation and coalescence along the line direction on the concave regions of the texture (shown in inset). Scale bars, 2 μm (large-scale view) and 100 nm (inset). Bottom, System frozen in metastable state after dewetting but before growth of significant Rayleigh-plateau instabilities along the cylinder's free surface. Scale bar, 1.5 μm. Inset, Cross-section of one line. Scale bar, 200 nm. (c) The different complex structures obtained: cross arrays (top left) triangular metasurface (top right), honeycomb structures (bottom left) and EPFL logo (bottom right). Scale bars: 2 μm. (d) Large-area SEM image illustrating a well-known V-antenna metasurface structure. Scale bars, 10 μm (large image) and 1 μm (inset).

2.2. In-air templated instabilities

2.2.3 Defect analysis

A critical element of any fabrication process lies in its accuracy, repeatability, and absence of defects. To critically assess the reliability of our method, the various kinds of defects generated by our structures have been classified and estimated.
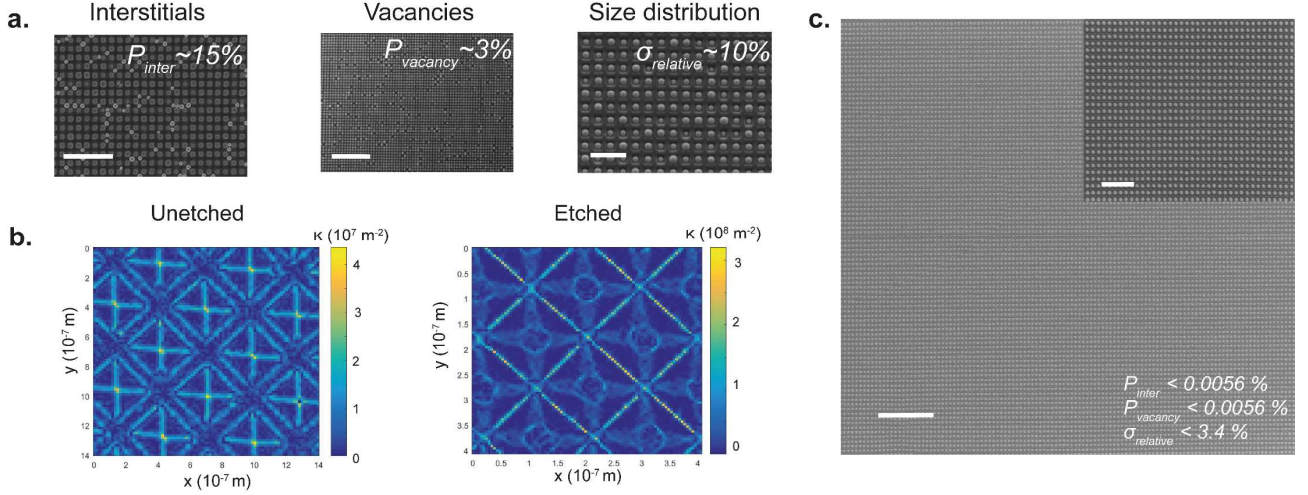
Figure 2.5 – Defect analysis. (a) SEM images showing the three main types of defect (from top to bottom): interstitial defects (scale bar, 2 μm), vacancies (scale bar, 5 μm) and large particle size distribution (scale bar, 1 μm). All particle arrays are 350 nm square lattices with Se nanoparticles. (b) Curvature colormaps corresponding to unetched and physically etched patterned SiO$_2$ substrates. Etching yields a large increase in the maximal curvature, as well as a better defined region of maximal curvature. These images are extracted from Atomic Force Microscopy profiles. (c). Large-scale SEM image showing nearly perfect arrays of Se nanoparticles obtained on a 350 nm square periodic lattice simply by increasing the local curvature with regards to (b). The scale bar of the large area picture is 5 μm, and the one for the inset is 2 μm.

As shown in Figure 2.5, three main kinds of defects have been identified:

1. Interstitial defects, whereby a particle is sitting in between two pits. Although interstitial particles could be desirable if they are ordered and defect-free, experimental observations suggest that, with the current textures, interstitials often appear at random. The presence of interstitial defects can however be eliminated by reducing the mesa size. These defects typically appear when the mesa (i.e. the size of the one in between pits) has a certain scaling factor with regards to the pit size. A transition between the 2D to the quasi 3D-arrangement is expected to lead to the disorderly, undesirable interstitial defects.

2. Vacancies, where material is absent from a given pit. Three factors that influence the presence or absence of vacancies have been identified. (i) The substrate curvature has the most obvious and strong influence of the appearance of such defects. By resorting to a dry etching step of a silica texture, local curvature at the pyramid edges is greatly enhanced while within the pyramid the height profile is evened out and the curvature reduced. This has a clear, largely favorable influence on the local Laplace pressure during reflow. As shown, corresponding defect quantity is largely reduced. (ii) Successive deposition, whereby thinner layers of material are successively deposited and dewetted, allows for a more even spreading of material within pits. The amount of vacancies can be reduced by resorting to this method, although this often happens at the detriment of interstitial defects, which appear on smaller length scales with reduced film thickness (iii) It is a well-known phenomenon that plasma treatment often improves adhesion by enhancing film-substrate chemical bonding. At the nanoscale, this enhanced bonding reduces contact angle and improves vacancy statistic on large areas, although often at the expense of residual interstitial defects.

3. Size distribution, which quantifies how homogeneously the material spreads from pit to pit. This is improved by resorting to the same techniques than for vacancies, which contribute to homogenously spread the material on the substrate.

For interstitials and vacancies we define the probability of finding a defect per unit cell as P_{inter} and $P_{vacancy}$, respectively (see Figure 2.5(a)). For the size distribution, we define the relative standard deviation $\sigma_{relative}$ as the ratio of the absolute particle size standard deviation over the lattice period.

When physically etching the substrate with Argon ions for a short duration, the texture is largely modified. More specifically, the maximal curvature is increased by one order of magnitude at the pyramid square edges, while the curvature of the pyramid vertices is reduced (Figure 2.5(b)). This helps define a clear cut-off domain for the film break-up upon reflow. As a consequence, the defect density upon deposition and dewetting is enormously reduced, as observed in with the deposition of 30 nm of Se on an etched SiO_2 substrate (Figure 2.5(c)). All three parameters characterizing the defects (P_{inter}, $P_{vacancy}$ and $\sigma_{relative}$) are largely improved. The control over local curvature is hence a key aspect of template dewetting that one must precisely control for efficient self-assembly.

2.3   In-fiber templated instabilities

We now turn to the dewetting of films fully encapsulated inside a polymer matrix. Resorting to a surrounding cladding significantly changes the dewetting dynamics and offers some novel opportunities regarding the attainable range of microstructures. In this section, we will present a novel fabrication method relying on template instabilities to obtain nanowires of tunable period and spacing, with feature sizes down to 50 nm. Interstingly, this templated instability results in linear features and not droplets, as typically occurs for cylindrical jets.[149,150] This process represents an attractive alternative to the stack-and-draw thermal drawing method,[148] which is subject to shrinkage due to consecutive thermal drawings and limited accuracy at the preform level.

We present here a process able to achieve meter-long periodic arrays of chalcogenide nanowires in a single drawing step. We combine angle deposition on nanoimprinted polymer substrate with thermal drawing to obtain large-scale periodic nanowire arrays. The proposed process, described in Figure 2.6(a)-(b), starts with an imprinting process to generate a templated polymer substrate. The imprinting process relies on the use of a single silicon master mould with line arrays of fixed periodicity P (P = 40, 20 or 10 um in this work), obtained by photolithography. Drop casting and curing of PDMS onto this primary silicon master mold provide an infinite amount of negative texture replicas can be obtained. We replicate the texture by hot embossing the negative PDMS stamp onto a thermoplastic polymer film. In this work, the final polymer film is essentially Polyetherimide (PEI), thanks to its high glass transition temperature Tg, which is compatible for co-drawing with chalcogenides such as As_2Se_3 [149,150]. Polysulfone (PSU) has also been employed in combination with Se, at a lower processing temperature. The next step involves thermal reflow of the texture. Controlled heating allows for decay of the square surface profile into a sinusoidal interface.[151] In a third step, the chalcogenide is thermally evaporated with a side angle. The previous step of thermal reflow insures the full continuity of the film by smoothing out sharper surface features. Meanwhile, sample rotation during deposition implies a varying deposition angle from -34° to +83°, with an average surface angle of +25°. The asymmetric angle fluctuation ensures a fluctuation in film thickness along the cross section. The semiconductor glass film remains however continuous, covering the whole polymer substrate.
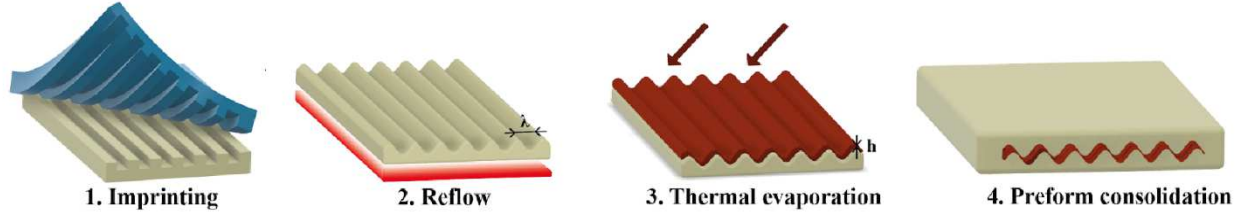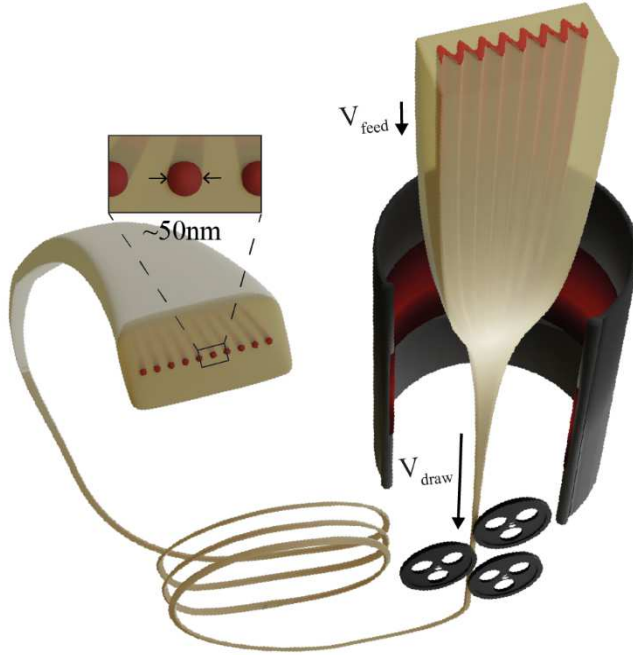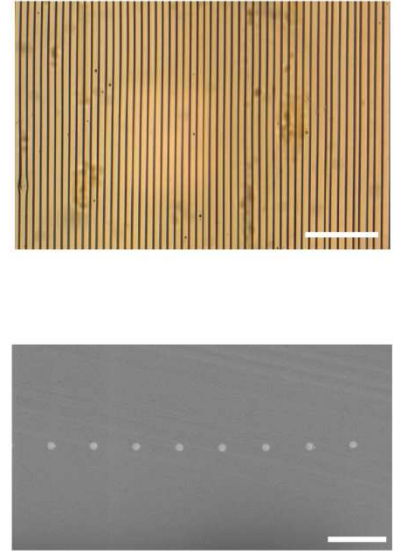
Figure 2.6 – In-Fiber templated filamentation process. (a) Schematics illustrating the fabrication process: 1. Imprinting of a microtextured onto a polyetherimide polymer for a silicon master mold using a negative PDMS stamp; 2. Annealing of texture to reflow the intial square pattern into a sinusoidal pattern; 3. Angle deposition of chalcogenide glass by thermal evaporation; 4. Addition of a polyetherimide encapsulation and consolidation. (b) A polymeric preform containing a chalcogenide film with periodically modulated thicknessesis is thermally drawn, reducing the cross sectional features to nanometric dimensions. (c) Top view optical micrograph and cross-sectional scanning electron microscopy image of the resulting microstructure, showing elongated periodic filaments. Scale bars: top 10 μm, bottom 2 μm.

The final and most critical step of preform preparation is the consolidation step, where the deposited chalcogenide film is encapsulated into another layer of the polymeric substrate material. This encapsulation step requires annealing under light pressure to soften and bond the two miscible polymer layers via chain interpenetration. It also ensures intimate conformity between the chalcogenide layer and polymer cladding. Inevitably, this step also leads to softening of the deposited chalcogenide layer, which, depending on the material, might be prone to dewetting prior to encapsulation. The issue at this stage is that dewetting occurs both along and perpendicular to the fiber axis, whereas the thermal drawing process suppresses the instabilities in the longitudinal direction.

The aim of this process is hence to generate instability in the fiber and not inside the preform, inducing break-up during the thermal drawing process according to the initially imposed thickness modulations. Based on this tailored instability evolution, we demonstrate the ability to produce meter-long ordered chalogenide nanowire arrays with a narrow associated size distribution, as apparent in the optical micrograph (Figure 2.6(c), top) and scanning electron microscopy images (Figure 2.6(c), bottom). Unlike the case of pure Rayleigh instabilities developing over flat thin films, the process allows to decorrelate to a certain extent the dominant instability wavevector from the initial film thickness. For templated instability wavelengths that becomes comparable to the initial film thickness, Laplace pressure takes on an increasingly limiting role, driving a quicker template instability reflow and final predominance of Rayleigh instabilities (e.g. random)

over templated instabilities (e.g. ordered). This limit will be studied in more details in Chapter 4.

Chapter 3   Modelling dynamics of in-air templated instabilities

3.1   Why a fluid mechanics model?

Given that the performance of many advanced optical devices such as Huygens meta-lenses or Fano-resonant metasurfaces can be sensitive to changes of even a few nanometers either in size or spacing, accurately predicting the final shape for a given initial system has been a fundamental question for advanced applications, that must be inevitably adressed. To gain full control over the resulting microstructure, a mathematical framework and modelling tools were developed to fully grasp the underlying physics of the rearrangement processes.

Focusing on the evolution of a thin film system over a pre-patterned substrate (e.g. in-air template instabilities), several elements hint at dynamics that follow the Navier-Stokes equation. Firsly, volume conservation of materials is verified over a broad range of initial film thicknesses. This indicates that there is no quantifiable material evaporation for
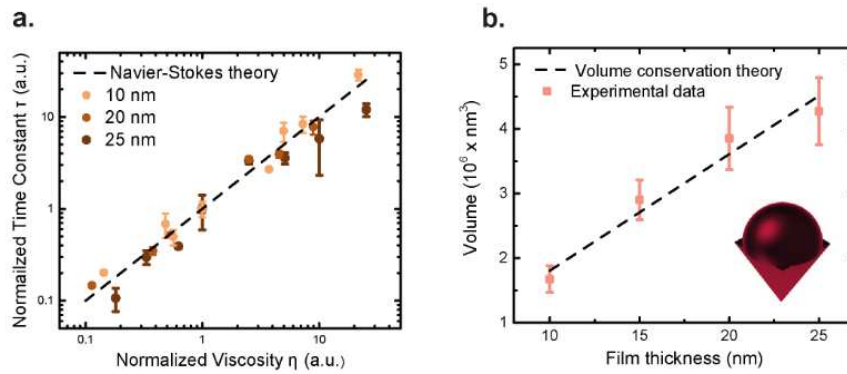
Figure 3.1 – Navier-Stokes formalism for template dewetting. (a) Evolution of dewetting time constants (extracted from colour evolution during the process) versus film viscosity. From the three primary colours, three values of a time constant τ can therefore be obtained from each sample. They are then used to calculate an average τ and a 95% confidence interval to define the error bars. The experimental data follow the theoretical scaling law predicted by the Navier–Stokes formalism. (b) Average volume of a single particle obtained after dewetting versus film thickness. The errors bars stem from the uncertainty in the image analysis, which is limited by the picture resolution. Experimental values match well the theoretical volumes calculated assuming no re-evaporation or material loss. Inset: Particle geometry used for calculation of the theoretical volume.

the chosen annealing temperatures, a pre-requisite for a fluid mechanics analysis of the film-pattern system. A second important indication that the system follows Navier-Stokes dynamics stems from colorimetric studies[152]. To measure the time constant τ associated with dewetting discussed in Figure 3.1(b), the color and temperature of an annealed film can be simultaneously monitored using an infrared and a conventional camera. To study the change in colour of the sample, the average value of each of the three primary colours over a large area of the sample was computed from a single frame, and their relative change was then plotted versus time. After a fluctuating initial stage, the dynamics followed an exponential law, yielding a time constant τ for three distinct thicknesses. As discussed in section 1.1.2.3, a linear stability analysis of thin film over flat substrates provides a characteristic time scale τ_s for spinodal instabilities, given by:

$$\tau_s = \frac{3}{\gamma h_0^3 K^4}\eta \tag{3.1}$$

Figure 3.1(a) plots the experimental normalized time constants measured for films of various thicknesses versus the viscosity of the film for the three thicknesses studied. It clearly appears that the experimentally obtained time constants

follow closely the trend expected by the linear stability analysis. This represents a second element that points to Navier-Stokes dynamics.

In this chapter, a first initial linear model is developed to qualitatively identify the conditions for proper re-arrangement. The novelty of the proposed linearized approach lies in the experimental approach taken. Direct experimental extraction of the various characteristic wavelengths (associated to reflow, spinodal instability, and Rayleigh Plateau instability) provides a way to predict the dominant mechanism and the potential final architectures. A second fully non-linear model adapting for the first time the precursor film approach on templated substrates to provide an accurate, quantitative description of the re-arrangement process in both 2D and 3D is developed. The model, developed in collaboration with the group of Prof. Francois Gallaire (LFMI, EPFL) spans several length scales, from atomistic (precursor film thickness ~1 nm) to typical capillary length scales (several microns for films investigated). It is remarkable that a continuum approach spanning such a large variety of length scales can provide a picture in line with experimental observations.

3.2 On the interaction between film and substrate

As discussed in section 1.1.3.2, the contact angle between the substrate and the film material is a key parameter linking microscopic Van der Waals interactions (Hamaker constant) with measurable macroscopic quantitites. Given that contact angles largely influence dewetting patterns both on flat films and in template systems, there is a strong interest in establishing a contact angle library.

Contact angles are considerably sensitive to several parameters, among which scale, dynamics, surface roughness, and chemical heterogeneities to cite a few. This raises the question of contact angle measurement accuracy for the present system of interest, which ranges from the hundreds of nanometer scale to tens of micron scale for droplet size. Moreover, the processing techniques and materials used raise the question of surface roughness, which may induce significant contact angle hysteresis.

	SiO$_2$ sol-gel	Ormocomp	Ormostamp
Substrate Material			
Variation	24.8 ± 3.8 nm	29.6 ± 5.6 nm	92.7 ± 7.5 nm
Roughness Rq (RMS)	0.60 ± 0.12 nm	0.89 ± 0.18 nm	0.99 ± 0.16 nm
Contact Angle θ	84.6° ± 6,1 °	64.9° ± 3,1°	84.2° ± 4,0°
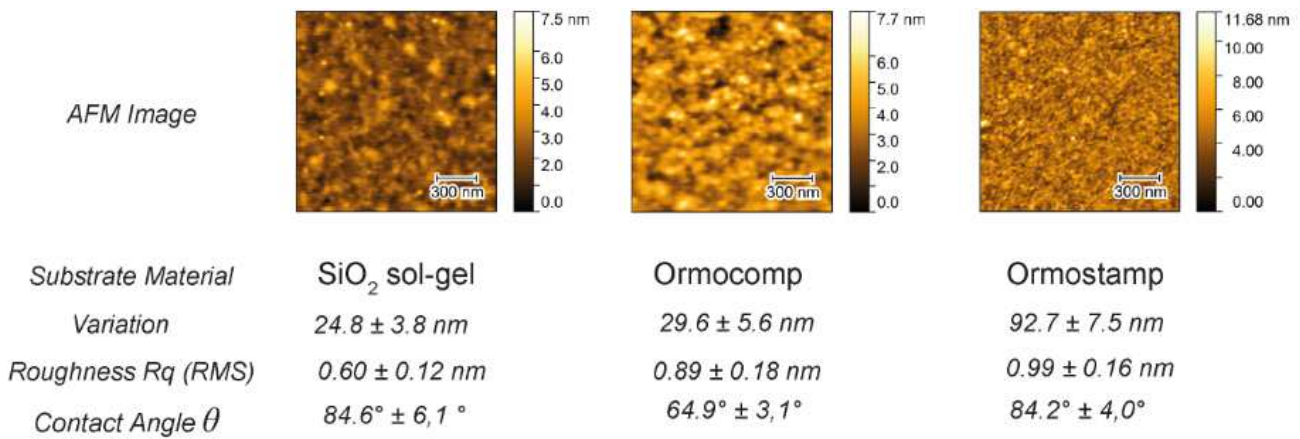
Figure 3.2 – Roughness parameters of the substrates used in this work. Root mean square Roughness exhibits values <1 nm. Variation values (i.e. integral of the absolute value associated to the local gradient) shows denser features in Ormostamp substrates than in other elements.

To address these multiple challenges, we proceed in successive steps. The first step consists in the preparation of substrates with low surface roughness. We resort to several substrates, including: (i) sol-gels baed on acid-catalyzed Methy(triethoxysilane), followed by a pyrolysis step at 400°C, (ii) thermoplastic polymers such as polycarbonate, which

exhibit ultra-low surface roughness due to reflow above their glass transition temperature, (iii) UV-curable commercial resins, in particular Ormocomp and Ormostamp from Microresist, Germany. The pyrolysis step for sol-gels helps to densify the resulting silica structure, while pyrolizing residual organic components. To control the resulting surface roughness of silica based on sol gel processes as well as the commercial UV resins, we proceed to characterize this quantity by atomic force microscopy (see Figure 3.2). All root mean squared (RMS) roughness values are inferior to 1 nm, which, although not competitive with typical Si wafer roughness, compares favourably with most other surfaces.

A second step aims at cleaning thoroughly the substrates to remove any chemical inhomogeneities. As reported in the literature, this is a critical step to insure a homogeneous substrate surface energy, and consequently homogeneous dewetting patterns. The extensive use of polymers largely restricts the use of typical aggressive solvents that are commonly used to clean traditional wafers such as H_2SO_4 of HF. Nevertheless, common cleaning procedure help to wash away nanoimpriting residues such as silicone oil traces from the PDMS (see Chapter 5.6) or other contaminants, All substrates are subsequently washed systematically using isopropanol (degreasing agent), ethanol, and water. The wash cycle is commonly repeated three times, followed by a gentle nitrogen or air gun to dry the substrate surface and blow away eventual debris or particles remaining at the surface.
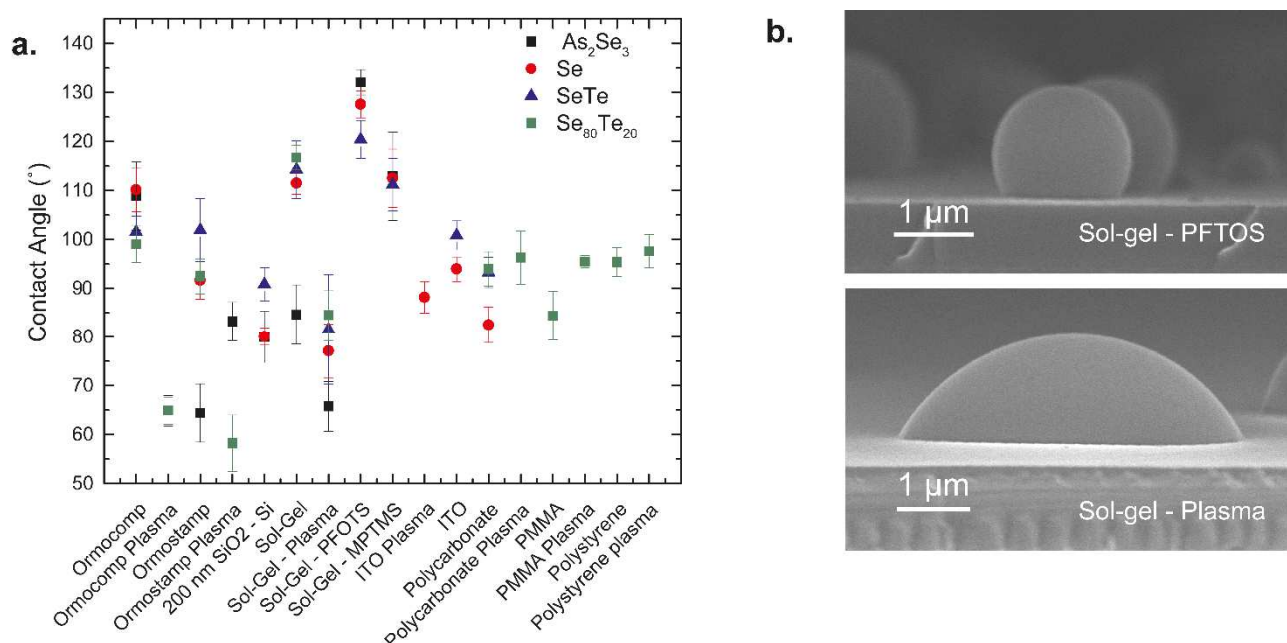
Figure 3.3 – Library of contact angles for various film-substrate systems. (a) Contact angle values and associated standart deviation based on Scanning electron microscope imaging in cross section post-dewetting. (b) Cross sectional Scanning electron microscope images for an identical 100 nm As2Se3 film dewetted on an silica sol-gel film using two different surface treatments: (top) a silane treatement based on Trichloro(1H,1H,2H,2H-perfluorooctyl)silane (labelled PFOTS), and (bottom) a substrate treatment based on oxygen plasma exposure. The substrate is made of an identical 400 nm sol-gel silica layer over a borosilicate glass slide, which is pyrolyzed after gelification process to ensure removal of residues and densification of the silica layer.

The hysteresis caused by roughness and chemical heterogeneity is further assessed by evaluating the standard deviation of contact angles measurement for a given film/substrate couple, shown as error bars in Figure 3.3. The error bars stem from a combination of imaging analysis related uncertainties and substrate surface roughness, which induce local triple line pinning and deviation for equilibrium contact angle. As apparent in Figure 3.3, limited contact angle hysteresis does occur in all systems studied. Further techniques to decrease the surface roughness of nanoimprinted substrate as well as improve the chemical washing procedure would be of considerable help to reduce contact angle standart deviation and thereby offer a better control over templated dewetting.

Following the preparation and cleaning procedure, substrate may undergo surface treatment to modify the free surface energy (explicitely mentioned in Figure 3.3). Two main substrate treatment are used. A first, more specific surface

treatement involves the use of silanes, using Trichloro(1H,1H,2H,2H-perfluorooctyl)silane (labelled PFOTS) or (3-Mercaptopropyl)trimethoxysilane (MPTMS). PFOTS is known to largely increase the hydrophobicity of silicon wafers, while MPMTS is a well-know adhesion promoter. A similar observation is made with all chalcogenide glasses on PFOTS-treated substrates, sensibly increasing the contact angles in comparison with the non-treated silica layers. A second, more ubiquitous treatment consists in a short oxygen plasma exposure. This short treatment is also known to improve hydrophilicity on silicon substres, and a similar trend is observed with chalcogenides, as plasma-treated substrates consistently show lower contact angles than their non-treated equivalent. Oxygen plasma treatement is a particularly key element in template dewetting. Reducing the contact angle has the beneficial effect of slower kinetics and in particular slow growth kinetics of nucleated holes. It is commonplace that in template systems, holes may not occur perfectly at the same time in symmetrical systems such as inverted pyramids, depending on a number of parameters including deposition symmetry. Given the large evolution time scale difference between growth of holes and reflow (reflow being much slower), this momentaneous asymmetry may lead to assymmetric dewetting patterns, which corroborates with the increased presence of defects. Reducing the contact angle leads to slower hole growth kinetics, and hence less asymmetry in final dewetting patterns. Substrate treatements are particularly attractive, since they allow tuning of interfacial energy between film and substrate without fundamentally impacting the final optical signature. Other materials such as Au or MgO with considerably high or low polarizabilities are also well known to influence wetting properties,[10] but these two materials (particularly Au, which is a plasmonic material) leave strong optical signatures even as nm-thick films.

3.3   Linear stability analysis of in-air templated instabilities

For thin films (tens of nanometer in thickness) undergoing dewetting, dewetting can unfold according to two main mechanisms: either dry spots are nucleated at defects, appearing at random locations on the substrate ("heterogeneous nucleation") or capillary waves are amplified spontaneously ("spinodal dewetting"). In the latter case, the amplification of a particular wavelength leads to a preferred distance in the dewetting pattern (see Section 1.1.3). This is observed in our systems for a reduced thickness range. In this section, we derive analytically a time constant for template capillary leveling ("template reflow"), and compare it to the one already identified for spinodal dewetting (see Section 1.1.3). By deriving and comparing these two timescales based on experimental data, we derive a model sequence for template dewetting and identify a condition to obtain ordered structures.

3.3.1 Spinodal dewetting vs. template reflow

3.3.1.1 *A linearized analysis of template reflow*

Let us now consider a film of initial thickness h_0 on top of a one-dimensional textured substrate $s(x)$. For simplification purposes, the texture has a sinusoidal profile with a wavenumber $K = \frac{2\pi}{\lambda_r}$. Spinodal dewetting and template reflow are supposed independent[15]. We now study the film reflow under the influence of the textured substrate (named 'template reflow' in the following section). We can introduce:

Figure 3.4 – Schematic illustrating film smoothening under the influence of Laplace pressure

$$h(t) = h_0 + u(t).sin(Kx) \tag{3.2}$$

$$\zeta(x,t) = h_0 + (u(t) + S_0).sin(Kx) \tag{3.3}$$

In this section, only reflow is considered. Disjoining pressure has a negligible role during the initial stage of our process when the film is thick enough, as shown later by experimental observations (see Section 4.3). We can rewrite equation (1.26): [12,13]

$$\partial_t h + \frac{\gamma}{3\eta}\partial_x(h^3\partial_{xxx}(h+s)) = 0 \tag{3.4}$$

The profile thickness can be re-inserted into equation (3.4). We further consider evolution over short times to linearize the equation:

$$\partial_t u = -\frac{\gamma h_0^3}{3\eta}K^2[(K^2)u(t) + S_0K^2] \tag{3.5}$$

A time scale can be associated to the growth of thickness modulations:

$$\tau_r = \frac{3\eta}{h_0^3\gamma K^4} \tag{3.6}$$

We note the linear dependence between time scale τ_r and viscosity. The solution of equation (3.4) reads:

$$u(t) = S_0(e^{-\frac{t}{\tau_r}} - 1) \tag{3.7}$$
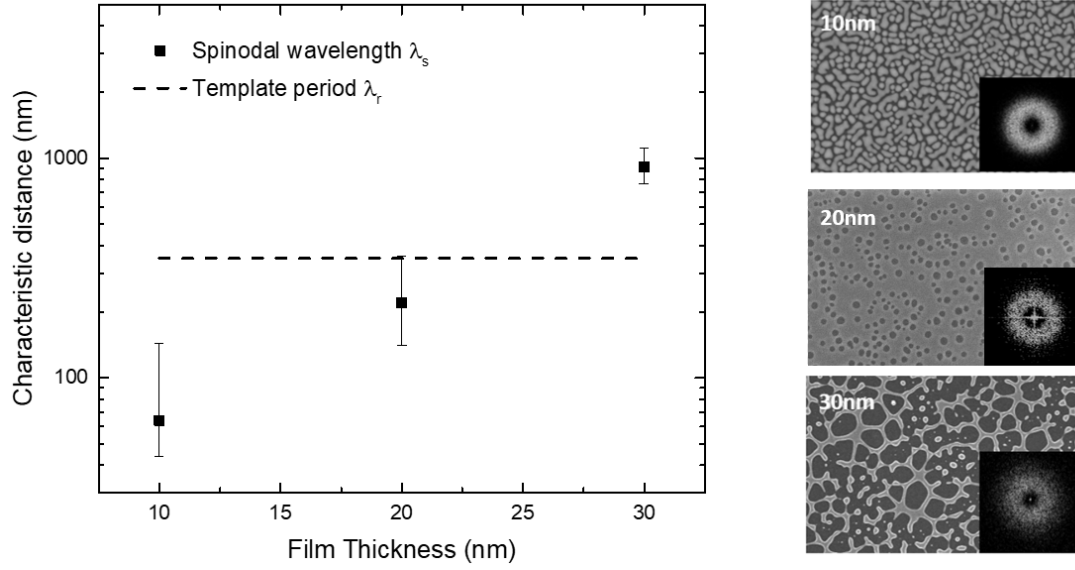
Figure 3.6 – Characteristic spinodal and reflow wavelengths. (Left) Spinodal wavelength as a function of thickness for three initial film thickness (10 nm, 20 nm, 30 nm) and (right) corresponding scanning electron microscope images. The preferred distance is obtained by Fast Fourier Transform (FFT) of initial stage dewetting patterns (inset).

3.3.1.2 *Experimental Validation*

Spinodal dewetting and template reflow have competing effects. This interplay between reflow and spinodal dewetting is largely dependent on the initial film thickness. Comparing the time scales associated to reflow and spinodal dewetting determines which phenomenon dominates during the various stages of the process.

According to the linear model, the time scales associated to reflow and spinodal dewetting are directly linked with a characteristic distance ($\tau \propto \lambda^4$) in the dewetting process. To stay in line with our theoretical linear framework[153,154], we analyze the initial dewetting stages where holes start appearing in the pattern using scanning electron microscopy. Contrarily to most investigations led on spinodal dewetting thus far, which involve spin-coating of polymer solutions on silicon wafers, our analysis differs in the process used to obtain the films. Owing to their low glass transition temperature, chalcogenide glasses easily dewet, potentially also directly during evaporation. This can be linked to the combination of the heat generated during the thermal evaporation process and the very high free surface energies for sub 10 nm-thicknesses. Systematic dewetting below a certain critical thickness ($h_c \simeq 15\ nm$) is observed upon evaporation. In such cases, the characteristic distance observed directly after thermal evaporation is analyzed without further annealing by Fast Fourier Transform (FFT) analysis. Thicker films (above ~ 15 nm) are annealed to initiate dewetting. The initial stage where holes appearing in the film exhibit a characteristic spacing is then analyzed with an FFT image analysis, as done in previous works on spinodal instabilities[17,154,155]. This characteristic spacing is in first approximation assimilated to the spinodal wavelength. Above 30 nm, long range order disappears in Fourier transforms: zones with spinodal instabilities coexist with zones where dewetting proceeds by random nucleation and growth of holes for the specific SeTe film studied. This coexistence is also reported in various polymer systems at comparable thicknesses[156,157]. As depicted in Figure 3.6, the preferred distance λ_{sp} becomes larger than the lattice period λ_r slightly above 20 nm. Bearing in mind that $\tau \propto \lambda^4$,
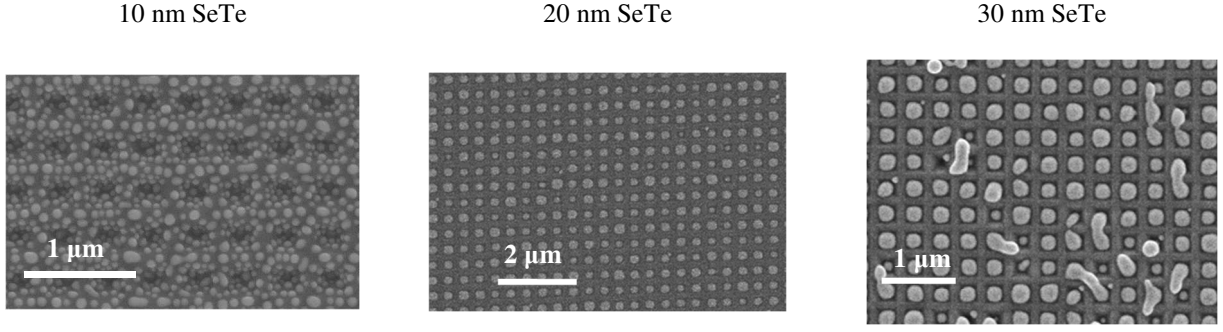
Table 1 - Time evolution of a SeTe film over a 350 nm period square inverted pyramid lattice.

this implies that reflow should dominates at large thicknesses ($\tau_{sp} \gg \tau_r$, around 30 nm), while spinodal dewetting dominates at lower thicknesses ($\tau_{sp} \ll \tau_r$, around 10 nm). When both time scales are comparable, the reflow amplitude $u(t)$ remains larger than the spinodal amplitude $\varepsilon(t)$ (since $\varepsilon_0 \ll u_0$), and hence reflow still dominates.

To validate experimentally the these first predictions based on flat substrate dewetting, we proceed to dewet SeTe films of various thicknesses (10 nm, 20 nm and 30 nm) on a textured sample (350 nm square periodic lattice). For a 10 nm film, it appears that dewetting does not follow the underlying texture. This corresponds to the prediction of the linear model at low thicknesses: the drive for spinodal instabilities is stronger than that for reflow from the onset of dewetting, and yields a disordered particle array that does not follow the pattern. To the opposite, 20 nm and 30 nm SeTe

film, reflow appears to dominate over spinodal instabilities: the material orders according to the underlying pattern. In the linear model, we demonstrated that, for a 20 nm film, the characteristic distance associated to reflow $\lambda_r \sim$ 350 nm was

slightly larger than spinodal wavelength $\lambda_s \sim$ 220 nm. Bearing in mind that $\varepsilon_0 \ll u_0$, our experimental observations are in line with the linear model that predicts a crossover between reflow and spinodal amplitudes slightly below 20 nm. Based on this analysis, the process unfolds in the following steps:

(i) Following a relatively thin film deposition ($\lambda_s \ll \lambda_r$), spinodal instabilities develop immediately to yield particles that do not follow the pattern.

(ii) After a relatively thick film deposition ($\lambda_s \gg \lambda_r$), reflow induces thinning of the film in concave regions (edges of the pyramid), while material tends to accumulate in other regions of the pattern (pyramid pit). During this whole initial stage, the analytical model predicts a linear relation between characteristic time scale and viscosity. In an intermediate stage, thickness modulations of the substrate due to reflow are large, and thus the quantity $u(t)$ can no longer be neglected with regards to the initial thickness h_0. The equations governing solid-state flow become highly non-linear. Reflow of material is still occurring, and the film gradually becomes thinner over the convex regions of the pattern. At the end of the process, spinodal instabilities eventually become dominant over reflow, ultimately leading to break-up.

As an important note, the emergence of spinodal instabilities in our system has been strongly dependent on the experimental substrate surface state, and sometimes could vary within a single sample. The results presented here are the most representative of each system. This remark highlights the importance of the cleaning procedure in this work with spinodal instabilities and at such strongly reduced thickness. Futher works to improve the the surface state of the substrates studied (here smooth polycarbonate sheets with RMS roughness < 0.2 nm) would be of high interest to validate the present results.

3.3.2   From particles to lines: a linear framework

It was previously demonstrated in Chapter 2 that the proposed process could not only achieve particle arrays, but also continuous optical glass linear structures. To produce such structures, we take advantage of the difference in time scale between template-induced reflow (τ_r), that reshapes the film into linear structures, and Rayleigh-Plateau (τ_{RP}) instability, which leads to capillary break-up of lines into particles. If the time scale associated to template reflow is shorter than the one associated to Plateau-Rayleigh instabilities, we can then freeze the system into linear structures.

3.3.2.1   *A linearized analysis of Rayleigh-Plateau instabilities*

To illustrate this competition between reflow and Rayleigh instabilities, we start by evaluating the time scales linked to both instabilities and further compare them. As seen previously (see Section 3.3.1), the template-induced reflow time scale reads:

$$\tau_r = \frac{3\eta}{h_0{}^3 \gamma K^4} \tag{3.8}$$

We now consider the Chandrasekhar formulation for Rayleigh-Plateau instabilities[158,159], where radial modulations of a viscous cylinder can be written as:

$$R = R_0 \left(1 + \varepsilon_0 e^{-ikz + \frac{t}{\tau_{RT}}}\right) \tag{3.9}$$

With R_0 the unperturbed cylinder radius, k the wavenumber of the Rayleigh-Taylor instability, z the coordinate along the cylinder axis, and t the time. In the asymptotic case where inertial effects are negligible in comparison with viscosity effects, we can write:

$$\left|\frac{\rho}{\eta.k.\tau_{RT}}\right| \ll 1 \tag{3.10}$$

Where ρ is the film density. In this particular case, the dispersion relation reduces to:

$$\frac{1}{\tau_{RP}} = -\frac{\gamma}{2\eta R_0} \cdot \frac{(1 - (kR_0)^2)}{1 + (kR_0)^2 \left(1 - \left(\frac{I_0(-kR_0)}{I_1(-kR_0)}\right)^2\right)} \tag{3.11}$$

With γ the film surface tension and η its viscosity during the dewetting process. I_0 and I_1 are the modified Bessel functions of the first kind of the zeroth and first orders respectively. Let us now evaluate the ratio of both time scales:

$$\frac{\tau_r}{\tau_{RP}} = -\frac{3}{2} \cdot \frac{1}{h_0{}^3 K^4 R_0} \cdot \frac{(1 - (kR_0)^2)}{1 + (kR_0)^2 \left(1 - \left(\frac{I_0(-kR_0)}{I_1(-kR_0)}\right)^2\right)} \tag{3.12}$$

We can note that the ratio here is independent of both the film's surface tension and its viscosity, i.e. of the material composing the film. The reasoning is thus extendable to any class of viscous material. Although viscosity does not appear in this ratio, the high viscosity state is still relevant because it induces slower system dynamics. It is therefore easier experimentally to freeze the system in its linear state.

For numerical evaluation, we consider three thicknesses of one material (As_2Se_3) deposited separately on top of a 350 nm periodic V-shape line lattice (silica substrate): 42 nm, 33 nm, and 25 nm. We determine k and R_0 by image analysis (ImageJ) from the dewetted line structures.
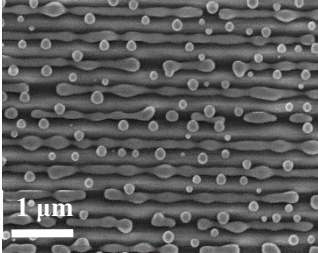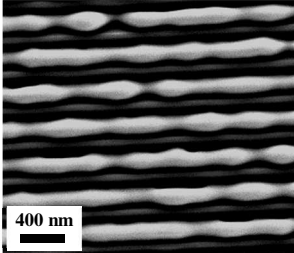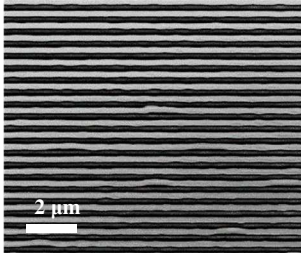
	SEM Image 1	SEM Image 2	SEM Image 3
h_0	25 nm	33 nm	42 nm
K	$\dfrac{2\pi}{350\ nm}$	$\dfrac{2\pi}{350\ nm}$	$\dfrac{2\pi}{350\ nm}$
R_0	50 nm	70 nm	80 nm
$\dfrac{2\pi}{k}$	400 nm	650 nm	1030 nm
$\dfrac{\tau_r}{\tau_{RP}}(As_2Se_3)$	2.53	0.34	0.62

Table 2 – Rayleigh-Plateau instability vs. reflow. Relative time evolution of Rayleigh-Plateau instabilities and template-induced reflow as a function of the As2Se3 film thickness on a periodic 350 nm line silica lattice

At low thickness (25 nm), Rayleigh instabilities appear to develop faster than template-induced reflow. According to the linear stability analysis, $\frac{\tau_r}{\tau_{RP}}(As_2Se_3) > 1$ and therefore obtaining linear structures is not favored. As the thickness increases (33 nm to 42 nm), the comparative influence of both phenomena is favorable enough ($\frac{\tau_r}{\tau_{RP}}(As_2Se_3) < 1$) to yield linear structures. For higher thicknesses (above 50 nm, not shown here), the drive for both reflow and Rayleigh-Taylor instabilities diminish. When further increasing thickness, the thermodynamic limit of template dewetting is eventually reached, and final structures no longer follow the underlying pattern but rather form particles sitting in between grooves.

3.4   Inhibition of Rayleigh-Plateau instabilities

As discussed previously in a linearized frame, Rayleigh-Plateau instabilities may propagate along the length of linear chalcogenide features onto a substrate. The previous section demonstrated the influence of the thickness to period ratio on the ability to obtain linear features, and successfully demonstrated that a specific range of thickness provided an optimal time frame over which the dewetting film could be frozen into lines. This approach relied on the Chandrasekhar formulation of Rayleigh-Plateau instabilities, which assumed a cylindrical shape for the linear features and largely neglected the role of the substrate, whose influence was solely taken into account through the template period. However, contact angles play a critical role in stability of such structures. In this section, we discuss on the influence of side wall angle on Rayleigh-Plateau instabilities and the possibility to enhance stability of linear features.
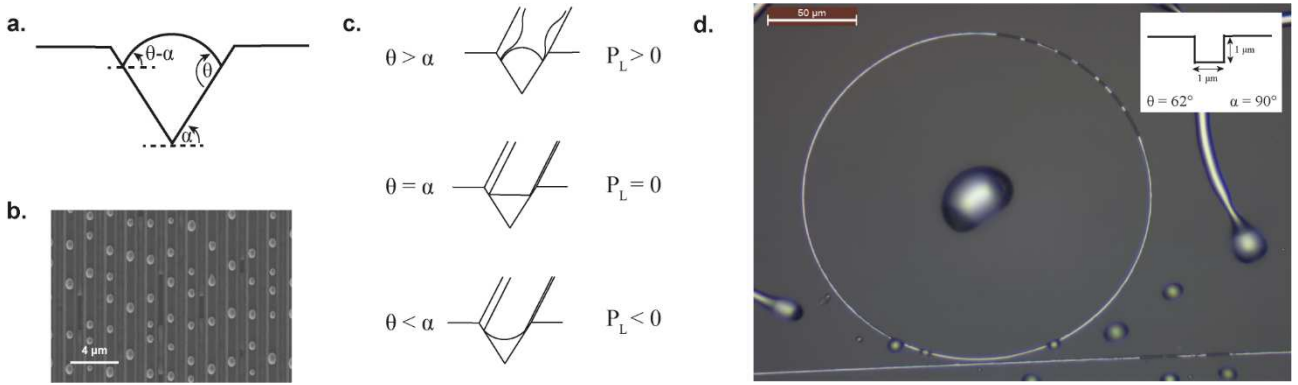
Figure 3.7 – Suppression of Rayleigh-Plateau instabiliites. (a) Schematic indicating the V-groove angle α, the equilibrium contact angle between the film and substrate θ, and the apparent contact angle θ-α. (b) Top view Scanning electron microscopy image of As_2Se_3 stripes of similar initial volumes after evolution over flat and V-grooved regions. The Rayleigh-Plateau instability evolves faster on the flat portion than the grooved portion. (c) Schematic illustrating the three ideal cases in the V-groove cross-section. (d) Ring-Resonator structure textured over a silica sol-gel substrate, over which a 500 nm As_2Se_3 was dewetted (θ = 62°, α=90°). The groove geometry is shown in inset.

A large amount of studies have already been dedicated to the stability analysis of elongated viscous features on substrates. The possibility to suppress Rayleigh-Plateau instabilities based on the use of tailored side walls has also been already discussed theoretically in two main studies.[160,161] The first study discussed about this possibility in crystalline materials, and theroretically demonstrated based on a linear stability analysis the possibility to suppress Rayleigh instabilities emerging in nanowires.[160] A second very thorough investigation discussed on the same topic and focused on polymers over silicon textures.[161] Relying on electrowetting to fine tune contact angles, this study demonstrated in particular the possibility for a large droplet to infiltrate microchannels by fine tuning contact angle below a certain critical value ("capillary filling"). Based on this same principle, we propose here to investigate the evolution of chalcogenide films undergoing dewetting over substrates with tailored sidewalls. To this end, we consider a V-shape trench with varying angle α to the horizontal (see Figure 3.7(a)). We further consider inside the groove a perfectly linear wire with fixed equilibrium contact angle θ with the substrate (see Figure 3.7(a)). If the film-substrate equilibrium contact angle θ is larger than α, the Laplace pressure P_L is positive, and the line is unstable. Rayleigh-Plateau instabilities propagate along the length of the film and a dominant (e.g. fastest growing) instability eventually leads to break-up (Figure 3.7(c)). If θ is equal to α, the Laplace pressure is completely suppressed and other elements (e.g. disjoining pressure) must be considered to determine film stability. When θ is inferior to α, Laplace pressure becomes negative, in which case the line minimizes its free surface energy by remaining inside the groove. In Figure 3.7(b), we show the microstructure upon partial dewetting of an 80 nm As_2Se_3 film over a plasma-treated Ormocomp texture (θ=64.5°) combining flat regions and V-grooves (α = 54.7°). The flat and groove regions have almost identical areal coverage, and hence wires inside the grooves and on top of the substrates involve quantities of materials that can be in first approximation also considered identical. Given that θ> α, Laplace pressure is still positive and Rayleigh-Plateau instabilities can still propagate. Upon partial dewetting, we observe that the instabilities have propagated significantly faster over the flat region than in the groove, where the chalcogenide glass still forms elongated features.

To place ourselves in an even more favorable situation, we create 1 μm - wide square grooves (see Figure 3.7(d)(inset)), with an associated angle α = 90° and an aspect ratio of 1, forming a ring resonating structure (particularly interesting in photonics for filters or frequency combs). Similarly to the previous case, we deposit a 500 nm - thick As_2Se_3 film over a plasma-treated silica texture (θ = 62°). After complete dewetting of the top film, we observe by optical microscopy in reflection the presence of still extensively elongated features inside the square grooves. The origin of the local break-up points still have to be fully elucidated, and their presence optimized, but the optical micrograph clearly

demonstrates the possibility to obtain extended linear features with grooves relying on controlled reflow and dewetting. While the underlying physics behind such phenonema may appear simple, it is particularly useful to understand the the cause for relative stability of linear features observed in Section 2.2.2. Based on simple tailoring of contact angle between substrate and film, stable linear features can be engineered inside grooves with custom side wall angles. While we demonstrate this for purely linear architectures here, it would be interesting to further study how this stability evolves with a change in groove geometry.

3.5 Non-linear modelling of in-air templated instabilities

In this section, we go beyond the simplified linearized model presented previously, which is rigorously only valid at the very onset of instabilities, and propose instead a continuum model predicting the evolution of a templated film evolving over pre-patterned substrates, based on modelling of atomistic-scale interactions occurring on various substrates, for contact angles less than 90°. By comparing experimental and simulated thickness profiles over various patterns, we demonstrate that the proposed model is suitable for the accurate prediction of the final morphology in both 2D and 3D, and over several length scales (nm to μm scale).

3.5.1 The precursor film approach on flat substrates

An accurate dynamic description of dewetting constitutes a particularly challenging problem. The theoretical framework for the description of fluid flow is based on approaches from continuum mechanics. We initially consider a flat horizontal substrate and introduce a coordinate system (x,y,z), where the z direction, along which the film thickness is measured, coincides with the vertical one. The integration of the Navier-Stokes equations along the z direction under the classical assumptions of the long-wavelength approximation[162,163] leads to an evolution equation for the thin film thickness h in the (x,y) directions, so-called lubrication or thin film equation, already discussed in the introduction:

$$\frac{\partial h}{\partial t} = -\frac{1}{3\mu} \nabla \cdot \left(h^3 \nabla (\gamma \nabla^2 h - \Pi(h)) \right)$$

(3.13)

Where ∇ operates in the (x,y) plane, μ is the fluid dynamic viscosity, γ is the surface tension coefficient between the fluid and the air, and Π is the so-called disjoining pressure. Following the results introduce in Section 1.1.3.2, let us now assume that the disjoining pressure term stems from a classical Lennard-Jones type potential:[18,164,165]

$$\varphi(h) = \frac{B}{h^8} - \frac{A}{12\pi h^2}$$

(3.14)

where A=A_{123} is the Hamaker constant of the system substrate (1) - film (2) - air (3) and B is the Born coefficient, that embed respectively the long range attractive and short range repulsive forces. The combination of a repulsive and an attractive term defines an equilibrium "precursor" film thickness h_{eq}, which ensures the boundedness of the potential for h>h_{eq}. The force derived from the Lennard-Jones potential stems from an imbalance in the dispersive interactions between the various constituent molecules. This imbalance is classically embedded in the Hamaker constant A_{123}, which establishes the influence of constituent materials in long range interactions (c.f Section 1.1). The Lennard-Jones potential is a powerful approach, in the sense that it allows through simple pairwise integration over the interaction volume to account

for geometrical contributions, so-called Hamaker procedure.[166,167] Nevertheless, it constitutes a largely simplified view of intermolecular interactions, which does not properly address the question of multi-body interactions. Such potential assumes pairwise additivity of forces, no longer valid as soon as more than two atoms are involved. The multi-body problem can simply be taken into account using a modified effective Hamaker constant obtained through the so-called Lifschitz approach,[168] which treats the interacting media as continuous with intensive properties. Combining the easy-to-use Hamaker procedure with an effective Hamaker constant hence provides an effective way to accurately account for multibody interactions[167,169]. Based on the results from Section 1.1.3.2, one can link the equilibrium contact angle with the Van der Waals potential:

$$1 + tan^2 \theta = \left(\frac{\varphi(h_{eq})}{\gamma} + 1 \right)^{-2}$$ (3.15)

Considering solely angles between 0° to 90°, relation (3.15) provides a bijective relationship between the contact angle and the precursor film h_{eq}.

In the rare previous works that developed a model based on the Lennard Jones potential, the contact angle was inferred from accurate Hamaker and Born constants data, with a good agreement between theoretically derived and experimentally measured contact angle values. This approach assumes the prior knowledge of the Born coefficient, which is significantly harder to quantify than the Hamaker constant, and constitutes a significant limitation for broader use of such modelling scheme. Moreover, this requires the knowledge of the precursor film thickness, a challenging quantity to experimentally measure (typically in the Angström range). In this chapter, we propose to use the Born coefficient, and thus the equilibrium thickness given by (3.15), as independent parameter to match the experimental and modelled contact angles. In contrast with previous works, the knowledge of a pseudo-wetting system's equilibrium contact angle and the Hamaker constant is sufficient to effectively model the thin film dynamics.

To validate this novel approach, we now proceed to simulate the evolution of a thin film and evaluate the resulting contact angle. The thin film equation is implemented with the full expression of the interface curvature:[170,171,172,173]

$$\varkappa_f = -\vec{\nabla}.\boldsymbol{n}$$ (3.16)

$$\vec{n} = \frac{1}{\left(1 + (\frac{\partial h}{\partial x})^2 + (\frac{\partial h}{\partial y})^2\right)^{1/2}}. \begin{bmatrix} -\dfrac{\partial h}{\partial x} \ \vec{e_x} \\ -\dfrac{\partial h}{\partial y} \ \vec{e_y} \end{bmatrix}$$ (3.17)

where $\vec{n}$ embeds the x and y component of the normal of the fluid free surface; the problem is completed with the disjoining pressure detailed above. To verify the consistency of the relation equilibrium thickness-contact angle, we perform numerical simulations with the finite-element solver COMSOL Multiphysics by implementing the weak form of equations (3.13), (3.14), (3.16), and (3.17) in conservative form. We fix the equilibrium thickness at 0.5 nm and determine using relations (3.13), and (3.15) the Born constant and the contact angle. Simulation results with $h_0 = 25$ nm, $\gamma = 3.10^{-2}$ N/m, $h_{eq} = 0.5$ nm are shown in Figure 3.8, for three different values of $A = 5.10^{-20}$ J, 1.10^{-19} J, and $2.5.10^{-19}$ J. Contact angle values numerically obtained matched the experimental contact angle with an accuracy below 1°, which validates the proposed approach on flat substrates. As outlined above, the approach for the simulation of experimental conditions is based on the choice of the contact angle and the retrieval of the corresponding equilibrium thickness and Born coefficient. While the simulated precursor film models an actual physical thin film occuring in materials, its thickness is used in the present work as a fitting parameter. As such, it deviates from the actual thickness, typically

around one atomic spacing.[17] Considering the contact angles involved, the volume error associated with this choice is in all cases presented here inferior to 1%, and is thus neglected.
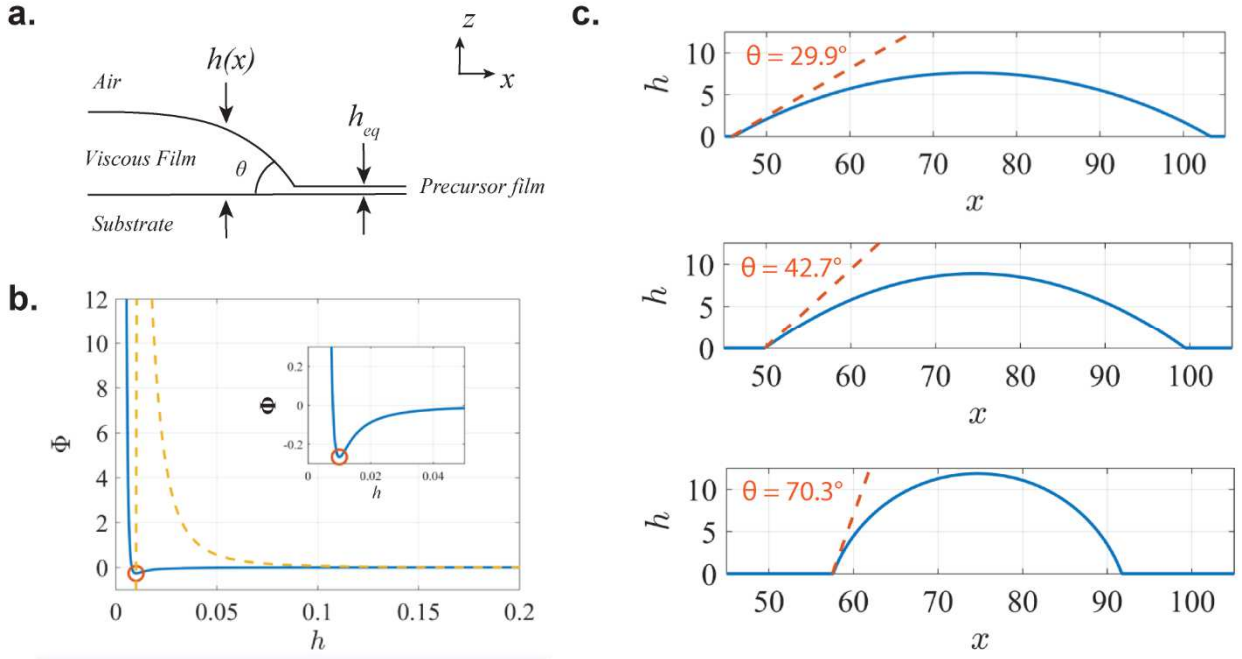
Figure 3.8 – Precursor film approach implemented on flat substrates. (a) Schematic describing the components of the system an the associated parameters in the precursor film approach. (b) Van der Waals potential associated to the viscous film on a flat substrate. The potential (blue curve) shows a minimum, which is further indicate by its derivative (dashed yellow curve) and the inset graph. The potential minimum correspond to the precursor film thickness h_{eq} indicated in (a).

The implementation of the complete curvature is essential to yield the proper results. The linearized curvature $\varkappa = -\frac{\partial^2 \varphi}{\partial x^2}$ in the long wavelength approximation gives contact angle values with over 10° error compared to the target value. Despite the small size of final drop states involved, the importance of the complete expression of the curvature to recover the final static shape is critical, as already highlighted in reference 171 for a similar problem at larger values of the thickness. At this point, an important question arises with the choice of the contact angle. During dewetting, it is common that contact angles evolve dynamically owing to the elasticity of the triple line. From a thermodynamic standpoint, such contact angle hysteresis should be absent if the triple line evolves under quasi-static conditions during the whole dewetting process. Several elements such as surface roughness or chemical heterogeneity may however threaten this assumption, and are commonly responsible for hysteresis. This induces a receding contact angle whose value is reduced with respect to the equilibrium contact angle (for angles <90°). The proposed model is hence valid essentially for the case with no hysteresis. To take into account hysteretical dewetting, a possibility consists in retaining the receding contact angle rather than the equilibrium contact angle. This point is further discussed in Section 1.1.3.2 , where Figure 3.3 summarizes contact angle values and the associated dispersions.

3.5.2   The precursor film approach on template substrates

We now turn to the evolution of a film with fixed contact angle θ over a templated substrate. We introduce a substrate of height profile h_0 measured along the z direction starting from the horizontal reference introduced previously. To accurately predict the thin film dynamics and the resulting microstructure, the previous thin film equation must be

Figure 3.9 – Simulated vs. experimental dewetted profiles in the 2 D case. (a) Simulated dewetted profile (blue) and experimental AFM dewetted profile (orange dots) in the case of a 2 μm period line pattern with a 850 nm pyramid base and a 60 nm initial film thickness of As$_2$Se$_3$. (b) Close-in view of (a) on a single period, showing the match between experimental and simulated contact angles.

adapted to take into account the role of the underlying substrate. The total surface curvature $\varkappa$ in this new configuration is modified, as the film's free surface profile is influenced by the underlying pattern. The curvature is now given by the curvature of the total free surface elevation h+h$_0$:[174]

$$\vec{t} = -\vec{\nabla}.\boldsymbol{n_t} \tag{3.18}$$

$$\vec{n} = \frac{1}{\left(1 + (\frac{\partial h}{\partial x} + \frac{\partial h_0}{\partial x})^2 + (\frac{\partial h}{\partial y} + \frac{\partial h_0}{\partial y})^2\right)^{1/2}} \cdot \begin{bmatrix} \left(-\frac{\partial h}{\partial x} - \frac{\partial h_0}{\partial x}\right) \overrightarrow{e_x} \\ \left(-\frac{\partial h}{\partial y} - \frac{\partial h_0}{\partial y}\right) \overrightarrow{e_y} \end{bmatrix} \tag{3.19}$$

Another difference with the flat substrate case lies in the film thickness definition in the Lennard-Jones potential. Recalling the definition of the potential (equation (3.14)), the contact angle is defined in part by the equilibrium thickness. Proper thickness definition is therefore key to reproduce identical contact angles over the whole substrate. On a flat substrate, thickness is defined straightforwardly as a vertical projection. However, in the general case with an underlying substrate, the accurate film thickness is defined as the shortest distance between film and substrate, which may be along an arbitrarily varying direction, i.e. the projection given by:

$$h^* = h.\cos\left(atan\left(\left(\frac{\partial h_0}{\partial x}\right)^2 + \left(\frac{\partial h_0}{\partial x}\right)^2\right)^{1/2}\right) \tag{3.20}$$

We adapt the numerical scheme with the latter thickness definition and ensure that it yields the desired contact angle over regular substrates (See Figure 3.9).

To validate the proposed numerical scheme, numerical simulations using experimental atomic scanning microscope profiles of substrates obtained by nano-imprinting are calculated. The experimental film profile upon dewetting is then superposed to compare the match between experimental and simulated data. First investigating the two dimensional case, the experimental and simulated dewetted film profile are compared in Figure 3.9 (period 2 μm, Inter-pyramid spacing 1.1 μm, film thickness 60 nm, contact angle θ=85°). The numerical scheme is further validated in three dimensions, using a pyramid with largely reduced spacing (Inter-pyramid spacing 150 nm, Period 1.1 μm, thickness 60 nm). It is remarkable that the model reproduces with accuracy the experimental profile for such reduced initial film thickness. Simulations also predict a critical film thickness h$_{crit}$ well in line with experimental observations. This critical thickness
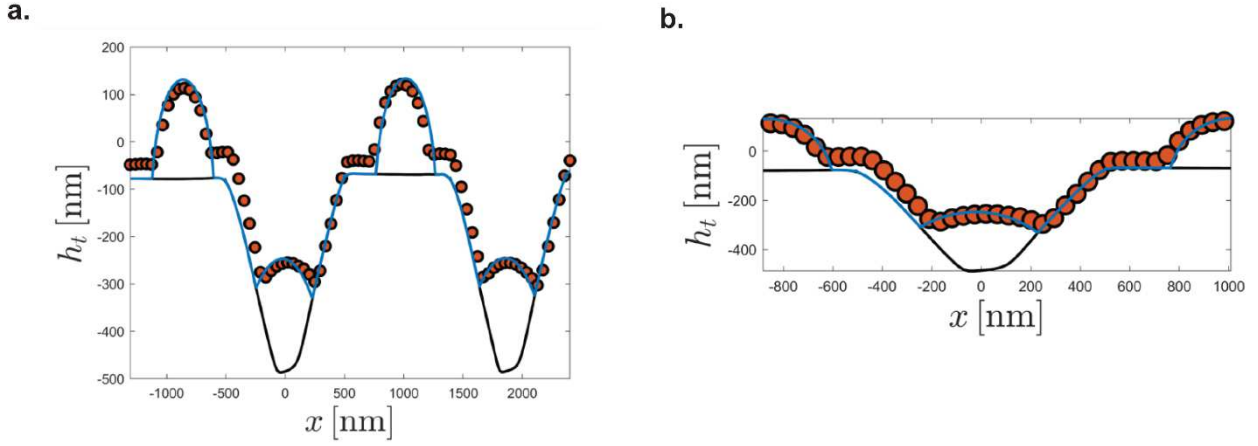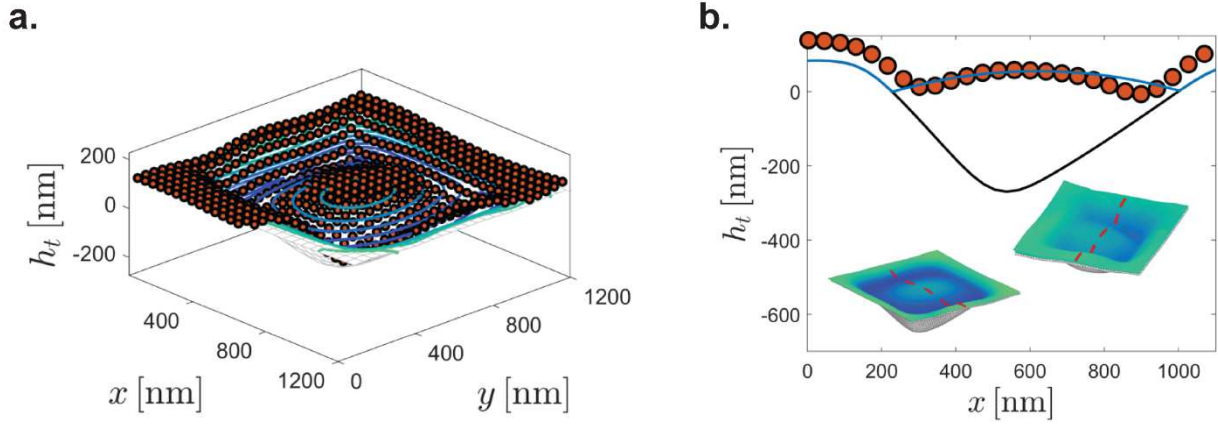
Figure 3.10 – Simulated vs. experimental dewetted profiles in the 3D case. (a) Simulated dewetted profile (Solid blue surface) and experimental AFM dewetted profile (orange dots) in the case of a 1.1 µm period line pattern with a 850 nm pyramid base.

sets a thermodynamic limit above which dewetting will unfold according to alternative non-periodic scenarios that occur by random nucleation and growth of holes. These results highlight the relevance of continuum mechanics schemes even at thicknesses that become comparable with atomistic length scales.

Given that the rearrangement of material is fundamentally linked to the increase in local curvature, the influence of curvature amplitude on final structures is further investigated (see Figure 3.12). For particularly high local curvature radii at the pyramid edge, pinned droplets may arise in simulation but decay with increased simulation time. It is noteworthy that such pinned states may also arise experimentally, typically at pyramid edges in three dimensions. The presence of pinned states occur solely when nano-imprinting does not involve pressing, which implies better conservation of
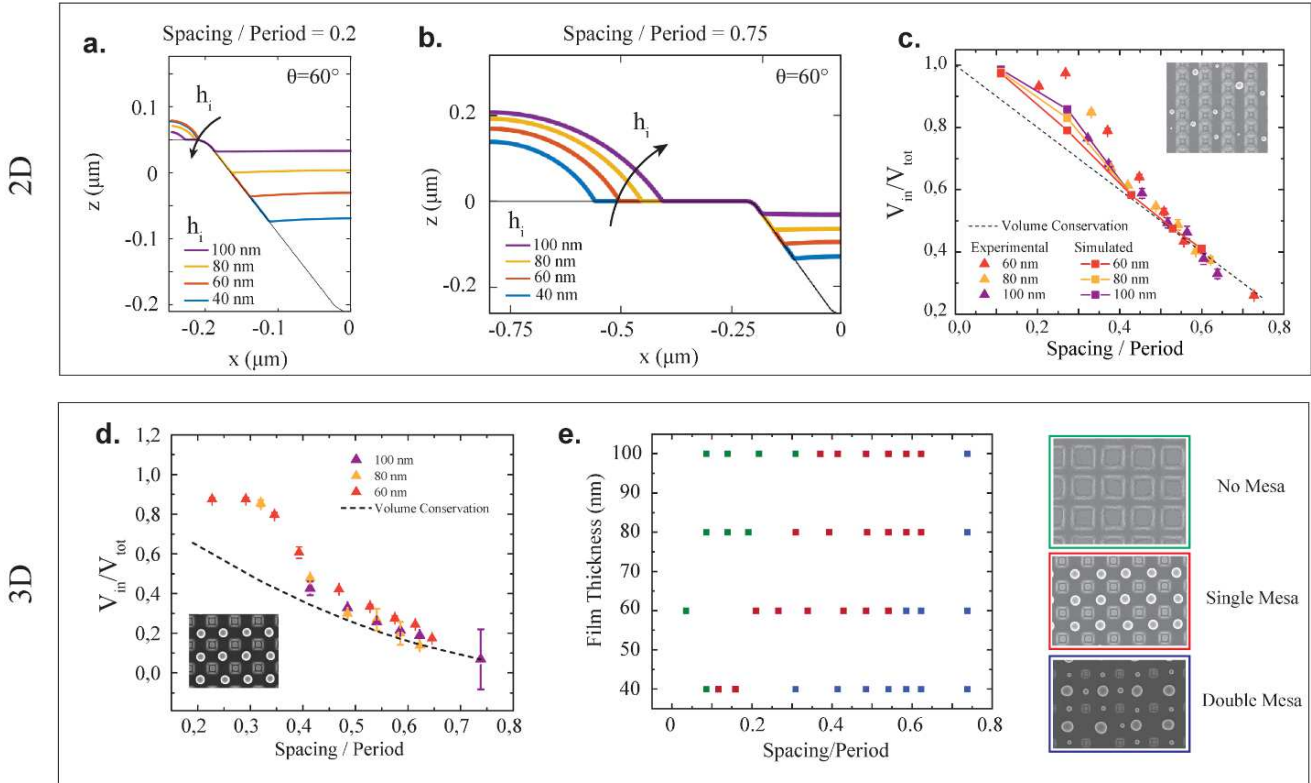
Figure 3.11 – Distribution of film material upon dewetting. (a) Two-dimensional final film profiles upon dewetting for spacing over period ratios S of S=0.2 (left) and S=0.75 (right). The mesa particle size grows with film thickness for S=0.75, while the trend is reversed for S=0.2. (b) Simulated pyramid volume over total volume ratio in the case of a two-dimensional geometry. Colors indicate the initial film thickness. Blue : 40 nm, Orange : 60 nm, Yellow : 80 nm, Purple : 100 nm. (c) Experimental (Triangular points) and Simulated (Solid line) pyramid volume over total volume ratio in the case of an inverted pyramid array with increasing distance along a single direction. (d) Experimental pyramid volume over total volume ratio in the case of an inverted pyramid array with increasing spacing along the two principal directions. (e) Diagram associated to inverted pyramids with varying spacing to period ratio and film thickness. The film material is composed of As2Se3 onto a plasma-treated Ormocomp® substrate.

sharp slope transitions. This is in line with the predictions from the two dimensional model, which predicts intermediate pinned states for diverging curvature radii.

A particularity of dewetting in such pyramid arrays pertains to the distribution of material in the final microstructure, which widely varies depending on the spacing to period ratio. In Figure 3.11, the final volume inside the pyramid V_{in} over the total volume V_{tot} is evaluated by simulation in the 2D case. In the case where the final pyramid volume would be solely constituted from the material initially deposited inside the pit, the pyramid volume should be constant with spacing and as a consequence follow a well-defined law, referred to in this work as volume conservation. The numerical results (Figure 3.11(a)-(d)) show a clear deviation from the volume conservation law at reduced spacing to period ratio, where the film located at the pyramid edges is preferentially pulled inside the pyramid. To the opposite, at larger spacings to period ratios, the ratio V_{in}/V_{tot} follows closely the volume conservation law. While the thickness dependence does not clearly appear in the experimental volume analysis, the deviating trend is observed for all configurations investigated, including lines with incremental spacing as well as pyramids with incremental spacing along both 1 and 2 dimensions. At reduced spacing, absence of mesa is observed for spacings up to 400 nm in some cases, while at very large spacing, the Rayleigh instability in the top plane gives rises to a double distribution in size and a new architecture. A stability map is provided in Figure 3.11(e) to provide the reader with an overview of the architectures as a function of spacing and thickness.
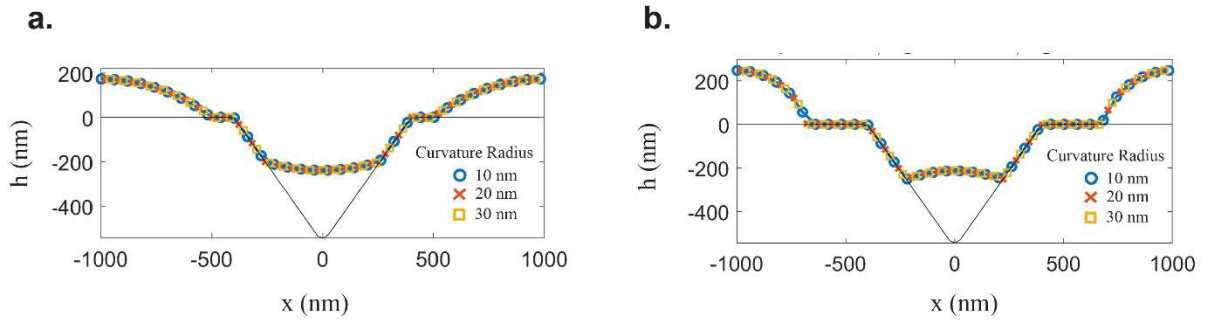
Figure 3.12 – Influence of the curvature radius of the dewetted stuctures in 2 dimensions. The radius of curvature at the edges has no visible influence on the final structure observed for the thicknesses and contact angles considered in this work.Contact angles used from left to right are: 40°, 60°, and 80°.

To conclude, we have introduced a novel modeling framework for the dewetting of films over a templated substrate based on a precursor film approach. By resorting to a Lennard-Jones potential, non-negative solutions to the dewetting problem have been identified, spanning the full evolution time frame (e.g. before and after the occurrence of holes). Comparison between final simulated an experimental film profiles show quantitative agreement, thereby providing for the first time an accurate predictive model of final dewetting shapes on templated substrates. Further works to speed up the simulation convergence in 3D would allow for fully integrated modelling combining dewetting models with Finite Difference Time Domain simulation tools, thereby significantly expand the opportunities to design nanophotonic systems based on template dewetting (see Chapter 5).

Chapter 4   Modelling dynamics of in-fiber templated instabilities

We now turn to the modeling of in-fiber templated instabilities. The additional presence of a cladding material as compared to in-air templated instabilities provides some advantages, such as delayed reflow. Just as in the in-air template instabilities, understanding the forces at play in such complex system is fundamental to understand the range of attainable architectures, as well as the corresponding initial parameters (film thickness, period, perturbation amplitude). This requires a model spanning several length scales which takes into account surface tension effects as well as Van der Waals forces.

4.1   Longitudinal vs. transversal instabilities in thermal drawing

In this section 4.1, results from the group of Prof. Daosheng Deng in Reference 175 are reproduced. These works lays the ground for our study in the following section, and is hence key to understand the process at hand. We start by considering a viscous optical glass sheet with viscosity μ_1 and thickness H_0, placed within a matrix of another viscous fluid of viscosity μ_2. Let us consider a thin film with a perturbation $\varepsilon \ll 1$ (e.g. linearized approach), without any stretching at this point. Given the high viscosities involved during drawing, one can safely neglect inertial effects. The absence of stretching implies that instabilities along and perpendicular to the fiber axis grow at the same rate Ω:[176]

$$\Omega_{\parallel} = \Omega_{\perp} = \Omega(K, \alpha, \eta) = -\left(\gamma - \frac{A}{k^2 \pi H^4}\right)\frac{K}{2\gamma}\frac{\eta(cosh(K) - 1) + (sinh(K) - K)}{\eta^2[sinh(K) + K] + 2\eta\,cosh(K) + [sinh(K) - K]} \qquad (4.1)$$

Where $H = H(z)$ is the film thickness at position z, $K = k.H$ is the adimensional wavenumber, $\eta = \frac{\mu_1}{\mu_2}$ is the ratio between the film and cladding viscosity, A is the Hamaker number, and γ_{12} is the interfacial tension between materials 1 and 2. From this first isotropic relation, it is clear that positive growth rates are only obtained when the first term $\frac{A}{H^2\gamma} - \pi K^2$ is itself positive. This can only occur for reduced wavenumbers, i.e. large instability wavelengths such that:
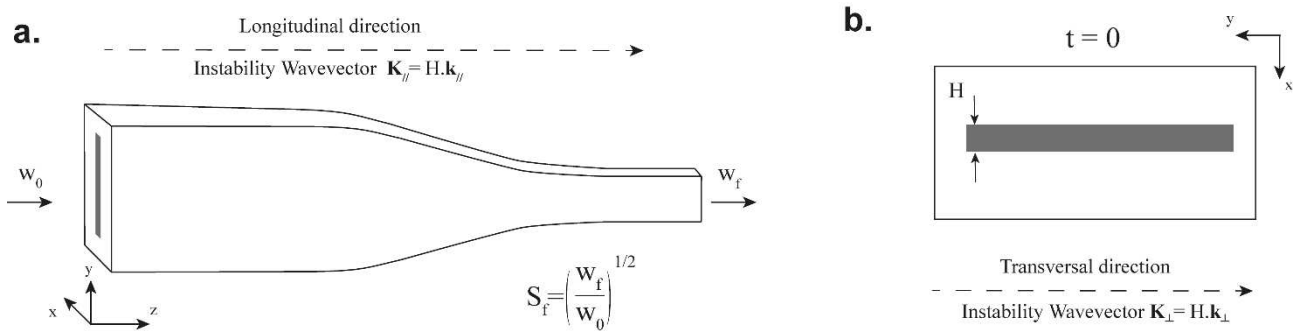
Figure 4.1 – In-fiber filamentation of flat films. (a) Schematic of the fiber undergoing thermal drawing: inlet velocity w_0, outlet velocity w_f, and scaling factor $S_f = (w_f/w_0)^{1/2}$. (b) Cross-sectional view of the initial flat film of thickness H inside the preform prior to drawing.

$$\lambda > 2\sqrt{\frac{A\pi}{\gamma}} \tag{4.2}$$

Let us now turn to the thermal drawing process, where the material assembly is stretched along the fiber axis. The ensemble is stretched by a pulling force, scaling down the geometry by a factor S_f (referred to as the scaling factor, see Figure 4.1 for illustration). The stretching-induced anisotropy entails modified wavenumber (and thus growth rates) for instabilities parallel and perpendicular to the stretching direction.[175] By considering the equivalent one-dimensional fiber limit case,[175,177] one can express the instability wavenumbers perpendicular ($K_{//}$) and parallel ($K_{\perp}$) to the fiber axis:

$$K_{\parallel}(t) = K_{\parallel}(t = 0) . S_f^{-3} \tag{4.3}$$

$$K_{\perp}(t) = K_{\perp}(t = 0)(\text{independent of } S_f) \tag{4.4}$$

Where S_f is the scaling factor, z_0 is the initial position. These two equations denote a distinct evolution along and perpendicular to stretching when scaling down. Along the longitudinal direction, as S reduces with z, the adimnesional wavenumber of a given perturbation with fixed wavelength is continuously reduced during the thermal drawing process (c.f. equation (4.3)), which disfavors the growth of Rayleigh-Plateau instabilities. This stability in the longitudinal direction can be understood as a form of "instability stretching", limiting at any single point in time the amplitude of the fastest growing instability. As a consequence, the amplitude growth rate is largely damped along the fiber axis direction.

To the contrary, the adimensional instability wavenumber with maximal growth rate is unchanged along the transversal direction (c.f. equation (4.4)). Transversal dynamic evolution of the textured film is the result of interplay between two competing phenomena. On one hand, interfacial surface energy γ is minimized by texture flattening, driven by Laplace pressure $P_L = \gamma.\kappa$. Flattening reduces thickness fluctuations, and thus stabilizes the film. As the fiber cross section is scaled down during drawing, the interface curvature κ (and hence Laplace pressure) correspondingly increases, providing supplemental drive for flattening. On the other hand, Van der Waals interactions in such a system are intrinsically destabilizing. The disjoining pressure associated with Van der Waals forces are at first largely negligible at the first stages of the process, but increase considerably with drawing at thicknesses below 100 nm. In the transversal direction, the fastest growing instability is hence enhanced by thermal drawing.

By assuming that all possible wavenumbers exist initially in roughly equal (but infinitesimal) amplitudes in a flat initial film, the size of the final filaments can be predicted by determining the fastest growing component (Rayleigh-type instability). This wavenumber will dominate and eventually pinch the film into filaments. However, given the randomness of the initial amplitude distribution, thermal drawing of flat films typically provides filaments with a broad distribution in both size and spacing.[175] This is particularly detrimental to many practical applications in photonics or optoelectronics which commonly require a high degree of order. The possibility to reduce in a tunable manner inter-filament spacings is also desirable in photonics, allowing for controlled collective interaction and interference effects.

4.2   Evolution of a templated transversal instability

In this thesis, we demonstrate how initial perturbations can be imposed to dictate the final microstructure periodicity. Under particular conditions that we identify, we show that this initial perturbation, although not favored by Rayleigh instability, can still dominate film rupture, achieving highly-ordered filament arrays.

4.2.1 Sinuous vs. varicose modes

Perturbation modes of freestanding films are classically decomposed into two independent contributions: (i) varicose modes, corresponding to symmetric perturbation along both interfaces, and (ii) sinuous modes, corresponding to the opposite case of anti-symmetric perturbations (see Figure 4.2). In the case of the proposed process, the underlying texture imparts the large sinuous perturbation amplitude. The angle deposition (or alternatively thermal reflow for thicker films) induces periodic film thickness fluctuations, which correspond to the additional varicose perturbation. Based on linear stability analysis, varicose modes may lead to instability growth if disjoining pressure is sufficient, while sinuous modes always decay. We observe in both fluid dynamics simulations and experiments the quick decay of the sinusoidal mode. The varicose mode usually remains pronounced over considerably longer times, even in the situation where it is also a decaying mode. Substrate nanoimprinting and angle deposition results in a combination of both sinuous and varicose modes, as illustrated in the bottom row of Figure 4.2. The underlying texture imparts the large sinuous perturbation amplitude, while the angle deposition (or alternatively thermal reflow for thicker films) induces periodic film thickness fluctuations, which correspond to the additional varicose perturbation. Only the varicose mode is however of interest for the study at hand, as it is the only potentially unstable perturbation.

We now consider an initial thickness perturbation to the film with significant varicose and sinuouse amplitude components (referred to as "template instability" or "templated perturbation"), and investigate how these two modes evolve during thermal drawing. Laplace pressure will largely dominate the dynamics, and the sinuous component of the templated instability will at first decay. Given the reduced roles of Van der Waals interactions for initial thicknesses considered, the varicose mode will also decay during the first part of this process, at a speed that must be properly engineered. When down-scaling film thickness, Van der Waals interactions play an increasing role, which first slow down the template varicose mode decay. The disjoining pressure ultimately drives local thinning and break-up at the prescribed locations when reaching smaller thickness. When Van der Waals interactions start inducing local thinning, two scenarii appear: (i)
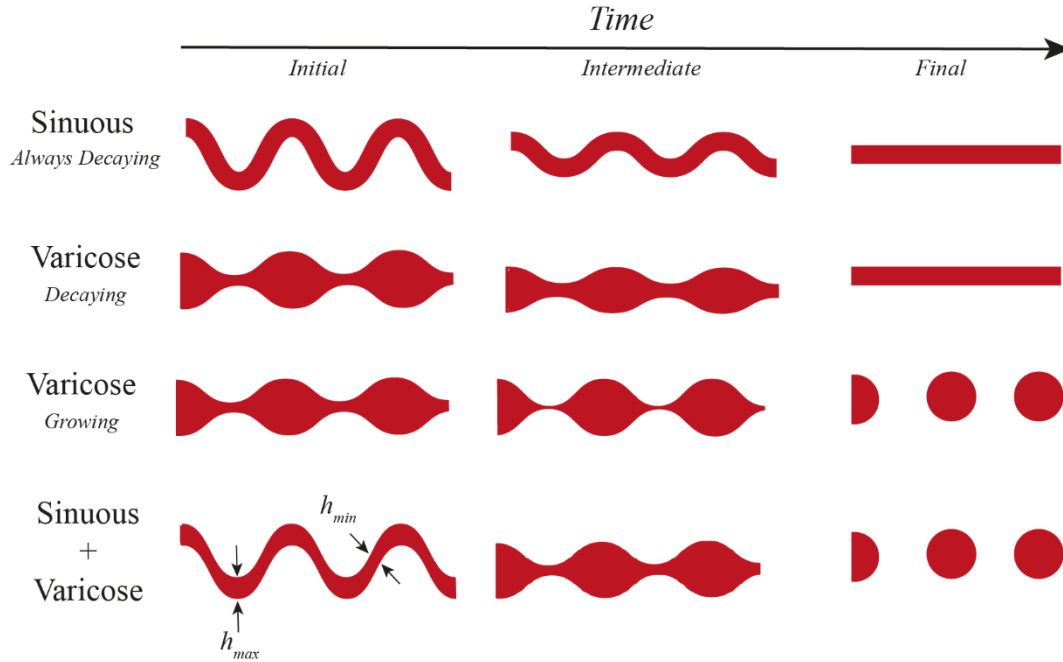
Figure 4.2 – Comparison of sinous and varicose modes. (From top to bottom) Evolution of a purely sinuous perturbation mode, which systematically decays with time; Evolution of a stable varicose mode, which decays with time due to predominant Laplace pressure and negligible Van der Waals interactions; Evolution of a growing varicose mode, whose amplitude increases with time due to predominant Van der Waals interactions over Laplace pressure; Combination of a sinuous mode with an unstable varicose mode.

the decaying initial template perturbation has become smaller than the Rayleigh instability perturbation, in which case the final structure will feature a broad distribution of break-up wavelengths; (ii) the Rayleigh perturbation with largest amplitude remains much smaller than the templated perturbation amplitude, ensuring a final ordered configuration upon dewetting.

4.2.2 Determination of physical parameters during the draw

To model effectively and accurately the template filamentation process during the draw, the proposed numerical scheme requires the knowledge of number of physical parameters, among which: the temperature distribution in the fiber, (ii) the viscosity distribution in the fiber, and (iii) the velocity profile. These three profiles vary dynamically with position z along the drawing axis. Knowing the velocity profile, one can then determine (i) the time discretization profile (vector of elementary time intervals $[dt_1; \dots; dt_n]$ over which the fiber evolves at constant cross section) and (ii) the scaling factor $S(z)$ at position z, where $S(z) = \sqrt{v(z)/v_0}$. It is important to note that the system dynamics are particularly sensitive to the fiber temperature. A change in a few degrees alters the viscosity by a sensible amount around the glass transition temperature, and can induce potentially significant changes in the numerical results. An accurate prediction of the temperature profile is hence essential to properly reproduce the experimental conditions in the numerical scheme.

We present here a derivation of the temperature, viscosity and velocity profile inside the fiber during thermal drawing using an iterative reconstruction procedure based on experimental temperature measurements.[181,260] For this first task, we keep an Eulerian description of the desired profiles. Their derivation is presented in more details in Appendix A. We introduce a purely extensional velocity profile of the following form:

$$\boldsymbol{V}(r,z) = u(r)\boldsymbol{e_r} + v(z)\boldsymbol{e_z} \tag{4.5}$$

The Navier-Stokes equations and continuity equations can be developed assuming a steady state-velocity profile (see Appendix A). Enforcing volume conservation of an elementary slice of fiber during the draw further, one can show that:

$$v(z) = \exp\left(\frac{\int_0^z \frac{dz}{\eta(z)}}{\int_0^1 \frac{dz}{\eta(z)}} \ln D^2\right) \tag{4.6}$$

Assuming the viscosity profile along z is known, the velocity profile can thus be extracted in the case of an extensional flow.

We now turn to the evaluation of the temperature profile, assuming a dependence along both r and z coordinates: $T = T(r,z)$. To determine the temperature profile, we evaluate the energy conservation equation in cylindrical coordinates, limiting ourselves to first order terms. We assume a parabolic temperature profile along r. One can now determine the temperature profile by solving a single partial differential equation in z (see Appendix A):

$$v(z)\langle T\rangle'(z) = -\frac{2h}{\rho c_p} \frac{\langle T\rangle(z) - T_{air}(z)}{R(z)(1 + \frac{h}{k}.R(z)/4)} \tag{4.7}$$

Where ρ is the fiber material density, c_p is its heat capacity, h is the heat transfer coefficient between fiber cladding and air, k is the thermal conductivity of the fiber material, and ⟨ ⟩ denotes the radial average of a physical quantity. Assuming

a.

b.

c.
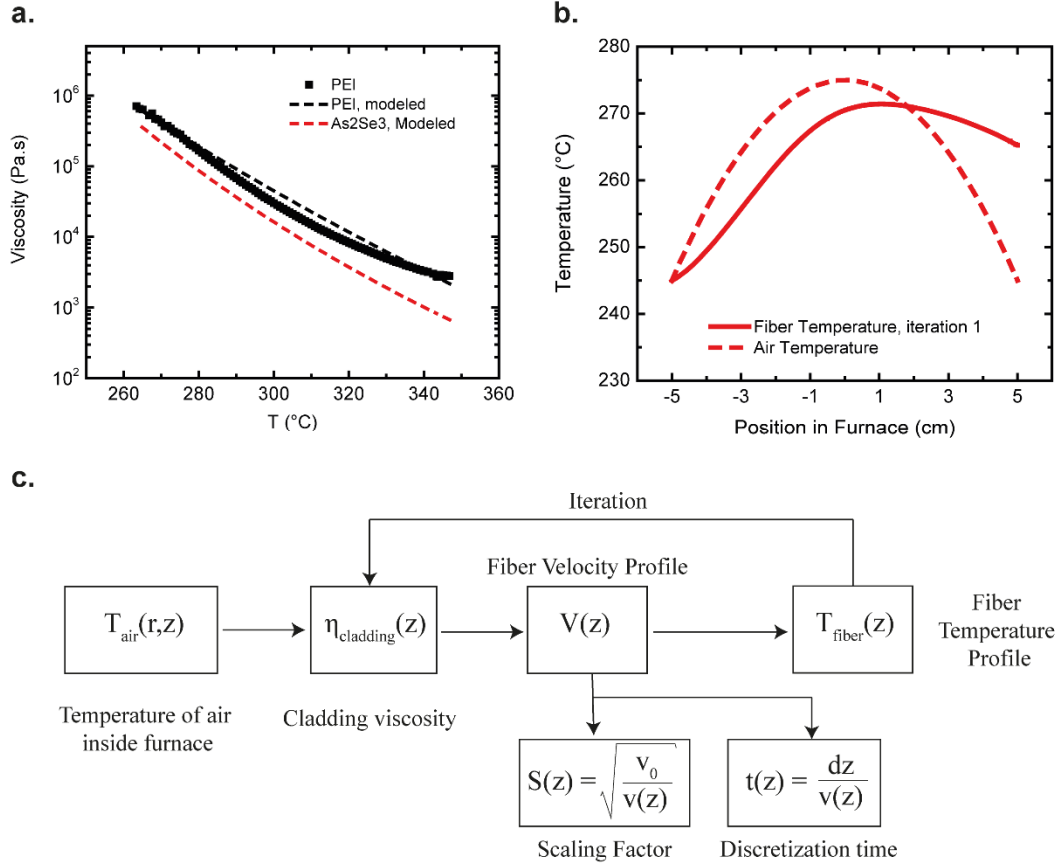
Figure 4.3 – Eulerian specification of relevant physical parameters. (a) Experimental (dots) and modelled (dash line) viscosity profiles for Polyeth-erimide (cladding) and As$_2$Se$_3$ (film).The experimental data for As$_2$Se$_3$ can be found in reference 1. (b) Air temperature profile in the furnace based on experimental measurement (dash) and modelled fiber temperature profile based on the calculatin scheme detailed in (c). (c) Methodology to determine the physically relevant parameters (viscosity, temperature, velocity).

that the velocity profile is known along z-coordinate, one can thereby determine the fiber radius $R(z)$ at position z, while the profile T_{air} is determined based on experimental measurements. To estimate the temperature profile within the fiber during the draw, we proceed according to the following procedure[181]: (i) we calculate the viscosity profile by using the temperature profile of the air surrounding the preform, and experimental viscosity data. (ii) we deduce the velocity profile using (4.6); (iii) we estimate the temperature profile according to equation (4.7); (iv) we repeat steps (i) to (iii) using the newly calculated temperature profile. With a single iteration, we obtain an assymetric temperature/viscosity profile with respect to z-coordinate, whose accuracy is significantly enhanced as compared to a sole estimation of viscosity based on the air temperature profile.[181] To conclude, we retain the viscosity, velocity and temperature profiles associated to the first iteration for the filamentation model introduced in Section 4.2.4.

4.2.3   Van der Waals potential: from linear to non-linear

Most dewetting studies rely on the hypothesis of small perturbations to linearize the Navier-Stokes equations. Destabilizing Van der Waals forces are also typically taken into account through a simplified disjoining pressure applied at the interface (usually that of a flat film of thickness h: $P_{disjoining} = A/6\pi H^3$). This is however not valid when interfaces are highly deformed. Given that the present study focuses on simulating interface perturbations with both arbitrarily large amplitudes and wavelengths, it is essential to take into account a more accurate contribution of Van der Waals interactions. Given that Van der Waals interactions scale with the inverse sixth power of inter-atomic distance, it is a particularly

challenging task to define a non-diverging potential. Based on the works of C. Maldarelli et. al.,[178,179,180] a full non-retarded Van der Waals body force can be expressed for both the cladding and the film. This body forces accounts for the excessive Van der Waals interactions caused by bringing together two interfaces from an infinite separation distance to a finite separation distance h. The works of C. Maldarelli and co-workers provide a general potential expression, which we apply to derive the body force in the case of our system with a top interface perturbation $\zeta(x,t)$ and a bottom interface perturbation $\eta(x,t)$ (see Appendix B for detailed calculations). This potential being constant in the film region, the resulting contribution is a non-diverging body force $\vec{F}_{V,i} = F_x^i \vec{e}_x + F_z^i \vec{e}_z$ applied solely on the top and bottom cladding layer (with respective index i=I and i=III):

$$F_x^I(x,z,t) = -\frac{3}{8\pi}\left(A_{I,I} + A_{II,II} - 2A_{I,II}\right)\left[\frac{\partial\eta}{\partial x}\int_{\alpha=-\infty}^{\infty}\frac{d\alpha}{\left(\left(z+\frac{h}{2}-\eta(x,t)\right)^2+(x-\alpha)^2\right)^{5/2}} - 5\int_{\alpha=-\infty}^{\infty}\int_{\beta=0}^{\eta(x,t)}\frac{(x-\alpha)d\alpha d\beta}{\left(\left(z+\frac{h}{2}-\beta\right)^2+(x-\alpha)^2\right)^{7/2}}\right] \tag{4.8}$$

$$F_z^I(x,z,t) = -\frac{3}{8\pi}\left(A_{I,I} + A_{II,II} - 2A_{I,II}\right)\left[\int_{\alpha=-\infty}^{\infty}\left(\frac{1}{\left(\left(z+\frac{h}{2}-\eta(x,t)\right)^2+(x-\alpha)^2\right)^{5/2}} - \frac{1}{\left(\left(z+\frac{h}{2}\right)^2+(x-\alpha)^2\right)^{5/2}}\right)d\alpha\right] \tag{4.9}$$

$$F_x^{III}(x,z,t) = \frac{3}{8\pi}\left(A_{I,I} + A_{II,II} - 2A_{I,II}\right)\left[\frac{\partial\zeta}{\partial x}\int_{\alpha=-\infty}^{\infty}\frac{d\alpha d\beta}{\left(\left(-z+\frac{h}{2}-\zeta(\alpha,t)\right)^2+(x-\alpha)^2\right)^{5/2}} - 5\int_{\alpha=-\infty}^{\infty}\int_{\beta=0}^{\zeta(x,t)}\frac{(x-\alpha)d\alpha d\beta}{\left(\left(-z+\frac{h}{2}-\beta\right)^2+(x-\alpha)^2\right)^{7/2}}\right] \tag{4.10}$$

$$F_z^{III}(x,z,t) = -\frac{3}{8\pi}\left(A_{I,I} + A_{II,II} - 2A_{I,II}\right)\int_{\alpha=-\infty}^{\infty}\left[\frac{1}{\left(\left(-z+\frac{h}{2}-\zeta(\alpha,t)\right)^2+(x-\alpha)^2\right)^{5/2}} - \frac{1}{\left(\left(-z+\frac{h}{2}\right)^2+(x-\alpha)^2\right)^{5/2}}\right] \tag{4.11}$$

As presented in Section 1.1.1.2, derivation of the Van der Waals body force for freestanding viscous fluid films relies essentially on the Hamaker procedure combined with the Lifschitz approach. The proposed body force has the advantage of providing the contribution of Van der Waals forces in a general case, applicable for both short wavelength and large perturbation amplitudes. Dispersive forces are commonly reduced as the separation distance between two atoms is increased (electromagnetic retardation), which could simply be implemented using a correction term within the body force integral. The complex dependence of this phenomenon with interparticle distance is here neglected for the sake of simplicity, but could make the object of a further study to refine the present model.

4.2.4   Time-discretized Lagrangian modelling

Previous models[175] of instabilities during thermal drawing have relied on a linearized model involving small perturbations as well as adimensional quantities. As highlighted in ref. 175, studying instability evolution along the transversal direction during the draw involves multi-scale simulations spanning several orders of magnitudes, from mm-scale to nm-scale, which has until now proven elusive. Moreover, linearized modeling fails to take into account non-linear effects, which become critical when considering short wavelength perturbation with large amplitudes. In this section, we propose a model addressing the issues of non-linearity and multiscale modelling.

In the general case of an arbitrary film cross-section, multiphase computational fluid dynamics (CFD) modeling must be used to solve the full (non-linear) Navier-Stokes equations. Using COMSOL Multiphysics interfaced with Matlab, we simulate the multi-scale physics constitutive of the thermal drawing process. We adapt a Lagrangian specification for the flow field, following an elementary fiber unit slice during the draw. The velocity field along the fiber axis is in first approximation assimilated to a plug flow.[181] We discretize in time the simulation, which works in two main steps: (i) Direct solving of Navier-Stokes equations determines the evolution of the two film interfaces at constant cross-sectional dimensions between times t and t+dt; (ii) The cross-sectional profile at t+dt is scaled down to account for the drawing process. The simulation then loops between steps (i) and (ii) until the final cross-sectional dimensions are reached. Re-meshing at every time step ensures solver accuracy spanning over a large set of length scales. To study the evolution of a film undergoing the drawing process, we now introduce the height ratio:
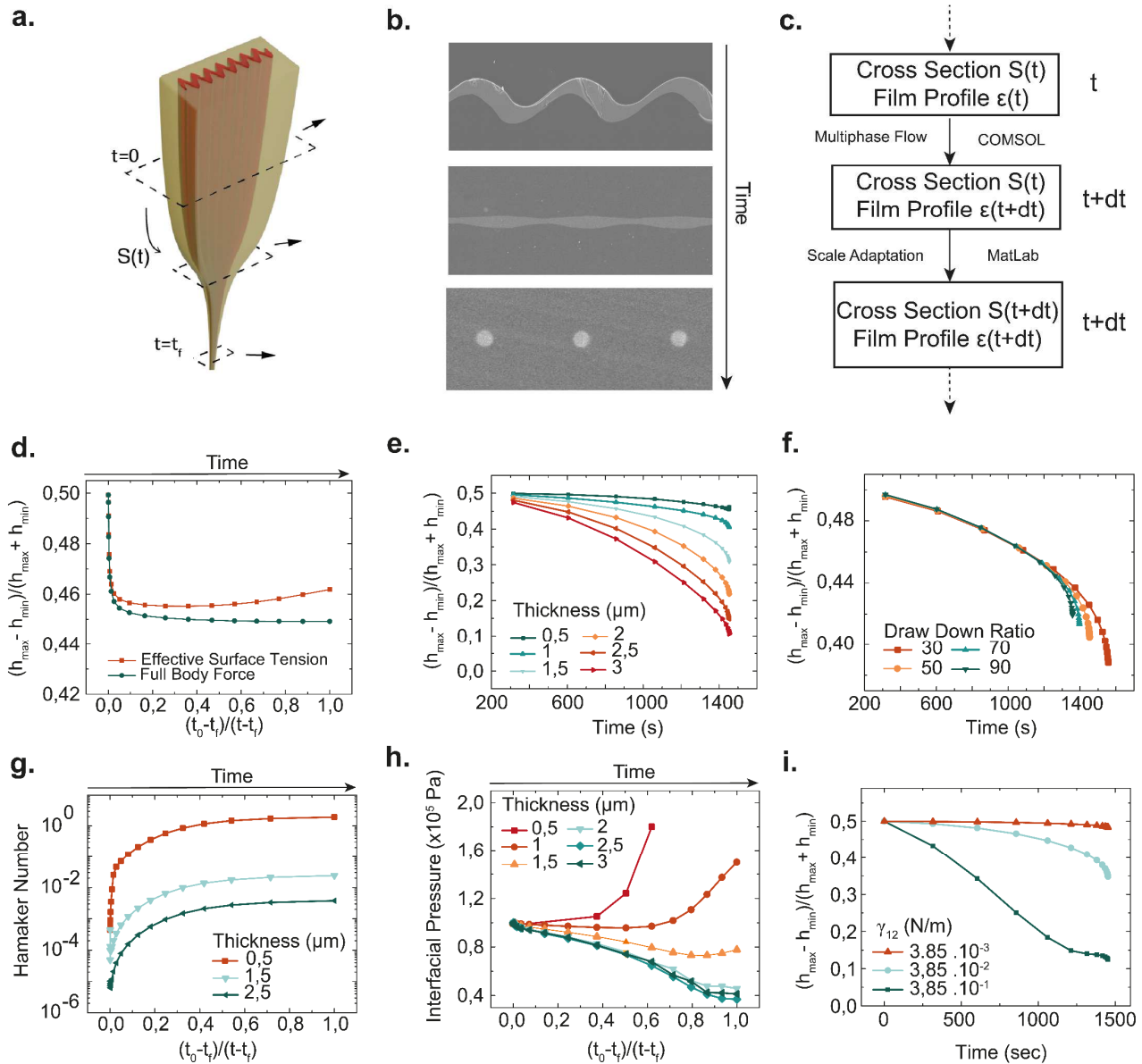
Figure 4.4 – Time-discretized Langrangian modelling of in-Fiber templated instabilities. A reference situation is defined as the case with initial film average thickness of 1.5 μm, draw down ratio of 50 and surface tension of 3.85 .10^{-2} N/m. (a) Schematic of a perform undergoing thermal drawing. (b) Scanning electron microscopy images illustrating three stages of the draw. (from top to bottom) Initial film showing a combination of sinuose and varicose modes, Intermediate film showing solely a varicose mode, Final architecture showing well-ordered filaments. (c) Schematic illustrating the functioning principle of the simulation process. (d) Height ratio evolution for film of initial thickness 0.5 μm and draw-down ratio of 50 using two distinct methods to incorporate the disjoining pressure: (i) through an effective surface tension and (ii) through a body force approach. (e) Height ratio evolution as a function of initial film thickness for a fixed drawn down ratio of 50. (f) Influencing of increasing draw down ratio on the height ratio evoluation as function of time. (g) Evolution of the Hamaker number (defined as the maximal Van der Waals surface pressure over the maximal Laplace pressure) as a function of film thickness. (h) Maximal Interfacial pressure. (i) Evolution of height ratio versus time for an increasing interfacial tension.

$$H = \frac{h_{max} - h_{min}}{h_{max} + h_{min}} \tag{4.12}$$

where h_{max} (resp. h_{min}) is the maximal (resp. minimal) thickness over a unit period. This height ratio essentially characterizes the reflow associated to the varicose mode: 0 indicates complete reflow, while 1 indicates film break-up. In the rest of this theoretical study, we solely consider perturbations with an initial height ratio of 0.5, which fixes the initial film perturbation amplitude, and a fixed period of 20 μm. We also introduce the Hamaker number, defined as the ratio of the maximal disjoining pressure to the maximal Laplace pressure at the interface over a unit period.

To validate the relevance of the body force approach instead of a purely interfacial disjoining pressure approach, we simulate the evolution of an identical film (thickness T=0.5 μm) using a body force approach or an effective surface tension approach. As observed in Figure 4.4(d), the height ratio shows significant differences between the two approaches, which would only be amplified for increased initial height ratios. The body force approach hence provides a significantly more accurate picture of reality than the interfacial disjoining pressure, and is hence selected for the rest of this work.

We now turn to the evolution of the height ratio as a function of thickness T (0.5 μm to 3 μm, see Figure 4.4(e)). The results shown in indicate that, for a fixed draw-down ratio (DDR=50), and fixed interfacial energy (γ_{12}= 38.5 mN/m, detailed derivation below), increasing the thickness leads to substantial increase in reflow during the draw. While smaller thicknesses (0.5 and 1 μm) barely experience any reflow, the perturbation in larger thicknesses almost entirely disappears. This can be related to the fact that Van der Waals interactions have a significant role earlier on in the case of thinner films, which helps to maintain their initial patterns during the thermal drawing process. A similar study of height ratio dynamics for an identical film thickness and varying draw-down ratio DDR=$T_{final}/T_{initial}$ reveals a limited influence of the draw down ratio on reflow (see Figure 4.4(f)). Indeed, similar reflow dynamics reflect the similarity of the initial systems, whose final reflow factor essentially depends on the final length scale involved.

We now turn to the evolution of the interfacial pressure during drawing in Figure 4.4(h). More precisely, we report the maximum of interfacial pressure along a unit period for films of increasing thicknesses (0.5 to 3 μm), considering an external atmosphere of pressure $P_{ext}=10^5$ Pa. The surface pressure decreases for higher thicknesses which is correlated to a texture reflow (e.g. both sinose and varicose modes decay). For lower thicknesses, the interfacial pressure increases beyond a certain time, which indicates the predominance of Van der Waals forces and explain either the reduced decrease or the increase in height ratio in the final stage of the draw (see Figure 4.4(e)). This predominance of Van der Waals Forces can also be captured using the adimensional Hamaker number, which evaluates the disjoining to Laplace pressure ratio (distinct from the Hamaker constant). For the sake of simplicity, the disjoining pressure is implemented using an effective interfacial tension coefficient. As apparent in Figure 4.4(g), the Hamaker number nears 1 at the end of the draw for films with 0.5 μm initial thickness, confirming the importance of Van der Waals forces in the texture conservation process. To the opposite, larger films exhibit Hamaker numbers negligible compared to 1, and hence point to the predominance of Laplace pressure in the reflow process.

Interfacial energy between the polymer matrix and the substrate is a fundamental parameter which largely determines the texture reflow dynamics. In Figure 4.4(i), the height ratio is plotted for interfacial energies increasing from γ_{12}= 3.85 mN/m to γ_{12}= 385 mN/m with a fixed draw down ratio of 50 and thickness of 1.5 μm. The reflow is significantly increased for higher surface energies, which leads to completely flat films for interfacial energies of the order of 0.385 N/m, The overall system sensitivity to this parameter is a crucial element of this study, and hence calls for particularly accurate values of interfacial energies. In the present case, the interfacial tension coefficient γ_{12} can be estimated based on geometric means[182]:

$$\gamma_{12} = \gamma_1 + \gamma_2 - 4\frac{\gamma_1^d \gamma_2^d}{\gamma_1^d + \gamma_2^d} - 4\frac{\gamma_1^p \gamma_2^p}{\gamma_1^p + \gamma_2^p} \tag{4.13}$$

with γ_i^d the dispersive component and γ_i^p the polar component of the surface tension associated to component i. In this equation, the interfacial tension of polymer with similar value of γ_i^d and γ_i^p would be much smaller than the surface tension of each component. In our case, considering the similarity of As and Se atomic electronegativity, we consider that there is no polar component in As_2Se_3. We thus consider $\gamma_1^p \sim 0$ and $\gamma_1^d \sim \gamma_1$. The interfacial tension γ_{12} thus amounts to γ_{12}=38.5 mN/m. This value is significantly lower than the free surface tension of the chalcogenide glass γ_{11}=100 mN/m, which would be the relevant surface tension parameter in the case of open-air reflow (e.g. exposed film). As a consequence, the use of a polymer cladding plays a key role to limit reflow and reduce the varicose mode decay. This is in line with previous observations in purely polymeric systems.[183]

Curiously, while the height ratio should reach 1 for systems that break up into filaments, this is never the case for the considered parameter set. We observe for most systems a limit in the reflow factor, and for a particular sub-set of favorable initial parameters, a slight increase in height ratio at the end of the draw, but which never fully reaches one. Several arguments could be put forward to explain this observation. First and foremost, as discussed above, the system dynamics is highly sensitive to the interfacial energy. The interfacial energy used in this section was derived from a simple geometric mean approach. One possibility could be that the actual interaction coefficient is actually lower that the one calculated, which would highly disfavor reflow and favor break-up. Further refinements to estimate the interfacial tension should hence be further made to shed some light on this point. Secondly, we have made a considerable approximation by considering a plug flow for the modelling. While this is supported by the system's translational invariance along the fiber axis, it does not reflect the actual velocity profiles inside fiber preform during the draw, which was demonstrated to be parabolic in nature.[181] This implies that additional shearing effect occur perpendicular to the cross-sectional profile studied here, which could have an influence onto the occurrence of break-up. This point also calls for futher investigations. Finally, the system's temperature profile could be more accurately determined, possibly increasing the system's viscosity at the final stages of the draw, when the interfacial pressure is significantly in favor of break-up (see Figure 4.4(h)).

To conclude this section, the interplay between destabilizing Van Der Waals interactions and Laplace pressure is instrumental to maintain a pre-imposed perturbation during thermal drawing. Our Lagrangian framework monitoring the evolution of in-plane instabilities during the draw unravels the rationale behind the process presented in this work.

Chapter 5   Photonic applications

5.1   High Q.F. metasurfaces for efficient refractive index sensing

5.1.1   Selenium-based sensing

The application of 2D planar metasurfaces for bio-molecule detection has been an active area of research in recent years.[184,185,186] In particular, noble metal based nano-structured devices have found wide usage as sensitive biosensors[187,188,189] due to their ability to create strong field enhancement using relatively simple designs. Such sensors, based on Localized Surface Plasmon Resonance (LSPR), have become novel industrial benchmarks for bio-analyte or chemical sensing. In spite of their capabilities to detect analytes down to single molecule level, they are however limited by the intrinsic losses associated to metals. Indeed, light absorption induces spectral broadening and local heating which results in potential degradation of the bio-analytes and thus a deterioration of the optical response. High refractive index dielectric metasurfaces,[185] have recently emerged as an alternative platform with reduced intrinsic losses,[190] which could potentially compete with the sensitivity of plasmonic devices.

In Chapter 2 (in particular Figure 2.3(h)-(i)), we have demonstrated that the interparticle distance could be tailored in a controllable manner down to 10 nm. Such dense high index geometries have particularly interesting consequences in terms of optical properties. In the case of a 350 nm periodic square lattice using selenium, we observe the emergence of Fano resonances at low interparticle gaps, exhibiting a characteristic asymmetric line shape in the transmission spectrum (see Figure 5.1(a)). This type of sharp resonance can be used in several ways from a photonics perspective. In this section, we first investigate the origin of this sharp Fano resonance in 350 nm square array Se nanoparticle arrays, and further demonstrate the applicability of tailored Fano resonances to sensing of biomolecules.

The change in particle interaction with different gap distance is first studied for a square array of Se nanoparticles with 350 nm periodicity using Lumerical FDTD simulation software. The influence of gap distance on the transmission spectrum and the electric field profile shown in Figure 5.2. The intensities of the electric field are all normalized. In the simulation, the particles size was decreased from 340 nm to 200 nm, corresponding to an increase in gap distance from 10 nm to 150 nm. A strong gap mode appears when the gap distance is 10 nm (Figure 5.2 (a) and (d)). This corresponds to a strong coupling regime between the driving (magnetic resonance) and driven (gap) mode, where the shape of the resonance is Lorentzian (10 nm in Figure 5.2 (a)). Furthermore, as the gap distance increases, the gap field becomes weaker and the sharp asymmetric resonance appears while shifting towards blue (Figure 5.2 (a) and (b)). This identifies the weak coupling regime when the Fano parameter |q| tends to 1. When the gap distance reaches 90 nm, the lattice collective resonance becomes prominent judged by the continuous electric field between the particle arrays (Figure 5.2(e)), and the Fano resonance shifts at a lower rate. Finally, when the gap increases continuously, the Fano resonance disappears owing to the absence of coupling between dipoles and in-plane scattered light (Figure 5.2 (c) and (f)). To sum up, by controlling the particle size and hence the inter-particle gap, we can tune the coupling regime, from an absence of coupling through weak coupling to strong coupling regime. The Fano-type resonance we use for bio-sensing corresponds to the weak coupling regime (Figure 5.2). To elucidate the mode components of the Fano resonance, we extracted the
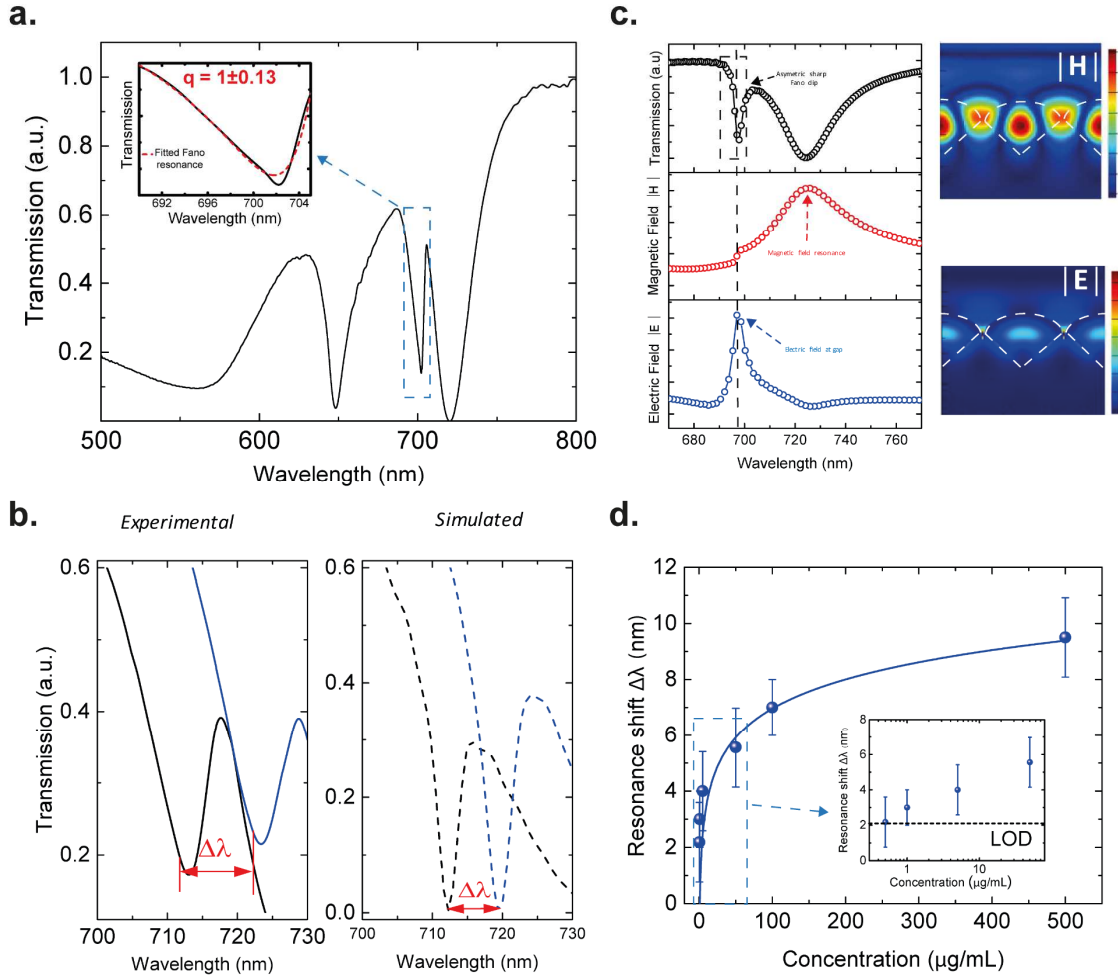
Figure 5.1 – Biosensing using 350 square Se metasurface with high Q.F. resonance. (a) Optical transmission spectra for a successively dewetted film (interparticle gap, ~30 nm) showing an asymmetric sharp Fano resonance. Inset, Enlarged view of the asymmetric resonance fitted with the Fano formula. The fit yields a q value of ~1, indicating a Fano resonance. (b) (Left) Simulated transmission (black), magnetic field (red) and electric field (blue) profiles of a Se nanoarray of periodicity 350 nm with a 30 nm interparticle gap. The simulated transmission spectra also show a Fano profile due to the interference of sharp discrete electric (gap) field resonance and broad (continuous) magnetic resonance. (Right) Cross-sectional magnetic (top) and electric (bottom) field profiles at their respective resonances. Field distributions are normalized to their own maxima. (c) A/G protein monolayer sensing: experimental (left) and simulated (right) transmission spectra before (black) and after (blue) addition of a 10 nm protein monolayer. For simulation, a 10 nm layer of protein (n= 1.5) was considered to be homogeneously distributed over the chalcogenide metasurface. (d) Sensitivity curve representing the spectral shift in the resonance as a function of protein concentration. LOD, limit of detection. (Inset) Dynamic range corresponding to the linear region of the concentration curve.

electric and magnetic field maps at the resonance wavelength using FDTD numerical simulation. Figure 5.1(c) shows that, with a 30 nm interparticle gap, the Fano resonance appears due to the interference between the broad magnetic resonance and the sharp inter-particle gap electric resonance. The transmission spectrum obtained by simulation is in agreement with the experimental spectrum shown in Figure 5.1(a).

The sharp Fano resonances we could achieve in the visible are a result of the particular architecture of our self-assembled arrays, but also of the lower optical losses of some chalcogenide glasses, including selenium, in this spectral regime compared to conventionally used materials such as silicon. Sharp photonic resonances are particularly relevant for refractive index sensing applications, whereby deposition of a material of different refractive index on the dielectric metasurface induces a global shift in the transmission spectrum. While this structure exhibits a good bulk sensitivity, with a Figure of Merit comparable with existing designs (Bulk refractive index sensitivity of ~150nm/RIU, see Figure 5.3), it is particularly relevant to the sensing of monolayers rather than bulk index changes. Indeed, our simulation results in Figure 5.1(b) show a strong enhancement of the electric field intensity (over 100 times) within the confined interparticle region, which should result in a high sensitivity to local index changes. To demonstrate this capability, we simulated and

5.1. High Q.F. metasurfaces for efficient refractive index sensing
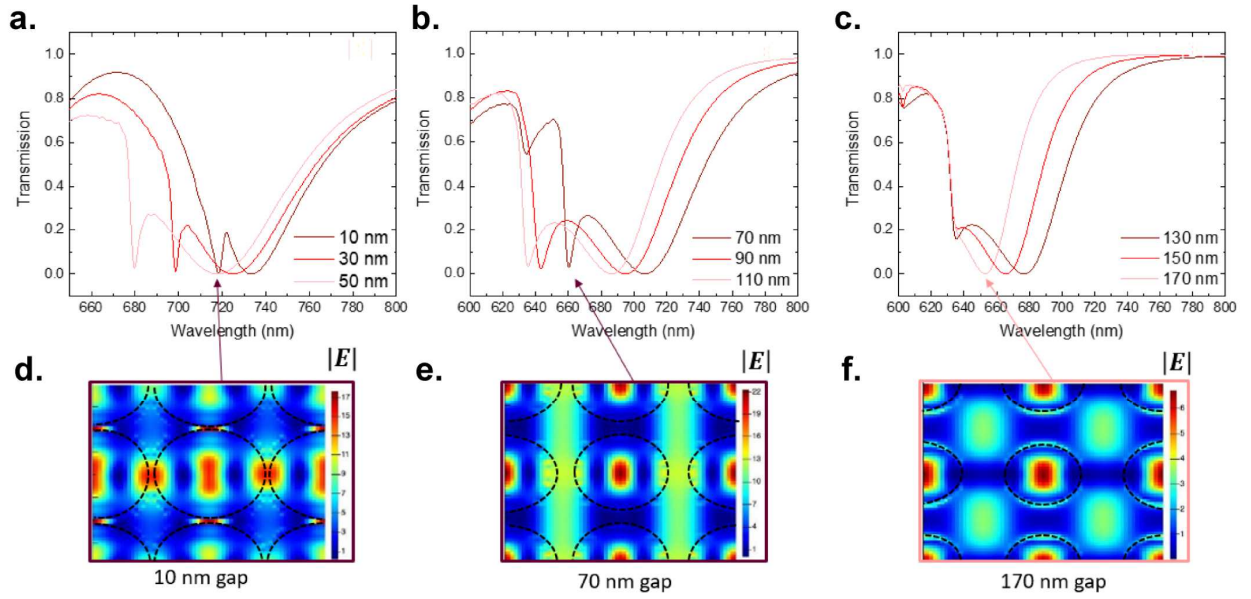
Figure 5.2 – Evolution of coupling with interparticle gap for a 350 nm square periodic selenium metasurface. The simulated results show that the gap resonance predominates when the gap is small. Figures (a), (b) and (c) represent transmission spectra for varying interparticle gaps from 10 nm to 170 nm. Figures (d), (e) and (f) illustrate the corresponding electric field distribution for gap distances of 30 nm, 70 nm and 170 nm respectively at the sharp resonance. With a 10 nm gap, there is a strong coupling regime where the driving mode (here the magnetic resonance) couples with the gap mode to give rise to the Lorentzian shape of the curve (Figure (a)). As the gap increases from 10 nm to 90 nm, the sharp asymmetric resonance appears (weak coupling regime) and further shifts towards the blue. The shift becomes less pronounced with a continuous increase in gap distance from 90 nm to 110 nm (Figure (b)), indicating a predominance of the lattice mode as illustrated in the field distribution plot (Figure (e)). Above a gap distance of 130 nm, the resonance disappears (Figure (c)), indicating the decoupling of dipole and the lattice resonance (Figure (f)).

experimentally measured the spectral variations in the presence of protein A/G (recombinant fusion protein with protein A- and protein G-binding sites) monolayers. In the experimental study, we incubated the Se nanoparticle arrays with various concentrations of protein A/G solutions, and measured the spectral shifts induced by the physio-adsorbed protein monolayers (Figure 5.1 (c) and (d)). A spectral shift of 10 nm was observed for a concentration of 500 µg/mL (Figure 5.1 (c)). The experimental data collected for different concentrations results in a calibration curve that saturates for higher concentration ranges (> 500 µg/mL), a typical phenomenon for surface sensors. We also calculated the Limit of Detection
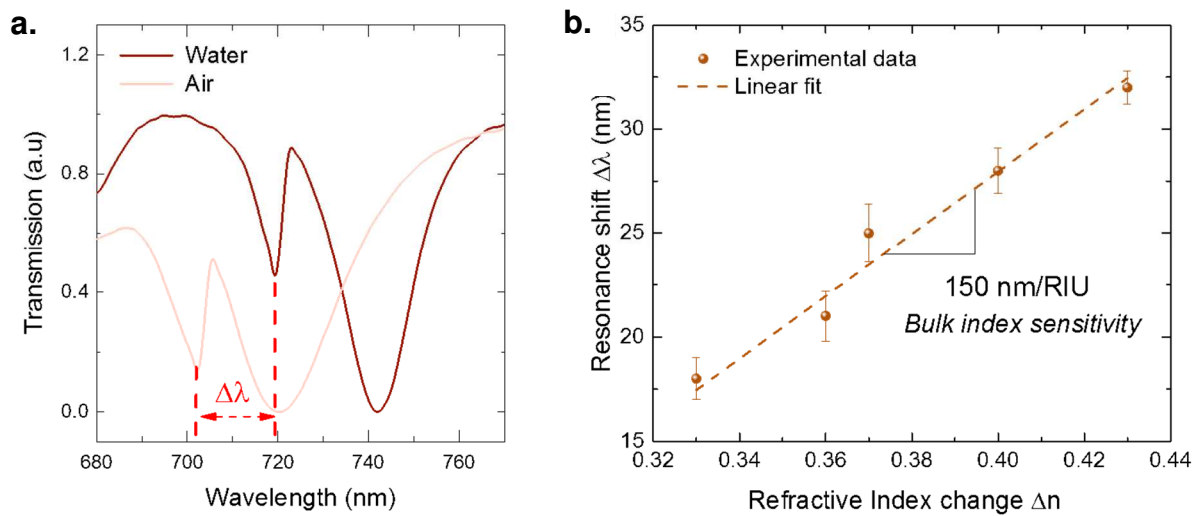
Figure 5.3 – Bulk index sensing with a 350 nm square periodic selenium metasurface for a 30 nm interparticle gap. (a) Transmission spectrum of the sample with (brown) and without (light red) water as a superstrate. The results show a 20 nm shift in the Fano resonance in presence of water. (b) Bulk index sensitivity curve, representing the Fano shift on varying the superstrate index from 1.33 to 1.43. The linear fit yields a bulk index sensitivity of 150 nm/RIU.

(LOD) of our experimental method. The intersection of the fitted saturation curve to the LOD yields the minimum detectable protein concentration, which can be evaluated as 0.5 μg/mL. This value is comparable with state-of-the-art plasmonic-based devices[191] (see Figure 5.1 (d)).

5.1.2   Arsenic Triselenide-based sensing

While the previous sensor showed outstanding sensing capabilities for ultra thin films, its sensitivity remains limited for thicker films to the value of 150 nm/RIU. In this section, we will investigate how alternative structures relying on sol-gel textured susbtrates with tunable refractive index enable to largely increase the BRIS Figure of Merit by a factor of 7 to values up to 1000 nm/RIU. The limited Figure of Merit observed in the previous section is linked to a difficulty commonly observed in dielectric architectures, that tend to confine the electric-field for the larger part inside the particles and hence not accessible to the surrounding molecules, unlike plasmonic arrays where the field is localized on the surface of the metal nanostructure. This has thus far limited the interaction between electromagnetic modes and bio-analytes, leading to lower sensitivity compared to Localized Surface Plasmon Resonance-based devices.

A simple way to design delocalized modes in such dielectric arrays is to utilize in plane non-radiative diffractive modes (e.g. lattice resonance) that critically couple with the radiative dipole modes of the individual particles. This type of collective mode, also referred to as Surface Lattice Resonances (SLR), remains delocalized over the whole surface of the sensor, hence becoming accessible and sensitive to the surrounding index variation. Therefore, to engineer an efficient metasurface sensing device, two figures of merit must be optimized: (1) maximal field enhancement and (2) spatial extension of the modes away from the particle volume to increase sensitivity to surrounding index change. We now investigate the targeted size of As_2Se_3 nano-objects, to yield resonant modes within the lossless region of the material , based on As_2Se_3 single spheroid particle scattering spectrum using Mie theory.[192] As the particle diameter is increased, these
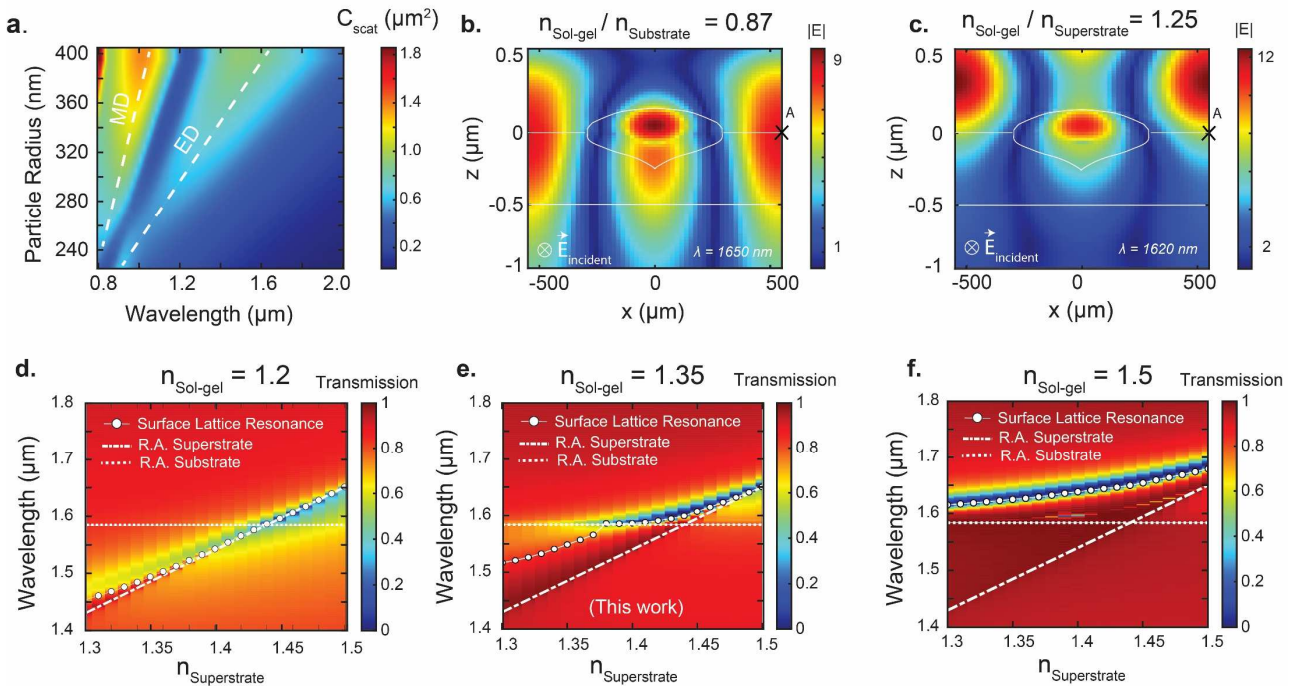
Figure 5.4 – Mode analysis and spatial extension with sol-gel layer index. (a) Numerical simulation illustrating 2D map of the scattering spectrum of single isolated As_2Se_3 ellipsoid particles in air as a function of radius. (b) –(c) Electric field map in the ellipsoid cross section for different radii/substrate index combinations: . (d)-(f) Transmission map as function of wavelength and superstrate index for three distinct values of substrate index value: (d) $n_{substrate}$=1.2, (e) $n_{substrate}$=1.5 and (f) $n_{substrate}$=1.35.

two dominant contributions red-shift. In order to exploit resonant modes in the lossless region of the spectrum above 1000 nm, we focus on a principal particle radius above 300 nm. For such radii sizes, the dominant mode in the Near-Infrared (NIR) range is the electric dipole, as apparent in Figure 5.4 (a).

To exploit lattice resonance, we then consider a square periodical arrangement of such As_2Se_3 particles onto a templated sol-gel-substrate, with fixed periodicity p = 1.1 µm. This choice of periodicity gives rise to a Rayleigh anomaly in the near infrared. This surface lattice resonance (SLR) can interfere with individual particle modes to provide sharp features in the transmission spectrum. The Rayleigh anomaly wavelength λ_{SLR} can be calculated using λ_{SLR} = a.n (normal incidence, 1st order diffraction), where a is the array period and n is the surrounding refractive index. This index will change in presence of analyte (without analyte n = n_{air} = 1). Considering a fixed particle size (r = 300 nm) and period (p = 1.1 µm) of the array, we performed numerical simulations to investigate the influence of the sol-gel substrate layer onto the transmission spectrum. Non-dispersive sol-gel layers with three different constant refractive indices (n = 1.2, 1.35 and 1.5) were chosen, and successively applied in the simulated structure. The transmission maps of these structures are represented on Figure 5.4(d)-(f). The superstrate refractive index was varied from 1.3 to 1.5, which is a common range for bio-analytes. Interestingly, when the sol-gel substrate has a low refractive index compared to the superstrate (Figure 5.4(d), with $n_{sol-gel}$ = 1.2), the resonant wavelength linearly increased with the change of the superstrate refractive index. On the contrary, when the sol-gel substrate has a high refractive index compared to the range of the superstrate (Figure 5.4(f), with $n_{sol-gel}$ = 1.5), the resonant wavelength is considerably less sensitive to the simulated bio-analyte medium..

Sensitivity of such sharp features to a surrounding index change hence appear to be intricately linked to the surrounding layer indices. To understand the physical roots of this trend, we further investigate the evolution of Rayleigh anomaly with wavelength. The Rayleigh anomaly typically extends in the medium surrounding the particle arrays, encompassing the superstrate, the sol-gel layer and the underlying substrate. Depending on the spatial extension of the electromagnetic field at lattice resonance, the index n associated to the Rayleigh anomaly λ_{SLR} (where λ_{SLR} = a.n) will be corresponding to a complex combination of the surrounding materials. We proceed to evaluate the spectral position of the electric field maximum $\lambda_A$maximum in between particles using a time monitor (denoted A in Figure 5.4(b)-(c)) for various sol-gel indices ($n_{sol-gel}$ = 1.2, 1.35, 1.5). Given that the lattice resonance occurs essentially in between particles, we assimilate this spectral position to that of the "global" Rayleigh anomaly λ_{SLR} (referred to as Surface Lattice Resonance, or SLR, for the rest of this work), i.e. $\lambda_A \sim \lambda_{SLR}$. This assumption is valid as long as the surface lattice mode is partially present at the interface, i.e. not totally leaking in either the superstrate or the substrate. To optimize the biosensor's performance, maximal shift of lattice resonance with increased superstrate index is desired. This optimal situation corresponds to the case where the SLR curve most closely matches with the Superstrate Rayleigh anomaly curve, defined as $\lambda_{superstrate}$=a.$n_{superstrate}$. From the peak Rayleigh anomaly evolution reported in Figure 5.4(d)-(f), it appears this criteria is maximized for a decreased sol-gel film index of 1.2. Conversely, an increased sol-gel film index of 1.5 leads to a minimal sensitivity.

To corroborate the role of sol-gel index on overall sensitivity, we investigate electric field plots for large and small sol-gel indices. Figure 5.4(b) (resp. Figure 5.4 (c)) shows the electric field profile induced by the As_2Se_3 particles with sol-gel substrate of low ($n_{sol-gel}$ = 1.2) and high values ($n_{sol-gel}$ = 1.5). The difference between those two situations can be investigated by defining a ratio N = $n_{superstrate}$/$n_{sol-gel}$ which here is evaluated as N > 1 and N < 1 respectively. In the first case where N> 1, the electric field is situated for the larger part inside the superstrate, while the opposite situation (N < 1) leads to a spatial extension of the electric field essentially inside the substrate. Increased modal extension into the superstrate implies a stronger sensitivity to change in superstrate index, a desirable feature for our sensing device. Beyond
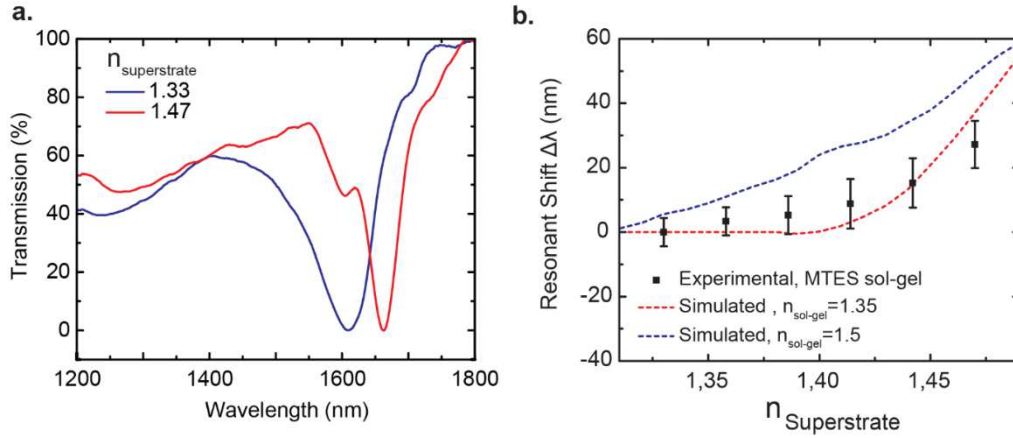
Figure 5.5 – Experimental validation of sensing capabilities for As_2Se_3-based sensors. (a) Experimentally observed transmission spectra when the sample was immersed in water (blue) and 100% glycerol (red) solution. (b) Plot illustrating the experimental shift in transmission dip (black) as the surrounding index is changed. Blue and red dashed curve reproduce the simulated spectrum of the shift in transmission dip for a particle size of 300 nm with respective sol-gel indices of 1.5 and 1.35.

the sensitivity $S=\Delta\lambda/\Delta n$, other important criteria impact the sensor's efficiency, such as resonance quality factor and sensitivity range, which appear to be optimized in the present case for the lowest sol-gel index of 1.2.

The final step of this study was dedicated to the fabrication and characterization of such optimized structures, first using a sol-gel based on MTES with an average refractive index of 1.37 in the spectral range of interest (based on ellipsometry measurements). We characterized the experimental optical transmission of our design with varying refractive indices of the surrounding medium (Figure 5.5). We observe that changing the surrounding refractive index from water (Figure 4a, blue curve) to glycerol (red) induces a spectral shift of approximately 65 nm. Figure 5.5(b) illustrates the experimental and simulated BRIS curve plotted for different aqueous glycerol solutions. From the slope of the experimental results (Figure 5.5(b), black points) the BRIS value S_{bulk} is determined as 440 nm/RIU for the two points with highest superstrate index. The experimental trend observed is coherent with the simulated trend for spectral shifts for sol-gel indices of 1.35 and 1.5 (Figure 5.5 (b), red and blue dashed curves respectively). Based on Figure 5.4, the best sensitivity observed corresponds to a sol-gel index of 1.2, with an outstanding sensitivity of 1000 nm/RIU. The next and final step in this work will hence consist in experimentally demonstrating the case of Figure 5.4(d) with $n_{sol-gel}$ = 1.2.The manufacturing of porous sol gels with considerably reduced refractive index are well established. In particular, base-catalyzed sol-gel relying on Tetraethylorthosilicate (TEOS, using $NH_3.H_2O$ as base)[193] provide a route to sol gels with refractive indices as low as $n_{sol-gel}$ = 1.23 with still very reduced characteristic agglomerate size around 10 nm.

In summary, we have engineered dielectric metasurfaces for highly-sensitive refractive index sensing based on the use of tailored sol-gel and our self-assembly process. Leveraging the transparency window of chalcogenides, we demonstrate here a sensitivity of around 440 nm/RIU, on par with plasmonic counterparts, and expect to obtain improved values by resorting to highly porous textured sol-gels. This paves the way for large scale yet efficient bio-sensing, with applications in label-free molecule detection.

5.2 High-Q.F. metasurfaces for resonantly-enhanced photodetection

We have seen in the previous section how resonances with high Quality factor enable to monitor a change in the surrounding medium. We have also seen that the spatial extension of the field outside of the resonators was beneficial to
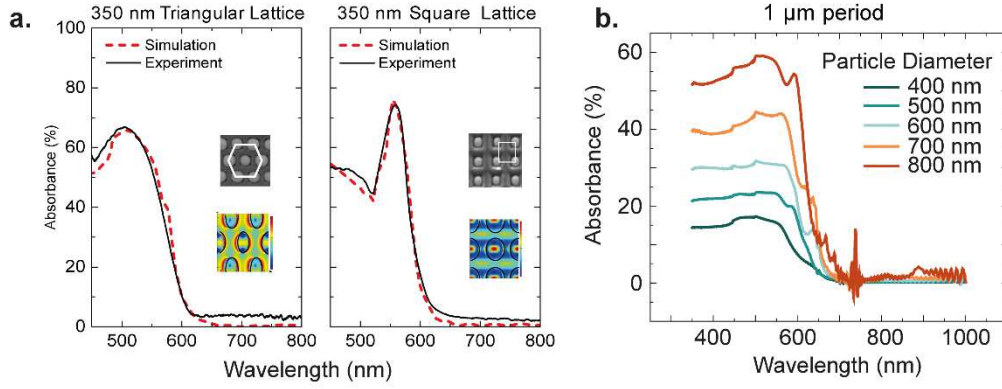
Figure 5.6 – Resonantly-enhanced absorption. (a) Experimental (red-dash) and simulated (black) Absorbance in 350 nm period square (left) and hexagonal (right) selenium metasurfaces. (b) Simulated absorption for a 1 μm period square Se metasurface.

the sensing figure of merit. In this section and the next, we now investigate the use of high quality factor resonances with a spatial extension confined within the nanoresonators, and show how these resonances can prove useful to demultiply the photon path and increase the interaction between the resonator material and the incident beam. An interesting feature of such nano-particle arrays is their ability to provide significant absorption enhancement, up to 80% in the 350 nm periodic selenium-based structures shown in Figure 5.6(a). This absorption enhancement stems from the electric dipole resonance of single particles in the absorbing region of selenium (see Figure 5.8(b)), which significantly increases the number of absorbed photons. This has interesting applications for energy-harvesting and photodetection.

We first investigate the incidence of geometry and material optical indices on the overall absorption. Such absorption is essentially the product of the array and resonator geometry. When switching from a 350 nm periodic square lattice to a 1 μm periodic square lattice, the absorption peak around 550 nm is largely attenuated or vanishes (Figure 5.6(b)), depending on the initial thickness considered. This can be simply explained by a red-shift in the electric dipole resonance, as the thicknesses increases (and hence the resulting particle sizes) for larger periods. Comparing Figure 5.6(a) and (b) with Figure 5.6(c) help clearly discriminate the role of instrinsic material absorption from the role of geometry (e.g. resonant enhancement). An absorption curve following the same trend as the imaginary part of the refractive index (written k in Figure 5.6(c)) indicates an absence of resonantly-enhanced absorption. The opposite observation cleary indicates the presence of a resonant Mie Mode in the spectral region of interest, responsible for the additional absorption observed.

High absorption has direct implications for photocarrier generation. An increase in the number of photons absorbed by the selenium nanoparticles induces in consequence an increase in excitons, e.g. electron-hole pairs inside the particles. These electron-hole pairs can then simply be harvested by means of an electrical biais applied on two opposite faces of a nanoparticle, with applications in energy harvesting (maximizing photocurrent value) or photodetection (maximizing photocurrent to dark current ratio). A reduced active layer thickness can further help to separate electron-hole pairs before they recombine. Flat selenium films are intrinsically excellent candidates for photodetection, because they commonly exhibit extremely low dark currents and hence considerable photocurrent to dark current ratios. Building on these favourable attributes of selenium, this thesis has aimed at demonstrating resonantly-enhanced photodetection using Se metasurfaces. By introducing transparent electrodes (using ITO) above and under the meta-array, a bias voltage can be applied across nanoparticles to separate generated electron-hole pairs (see Figure 5.8(a)), without significantly hampering the metasurface's absorption peak. Another favourable element of the investigated metasurfaces is the reduced
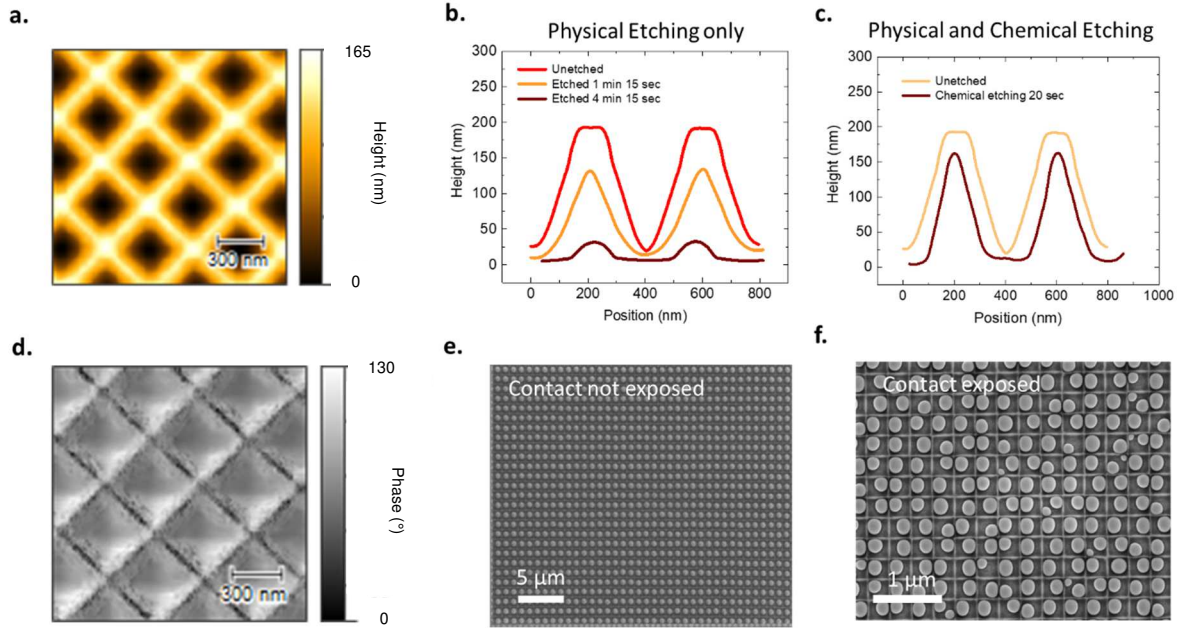
Figure 5.7 – Role of etching on thin multilayer structures. (a) AFM 2D height profile of a 350 nm pyramidal texture upon physical etching for 85 seconds.(b) Line profile of the identical 350 nm periodic texture for various etching times using purely physical etching. The etch is clearly anisotropic and incudes maximal curvature for 85 seconds etching time. (c) Line profile of the identical 350 nm periodic texture for various etching times using reactive ion etching. The etch is isotropic and incudes a rupture in slope when the contact (underlying ITO layer) is exposed. (d) AFM 2D phase profile of a 350 nm pyramidal texture upon physical etching for 85 second, showing that the contact is not yet exposed. (e) Top view Scanning Electron Microscopy upon dewetting a 40nm Selenium layer on texture presented in (a) and (d). (f) Top view Scanning Electron Microscopy upon dewetting a 40nm Selenium layer on the reactive ion etched texture presented in (c).

distance over which the charge has to travel for separation. Since the particle is about 200 nm in height in the 350 nm period configuration, excitons only have to travel reduced distances before being collected at the electrodes. The charge depletion region width is commonly of the order of 0.1 - 1 μm, which accounts for the increased charge collection efficiency.

To achieve the proposed device architecture, a high degree of order and absence of defect upon dewetting is required over the full contact area. As briefly mentioned in Chapter 2, defect density can largely be improved by resorting to etching methods, which can increase selectively the curvature at pyramid edges. In Figure 2.5, we further investigate the influence of various etching methods on the final post-dewetting result. The choice of etching method is particularly critical, since it influences the substrate shape and curvature. Let us consider a SiO_2 sol-gel texture over a soda-lime glass substrate, which is etched in two different ways. By resorting to physical etching, the maximal curvature is first increased at the pyramid edges, before decreasing upon further etching (see Figure 5.7(b)). This first etching method hence appears largely anisotropic. This is in stark contrast to the observations upon etching of the same pure SiO_2 textured system upon combined chemical and physical etching, which appears to be essentially isotropic, as shown in Figure 5.7(c). The use of physical etching allows for ordered dewetting as shown in Figure 5.7(e), which is not the case for the combined chemical-physical etching process considered here.

Additional problems arise when considering the incorporation of ITO back electrodes in such systems. In this configuration, etching is required to expose the back ITO electrode to the selenium. The ITO back electrode layer, although thin (typically 15 nm) is physically etched at a different speed than the SiO_2 layer, owing to its distinct mechanical properties. This induces a local change in curvature at the ITO-SiO_2 interface as soon as the ITO is exposed, and largely influences the subsequent dewetting process. Therefore, although etching of the SiO_2 texture in the absence of back electrode yields highly ordered dewetted arrays (c.f. Figure 5.7(e)), the situation completely changes when a back electrode
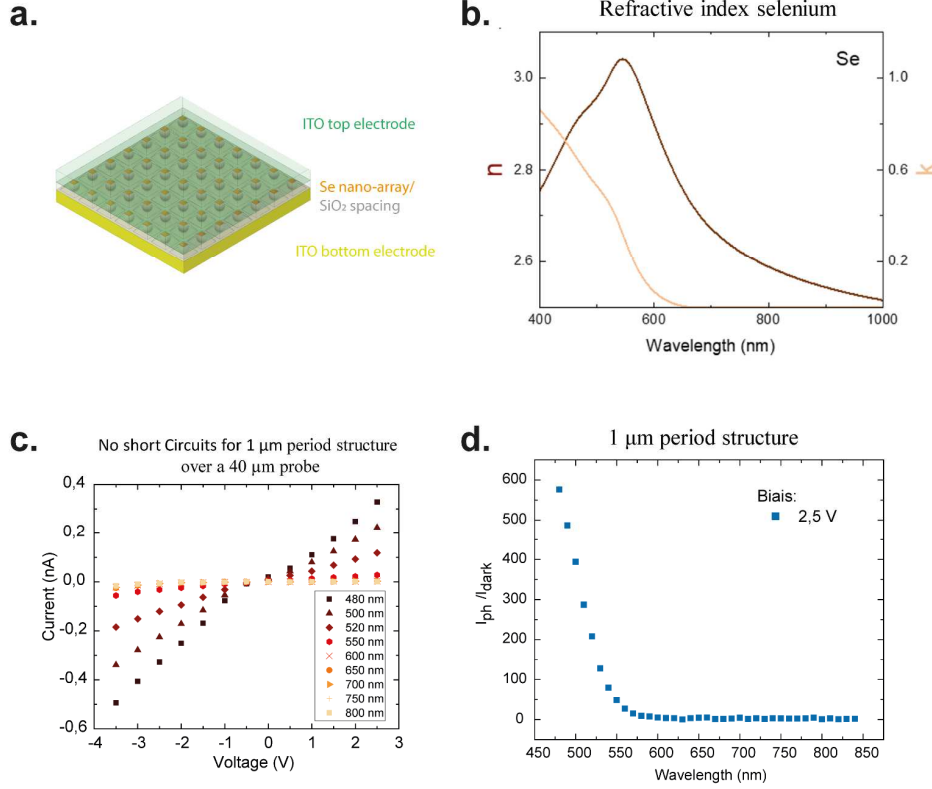
Figure 5.8 – Resonantly-enhanced photodetection. (a) Schematic of the proposed device: transparent glass substrate, ITO bottom electrode (15 nm thick), textured SiO_2 spacing layer with Se nanoparticle array, ITO top electrode (1 μm thick). (b) Real and imaginary part of the refractive index of selenium, provided for comparison with (c) and (d). (c) Intensity-Voltage curves obtained for a 1 μm period over a 40x40 $μm^2$ top contact. The observed contact interface is ohmic in nature. (d) Photocurrent to dark current ratio at 2.5 V for the wavelength range 470 nm – 850 nm. The increased absorption observed at low wavelengths is solely due to the material absorption, as shown in (b), and not to the structure.

is added, as shown in Figure 5.7(f). In this thesis, considerable efforts have been dedicated to engineer ordered dewetting with improved regularity when a back electrode is exposed. To overcome this issue, the only alternative discovered in this work consisted in resorting to 1 μm period arrays instead of 350 nm periodic arrays. The rationale behind this result lies in the finer control over the etching process when using increased thicknesses for the sol-gel films. By exposing the contact over a smaller areal percentage of a unit cell, the influence of local curvature change due to ITO exposure was attenuated. These observations on dewetting regularity directly translated in photoconducting measurements. For the 350 nm period architecture, only a single contact out of 50 initial probes has shown a (non-stable) photoconducting effect, while a stable photoconducting effect was observed for half of all contacts in the 1 μm period architecture.

The opto-electronic properties of the 1 μm architecture was characterized with and without illumination to confirm the expected absorption behavior. Although this architecture shows little or no resonantly enhanced behaviour as discussed in Figure 5.6, it was characterized with the aim of demonstrating the feasibility of the device for 1 μm period. Imposing a bias voltage V spanning from -3.5 V to 2.5 V, the current I flowing through the structure was measured under illuminations of a 100 mW supercontinuum laser for various wavelengths, as well as under no illumination (dark). The I-V curves for different incident laser wavelengths clearly show a linear behaviour, which indicates that the ITO-Se interface behaves as a purely Ohmic contact. Now fixing the biais voltage at 2.5 V, the ratio of the photocurrent to the dark current was plotted as a function of wavelength (Figure 5.8(d)), to compare with the instrinsic absorption properties of selenium over the visible spectrum. As expected, the absorption of the meta-device essentially increases in the blue, in strong correlation with the evolution of absorption for pure Selenium.

To conclude, this section demonstrates conceptually the possibility to realize in a scalable manner resonantly-enhanced selenium-based photodetectors through tailored dewetting. Technical hurdles linked to substrate curvature upon etching have impeded the realization of a meta-devices at the optimal period of 350 nm, required to observe such resonant effects in the targeted spectral region (e.g. absorbing region of selenium). This was however demonstrated for 1 μm period, which bears interesting possibilities if selenium is replaced with a chalcogenide material with an red-shifted absorption curve compared to that of selenium, such as for instance Selenium tellurides or pure tellurium.

5.3   Second harmonic generation using high Q.F. metasurfaces

Relying on high Q.F resonances, one can engineer strong interaction between light and matter, as illustrated in the previous section with the case of photodetection. The high field enhancement stemming from sharp resonances can also be used to enhanced non-linear processes within resonating structures using specific particle symmetry. In this section, we investigate the use of Fano resonances studied in Section 5.1.1 to enhance Second Harmonic signal by relying on our high Q.F resonant metasurface in combination with partial crystallization of the particles. As discussed in reference 194, this enables to break the symmetry both at the nanoparticle interface and at the various crystal boundaries, and hence limits destructive interferences between second harmonic (SH) processes within the nanoparticle.

To demonstrate the potential of our metasurfaces design capabilities, we used the previously demonstrated nanophotonic structures with optimized light-matter interactions studied in Section 5.1.1 to enhance through resonance second harmonic processes. The resonance observed in the simulated linear transmission spectra (Figure 5.9(a), wine-red curve) leads to an enhancement of the electric field intensity by two orders of magnitude (∼90x) in comparison with off-resonance spectral regions (Figure 5.9 (b), light red markers). Second harmonic (SH) measurements were performed in reflection using a previously reported setup.[195] From each of the obtained scanned image, the SH intensity at particular wavelength was calculated from the mean value of those images as shown in Figure 5.9(c) (light red dots) when the pump wavelength is tuned between 680 nm and 780 nm. The conversion efficiency η is defined as:

$$\eta = n_{photon}^{SH} \Big/ n_{photon}^{Fundamental} \tag{5.1}$$

Where n_{photon}^{SH} and $n_{photon}^{Fundamental}$ are the photon counts of the generated second harmonic (SH) and the fundamental incident signal respectively. The intensity I is related to the photon count according to the following equation:

$$I(\lambda) = nh\frac{c}{\lambda} \tag{5.2}$$

where I is the energy and λ the corresponding wavelength. We proceed to measure the re-emitted SH intensity I_{SH} over a fixed integration time (10 second), as well as the intensity of the fundamental $I_{Fundamental}$ reflected from a gold mirror surface over a reduced integration time to avoid saturation (1 second). All measurements are done under normal incidence. Normalizing these powers with time and combining relations (ii) and (iii) finally provide the conversion efficiency, which is evaluated here at 10^{-8} at 800 nm (off-resonance). The normalized SHG power shows a peak at the asymmetric electric resonance (700 nm) due to the electromagnetic field enhancement (Figure 5.9(a)). When exciting at the resonant wavelength of 700 nm (i.e. maximal field enhancement), SH signal normalized with the incident power exhibits a 100 times
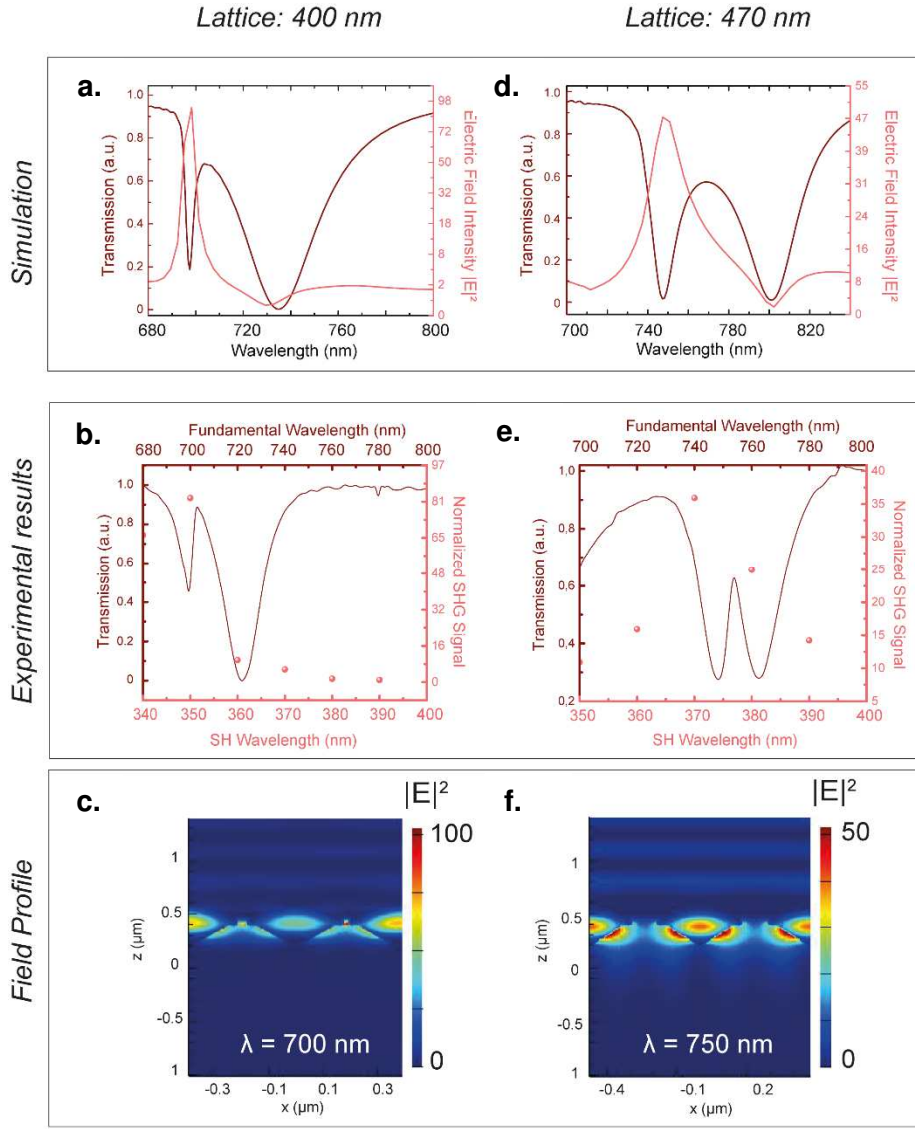
Figure 5.9 – Resonantly Enhanced Second Harmonic Generation in critically and strongly coupled conditions. (a)-(c): Fixed period of 400 nm and particle size of 350 nm, providing critical coupling conditions. (a) Simulated linear transmission spectrum (wine-red) and electric field intensity evaluated at the Se nanoparticle center (light red). (b) Experimental transmission spectrum (wine-red curve) and normalized second harmonic signal (with respect to the incident power, in light red dots) showing a ~90x signal enhancement. (c) Distribution of the electric field intensity in a plane perpendicular to the metasurface for an incident wavelength λ = 700 nm. (d)-(f): Fixed period of 470 nm and particle size of 350 nm, yielding a strongly coupled regime. (d) Simulated linear transmission spectrum (wine-red) and electric field intensity evaluated at the Se nanoparticle center (light red). (e) Experimental transmission spectrum (wine-red curve) and normalized second harmonic signal (with respect to the incident power, in light red dots) showing a ~ 38 x signal enhancement. (f) Distribution of the electric field intensity in a plane perpendicular to the metasurface for an incident wavelength λ = 750 nm.

enhancement with respect to the non-resonant region (800 nm), and almost 4 orders of magnitude enhancement as compared to the non-patterned Se thin film of comparable thickness in the off-resonant region (800 nm).

Figure 5.9(d)-(f) reproduce the study done for Figure 5.9(a)-(c) for an increased period of 470 nm with a fixed particle size of 350 nm. Based on the transmission spectrum, this situation is akin to strong coupling, and demonstrates comparatively broader symmetric resonances with lower Q.F. and field enhancement and SHG emission as compared with the critically coupled case of Figure 5.9(a)-(c). The dependence of the field intensity enhancement ($I_\omega=|E|^2$) on the lattice period (P) for these structures, follows a quadratic law defined by $I_\omega=A_0|P|^{-2}$, where A_0 is determined by the nature of meta-atoms and metasurface design. This further confirms that the signal observed stems from second-order non-linear processes.

Investigating larger sets of geometries with tailored symmetries could certainly help to further enhance the SHG signal obtained, which would make an interesting future axis of research. On a more general concluding note for high Q.F metasurfaces, it is remarkable that that the easily implementable templated dewetting process allows for such strong optical performance. This opens up a large field of applications, spanning from sensing applications to non-linear signal generation, that encourages further investigations to push the current boundaries in terms of geometrical complexity and degree of control over geometrical parameters.

5.4 Full 2π phase control

In the introduction of this thesis, two main axis of applications for metasurfaces have been presented: high Q.F. metasurfaces and metasurface for wavefront shaping. Sections 5.1, 5.2, and 5.3 have been dedicated to the study of high Q.F. metasurfaces based on in-air template instabilities. We now investigate the possibilities offered by this same process for phase control and wavefront shaping.

5.4.1 Phase control based on selenium quasi-3D architectures

In Chapter 2 (Section 2.2.2), we had demonstrated the possibility to obtain quasi-3D nanoparticle arrangements. In Chapter 3 (Section 3.5), we had further studied this architecture from a fluid dynamics perspectives, and showed that one could precisely control the how the glassy film material spreads between pyramid and mesa positions in such architectures. Interestingly, this particle arrangement shows peculiar photonic properties.

In this section, we show conceptually the ability of phase modulation across such architectures with selenium glass based on the quasi-3D arrangements that we demonstrated in Figure 2.3(e)-(g). Built-in S parameter analyzer from FDTD solver package (Lumerical) was used to extract the complex transmission and reflection coefficients. This analysis script calculates the following quantities: (i) Fraction of transmitted and reflected power, using 2D monitors and transmission function and (ii) reflection and transmission coefficients (S-parameters). These are calculated from the amplitude and phase of the fields as measured by the point monitors. This technique assumes the system is single mode (only one grating order) and that the monitors are far away enough from the structure so that the fields are propagating like a plane wave. It is also necessary to do a phase correction to compensate for the phase that accumulates as the fields propagate through the background medium from the source to the metamaterial, and from the metamaterial to the monitors.

In Figure 5.10(a) and (b), we simulated the complex transmission spectrum using the S parameter. The simulated architecture had a 1000 nm periodicity with 300 nm diameter of particles in the pyramid and 500 nm diameter on the mesa, as shown in the SEM micrograph inset of Figure 5.10 (a) (top). The simulated transmission dip position matches well with the experimentally obtained value showing a similar dip around 1050 nm. The simulated complex amplitude also yields the phase of the transmitted light beam. It shows a 2π phase change around the transmission dip, which is attributed to the overlap between electric and magnetic fields (Figure 5.10 (b)), fulfilling the second Kerkers condition[196].

It is interesting to note that smaller phase shifts can be observed at lower wavelengths in Figure 5.10(d)-(g), where these two resonances do not exactly coincide. On changing the architecture of the particles from a quasi-3D to a 2D lattice, the orientation changes and the spectral overlap disappears, resulting in phase tailoring over a smaller range.

The quasi 3D architecture hence offers quite novel possibilities in terms of phase modulation over the complete 2π-phase range with transmission values up to 70%. It is important to note that the present study using selenium nanoparticles has focused on a spacing to period ratio. To tailor phase based on the Huygens meta-atom concept[59] would require the demon-
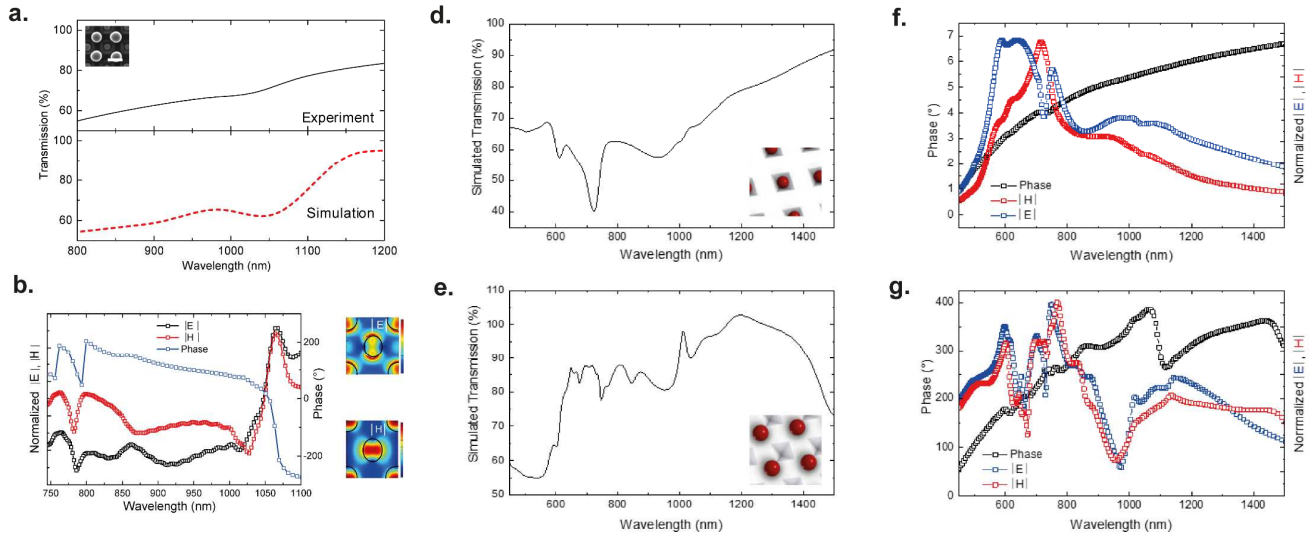
Figure 5.10 – Huygens-style meta-atoms by dewetting for meta-gratings. (a) Experimental (top) and simulated (bottom) transmission spectra for quasi-3D structure showing a dip around 1,050 nm. Inset, Top view of the simulated structure. Scale bar, 500 nm. (b), Simulated phase and corresponding electric and magnetic field plots showing a 2π phase change within 75 nm of wavelength. The phase shift is attributed to the coincidence between electric and magnetic field lattice resonance. This is supported by the electric and magnetic field plots (left) and field maps (right) at 1,050 nm. (d) Simulated transmission and spectrum for a 1000 nm square lattice without the quasi-3D structure (single particle of size 300 nm in diameter inside the pyramid, as shown in inset). (f) Simulated phase, electric and magnetic fields for the same sample. The simulation shows no abrupt phase change. This is due to the mismatch between the electric (blue) and magnetic (red) resonance, invalidating the second Kerkers condition. (e)-(g) Similarly, having only the surrounding particles of size 500 nm on the mesa (as shown in inset of (e)) does not either provide a 2π phase shift.

stration of elements with tailored spacing to period ratios, so as to provide various phase levels at a given wavelength. As such, the possibility to tailor phase using quasi-3D architecture requires further validation. In the next section, we focus on phase modulation for architectures that closely reproduce geometries observed experimentally following an increase in period to spacing ratio.

The incident wavelength is here of the order of the structure size, which defines these structures as photonic crystals rather than as metamaterials (See Section 1.2.1.1). Nevertheless, recent works have discussed the interesting possibilities offered by meta-gratings, e.g. periodic structures with sizes of the order of the incident wavelength, which could tailor with high efficiency phase profiles without loosing signal into diffracting orders ≥ 1, highlighting the relevance of the present architectures for phase control.

5.4.2 Phase control based on As₂Se₃ quasi-3D architectures

Achieving full control over phase imposes stringent requirements, since geometrical changes of a few tens of nanometer may have significant impact on optical response. In this section, we focus on the modelling of optical properties (essentially reflection and phase) arising from experimental dewetted structures following an increase in spacing to period ratio. Based on the match between experimental and simulated reflection response, we explore the possibility to accurately tailor the phase of an outbound beam over the complete 0-2π range. The present study focuses on As₂Se₃ instead of pure selenium for purely pratical reasons, but could also be equivalently done with selenium. We now focus on the reflected signal, since spectral features, although weaker, are easier to distinguish in reflection than in transmission.

a.

Period 1270 nm   Period 1440 nm   Period 1550 nm

b.
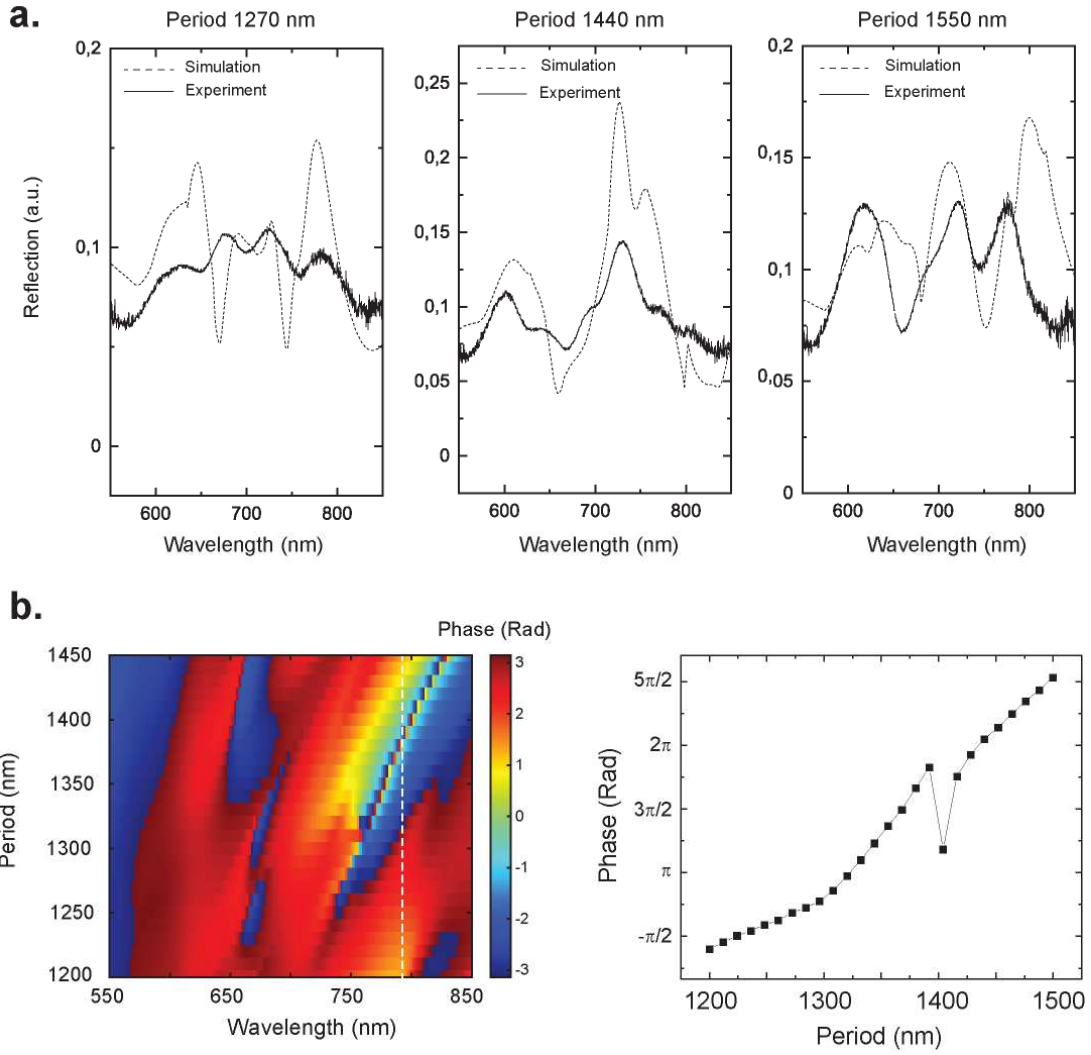
Figure 5.11 – Phase control for meta-gratings based on dewetted 3D As$_2$Se$_3$ architectures. (a) Simulated (Dash) and experimental (solid) reflection spectra for three periodicities (P=1270 nm, 1440 nm, 1550 nm) and fixed pyramid size of 850 nm. The spectra are not normalized with their own maximum, but rather compared in absolute value.

We now turn to the optical properties arising from periodic architectures based on inverted pyramids with increasing spacing along the two principal axis, as studied in Chapter 3 (Section 3.5.2). We proceed to evaluate the meta-assembly's spectrum in reflection for three distinct period values (P = 1270 nm, P = 1440 nm, P = 1550 nm), keeping the pyramid base constant at 850 nm. Since the system is highly sensitive to slight geometrical changes as low as 10 nm, the experimental and simulated reflection spectra shown in Figure 5.11 appear relatively well in line, as apparent in Figure 5.11(a). Looking at the evolution of the corresponding simulated phase for a range of periods ranging from 1200 nm to 1500 nm in Figure 5.11(b), interference between the various individual particle Mie modes add up to yield a cumulative phase shift over 4π at λ= 784 nm, with a particularly sharp 2π phase shift occurring for periods around 1410 nm. The phase shift is very gradual, spanning from 1200 nm to 1500 nm, hence

allowing for phase control with experimentally attainable accuracies. Implementing such geometry for FDTD simulations is not straightforward, given that we are in a range of spacing-to-period ratio where volume conservation (in the sense of Section 3.5) is not valid. Reproduction of the exact geometry hence required in this case scanning electron microscopy images of all three simulated periods to extract the precise spacing, period, and particle diameters. Contact angle values from Section 3.2 are further used to define spherical cap volumes. The accuracy of these metrics hence ensured a precise reconstruction for FDTD simulation. These quasi 3-D architectures hence show some promising perspectives in terms of

phase modulations. A more thorough understanding of the rationale and physics behind such double structures would certainly be of great use, as was developed for reflect-arrays for instance.
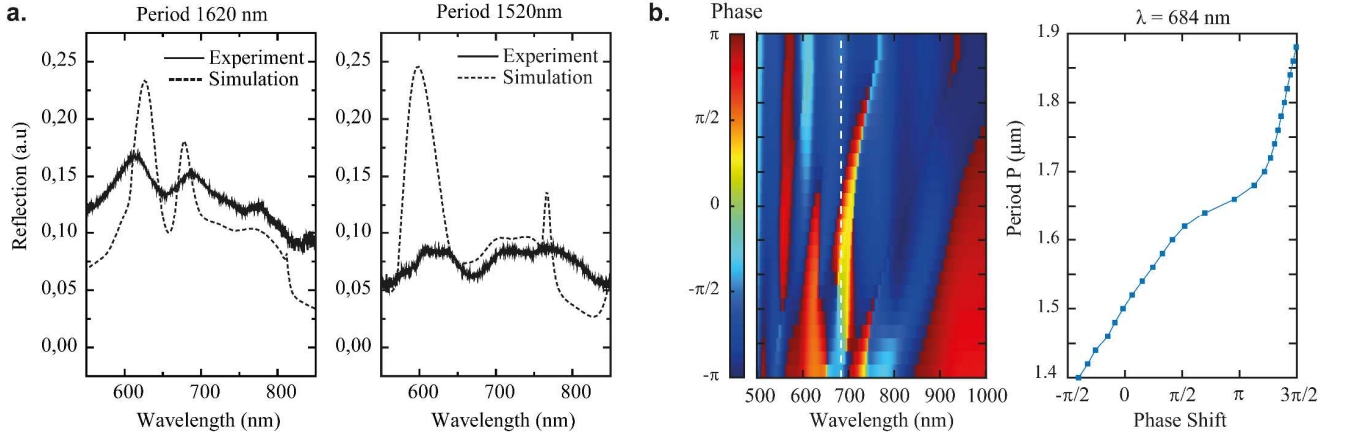
Figure 5.12 – Phase control through meta-gratings based on semi-dewetted 2D As$_2$Se$_3$ architectures. (a) Reflection spectrum of quasi-3D As$_2$Se$_3$ structures with increasing period and fixed pyramid size. The simulated blue and red curves are modeled purely enforcing the volume conservation hypothesis, with respective periods of 1620 nm and 1520 nm and an initial film thickness of 85 nm. The experimental data is obtained for a film thickness of 80 nm based on microbalance measurements in-situ during evaporation and respective periods of 1600 nm and 1700nm. (b) Phase shift in reflection of the quasi-3D As$_2$Se$_3$ nanopraticle array. The colormap shows the phase map in reflection, and show a sharp transition around 690 nm. The phase shift is plotted for λ=684 nm, showing a clear 2π phase shift for a range of periods spanning from 1400 nm to 1900 nm.

A similar comparison of simulated and experimental reflection spectra for the quasi-3D line array investigated in Section 3.5.1 also yield a coherent match. Considering the spacing-to-period ratios studied here, we can resort solely to the volume conservation hypothesis discussed in Section 3.5 to link thickness with resulting geometrical parameters. This allows for a completely "blind" implementation of geometry in FDTD simulation software, which bears significant advantages in terms of design scalability. The phase profile shows extended phase control possibilities around 684 nm (see Figure 5.12), with an extended range of period to tune the phase spanning from 1400 nm to 1900 nm. The mismatch between experimental and simulated reflection spectra appears larger in the linear case than in the square array case. A simple explaination lies in the evolution of Rayleigh instabilities along the line length, which induce fluctuations in the optical response that are challenging to avoid at this stage. Further works relying on the used of lines in grooves with tailored edge slope, will help in producing line arrays with sharper optical properties. This is interesting not only for in-air template instabilities but also for in-fiber tempated instabilities, which provides an alternative reliable route to generate nanoscale filaments over macroscopic scales with tunable diameter-to-period ratios. Just as in the previous section, the incident wavelength is here of the order of the structure size, which sets theses structures outside of the metamaterials framework (See Section 1.2.1.1), but they remain however attractive for meta-grating applications.

5.5   All-dielectric meta-reflectors based on suppressed forward scattering

The ability to control scattering properties is key in metasurfaces. As discussed in the previous section, this can consist in tailoring the emitted phase from each meta-atom to engineer a far-field phase profile. Controlled scattering could also consist in fully suppressing forward- or backscattered signal, which requires constructive or destructive interference between the main radiant modes in specific directions. This tailored destructive or constructive interference relies
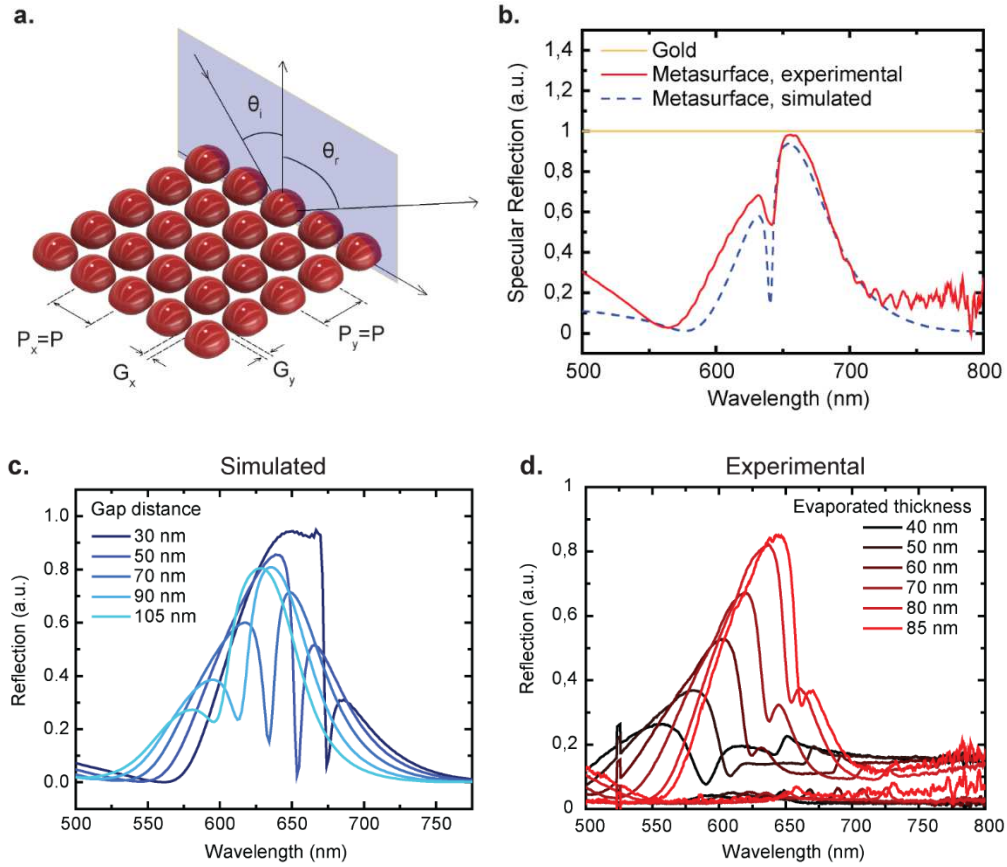
Figure 5.13 – Enhanced backscattering in dense selenium meta-arrays. (a) Schematic describing the array geometry and introducing the relevant geometrical constants. (b) Specular reflection experimentally measured (red) and simulated (blue dash) for selenium meta-arrys with interparticle gap ~ 30 nm. (c)-(d) Evolution of the reflected signal with an increase in particle size, e.g. evaporated thickness. (c) Simulated reflectance spectra for decreasing interparticle gap from 105 nm to 30 nm. (d) Experimental reflection spectra associated to a gradual increase in initial film thickness, e.g. particle size.

on the existence of multiple radiant modes. While electric modes are ubiquitous in plasmonics, achieving optical magnetism using metals typically requires flat and asymmetric structures such as split-ring resonators (SRR)[49,197,198], which limits the metamaterial properties to a limited set of incident angles, contrarily to 3D resonators that typically support modes which are significantly less sensitive to the excitation angle[199]. Until now, investigation of Mie resonances have however largely focused on the assumption of isolated cells[199,199] , considering relatively sparse meta-arrays. Coupling effects are rarely consider[200,201], although interactions between meta-atoms can be pivotal to achieve singular optical properties. In this section, we investigate the role of nanoparticle shape and packing density (or equivalently interparticle gap) on the reflective properties of selenium metarrays, and demonstrate the possibility to achieve near-complete suppression of forward scattering over an extended range of incident angles. Starting from the previously decribed selenium inverted pyramid square arrays, we proceed to slightly etch the texture using Argon ion beam prior to evaporation. This step fundamentally changes the nano-resonator shape, and, as a consequence, also changes the particle Mie modes. By further resorting to successive evaporation, a fine control over the interparticle gap is achieved, as schematically illustrated in Figure 5.13(a). This provides a second lever to tailor interaction between the various Mie modes.

The experimental specular reflection data for a selenium meta-array with interparticle gap 30 nm is reproduced in Figure 5.13(b), along with the simulated spectrum based on a fitted geometrical shape. Interestingly, such structures exhibit an experimental specular reflection peak up to 95%, taking specular reflection on gold as a base reference (yellow curve in Figure 5.13(b)). The magnitude of this reflection peak appears to be strongly correlated to the interparticle gap,

as inferred from Figure 5.13(c)-(d) both experimentally and by simulation. A likely scenario that could account for this suppression in scattering is based on the interference between electric and magnetic dipole, which according to the second Kerkers condition can destructively interfere in forward scattering. Cross sectional electric and magnetic field profiles at the resonance show however complex field patterns at the reflection peak (660 nm). While the presence of a magnetic dipole is apparent at 660 nm, the electric field distribution is difficult to attribute to either an electric dipole or quadrupole. The origins of this reflection peak hence remain to be fully understood in terms of Mie mode interferences. Computational analysis of field profiles using analytical mode decomposition could provide a way to pinpoint the exact modes interfering at 660 nm. Beyond the pronounced peak, reflection spectra exhibit another interesting feature, namely a prounced drop in reflection around 640 nm in Figure 5.13 (b). To better understand the origin of this spectral feature, we now turn to the scattering and absorption spectra of such selenium meta-arrays with a fixed 30 nm interparticle gap. A strong decrease in scattering and a parallel increase in absorption exactly in the wavelength range where reflection drops is observed, which is interestingly not seen in single particle spectra with identical geometry, highlighting the collective origin of the enhanced absorption and reduced scattering. Spatial maps of electric and magnetic fields at the resonant wavelength (not reproduced here) indicate a mode profile that is strongly analogous to anapole modes observed in thin dielectric cylinders.[202] Interestingly, the anapole modes are also predicted to induce a suppression in scattering, which is to a large extent observed in the present selenium meta-arrays at 640 nm. The very high values of electric field intensity enhancement are particularly interesting for the resonantly-enhanced photodetection discussed in Section 5.2. Indeed, one of the considerable advantages of small-gap arrays is that they are considerably easier to manufacture with very low defect density, which is crucial for photodetector architectures discussed in Section 5.2. Since the occurrence of anapole modes was discovered and understood late in this thesis work, photodetection experiments were not undertaken to investigate their potential for resonantly-enhanced photodetection, but would be a promising undertaking for future works.
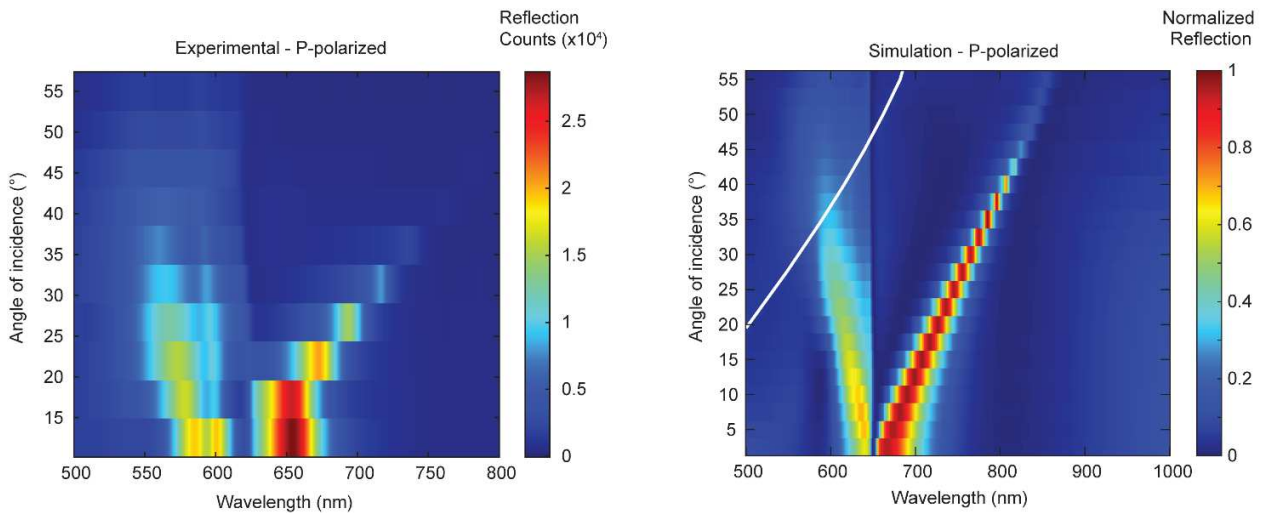
Figure 5.14 – Specular reflection maps vs incident angle. (a)-(b) Experimental (a) and simulated (b) specular reflection measured for incident angles varying from 0° to 55°. The trend observed appears in line, although experimental measurements fail to observe the reflection peaks over the same angular range that by simulation. The anapole mode is visible both in simulation and experiment as the blue lline separating the two main reflection peaks.

Finally, the angular behaviour of the meta-array is investigated in reflection (see Figure 5.14). As explained in this section's introduction, 3D resonator geometries tend to show more isotropic emission patterns and hence possess responses that are less dependent on the incident angle than 2D resonator geometries. We investigate in the present case the selenium meta-array's angular behaviour. Figure 5.14 reports the corresponding experimental and simulated specular relection spectra for incident angles varying from 0° to 55°. The trend observed in both cases is relatively in line, although experimental measurements fail to provide significant reflection at increased incident angles beyond 35°. The meta-array

can still provide a significant specular reflection response over a 60° range experimentally and up to 80° by simulations. The angular behavior of the dielectric mirror presented here is clearly less angle sensitive than previous metallic-based asymmetric structures,[203] but still more angle-sensitive than sparse perfect dielectric sphere arrays such as with silicon.[199] There appears to be a trade-off between broad angular response and reflection in this particular architecture, since the strong reflection only appears at smaller interparticle gaps.

In this section, we have demonstrated the possibility to engineer all-dielectric meta-reflectors over an extended incident angle range using our selenium nano-array platform. While the occurrence of anapole modes in such structures has been identified, further mode analysis is however required to pinpoint the exact origin of the reflection peak. Although better dielectric mirrors exist to reflect signal over extended angle ranges (e.g. Bragg mirrors), the present work demonstrates how simple shape and geometrical tuning can give rise to a very fine optical response through tailored interference between Mie modes, demonstrating the versatility of the present platform for nanophotonics.

5.6   Stretchable metasurfaces

As a last perspective for in-air template instabilities, we now turn to the use of the dewetting process over elastomeric substrates. The possibility to mechanically deform the substrate offers novel perspectives in terms of dynamic optical signal tuning, in contrast with previous applications in this chapter, that were all passive in nature (e.g. fixed after
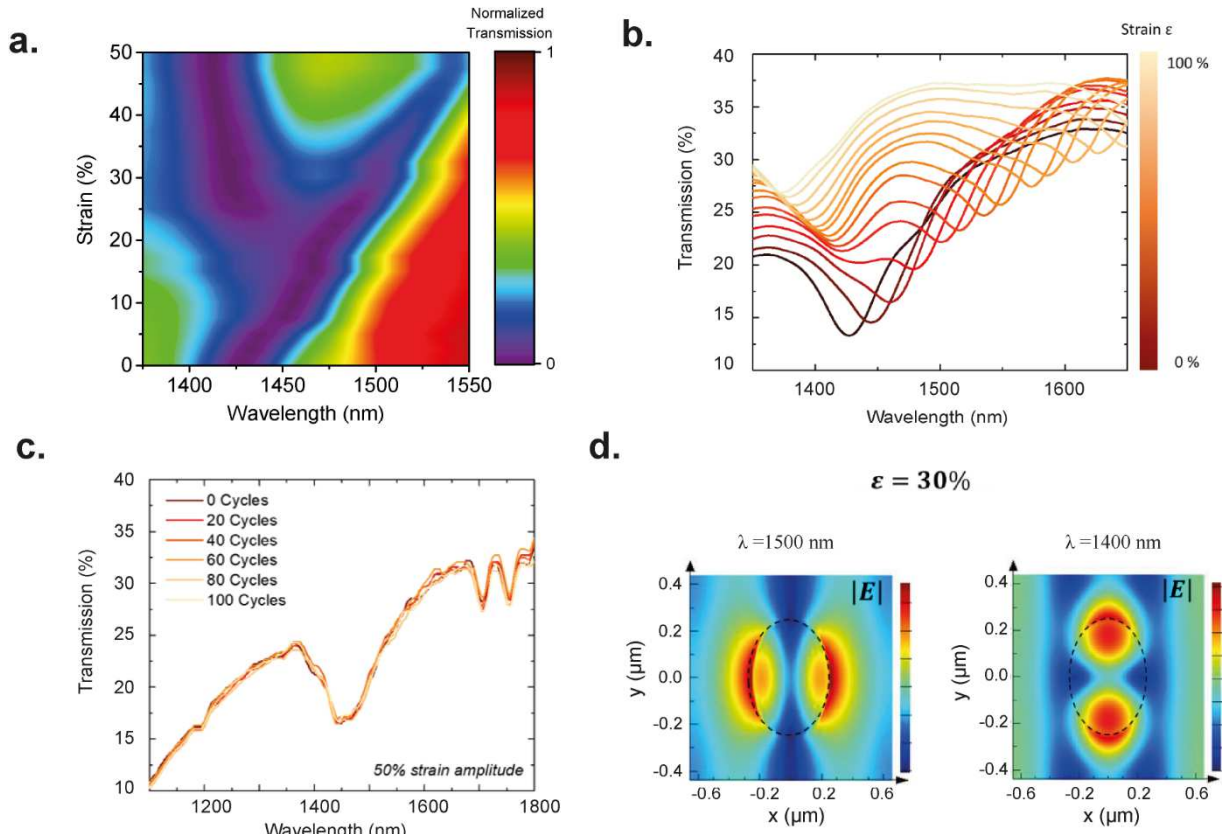
Figure 5.15 – Stretchable metasurfaces with Chalcogenide glasses. Active tuning of resonance in the near-infrared region on applying a mechanical strain from 0 to 50%. (a) The 2D plot shows the single transmission dip split into two transmission dips at around 15% tensile strain. The increase (decrease) in interparticle distance along (perpendicular to) the stretching direction leads to a redshift (blueshift) in the transmission dip. Graphs on the right show the experimental transmission spectra with 50% (top) and 0% (bottom) applied strain. (b) Experimental optical transmission spectra showing the dynamic tuning of the resonance for a 1000 nm square lattice on an elastomeric substrate with an increase in tensile strain from 0% to 100%. (c) Transmission spectra of an identical sample at 0% strain after cycling at 50% strain amplitude over 100 cycles. Negligible change in the optical spectrum is observed over the complete range. (d) Simulated electric field distribution at 1400 nm (top) and 1500 nm (bottom) for 30% tensile strain, indicating that the resonance dip is due to the inter-particle resonance.

design). While chalcogenide glasses are rigid in nature, we demonstrate here that isolated chalcogenide components placed on a stretchable substrate can undergo elongation without inducing any visible damage to the resonating elements. In Figure 5.15(a), we show the strain vs. wavelength 2D map of the optical transmission for a selenium array deposited on an elastomeric substrate. The graphs of the experimental transmission at 0% and 50% strain are highlighted on the right, and complete experimental data is provided in Figure 5.15(b). The transmission evolves from a single dip in our spectral range (at 1425 nm) at 0% strain, to two dips that either red or blue shift as the strain increases (shown by arrows on the 2D plot). The stretchable dielectric metasurface shows identical transmission spectra at 0% strain before and after 1 cycle at 100% strain amplitude. The red and blue shifts are attributed to the change of inter-particle distance along and perpendicular to the strain direction and hence a shift of the associated resonance (Figure 5.15(d)). To further test the resistance of our sample to fatigue, we investigate the change in transmission spectrum upon cycling over 100 cycles at 50% strain amplitude. No visible change is noted, supporting the absence of delamination (Figure 5.15(c)). Such simple opto-mechanical nano-structures hence offer new perspectives in stretchable metasurface, which could have interesting applications in strain and deformation sensing. Given that chalcogenide glasses are intrinsically brittle, the range of geometries compatible with this process are restricted to particle-like geometries, and forbid the use on elongated features that would not support the strain imposed by the substrate. The following chapter is dedicated to the investigation of a new class of materials, liquid metals, which are intrinsically stretchable and are interesting candidates for mechanically-actuated metasurfaces.

Chapter 6   Liquid metals for mechanically-actuated active metasurfaces

6.1   Why liquid metals?

Stretchable electronics has recently attracted much attention thanks to the enhanced capabilities offered by soft materials, with a wide range of applications such as in soft robotics [204,205,206] or consumer electronic displays.[207,208] Soft devices require conducting materials that must maintain proper conductivity under extended deformation and remain easy to pattern at reduced length scales[204]. Such materials also bear potential in the growing field of stretchable metamaterials and metasurfaces, whose artificially engineered structure made of periodic arrangements with subwavelength dimensions enable manipulation of an incident wave in unusual ways. This field has thus far remained restrained to integration of rigid optical materials onto soft substrates,[209,210,211] imposing limitations in terms of optical signal actuation.[212,213,214,215,216,217] To address these challenges, liquid metals represent a particularly promising class of candidate given their excellent combination of fluidity and conductivity.[204] Gallium for instance has a viscosity twice that of water[218] at room temperature, while maintaining excellent conductivity ($3.86 . 10^4$ S.cm^{-1}),[219] In addition, gallium has a low toxicity,[220] in opposition with other liquid metals such as Mercury, and a low vapor pressure.[221] Pure gallium has a melting point around 28°C, which can be further reduced by adding alloying elements such as Indium and Tin. Despite the comparative advantages of liquid metals, their very high free surface energies as well as the hysteretic behavior of their solid oxide layer makes them complicated to manipulate, shape and pattern. For instance, Gallium has a free surface energy[222,223] of 0.68 J.m^{-2} at 30°C, which decreases linearly down to 0.6 J.m^{-2} at 876 °C[223]. Galinstan (68.5 %wt Ga, 21.5 %wt In, and 10.0 %wt Sn), another popular liquid metal, has a free surface energy of 0.53 J.m^{-2} at 28°C.[224] This proves problematic when trying to increase pattern resolution for lateral feature sizes (width/diameter) below tens-of-micrometers length scale.[225,226,227,228] Denser structures are usually associated with thinner layers of controlled and preferably smooth thickness, two key points that remain a longstanding challenge.[204,228]

A few studies have previously investigated the resolution limit associated with liquid metals, for lateral dimensions below the capillary length scale, using various processes. By injection, liquid metal channels can reach diameters down to 10 μm,[229] below which it is typically subject to Rayleigh instability (for cylinders). Interesting possibilities to pattern liquid metals at the tens-of-micrometer scale were previously demonstrated, as for instance by lift-off[230] (20 μm), microcontact printing[231] (>100 μm), microfluidic-based inkjet dispensing[228] (10 μm) or selective wetting[226] (25 μm). Solution-based inkjet printing[227] and micro-transfer printing[225] also show interesting feature sizes down to 1 μm, but do not involve precise control over a number of process parameters including thickness and uniformity. Alloying the liquid metal with another solid metal is another alternative which shows promises in terms of resolutions,[232,233] but inevitably induces index inhomogeneities within the material both at rest and during stretching, which are undesirable for optical applications. Thermal evaporation is a widely used method to efficiently manufacture thin films with a fine control over process parameters and over large areas. Yet, owing to the large surface tension associated with liquid metals and conditions of evaporation, solely evaporating liquid metals on an elastomeric substrate usually leads to non-percolated particle array[232]. A better understanding of the physical phenomena at play during evaporation of Ga-based liquid metal is required to

propose innovative strategies and unlock the tremendous potential of thermal evaporation for the realm of soft electronics and photonics.

In this chapter, we develop a reproducible and scalable evaporation-based method to produce sub-micrometric highly stretchable liquid metal films and optical nanostructures over large areas. We use a combination of surface treatment and oxygen level control during thermal evaporation to realize films with a percolation threshold of 90 nm, well below previously reported values typically beyond 1 μm. We demonstrate both experimentally and theoretically that surface treatment prior to evaporation, and high oxygen concentration ($> 10^{-2}$ mbar) are paramount to both ensure percolating films during evaporation and film integrity during stretching. Based on these findings, we demonstrate two interesting applications of our approach. Encapsulated gallium films of thickness 240 nm and 400 nm exhibit relative change in resistance as low as 3% over 50% strain amplitude, and remain stable during cycling at 25% strain amplitude over 15 000 cycles, bearing interesting applications for stable yet stretchable interconnects. By further patterning the film into a meta-array, we show that stable liquid-metal can be used to produce stretchable metasurfaces with tunable gap resonances in the infrared, opening up interesting possibilities in all-soft stretchable optics.

6.2   Tailored dewetting of liquid metals

Given liquid metals' high surface tension, such materials tend to naturally bead up into separated particles when evaporated on a glass or polymer substrate. Free surface energy associated to the substrate is hence highly critical when attempting to produce thin liquid metal films via thermal evaporation. In polydimethylsiloxane (PDMS), a material commonly used as a substrate for soft devices, residual non-crosslinked monomers and oligomers commonly remain within the final material[234] after curing. While not explored thus far, controlling the amount of residual monomers can be an effective way to tailor the surface interaction and ultimately the film's morphology after evaporation. To evaluate this influence, identical amounts of gallium were evaporated onto both non-treated PDMS substrates and treated ones where the residual monomers were removed by washing with solvents[234] (see Figure 6.1(a) for process details). The final microstructure yields considerably different results in the two cases. SEM cross-sectional images prior to any treatment of standard PDMS (10:1 monomer/curing agent ratio) shows evidence of a Gallium nanoparticle-silicone oil emulsion (see Figure 6.1(b)-(c)), with very fine Gallium nanoparticles stacking without coalescing. As the treatment time increases, and the corresponding residual monomer concentration decreases, the nanoparticle array structure switches from 3D (no treatment) to 2D (one day treatment or more), while the particle size largely increases (Figure 6.1(b) (left)). Particularly soft PDMS (Sylgard 184 with 20:1 monomer/curing agent ratio, see Figure 6.1(b), middle) is further treated to assess the gradual influence of residual monomer chains on the size of Gallium particles, for a fixed evaporated thickness. After a single day of treatment, cross-sectional imaging reveals a residual liquid layer in insertion between Gallium particles (Figure 6.1 (b), right). Furthermore, particles grow gradually in size with treatment time, as a direct consequence of the absence of silicone oil layer. There is hence a gradual shift from a liquid silicone–liquid metal interfacial interaction to a solid elastomeric-liquid metal interfacial interaction. The conformal nature of the oxide skin induces intimate contact between the PDMS and the liquid metal, and is responsible for the high adhesion strength between the two.[235]

Another important factor in the wetting dynamics of Ga-based liquid metal on elastomeric substrates is the formation of an oxide layer (typically a native nanometric solid Ga_2O_3 surface layer[236]) at the surface of the liquid metal. This has been already widely exploited to maintain liquid metals into non-equilibrium shapes[235] and play in favor of liquid
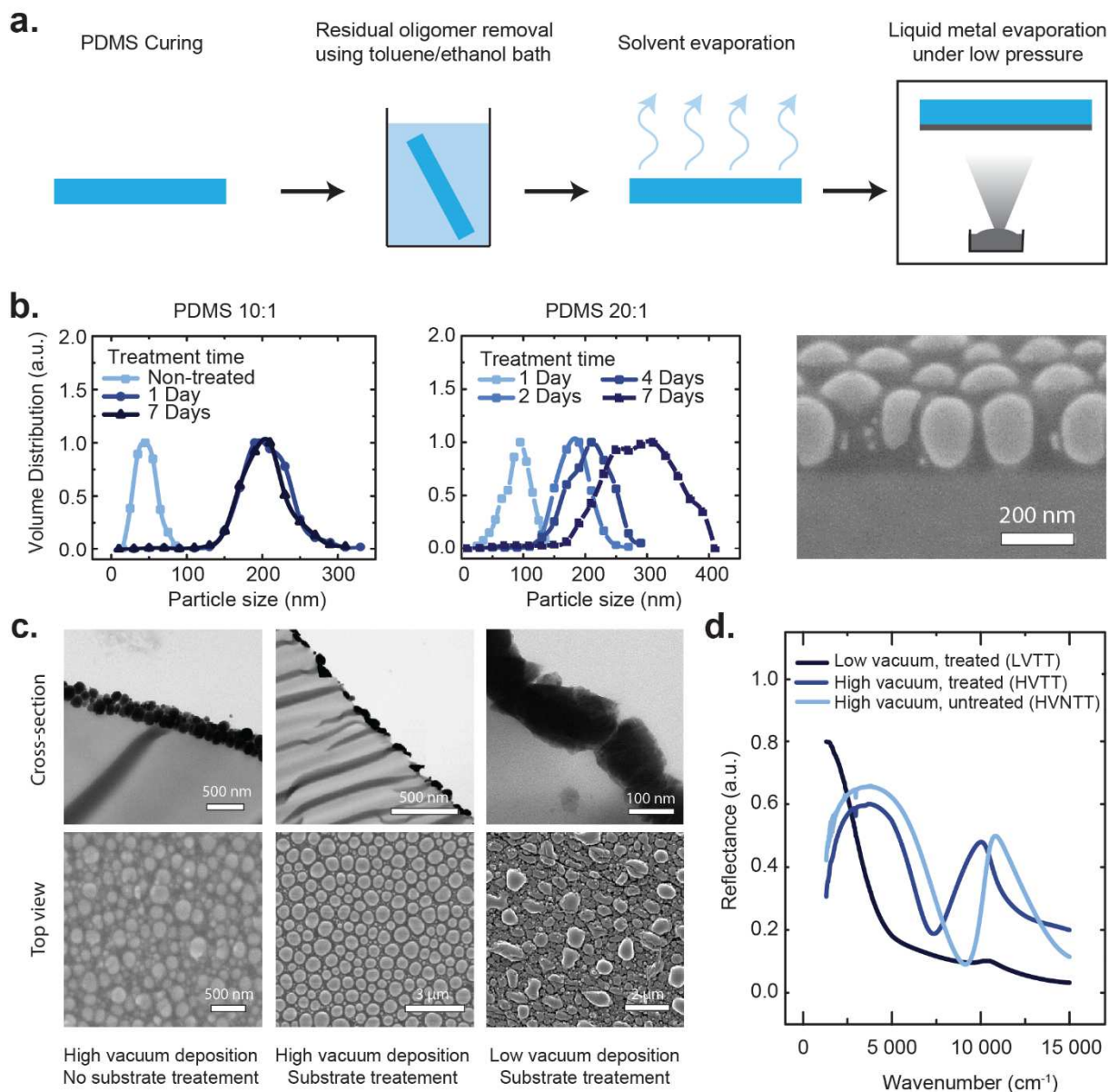
Figure 6.1 – Presentation of the process allowing for percolated liquid metal thin films. (a) Schematic depicting the fabrication process: PDMS curing, solvent washing in a toluene/ethanol mixture, solvent evaporation, and finally evaporation of liquid metal in low vacuum environment. (b) Particle size distribution obtained of a 240 nm Gallium on (left) PDMS 10:1 and (middle) PDMS 20:1 (monomer/curing agent ratio) samples with various treatment times and (right) contrast-enhanced cross-sectional SEM image of a 240 nm Gallium film evaporated on a PDMS 20:1 treated for a single day. A liquid layer is seen in insertion between the Gallium particles, which we attribute to the presence of residual silicone oil[234]. (c) Cross-sectional TEM images (top) and top view SEM images (bottom) of 400 nm Gallium evaporated onto (left) non-treated PDMS under high vacuum (HVNTT), (middle) treated PDMS under high vacuum (HVTT), and (right) treated PDMS under low vacuum (LVTT). (d) Fourier Transform Infrared Spectroscopy (FT-IR) reflectance of 400 nm-thick equivalent Gallium films evaporated under different vacuum levels ($P_{LV} = 10^{-2}$ mbar and $P_{HV} = 10^{-7}$ mbar), and onto treated (TT) and non-treated (NTT) substrates.

metal wettability. However, it has not yet been used as a leverage to tailor the film morphology during thermal evaporation. To assess the influence of oxide layer growth dynamics on the final microstructure, we evaporated liquid metal films under two separate oxygen partial pressures (10^{-7} mbar and 10^{-2} mbar) onto treated and untreated PDMS substrates. Each vacuum level gives rise to a distinct morphology. Evaporating under high vacuum (10^{-7} mbar) yields an array of separated spherical particles with a broad size distribution (Figure 6.1(c) (left and middle)), whereas a lower vacuum (10^{-2} mbar) yields a percolated film (Figure 6.1(c) (right)).

To quantify the amount of evaporated material, thicknesses are measured using concomitant deposition on non-toluene treated substrates for which roughness is significantly lower (see Figure 6.2(a)-(c)). For each sample, we can

a.

b.
Non-treated　　　　Treated　　　　Treated
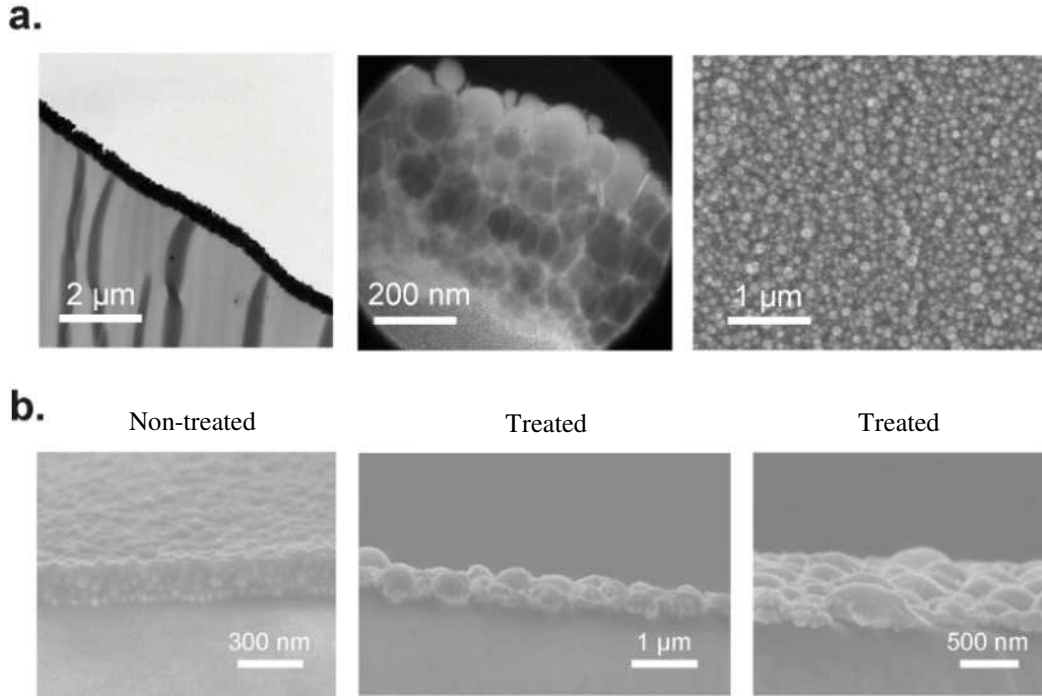
Figure 6.2 – Quantifying evaporated liquid metal thickness. (a) Cross-sectional (left) dark and (middle) bright field TEM imaging along with (right) top view SEM image of low vacuum non-treated (LVNTT) samples. The particle size distribution is very fine and is not percolating according to DC resistance measurements.(b) Cross-sectional SEM images corresponding to (a)-(c) a given equivalent thickness e=240 nm . The thickness t_{Ga} is further identified to the thickness on non-treated samples.

extract an equivalent thickness t_{Ga} that refers to the measured thickness during the same evaporation experience on a non-treated PDMS sample.

6.3　　Analysis of percolation behavior

To corroborate these first observations concerning residual monomers and vacuum level, Fourier Transform Infrared Spectroscopy (FT-IR) is used to optically characterize the samples, and further enables to electrically characterize conductivity on a particular length scale (Figure 6.1(d)). High Vacuum Non-Treated (HVNTT), High Vacuum Treated (HVTT) and Low Vacuum Non-Treated (LVNTT) samples, all apparently close to percolation threshold according to SEM images (Figure 6.1(c)) yet isolating by DC resistance measurements, exhibit strong reflection peaks at specific wavelengths, associated to the isolated metal particle's localized surface plasmon.[237] Starting with HVNTT samples, a peak appears at around 12 000 cm^{-1}, which red shifts in the case of HVTT Gallium films, correlated with an increase in metal particle size. In the case of LVTT Gallium films, particles become fully connected above a critical thickness. At low frequency (low wavenumbers), the relatively high reflectance matches with a Drude-type behavior, characteristic of unbounded electrons, propagating freely throughout the percolated network. This optical measurement correlates well with the high DC conductivity ($\sim$30 Ω.sq^{-1} at 400 nm thickness) we measured with a four point probe setup. Shifting to higher frequencies (higher wavenumbers), there is a clear drop in reflection, corresponding to the cut-off above an effective plasma frequency. Two factors are hence key to obtain percolated liquid metal films: (i) the eventual presence of uncross-linked polymeric chains at the surface of the substrate before evaporation and (ii) the vacuum level during evaporation, which can be set to high vacuum (10^{-7} mbar, abbreviated HV) or low vacuum (10^{-2} mbar, abbreviated LV). Considering that the film treatment can simply be replaced by commercially available low liquid content polymers or
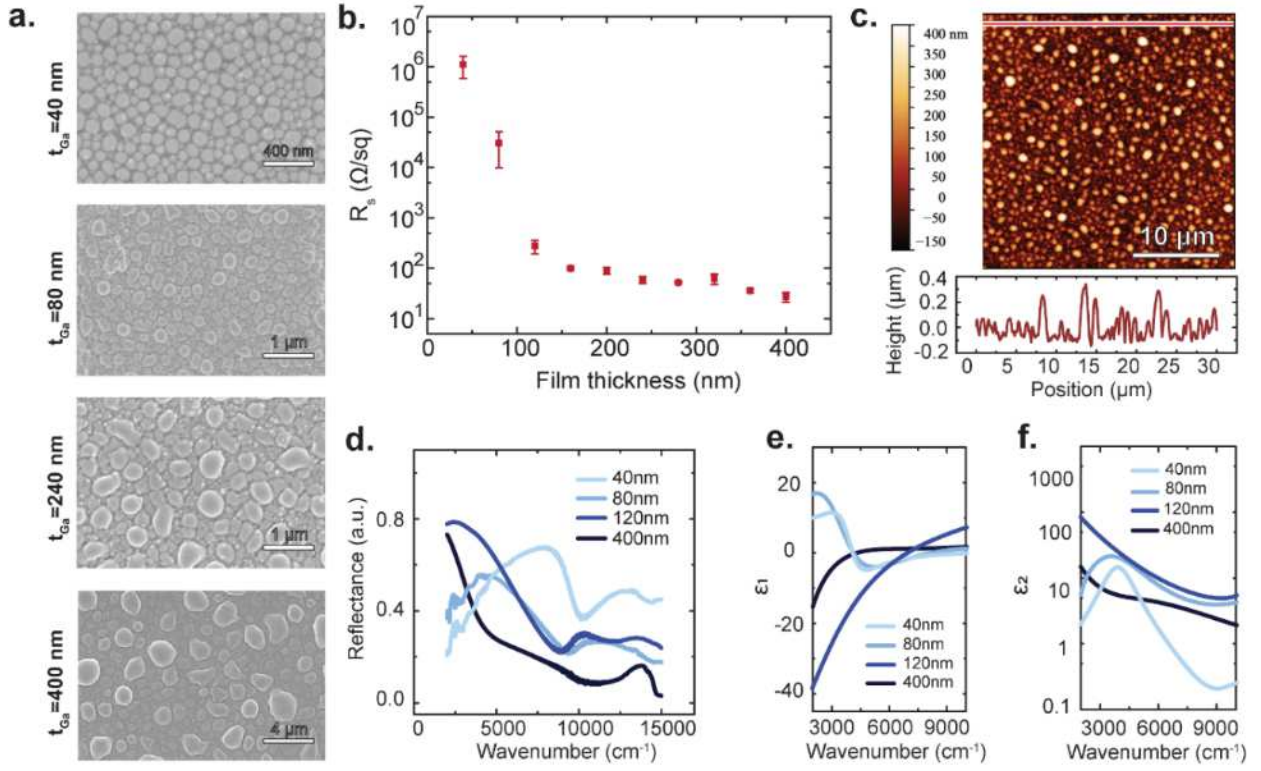
Figure 6.3 − Identifying the percolation threshold in low vacuum Gallium films on treated PDMS substrate. (a) (from top to bottom) Top view SEM images of the Gallium films, with increasing thickness t_{Ga}. (b) Electrical sheet resistance as a function of equivalent film thickness. The continuous decrease indicates the switch from non-percolating to percolating array. (c) (top) Atomic force microscope (AFM) image of a 240 nm thick Gallium film over a 30 μm x 30 μm area and (bottom) cross sectional line profile corresponding to the red line on the AFM image. (d) Associated reflectance of the films measured by FT-IR. (e)-(f) Corresponding real (ε_1) and imaginary (ε_2) extracted permittivity.

using physically cross-linked elastomers, the proposed single step process is scalable (only one evaporation needed) and can be applied to large substrates (simply limited by the size of the evaporating chamber), while providing good reproducibility.

Percolation threshold is an important parameter to characterize, deepen our understanding but also for future applications. As shown in Figure 6.3(a)-(b), there is a clear trade-off between equivalent film thickness and conductivity, defining a metal-insulator transition. To identify the percolation threshold in LVTT films, sheet resistance for samples with a wide range of thicknesses were measured upon evaporation. We further proceed to study films with equivalent thicknesses ranging from 40 to 400 nm. A strong drop in resistance is observed throughout this range, with a large standard relate this first experimental finding with the predictions from percolation theory, whereby conductance Σ of a resistor network just above percolation scales as[238,239,240]

$$\Sigma \propto (p - p_c)^\nu \tag{6.1}$$

With p the fraction of conductive lattice sites, p_c the percolation threshold and ν the conductivity exponent. Previous Monte Carlo simulation on infinite binary lattice systems by Levinshtein et.al.[239] have estimated the conductivity exponent in 2D ($\nu = 1.33 \pm 0.05$) and 3D ($\nu = 0.8 \pm 0.05$) random lattices around percolation thresholds. Considering evaporated Gallium thickness and fraction of conductive lattice sites as proportional,[240] we obain an estimate for p and proceed to fit electrical conductivity with the percolation power law. This yields an exponent of $\nu = 1.33 \pm 0.24$ for all thicknesses above 120 nm (excluded). These values are therefore relatively well in line with theoretical predictions for 2D systems just above percolation[238,239], placing our system in the framework of classical percolation theory.

At the onset of percolation for LVTT films, exclusively very thin connected particles relatively homogeneous in size are observed. Further increase in thickness leads to a minimal increase in resistance and accumulation of liquid metal in isolated droplets. This can be understood as the consequence of the liquid metal's high free surface energy, which drives a dewetting-type phenomenon during evaporation, in competition with the oxide layer formation kinetics. Cross-sectional scanning electron microscopy reveals a thin liquid metal film connecting larger blobs (Figure 6.2).

To further study the percolation threshold in LVTT films, Fourier Transform Infrared Spectroscopy (FT-IR) reflection spectra of Gallium samples with equivalent thicknesses ranging from 40 nm to 400 nm (i.e. around the percolation threshold) are measured (Figure 6.3(d)). When increasing thickness, peaks in the reflection spectra gradually red-shift while reflectance clearly increases at large wavelengths. By means of a variational dielectric fit[241] using RefFit software[242], Kramers-Kronig consistent dielectric functions ε_1 and ε_2 are extracted (Figure 6.3 (e)-(f)) from the reflectance data. Below Metal-Insulator-transition (M-I-T), the static conductivity ($\sigma_{dc} = \sigma_1 (\omega \to 0) \sim 0$) is not apparent and $\varepsilon_1(\omega)$ is positive (thickness 40 nm and 80 nm, Figure 6.3(e)), corresponding to the absence of delocalized electrons, and a resonance peak in Mid-IR (see Figure 6.3(f)), caused by the ensemble of isolated particles or clusters. As the metal particle increase in size, the absorption peak in ε_2 gradually increases. When percolation is reached, the spectrum exhibits both a Drude tail (around ~120 nm) and a plasmon peak. When further increasing thickness, this plasmon dies out gradually. Based on the scanning electron microscopy images, the presence of such plasmon modes beyond electrical percolation could be understood by the presence of the rough surface, which still contributes to the dipole interaction. Two cases hence emerge: (a) a connected film for thicknesses above ~90 nm and (b) individual unconnected cluster films below ~90 nm. The percolation threshold t_c extracted through FT-IR reasonably matches with previous DC measurements.

6.4 Stability of nanoscale liquid metal films

We now turn to the mechanical properties of the deposited films. First, the film electrical resistance under strain exhibits negative gauge factors instead of a positive one that one would expect from sole geometrical deformation. As shown in Figure 6.4(a), the resistance of Gallium films decreases in a similar fashion for 240 nm and 400 nm thick film by as little as 8% at 50% strain. Adding an encapsulation layer above the film changes slightly this behavior, and enables resistance changes of less than 3% up to 50% strain. A tilted view of the associated microstructure under strain is shown in Figure 6.4(b). This figure reveals the flattening of droplets under strain without encapsulation, as well as the appearance of dispersed holes. Adding an encapsulating layer yields a distinct resistance response to non-encapsulated films, which could be correlated to the additional mechanical stress exerted by the encapsulating layer during elongation. We interpret the relative resistance change through a simple compromise. As the sample is deformed, droplet regions become more separated along the tensile axis, increasing current pathways between droplets intrinsically associated to higher resistivities. However, they are also brought closer perpendicular to the stretching direction, also creating in parallel more conductive current pathways. The interplay between these two competing phenomena define the actual global change in resistance along the tensile axis. Meanwhile, the resistance perpendicular to the tensile direction is exclusively driven by the reduction in distance transversally between high conductivity regions, accounting for the continuous decrease in resistance also observed experimentally.

Alternative liquid metals or substrates are also compatible with this process. We introduce another liquid metal, $Ga_{86}In_{14}$, with a melting point slightly below 20°C, demonstrating the possibility to further reduce the limit working
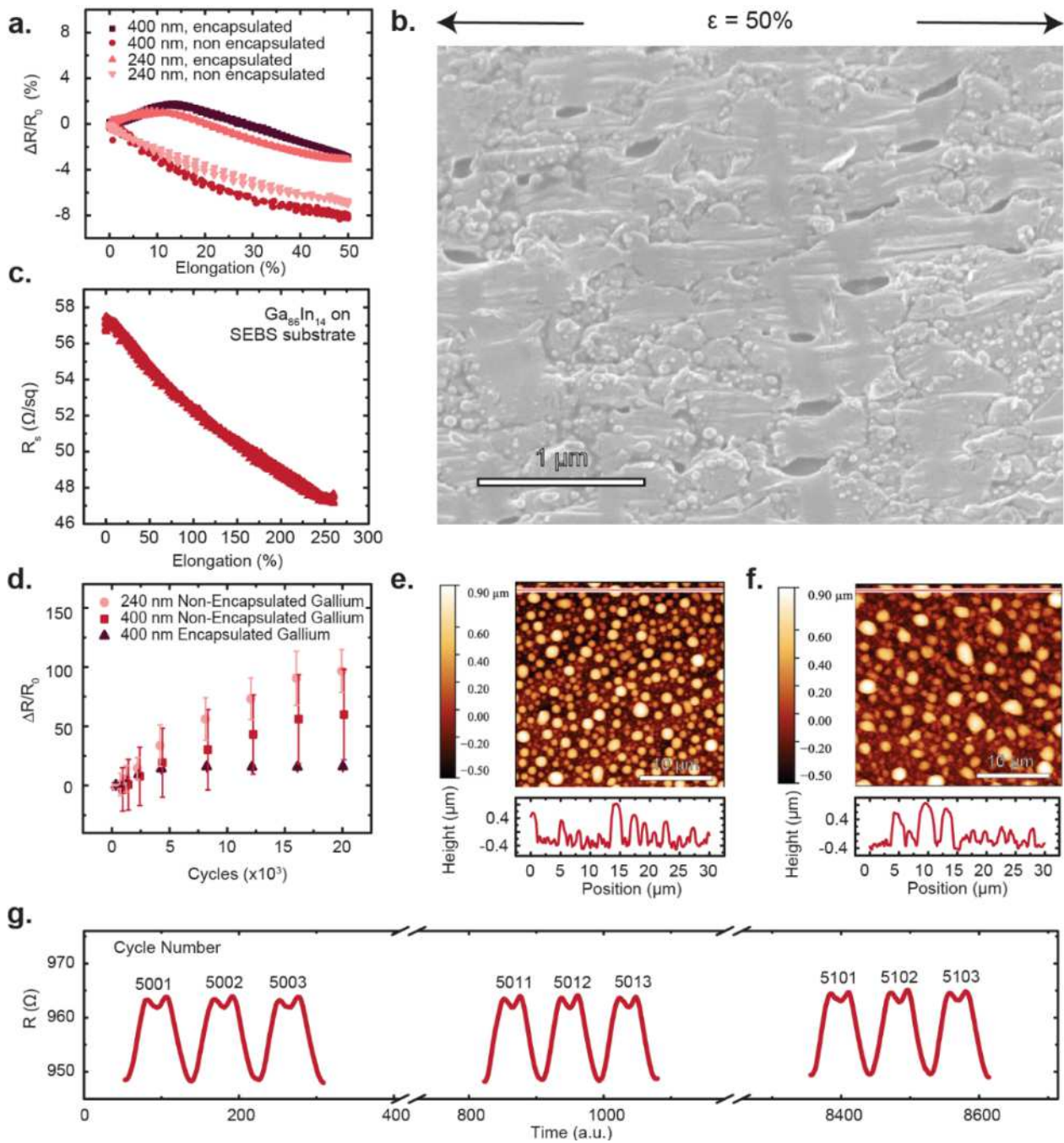
Figure 6.4 – Electromechanical characterization of the thin liquid metal films. (a) Relative change in resistance over 2 cycles for gallium films of 240 nm and 400 nm, encapsulated and non-encapsulated, on a treated PDMS substrate. (b) 20° tilted-view SEM image showing the microstructure of a 240 nm-thick Gallium film at 50% tensile strain. (c) Change in sheet resistance over 2 cycles for $Ga_{86}In_{14}$ films of 400 nm equivalent thickness on an untreated Styrene-Ethylene-Butylene-Styrene (SEBS) elastomeric substrate. (d) Relative resistance change at 0% strain upon cycling at 25% strain amplitude for various Gallium samples. (e)-(f) (top) Atomic Force Microscopy (AFM) image of gallium films (f) un-stretched and (e) stretched at 50% strain for 20 000 cycles, along with (bottom) cross sectional profile corresponding to the red line in the AFM image. (g) Resistance vs. time for a 240 nm encapsulated Gallium film cycled at 50% strain amplitude, illustrating signal stability.

temperature. This alloy is almost identical with the eutectic Gallium-Indium composition (Ga$_{83}$In$_{17}$, commonly refered to as E-GaIn), which can also be obtained by simple thermal evaporation, and shows similar mechanical behavior. Co-evaporation could provide a more reliable alternative to finely control the composition of liquid metal alloys by evaporation, allowing for Galinstan or pure E-GaIn based thin-films for instance. Such liquid metal films can be obtained on PDMS as well as onto alternative substrates such as Styrene-Ethylene-Butylene-Styrene (SEBS), a highly deformable elastomer which does not require any treatment prior to liquid metal evaporation. Ga$_{86}$In$_{14}$ films on SEBS down to 400 nm thickness remain conductive up to 250% strain (Figure 6.4(c)).

As shown in Figure 6.4(d), relative resistance change of as-deposited Gallium films show significant drift with cycling. An AFM image analysis can further confirm our observations. Figure 6.4(e)-(f) indicate this drift is correlated with an evolution of non-encapsulated droplet microstructure upon cycling. Some droplets grow in size to the detriment of their neighbors, accumulating liquid metal in localized areas. To limit this drift, the film is encapsulated with a thin non-treated PDMS layer. This notably stems the drift in fatigue and stabilizes the microstructure, allowing for thin yet stable stretchable conducting films (Figure 6.4(d)-(g)). Given the nanoscale thicknesses involved, these films do not escape well-known electro-migration limitations[204,233], and are thus most adapted for applications involving sufficiently low currents. However, as we demonstrate in Figure 6.6, such limitations do not represent a fundamental limitation for photonic applications given the very high frequency ($>10^{13}$ Hz) and comparatively low currents involved.

6.5 Role of oxidative environment on stability

To better understand the physics at play during deformation, and particularly the anticipated interplay between dewetting[243,244] and oxide growth, identical liquid metal films are stretched under various oxidative environments. As can be seen in Figure 6.5(a), holes are apparent upon stretching and the lateral defect size distributions of these defects are plotted as a function of the oxygen partial pressure. Above an oxygen partial pressure threshold of $P_{O_2} = 1.2 . 10^{-1}$ mbar, the oxide layer ruptures and immediately reforms a fresh flat oxide layer (Figure 6.5(a)(top left)) within a very short time τ_{oxide} (estimated below). Inversely, for an oxygen partial pressure of $P_{O_2} = 1.8 . 10^{-3}$ mbar, these holes consistently coalesce to form long lines throughout the film (see Figure 6.5(a)(bottom left)).
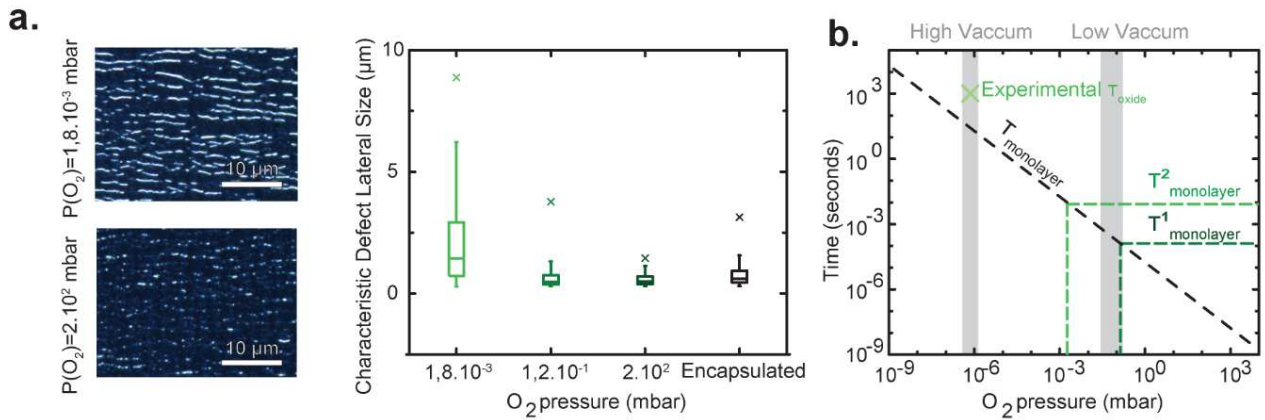
Figure 6.5 – Influence of oxidative environement on liquid metal stability. (a) Dark-field optical microscopy image of 400 nm gallium films at 50% strain under (top left) $1.8 . 10^{-3}$ mbar oxygen atmosphere and (bottom left) ambient atmosphere. (Right) Defect lateral size distribution as a function of the oxidative atmosphere. The crosses delimit the 99% threshold. (b) Plot representing the theoretical monolayer formation time as a function of oxygen partial pressure along with experimentally measured oxide formation time[245] τ_{oxide} at high vacuum. The two gray rectangles delimit the high and low vacuum regions during evaporation. Theoretical monolayer formation times for $1,8 . 10^{-3}$ mbar O_2 ($\tau_{monolayer}^2$) and $1.2 . 10^{-1}$ mbar O_2 ($\tau_{monolayer}^1$) concentration are reported on the graph.

To explain this unexpected role of O_2 concentration on both film stability during elongation and evaporation, we

rely on the Maxwell-Boltzmann kinetic theory of gases. In a gaseous phase, the constant collisions produce a wide distribution of velocities. Maxwell and Boltzmann expressed the distribution of velocities as:

$$\frac{1}{n}\frac{dn}{dv} = f_v = \left(\frac{m}{2\pi kT}\right)^{1/2} exp\left(-\frac{mv^2}{2kT}\right)$$

(6.2)

Where dn is the fractional number of molecules in the velocity range between v and $v + dv$, m the mass of the gaseous specie, T the temperature, and k the Boltzmann constant. This expression can be projected onto a single axis, such that:

$$\frac{1}{n}\frac{dn_x}{dv_x} = f_v = \left(\frac{m}{2\pi kT}\right)^{1/2} exp\left(-\frac{mv_x{}^2}{2kT}\right) \tag{6.3}$$

The number of molecules striking an element of surface (perpendicular to the x-direction) is given by:

$$\phi = \int_0^{+\infty} v_x dn_x \tag{6.4}$$

Combining (6.3) and (6.4) yields:

$$\phi = \frac{n}{\sqrt{2\pi}}\left(\frac{kT}{m}\right)^{1/2} \tag{6.5}$$

We can re-expressed this flow rate using the law of perfect gases:

$$\phi = \frac{1}{\sqrt{2\pi}}\left(\frac{N_a}{M_{O_2}kT}\right)^{1/2}.P_{O_2} \tag{6.6}$$

This reduces to:

$$\phi = 3.324.10^{22}\left(\frac{1}{M_{O_2}T}\right)^{1/2}.P_{O_2} \tag{6.7}$$

Considering conservatively that the atmosphere in the chamber remains at 25°C, we obtain:

$$\phi = 1,08.10^{22}.P_{O_2} \text{ molecules.m}^{-2}.\text{s}^{-1} \tag{6.8}$$

where P is in mbar. We now proceed to estimate the gallium atomic density ρ_N:

$$\rho_N = \frac{N}{V} = \frac{\rho.N_a}{M(Ga)} = 5,09.10^{28} \text{ molecules.m}^{-3} \tag{6.9}$$

To extract the gallium surface density, we first estimate the characteristic length L associated to one atom of Gallium.

$$L = (V_{atomic})^{1/3} = (\rho_N)^{-1/3} \tag{6.10}$$

$$\rho_S = \rho_N.L = (\rho_N)^{2/3} = 1,37.10^{19} \text{ molecules.m}^{-2} \tag{6.11}$$

Hence:

$$\tau_{monolayer} = \frac{\rho_S}{\phi} = \frac{1.37.10^{19}}{1,07.10^{22}.P_{O_2}} = \frac{1,28.10^{-3}}{P_{O_2}} \text{ seconds} \tag{6.12}$$

The monolayer formation time for Gallium oxide as a function of oxygen concentration is represented in Figure 6.5(b). The resulting microstructure in Figure 6.5(a) can thus be pictured as the result of two phenomena that unfold in parallel: (i) the formation of an oxide skin, characterized by a formation time scale τ_{oxide} and (ii) dewetting of the condensate from the substrate, characterized by the time scale[243,244] $\tau_{dewetting}$. In the first case, oxidation takes places fast enough to prevent these holes from coalescing, whereas in the second case oxidation occurs slower than the nucleation and growth of holes. A characteristic film dewetting time scale $\tau_{dewetting}$ can hence be experimentally estimated, such that:

$$\tau_{oxide}(1.2 \cdot 10^{-1} \, mbar) < \tau_{dewetting} < \tau_{oxide}(1.8 \cdot 10^{-3} \, mbar) \tag{6.13}$$

Characteristic defect size distributions apparent in encapsulated films under ambient conditions show that PDMS gas permeability is also sufficient to insure oxidation kinetics still dominate over dewetting. The microstructure of the film upon stretching is therefore the result of a competition between dewetting and oxide growth. This insight also enables to better grasp the physics at play during evaporation. When the oxygen partial pressure is reduced during evaporation under high vacuum, gallium oxide growth dynamics (time scale τ_{oxide}^{HV}) are fundamentally modified and oxide layer formation is considerably slowed down[245], allowing for dewetting to occur first. Inversely, a high oxygen partial pressure during evaporation (low vacuum) allows for the oxide layer to form before dewetting can take place (time scale τ_{oxide}^{LV}). To support this scenario, τ_{oxide} and $\tau_{dewetting}$ are estimated and compared. In first approximation, the oxidation time can be estimated equal to the time to cover the surface with an oxygen monolayer by diffusion[246], such that $\tau_{oxide} \sim \tau_{monolayer}$ (see Figure 6.4(a)). In the previous analysis on film deformation upon stretching, a range for $\tau_{dewetting}$ has been identified (see Inequation (6.14)). Comparing the values for various vacuum levels yields the following inequality:

$$\tau_{oxide}^{LV} \leq \tau_{dewetting} < \tau_{oxide}^{HV} \tag{6.14}$$

Experimental data from previous studies[245] measuring the time needed to cover half of the surface with oxide shows that $\tau_{monolayer}$ underestimates the actual oxide formation time τ_{oxide} in high vacuum, supporting that the right inequality is actually conservative.

6.6   Liquid metal based-photonic crystals

The above analysis can now be exploited to realize micro-scale architectures of soft conductors onto soft substrates. It indeed turns out that the deposition conditions we have identified are key to realize all-soft photonic crystals. We proceed to spin coat and pattern a photoresist onto a treated PDMS substrate from which all residual oligomers have been removed. The photoresist is then exposed and carefully developed to avoid delamination from the elastomeric substrate or development of cracks caused by substrate swelling. By subsequent evaporation of the liquid metal film under low vacuum conditions and lift-off, complex structures with resolutions on par with the state-of-the-art in liquid metal patterning (~1 μm) can be achieved. Resolution could be further improved using alternative techniques such as deep-UV photolithography. As apparent in SEM images (Figure 6.4(b) and Figure 6.6(c)), the photonic crystals exhibit a rough top surface, while the surface directly in contact with the substrate is however conforming, providing a smooth interface. In the following part, the optical nanostructures are probed from the smooth side.

To study the influence of processing parameters on the photonic crystal's optical signature, transmission and reflection spectra of identical non-treated high-vacuum (HVNTT) and treated low-vacuum (LVTT) photonic crystals are compared (see Figure 6.6(a)), using a 2 μm periodic array with 1.2 μm diameter particles. Whereas patterned Gallium films evaporated in low vacuum onto treated PDMS 10:1 films (lower residual monomer content) retain optical properties relatively in line with those expected from simulation, patterned Gallium films evaporated in high vacuum onto non-treated PDMS 12:1 films (higher residual monomer content) exhibit a very broad and faint optical signature, which cannot be related with optical simulation. Evaporating Gallium films under high vacuum onto non-treated PDMS 10:1 films yields an intermediate situation where optical response varies largely depending on position. This suggests the structure is near the percolation threshold and that percolation occurs on different length scales in different regions. We attribute

this effect to the partial solvent washing during the development step, which removes surface monomer layer and allows for particle coalescence under low vacuum. The observations for both non-treated and treated PDMS substrates highlight the essential role of substrate treatment and deposition conditions in obtaining proper liquid metal-based photonic crystals.
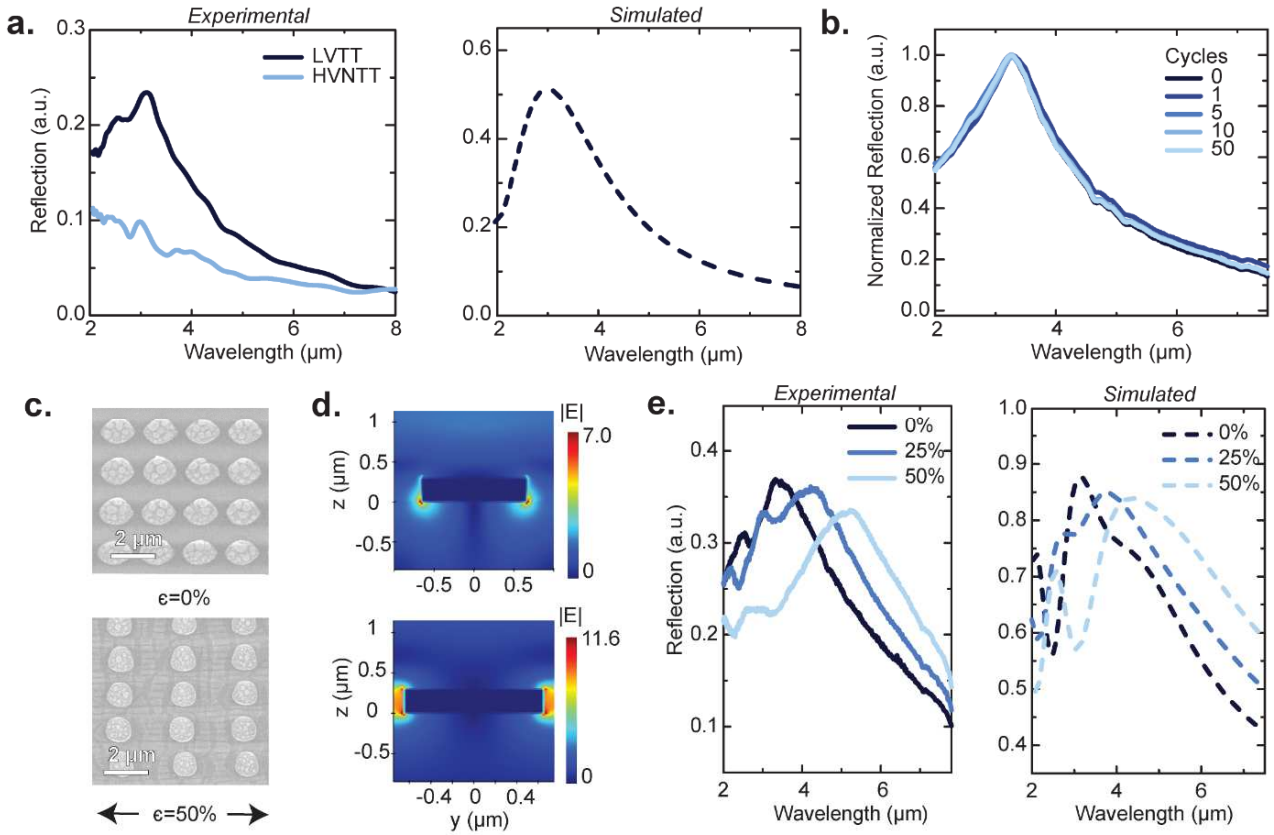
Figure 6.6 – All-soft photonic crystals using controlled oxidation of liquid metals. (a) (left) Experimental and (right) simulated reflection spectra for non-encapsulated 2 μm period square photonic crystals with 1.2 μm diameter particles made with (LVTT) and without (HVNTT) the process described in this work, using respectively PDMS 10:1 substrate (LVTT) and PDMS 12:1 substrate (HVNTT). (b) Reflection spectra of the same photonic crystal after stretching at 50% strain for an increasing number of cycles. (c) Scanning electron microscopy image showing the 1.2 μm size structure at 50% strain. (d) Cross-sectional electric field profile distribution at 0% and 50% strain in the 1.2 μm diameter particle array with 2 μm period. (e) Experimental (left) and simulated (right) reflection spectra for 2 μm period square photonic crystals with 1.5 μm meta-atom size at various strains using light polarized perpendicular to the tensile axis.

We further focus exclusively on LVTT photonic crystals. Under strain, LVTT photonic crystals show stable optical response over 50 cycles at 50% strain amplitude (Figure 6.6(b)). All stretching experiments are done in a controlled temperature atmosphere where T~50°C, ensuring that the Gallium remains in its liquid state. Interestingly, the particles barely deform at 50% elongation, where most of the strain is accommodated by the PDMS (Figure 6.6(c)). The high adhesion energy[235] associated to the liquid metal oxide layer disfavors rupture of the oxide layer in place. Simulating cross-sectional electric field profile distribution at 0% and 50% strain in this same array reveals a strong increase in electric field enhancement (Figure 6.6(d)). We further show using a 2 μm periodic array with a slightly increased particle size of 1.5 μm that the reflection peak associated to the resonance can be shifted reversibly from 3.5 μm to 5.3 μm (Figure 6.6(e)). Further work to reduce the pattern resolution and hence access the telecom bandwidth around 1550 nm could open up a host of technologically relevant applications for such active devices.

Chapter 7   On the role of order in conductive stretchable materials

7.1   Introduction to conductive stretchable systems

In the previous chapters, we have largely turned our focus on the role of nano and micro-structures for photonic applications based on the concept of transformation optics. When the considered structures were sub-wavelength in nature, optical properties could be viewed as arising from an "effective" medium, which is the basis of the metamaterial approach. In this section, we turn our attention away from transformation optics, but we leverage our previous findings based on effective media and micro-texturing approaches to develop effective media with tailored electrical properties instead of photonic properties. More specifically, we investigate the possibility to tune electro-mechanical reponse in various systems under elongation based on periodic elements with distinct conductivity from their substrate. As discussed in Section 1.2.2, microstructure may gives rise to peculiar behavior in stretchable electronic systems. In the frame of Chapter 5, we have actually already encountered counter-intuitive electro-mechanical responses. In particular, Figure 6.4(a) showed multiple instances where the resistance response is nearly insensitive to strain. Not only was this response insensitive to strain, but it also appeared sensitive to the encapsulation layer, whose presence modified the electromechanical response. The initial aim of the present chapter was simply to account for these unexpected behaviors. As a corresponding model was developed, interesting perspectives arised in fully ordered systems. This motivated a more thorough study, which is the object of the present chapter.

We propose here a new methodology introducing periodic arrays in stretchable conductive systems to engineer pre-defined resistance-strain relationships. We first develop a code to accurately calculate the resistance of an NxN grid of 2D resistors with two distinct conductivities. Using this model, we show that the effective medium approach is inappropriate for dense periodic arrays in stretchable conductive systems. We then demonstrate how, by fine-tuning the periodic arrangement and the choice of materials, one can design resistance-strain relationships with completely tunable Gauge factor from positive to negative passing through zero, which has particularly interesting implications for stable stretchable interconnects. To limit computing cost, we further introduce the concept of shortest resistive path to understand the evolution of resistance during elongation. Given an initial set of microstructures and materials, this approach allows in particular to provide at reduced cost the best combination of materials and microstructure to achieve a targeted response. Using an optimization algorithm, we identify by simulation the best microstructures to provide a constant resistance over extensions up to 50%. We further experimentally demonstrate such microstructures (deviation <3%) using a single micro-textured conductive stretchable material. By integrating three distinct set of materials, we discuss the possibility to deviate from purely linear responses and demonstrate counterintuitive sinusoidal resistance-strain responses, which could find interesting applications in sensing and soft robotics. Finally, we address the initial aim of this study by demonstrating that this simulation framework also offers a qualitative understanding of the semi-ordered thin liquid metal films presented in Chapter 5.6.

7.2   Breakdown of effective medium approach in bi-conductive architectures

Continuum mechanics provides a well-established framework linking resistance of a homogeneous material with deformation through the Gauge Factor G[247]:

$$G = \frac{\Delta R / R_0}{\Delta L / L_0} = 1 + 2\nu + \frac{\Delta \rho / \rho_0}{\varepsilon} \qquad (7.1)$$

Where ν is the Poisson ratio ε is the strain, ρ_0 the initial material resistivity, $\Delta \rho$ the material relative change in resistivity. The first contribution to the Gauge Factor, also known as the geometrical contribution $(1 + 2\nu)$, is fixed by the material's properties. Although the Poisson ratio can vary largely between materials, common elastomeric materials required for large reversible deformations are typically incompressible $(\nu \sim 0.5)$[248], limiting the tunability of the geometrical term. The second contribution $(\frac{\Delta \rho / \rho_0}{\varepsilon})$ accounts for piezoresistive effects, and can become dominant in some materials (as high as 200 in p-type [110] single crystalline silicon[249, 250]). This term is also strongly dependent on the choice of materials, and usually occurs in systems that cannot sustain reversibly large deformations.[249,251,252]

The approach detailed above is commonly used for materials that can be considered homogeneous. Let us now consider a composite that blends two different materials (called materials A and B). This material is hence heterogeneous, typically with small inclusions of material A dispersed within a matrix of material B. To assess the resistance of such a material under deformation, one could resort to the previous homogeneous framework by considering the effective resistance of the composite R_{eff}, i.e. the resistance of each material pondered by their respective share of the total composite volume:

$$R_{eff}(\varepsilon) = X_A R_A(\varepsilon) + X_B R_B(\varepsilon) \qquad (7.2)$$

Where X_A and X_B are the volume fractions of materials A and B respectively, R_A and R_B are the resistance associated to materials A and B. The effective medium approach is however no longer appropriate when the small inclusions of materials increase in size and the system approaches the percolation threshold. To assess the accurate resistance (called equivalent resistance R_{eq} in the rest of this work) in 2D composites, we develop a model which evaluates the resistance of a random 2D resistor network made of two distinct types of resistors (total size N x N). Kirchoff's rule states that, for every
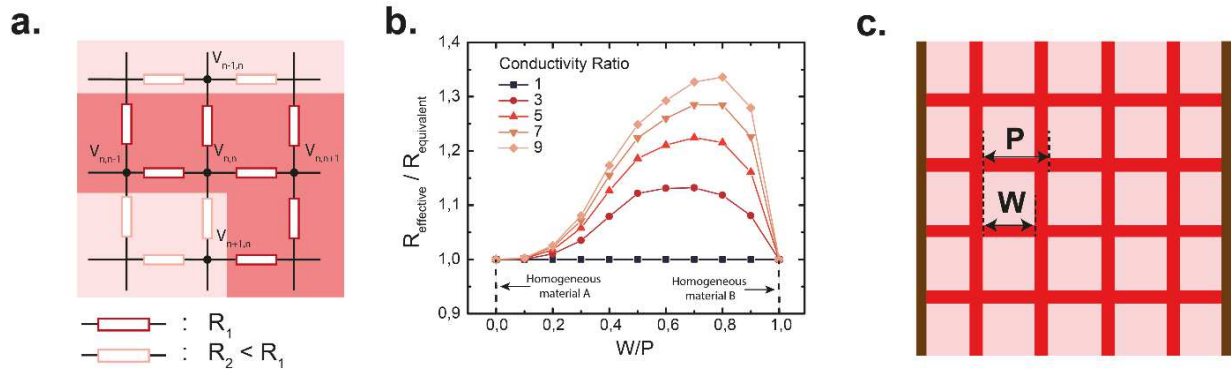
Figure 7.1 – Breakdown of effective medium approach near percolation threshold in bi-conductive materials. (a) Schematic illustrating the 2D resistor network approach to model a bi-conductive material. The network is composed of resistors R_1 and $R_2 < R_1$ (b) Ratio of effective resistance (effective medium theory) over the equivalent resistance (exact value of network using matrix inversion method) versus the fill ratio W/P. (c) Schematic of the bi-conductive structure, indicating the values of W (particle width) and P (period). The brown lines on the edges of the sample indicate the contacts for resistance measurement.

site between four resistors, the sum of the currents is zero, defining a solvable linear set of N^2-1 equations. By injecting

and extracting a known current at predefined locations, the resistance of the network between these two points can be evaluated. Given a fixed microstructure, the 2D resistor network hence allows one to calculate the accurate resistance-strain relationship for arbitrarily complex grids of reasonable size using direct matrix inversion method (see Figure 7.1(a)). We define material A as the background low conductivity material (in dark red) and material B as the isolated squares of high conductivity (in light red).

To evaluate the deviation of R_{eff} with regards to R_{eq}, we now consider a heterogeneous film microstructure composed of a periodic square array of material A with conductivity σ_A onto a substrate of material B with a conductivity σ_B (see Figure 7.1 (b) -(c)), without any elongation at this point. The square width W is gradually increased while the period P is kept fixed. Contacts of infinite conductivity are applied on the two edges of the network to calculate the equivalent resistance R_{eq}. For a fixed conductivity ratio $\gamma = \frac{\sigma_A}{\sigma_B} > 1$, an increase in the ratio W/P leads to a stronger deviation between effective resistance R_{eff} and actual resistance R_{eq} until W/P = 0.8, where a maximum is reached (see Figure 7.1 (b)). Keeping a fixed ratio W/P = 0.8, an increase in the conductivity ratio from 1 to 9 amplifies the deviation between R_{eff} and R_{eq} up to 35%. This deviation highlights the inadequacy of the effective medium approach in composite systems near percolation. For the rest of this work, we focus on direct evaluation of equivalent resistance to accurately determine the resistance of 2D resistor networks. We also neglect any piezo-resistive behavior for both materials given the strains involved.

7.3   Influence of conductivity ratio on electro-mechanical behavior

Next, using the introduced model, we study the resistance evolution of the 2D composite under tensile deformation. We first focus on the resistance-strain relationship parallel to the tensile axis. For the periodic square array shown in Figure 7.2(a)(i), an increase in conductivity ratio essentially induces negligible change in the resistance-strain curve.
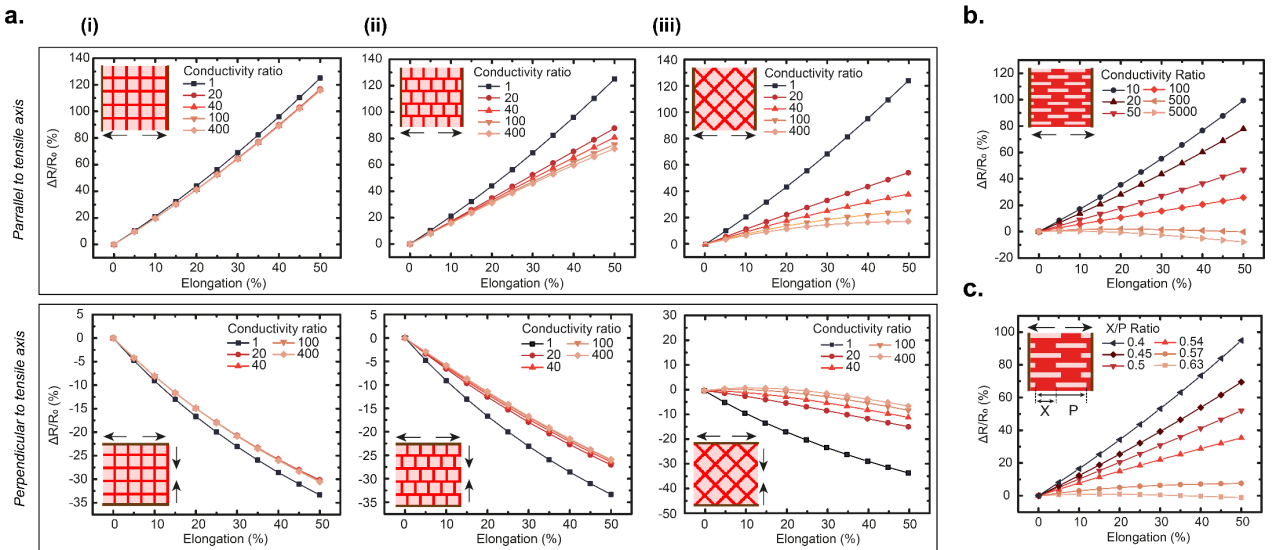
Figure 7.2 – Influence of structure on electro-mechanical response. (a)-(c) Relative resistance change as a function of strain for the respective bi-conductive structures shown in inset using direct calculation method. The deformation directions is indicated by arrows, and the contacts by brown lines. (a) Investigation of three distinct structures with an identical highly conductive square element: (i) regular square array, (ii) shifted square array and (iii) rotated square array. The light red (resp. dark red) in the inset schematic denotes the high (resp. low) conductivity regions. Top figures correspond to stretching parallel to tensile strain, while bottom figures correspond to the associated compression perpendicular to the elongation axis. (b) Electromechanical response of periodic line array with an increase in conductivity ratio γ from 5 to 5000 (c) Electromechanical response of a periodic line array with a change in microstructure (variation in spacing X between periodic lines). Lines are of fixed length and width, and conductivity ratio is set at 500.

Adapting the structure with particular order can change this behavior in counterintuitive ways. By introducing a shift in the structure (Figure 7.2(b)-(c)) along the elongation direction, the observed response deviates from the linearly increasing resistance-strain relationship with an increase in conductivity ratio. Interestingly, this behavior is not present when the periodic shift is introduced perpendicular to the elongation direction. This evolution of resistance can be understood through a simple compromise. As the sample is deformed, high conductivity regions become more separated along the tensile axis, creating more resistive current pathways. This effect is counterbalanced by the compression perpendicular to the stretching direction, which creates additional conductive current pathways (see Figure 7.3(a) for a detailed illustration). The interplay between these two competing phenomena define the actual global resistance change parallel to the tensile axis. Meanwhile, the resistance perpendicular to the tensile direction is exclusively driven by the reduction in distance transversally between high conductivity region, accounting for the continuous decrease in resistance. Varying the conductivity ratio can allow for Gauge factors switching at will from negative to positive passing through zero for linear arrays (Figure 7.2(b)-(c)). We hence identify a particular set of structures whose resistance is insensitive to strain under extended elongation. This is a particularly relevant point for stable yet stretchable electrical interconnects that can provide constant current (deviation < 5%) to interfacing chips within a stretchable matrix.

7.4   Resistance, strain and microstructure: the reverse problem

The reverse problem, i.e. determining the proper combination of materials and microstructures to yield a desired resistance-strain response, is a relevant technological problem that requires a link between microstructural parameters, strain and resistivity. Given a library of materials and microstructures (discretized in a mesh of size NxN), a first brute
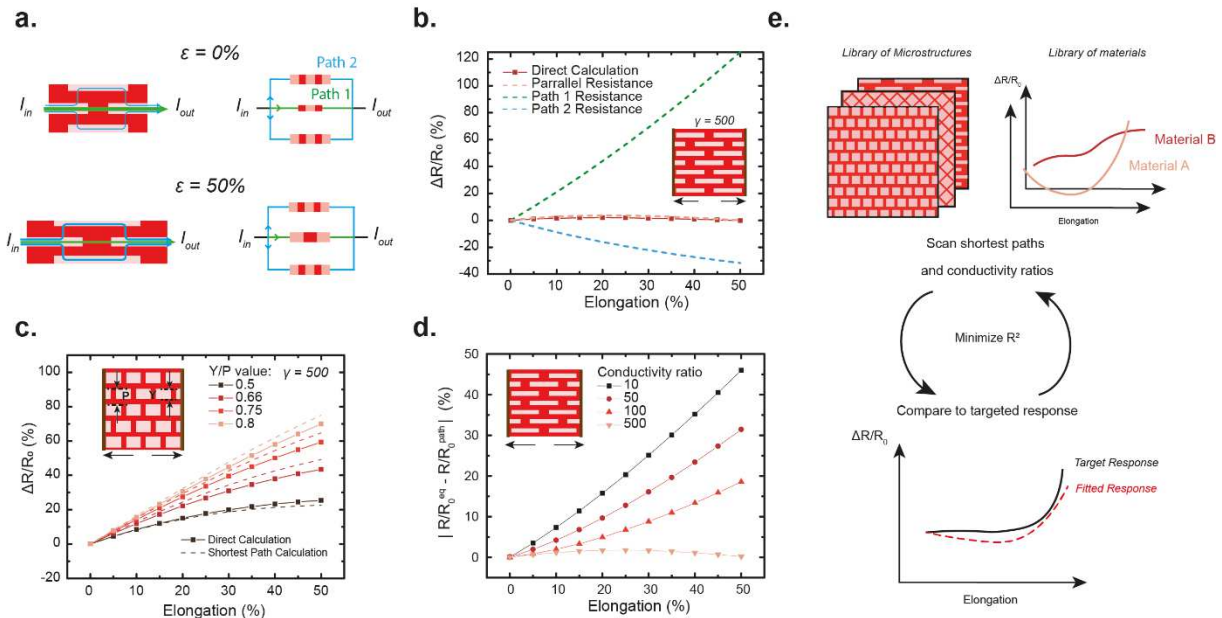
Figure 7.3 – Shortest path method and perspectives. (a) Schematic illustrating the different shortest paths (green and blue arrows) preferentially taken by the current under 0% and 50% elongation. (b) Calculation of resistance-strain relationship by direct calculation for the whole assembly (red dotted line) and by shortest path method at 0% strain and 50% strain (respectively green and blue dotted lines). Combining shortest path at 0% and 50% strain as a set of parallel resistor (light red dotted line) provides a good agreement with the direct calculation. All calculations are done with a fixed conductivity ratio of 500. (c) Variation of the width Y between periodic lines of fixed length and spacing. The conductivity ratio is fixed to 500. Dotted lines indicate the results obtained through shortest path method. (d) Difference between relative resistance obtained through direct calculation and shortest path method for the structure shown in inset, with a conductivity ratio increased from 10 to 500. (e) Schematic illustrating the working principle of the reverse problem: starting from an initial library of microstructures (shortest paths) and materials (resistance-strain relationship for the homogeneous material), a resulting response (labeled "fitted response" on the bottom graph) for a microstructure combining two distinct materials can be determined at low computational cost. Scanning through the possible combinations of materials and microstructure, we minimize the deviation between fitted and target response using the determination coefficient R^2.

force approach could consist in scanning through the various combinations of the library elements using the direct resistance calculation method detailed above. This approach may however prove computationally expensive: assuming Gauss-Jordan elimination, this yields a complexity in $O(N^6)$ associated to matrix inversion. An alternative approach consists in simplifying the 2D resistor model into a reduced set of privileged resistor paths, corresponding to the shortest resistive paths for the current. A particular advantage of the present system is that, thanks to periodicity, the shortest path analysis can be done on matrices of reduced size.

Let us now consider a microstructure where all the electrical current flows through a reduced set of shortest paths (see Figure 7.3(a)-(b)). Using Yen's shortest path algorithm[253], we can associate a cost to each shortest path, which helps discriminate which paths contribute most to current flow. In the particular case of the structure shown in Figure 7.3(a)-(b), two Paths (named Path 1 and Path 2), minimize the resistance to current at 0% strain. Additional shortest paths all show costs superior by a factor of at least 2, and are therefore further neglected. Paths 1 and 2 determined by Yen's algorithm include: (i) a first shortest path set (named Path 1, in green), made of the straight lines connecting the two contacts through the regions of lowest conductivity; (ii) a second shortest path set (named Path 2, in blue), made of the paths connecting transversally consecutives lowest conductivity regions. We now make the assumption that each path acts as a closed channel for current: current can only flow in or out at the extremities, i.e. the contacts. In this case, an equivalent resistance associated to each path $R_{Path\,1}$ (resp. $R_{Path\,2}$) can be evaluated by treating all consecutive resistor elements as a series assembly. By distinguishing elementary pathways situated parallel (//) or perpendicular ($\perp$) to the applied strain, a direct link between microstructural parameters and strain appears:

$$R_{Path\,j} = \sum_{Path\,j} R_i \tag{7.3}$$

$$R_{Path\,j} = \sum_{\substack{i\,\epsilon\,Path\,j \\ i\,\epsilon\,\perp}} f_i^{\perp}(\rho_i, L_0, S_0, \varepsilon, \nu, G_i^{\perp}) + \sum_{\substack{i\,\epsilon\,Path\,j \\ i\,\epsilon\,//}} f_i^{//}(\rho_i, L_0, S_0, \varepsilon, \nu, G_i^{//}) \tag{7.4}$$

Where ρ_i represents the resistivity of the i-th element of Path j, L_0 its length along the current direction without deformation, S_0 its cross section perpendicular to the current direction without deformation, ε the deformation along the tensile deformation axis, and ν the associated Poisson Ratio. $f_i^{//}$ (resp. $f_i^{\perp}$) represents the i-th elementary resistance along the shortest path parallel (resp. perpendicular) to the applied strain, and $G_i^{//} = L^{//}/W^{//}$ (resp. $G_i^{\perp} = L^{\perp}/W^{\perp}$) is a geometrical factor to take into account the actual width W and length L of the shortest path along the direction parallel (resp. perpendicular) to the tensile deformation. In the particular case of a homogeneous isotropic conductive material such as liquid metal, $f_{\perp}$ and $f_{//}$ can be explicitly expressed: $f_i^{\perp} = G_i^{\perp}.\frac{\rho_i L_0}{S_0}.(1+\varepsilon)^{1+2\nu}$ and $f_i^{//} = G_i^{//}.\frac{\rho_i L_0}{S_0}.(1+\varepsilon)^{-1}$. The range of Poisson ratio accessible using conductive elastomers defines a set of function $(f_i^{\perp}, f_i^{//})$ whose linear combination defines the full space of resistance-strain relationship attainable. The homogeneous isotropic criterion is however not validated for a number of stretchable composites, such as those based on carbon nanotubes or silver nanowires, which lead to more complex resistance-strain relationships. This indicates that the dimensionality of the resistance-strain behavior space group could be further extended, a point that is further discussed in Figure 7.4.

Using relation (7.3), we proceed to evaluate the path resistance associated to the two shortest paths of the line array microstructure shown in Figure 7.3(a)-(b).These two individual resistive paths let through a different amount of current, which varies with elongation. Without elongation, both contribute at the same level to the overall sample resistance (same cost in Yen's shortest path algorithm). When stretched, the resistance associated to the second shortest

path set is largely reduced, whereas the resistance associated to the first shortest path increases (see Figure 7.3(a), top left and bottom left). To take into account the contribution of both path sets to the total resistive behavior, each path is considered as a resistor assembled in parallel between the two contacts, with respective resistance $R_{Path\,1}$ and $R_{Path\,2}$, yielding the equivalent resistance R_{eq}:

$$R_{S.P} = \left(\sum_{j=1}^{K} R_{Path\,j}^{-1} \right)^{-1} \tag{7.5}$$

$$R_{S.P} = \left(\sum_{j=1}^{K} \left(\sum_{\substack{i\,\epsilon\,Path\,j \\ i\,\epsilon\,//}} f_i^{//}(\rho_i, L_0, S_0, \varepsilon, \nu, G_i^{//}) + \sum_{\substack{i\,\epsilon\,Path\,j \\ i\,\epsilon\,\perp}} f_i^{\perp}(\rho_i, L_0, S_0, \varepsilon, \nu, G_i^{\perp}) \right)^{-1} \right)^{-1} \tag{7.6}$$

Considering a solely isotropic homogenous conductive media, this yields:

$$R_{eq} = \left(\left(\sum_{\substack{i\,\epsilon\,Path\,1 \\ i\,\epsilon\,\perp}} G_{i,\perp}.\frac{\rho_i\,L_0}{S_0}.(1+\varepsilon)^{-1} + \sum_{\substack{i\,\epsilon\,Path\,2 \\ i\,\epsilon\,//}} G_{i,//}.\frac{\rho_i\,L_0}{S_0}.(1+\varepsilon)^{1+2\nu} \right)^{-1} \\ + \left(\sum_{\substack{i\,\epsilon\,Path\,1 \\ i\,\epsilon\,\perp}} G_{i,\perp}.\frac{\rho_i\,L_0}{S_0}.(1+\varepsilon)^{-1} + \sum_{\substack{i\,\epsilon\,Path\,2 \\ i\,\epsilon\,//}} G_{i,//}.\frac{\rho_i\,L_0}{S_0}.(1+\varepsilon)^{1+2\nu} \right)^{-1} \right)^{-1} \tag{7.7}$$

Figure 7.3(b)-(d) compare the relative equivalent resistance obtained by shortest path method and by the direct matrix inversion method. In Figure 7.3(b), we compare the resistance-strain relationship from direct calculation (full red line) and by the shortest path method considering (i) the first shortest path (green dotted line, single path), (ii) the second shortest path (blue dotted line set, single path) and (iii) the parallel assembly of the first and second shortest path (red dotted line) set based on the combination of a single path of type 1 with a single path of type 2. The good match between both methods in predicting the overall resistance-strain curve highlights the validity of the shortest path approach. In Figure 7.3(c), we show that the shortest path method can account properly for a changing set of structures. The predictions provided by the shortest path method are however validated for sufficiently high conductivity ratios (Figure 7.3(d)). This is directly related to the closed channel assumption. As highlighted in Figure 7.3 (b)-(d), this approach provides a reasonable estimation of resistance-strain relationship for a broad range of periodic structures. For structures where the shortest path at 0% and 50% strain zare identical, the reasoning can more simply be limited to a combination of shortest paths at 0% strain.

In Figure 7.3 (e), we detail the working principle of the reverse problem algorithm, which determines which set of microstructure and materials can yield a desired resistance strain-relationship (labeled "target response" on the bottom graph). Given an initial library of microstructures (each with a set of associated shortest paths) and materials (resistance-strain relationship for the homogeneous material), a set of resulting responses (labeled "fitted response" on the bottom graph) can be determined for each microstructure combining two distinct materials at low computational cost (worst case complexity in $O(N^2)$, where N x N is the microstructure size) . Relying on the direct calculation method would quickly prove expensive given the $O(N^6)$ complexity of the N^2-1 x N^2-1 matrix inversion method. Scanning through the possible combinations of materials and microstructure, we minimize the deviation between fitted and target response using the determination coefficient R^2. The accuracy of the method can further be refined using direct resistance calculation if

necessary, once the shortest path approach has narrowed down the search of potential candidates. The match between fitted and target response is largely determined by the degree of freedom provided by the input materials and microstructures. In this work, we show that linear target responses can be accurately fitted using solely materials with a classic linear Gauge factor of 2. However, one could also envision fitting non-linear responses, provided that the materials library be expanded to include for instance near-percolation materials such as carbon nanotubes or silver nanowire networks.

Using this same category of materials and all the microstructures presented from Figure 7.2 to Figure 7.4, we apply this selection algorithm to identify the combination providing the most constant resistance-strain response, imposing a conductivity ratio in the range 1 to 5000. The results indicate that all linear arrays (e.g. microstructures shown in Figure 7.2 (b), (c), Figure 7.3(b), (d), Figure 7.4 (b), (d)) are potentially suitable candidates, while eliminating other microstructures. Focusing now on the microstructure used in Figure 7.3(b)-(d), the reverse problem algorithm (shortest path pre-selection followed by direct calculation refinement) converges towards a constant resistance response with strain for an optimal conductivity ratio $\gamma=208$ using solely shortest path pre-selection, and further converges to $\gamma=510$ using the direct calculation refinement method. The following section deals with the experimental implementation of a constant resistance response based on this set of parameters (microstructure and conductivity ratio).

7.5   Experimental validation and perspectives

The study has thus far focused on periodic surfaces using two different conductivities. This can straightforwardly be achieved using two materials with distinct electrical properties. This is particularly interesting given the wealth of resistance-strain relationships available for different families of stretchable conductive materials. An alternative consists in using a single stretchable conductive material but with engineered modulations in thickness, which can be equivalently seen as a system with two distinct conductivities and one identical thickness. Such a system presents two advantages: (i) it allows to validate the reverse engineering approach proposed above and (ii) it demonstrates how simple the experimental implementation can be. We proceeded by coating Eutectic Gallium-Indium (E-GaIn) alloy onto a textured Poly-dime-thylsiloxane (PDMS) substrate. The textured PDMS is coated with a thin (60 nm) interfacial layer of Gold to allow for proper wetting of E-GaIn[232] By successive adsorption, the thickness of the zone between pits, labeled t_1, can be tailored, while the film thickness within the pits, labeled t_2, can be in first approximation considered constant. Gradually reducing the value of t_1 (or equivalently gradually increasing the conductivity ratio γ) gives rises to the wide range of resistance-deformation curves (see Figure 7.4(c)-(d)). Using direct resistance calculations, a fitted conductivity ratio γ_{fit} can be associated to each thickness t_1. We now turn to the relative evolution of the initial resistance at 0% strain (labeled R_0) associated to the various conductivity ratios ($\gamma_{fit}= 120, 475,$ and 1300), using (i) the experimentally measured R_0 and (ii) the resistance obtained through direct calculations. To facilitate comparison, results are normalized with respect to R_0 ($\gamma=120$), as shown in Figure 7.4(c). The change in the initial resistance follows a similar trend between experimental and calculated data. This good overlap between experimental and simulated data highlights the validity of the proposed model. Besides from the semi-ordered structures demonstrated in Chapter 6, this constant resistance behavior has never been demonstrated to our knowledge at extended deformations (>~30%), and moreover with intrinsically stretchable materials. Given the high conductivity of liquid metals compared with other state of the art stretchable composites such as embedded silver nanowire networks,[254] the proposed approach enables the design and fabrication of microstructures with both tailored response and reduced size footprint, a critical point given the increasing miniaturization of integrated systems.
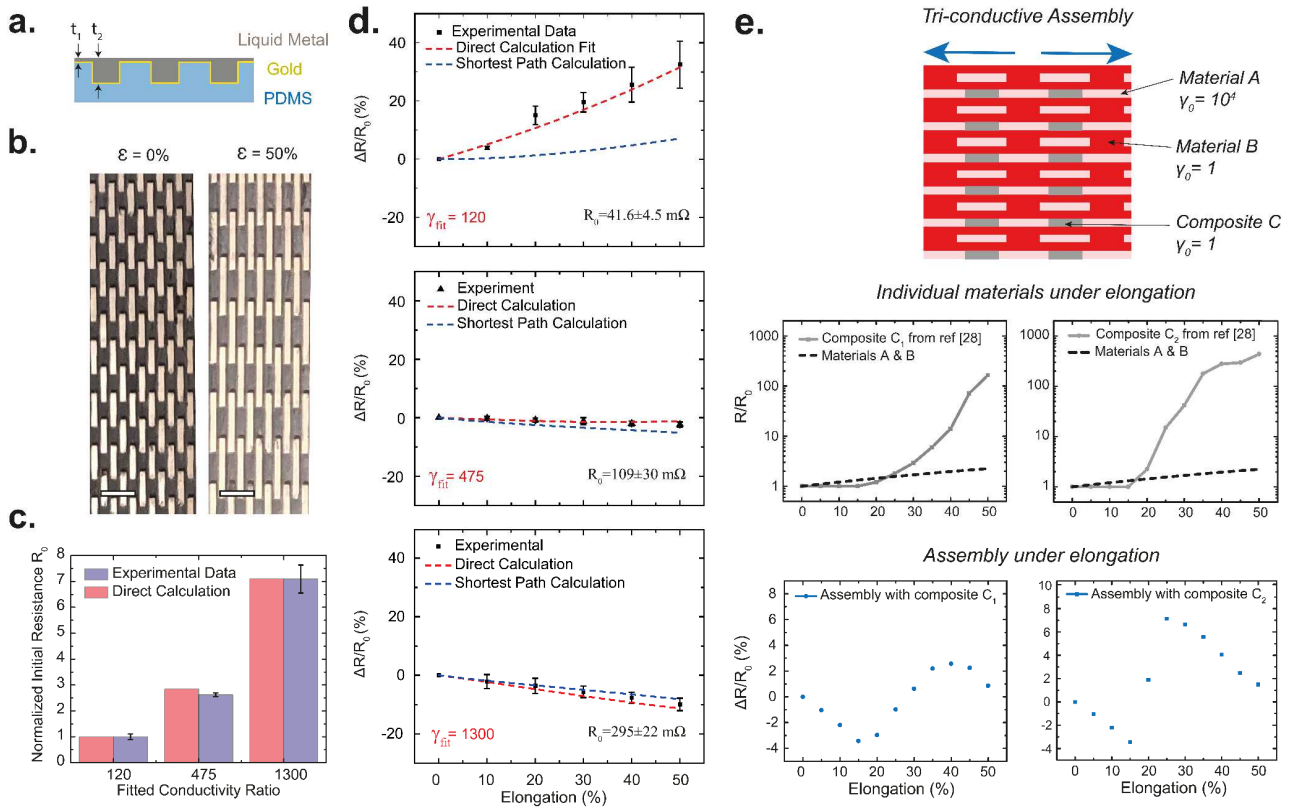
Figure 7.4 – Experimental validation of the model and perspectives. (a) Schematic of the experimental sample implemented. The modulation in thickness defines an equivalent conductivity ratio between the different regions of the sample. (b) Optical Image showing the textured PDMS with liquid metal, seen from the texture side. The scale bar is 400 μm. (c) Relative change in initial resistance for different fitted conductivity ratios γ. The experimental trend observed is in line with predictions from direct calculations. (d) Relative change in resistance with strain for liquid metal films of decreasing thickness t_1 and nearly constant thickness t_2, i.e. increasing conductivity ratio γ. Using direct calculations, a corresponding fitting conductivity ratio $γ_{fit}$ can be associated to each sample. Shortest Path calculations using $γ_{fit}$ allow for proper estimation of the experimental behavior for sufficiently large conductivity ratios. (e) (Top) Schematic of a architecture combining three materials (named A, B, and Composite), with respective (relative) initial conductivities 5000, 1 and 1. (Middle) Representation of the resistance response under strain of the three materials taken individually. The materials A and B follow the traditional Ohm law with a Gauge factor of 2, while the composite material shows a strong increase in resistance typically associated to near-percolation systems. The behavior of composites 1 and 2 is based on reference [257]. (Bottom) Relative change in resistance for the corresponding assembly.

We have shown how, by solely resorting to thickness modulation with a single conductive material, one can engineer tailored conductivity ratios. Combining thickness modulation with materials of distinct conductivities also provides additional design flexibility. If an identical thickness is imposed, the integration of distinct materials would require a precise conductivity ratio that could only be obtained by a careful choice of intrinsic material conductivities. Resorting to thickness modulation offers an additional lever in design, allowing for the integration of materials whose sole intrinsic conductivity ratio may not be sufficient to meet design requirements.

To provide additional degrees of freedom, this concept of controlled electrical response in stretchable systems can be extended to more than two materials. Using near-percolation composites, we show here that resorting to three distinct materials allows for a much wider set of resulting resistance-strain curves, in particular non-bijective relationships. In Figure 7.4(e), we propose a theoretical microstructure using three materials selected from the literature to create a non-bijective response. We select materials A and B that both exhibit a classical linear resistance-strain behavior and a Gauge factor of 2 (Figure 7.4(e)(middle)). Material A is composed of Ag nanowires embedded into a poly-dimethylsiloxane (PDMS) matrix ($γ_{AgNW} \sim 1.8 \times 10^3$ S.cm^{-1}, based on reference 255), while material B is made of carbon black dispersed into a PDMS matrix ($γ_{CB} \sim 1.7 \times 10^{-2}$ S.cm^{-1}, based on reference 256). For the composite C, we select a carbon nanotube/fluoro-elastomer with a double percolated network based on reference 257 ($γ_{C1} \sim 1.4 \times 10^{-2}$ S.cm^{-1} and $γ_{C2} \sim 3.3 \times 10^{-6}$ S.cm^{-1}, see Figure 7.4(e)(middle)). Using an identical thickness for materials A, B and C$_1$ provides approximately the

conductivity ratios given in Figure 7.4(e) (respectively 10^4, 1 and 1). C_2 being much less conductive, the thickness should be largely increased with respect to materials A and B so as to provide the same relative conductivity ratios. By direct matrix inversion using the 2D-resistor network model, we evaluate the evolution of such a microstructure under elongation. Interestingly, the microstructure using composite C_1 shows a nearly sinusoidal response (Figure 7.4(e)(bottom)). Similarly, composite C_2 shows a non-bijective response, but with a sharper transition between positive and negative values. By gradually shifting the composite's percolation threshold in consecutive linear features, one could envision a sinusoid function that would extend beyond a single period. This could open up novel applications for sensing or soft robotics, allowing for a system to come back through a given state with multiple input values simply relying on a material's microstructure.

7.6   On the behavior of semi-ordered thin liquid metal films under elongation

The mechano-responsive mechanism described in this chapter can also be applied to the observations made in Chapter 5.6 with the behavior of thin Gallium films under elongation (240 nm and 400 nm equivalent thickness). The relative resistance with strain appears to deviate less than 3% over an extended deformation of 50% strain. Before looking for a microstructural explanation to this phenomenon, it is important to validate that this is not a measurement artefact. To insure the accuracy of the measurements, the resistance measurement test are done using liquid metals as contacts to avoid mechanically brushing off the thin gallium film when the film is stretched. Morover, the test is implemented with a four point probe measurement to remove the influence of any potential contact resistance. Despite these experimental precautions, the film still exhibits a nearly constant resistance with strain.

Now that the possibility of a measurement artefact is cast aside, how can one account for such a peculiar evolution of resistance with strain? One could reframe the previous model in this particular system. However the microstructure responsible for the actual response, which appears semi-random in this particular case, is much less straightforward. Two main hierarchical microstructures emerge in the thin film case. (i) As apparent in Figure 6.4(b), the film exhibits significant roughness. As was discussed in section 7.4, thickness fluctuations within a single-material film can also equivalently been seen as a structure with identical thickness and distinct conductivity ratios, which constitutes a first potential representation of the film system. (ii) In parrallel, Figure 6.4(b) also clearly shows the emergence of randomly distributed holes in the film microstructure. One could hence also represent this system with two distinct conductivity ratios, namely that of the Gallium (considered homogeneous) and a zero conductivity to account for the holes.

To discriminate which of these two microstructures is responsible for the observed behavior, we investigate the role of the encapsulation layer on response (See Figure 6.4(a)). The encapsulation layer comes in contact with the rough film microstructure, and consequently influences the deformation mode of droplets under elongation. Turning to Figure 7.5(f), it clearly appears that the encapsulation changes the electro-mechanical response in thin films of different thicknesses, which hints towards a predominance of film roughness in overall response, to the deteriment of holes formation. In absence of a PDMS superstrate, liquid metal droplets will be free to deform on the substrate side, and their equilibrium shape will result from a compromise between the liquid metal's high free surface tension and the native solid oxide layer, which exhibits some elasticity. In the presence of a PDMS superstrate, local droplets will deform under the combined influence of the PDMS substrate and superstrate, which will exert a compressive force normal to the film upon elongation. The resulting shape will hence be the result of a complex interplay between a compressive normal stress, an elastic oxide layer, and the liquid metal interfacial tension with PDMS. As an additional element in favor of the rough microstructure,
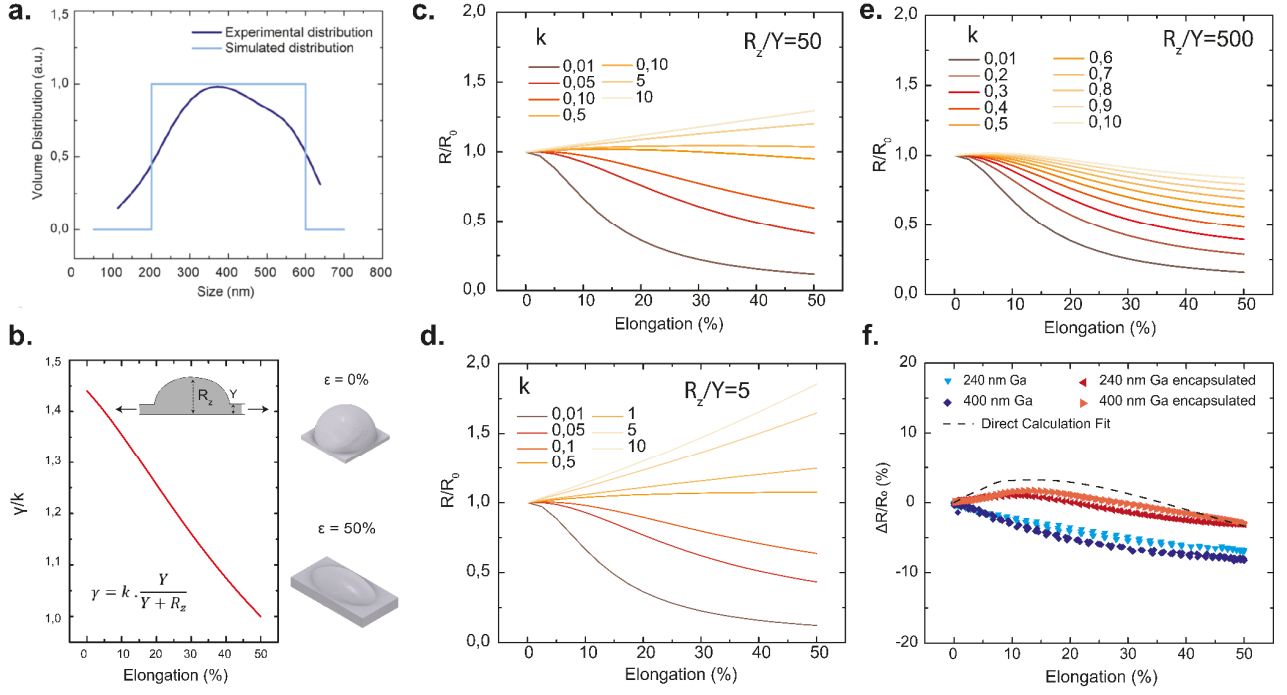
Figure 7.5 – Thin film Electro-Mechanical modelling. (a) (dark blue) Experimental particle size distribution based on AFM images of 240 nm gallium films using watershed thresholding method, (light blue) simulated particle size distribution. (b) (left) Dependence of conductivity ratio ($\gamma_{high}/\gamma_{low}$) as a function of elongation for normaly-distributed particle network corresponding to a fix set of parameters { R_z/Y, k}={50, 0.5}; (right) schematic illustrating the geometry of the droplet at rest and under 50% strain. The conductivity ratio accounts for droplet flattening (pure geometrical contribution) by assuming proportionality between relative resistance increase and geometrical parameters, as indicated in inset. (c)-(e) Normalized resistance vs. strain evolution for a wide-ranging set of parameters {R_z/Y,k}. (f) Fitted relative resistance change for a resistor network with a 50 % surface coverage compared with experimental measurements. Fitting Parameters are {R_z/Y =50, k=0.5}.

simulations reproducing the characteristic distribution of holes within a film under strain were not able to reproduce the experimentally-observed response, contrarily to the rough film structure, as discussed below.

We now investigate the role of roughness on the film's electro-mechanical response. As previously discussed, one can assimilate the rough microstructure to a system with two distinct conductivity ratios: the high conductivity ratio being associated to the droplets and the low conductivity ratio being associated to the inter-droplet regions. This assumes that all droplets are similar in height, which is in first approximation valid for 240 nm liquid metal films (see Figure 6.3(a)-(c)). To account for the change in conductivity ratio with elongation, we make two key assumptions: (i) volume conservation (non-volatile, incompressible materials) and (ii) shape preservation (linked to the encapsulation). We estimate the average characteristic droplet size by statistical analysis on AFM Images of 240 nm Gallium films. (Mean = 457 nm and Standard deviation = 147 nm using Gaussian fit; Surface Coverage = 49% , determined using the watershed thresholding algorithm with Gwyddion Software). We consider, in reasonable agreement with our statistics, a constant particle size distribution ranging from 200 nm to 600 nm with an inter-droplet region of ~200 nm width (see Figure 7.5(a)). The code maximizes particle surface coverage while ensuring no direct electrical contact between any two neighborhooding particles, similarly to Scanning Electron Microscopy observations in Chapter 5. Simulation surface coverage values for such a distribution range from 48% to 52%, which is in good agreement with our experimental statistical analysis above. Volume conservation implies that:

$$V_{0\%} = V_{50\%} \tag{7.8}$$

$$\frac{2\pi R_0{}^3}{3} = (2.R_0)^2.(1+\varepsilon)^{1-\nu}.Y + \frac{2\pi}{3}R_0{}^2.Z.(1+\varepsilon)^{1-\nu} \tag{7.9}$$

$$Y = \frac{\pi}{6}[2.R_0.(1+\varepsilon)^{1-\nu} - Z] \tag{7.10}$$

The surface of the ellipsoid $S_{ellipsoid}$ can be estimated by the Hölder mean of its principal axis (using p = 1.6 yields relative error inferior to 1.2%):

$$S_{ellipse} \approx 2.\pi.\sqrt[p]{\frac{R_0^{2p}(1+\varepsilon)^{p(1-\nu)} + Z^p R_0^p[(1+\varepsilon)^p + (1+\varepsilon)^{-\nu p}]}{2}} \tag{7.11}$$

Considering that the solid oxide layer remains unruptured and the initial structure to be a half-sphere, one can write:

$$S_{ellipse} = 2.\pi.R_0^2 \tag{7.12}$$

Developing the calculations, we find that:

$$Z = R_0 \sqrt[p]{\frac{3 - (1+\varepsilon)^{(1-\nu)p}}{(1+\varepsilon)^p + (1+\varepsilon)^{-\nu p}}} \tag{7.13}$$

Reinjecting (7.13) into (7.10) yields

$$Y = \frac{\pi}{6}\left[(1+\varepsilon)^{1-\nu} - \sqrt[p]{\frac{3 - (1+\varepsilon)^{(1-\nu)p}}{(1+\varepsilon)^p + (1+\varepsilon)^{-\nu p}}}\right] \tag{7.14}$$

We now assume that the evolution of the conductivity ratio γ in the 2D resistor network model is directly proportional to ratio of the maximal over the minimal height within the modeled structure:

$$\gamma = k \cdot \frac{Y}{Y + R_z} \tag{7.15}$$

This assumption is based on the same scaling argument used in Section 7.5, which considers thickness and conductivity ratio equivalent. The evolution in the ratio R_z/Y is supported by scanning electron microscope analysis as discussed in Chapter 6 and profilometry measurements[258], which show that droplets clearly flatten under strain in the absence of encapsulation. Heat dissipation measurements[258] in similar gallium films have also demonstrated homogeneous emissivity pattern in stretched films, which represents further proof of droplet flattening. Encapsulation ensures the link between all geometrical parameters under the assumption of incompressibility. Without encapsulation, the straightforward link previously obtained in Equation (7.14), which was obtained assuming shape preservation, is no longer valid. Using the model discussed above, we determine an optimal fit between experimental and simulated data for fitting parameters {k=50, $R_z/Y=0.5$} (see Figure 7.5(b)).

To conclude on the electromechanical modelling of thin liquid metal films studied in Chapter 6, we have been able to understand from a qualitative perspective the origin of the negative gauge factor under elongation, and in particular link the electromechanical with the intrinsic thin film microstructure. A certain number of hypotheses have been made to demonstrate this link (namely volume and shape preservation, as well as proportionality between conductivity ratio and relative height change). The ambition of this analysis is therefore essentially explicative, demonstrating that microstructure can give rise to peculiar electrical properties in semi-ordered systems as well, broadening the scope of the present study.

Chapter 8   Conclusion

8.1   Achieved results

This thesis work has focused on novel fabrication processes mainly for photonic applications, drawing some fundamentally new perspectives on the combination between photonics and fluid mechanics. This thesis has led to a number of key results on several fronts:

- We have developed novel insights into amorphous thin film instabilities on a template substrate, both from a qualitative, linear perspective and a quantitative, non-linear perspective. These models have established a novel framework to accurately predict thin film flows with arbitrary template geometries spanning several length scales, multiple features that were not possible with previously existing models.

- Capitalizing on the understanding accumulated in fluid mechanics and associated re-arrangement mechanisms, this thesis work paved the way for the development of a process taking advantage of fluid instabilities in thin chalcogenide films to fabricate passive metasurfaces in a scalable fashion. While the dewetting process is not in itself a discovery, the use of high index amorphous materials as well as the understanding in the process dynamics have pushed further the realm of possiblilities, achieving final architectures with unprecedented complexity and increased functionality. These findings address the key fabrication challenge faced today by optical metasurfaces, which rely heavily on costly high-end nanofabrication techniques to achieve required resolution and repeatability criteria. As such, the proposed method offers novel industrial perspectives to a field of study that has remained thus far largely limited to laboratory demonstrations.

- Relying on the previous fabrication process, multiple advanced photonic meta-devices have been demonstrated in the visible or near infrared, with several important and technologically relevant applications. A first important axis of research has focused on the potential of such a process for meta-lenses based on quasi-3D architectures for wavefront control. Using pure 2D architectures, we further demonstrated the possibility to control scattering properties with high efficiency, with specular reflections reaching 96% of the incident signal. A second axis of research has investigated high Q.F. metasurfaces for application in enhanced second harmonic generation. Careful engineering of interference between Mie and lattice modes has also enabled the demonstration of several efficient architectures for bio-sensing, adapted for layers spanning a large thickness range and broad refractive index values.

- Inspired by the intial work on thin film instabilities with free interfaces, we developed an entirely novel fabrication scheme to produce highly ordered 2D nanowire arrays with unprecedented control over final geometry. Starting from a high index film of modulated thickness placed inside a polymer matrix, we show in particular the ability to decouple nanowire radius to the period ratio, allowing to go beyond the previous constraints imposed by Rayleigh-type instabilities. The development of a multi-scale non-linear model taking into account the evolution of both short and long wavelength perturbations during thermal drawing has been instrumental to understand the process and identify the range of achievable architecture for a given set of initial paramters.

- This thesis work further investigated some of the challenges faced by active metamaterials, and more specifically mechanically-actuated metasurfaces. Relying on controlled oxidation dynamics during thermal evaporation, a process to obtain percolated thin liquid metal films has been demonstrated. The rationale behind the process, based on a tailored competition between dewetting and oxidation, has been thoroughly explained. Using this framework, mechanically-actuated liquid metal photonic crystals have been demonstrated, exhibiting a reflection peak with tunable position from 3.5 μm at 0% elongation to 5.3 μm at 50% elongation.

- Capitalizing on the findings on liquid metal thin film stability and texturing in optical micro- and nano-systems, this thesis work made some serendipitous discoveries with far-reaching implications in the behavior of stretchable electrical materials. The combined simulations and experimental framework developed offers a very general understanding of yet misunderstood stretchable electrical systems with peculiar electromechanical behavior, and opens up several important opportunities in the field of soft robotics.

8.2 Future developments

This thesis work has traced multiple new perspectives that call for futher investigations on several points:

- Lack of film continuity at reduced thicknesses is one of the key limiting aspects in terms of resolution for in-air template instabilities. Even when the film is fully percolated, the presence of undesirable dewetting holes upon evaporation represent defect sites that commonly induce disorder in the final structure, particularly for chalcogenides with low glass transition temperature such as selenium. Therefore, future efforts to improve the conformity of chalcogenide films upon deposition would greatly help expand the possibilities of this process.

- The recent understanding developed around stability of linear dewetted features and suppression of Rayleigh-type instabilities are the key to further deployement of dewetting for manufacturing of metasurface based on thin film dewetting, which calls for follow-up work.

- Further investigations quantifying the influence of soft substrates (which strongly influences wetting properties) on dewetting would be of high interest from both a scientific and an applicative perspective.

- The proof-of-concept demonstration of engineered wicking bears great potential to achieve arbitrary structures, which are extensively used for metasurfaces. The demonstration of a well-established metasurface architecture and validation of its optical characteristics would be the ideal next step to validate the use of this process.

- Futher efforts to decrease the computational cost of the dewetting simulation could be instrumental to develop an end-to-end design scheme combining fluid mechanics and optical simulation platforms. This would help establish dewetting as a viable alternative to existing processes, providing the research community with the required design tools.

- Regarding in-fiber templated instabilities, the proposed model could be further improved by including retardation effects. Further investigations into the exact role played by shearing as well as an accurate characterization of interfacial tension could help shed light on the difficulty to induce break up by simulation.

- The results from liquid metal offer interesting insights into the potential stability of such films on elastomeric substrates. The limited deformation of liquid metals under elongation however calls for new studies to evaluate the precise cause for this behavior, and discriminate whether this is simply the consequence of the material's high surface tension or stems from other physical phenomena.

Appendix A – Determination of physical parameters during thermal drawing

In this section, we develop analytically the velocity, temperature and viscosity profile within a fiber undergoing thermal drawing. The proposed treatment of the problem is adapted from several previous works on the topic.[181,259,260,261,262] We introduce the initial ("feeding") speed v_0, and a final speed $v_f = D^2 . v_0$, with D the draw down ratio. We further introduce the fiber radius $R(z)$ at a fixed point z varying from 0 to L. The material has a density ρ, a heat capacity c_p, a thermal conductivity k, a heat transfer coefficient h, and a viscosity η.

As discussed in Chapter 1, the continuity equation describing the flow, with a density assumed constant with time (e.g. incompressible), is:

$$\text{div } \boldsymbol{v} = 0 \tag{A.1}$$

The steady-state flow is considered, neglecting inertia, gravity and surface tension, therefore the Navier-Stokes equation can be simplified:

$$\boldsymbol{\nabla} . (\eta(\boldsymbol{\nabla} V + (\boldsymbol{\nabla} V)^{\mathrm{T}}) - p\boldsymbol{I}) = \boldsymbol{\nabla} . \boldsymbol{\sigma} = \boldsymbol{0} \tag{A.2}$$

Where $\boldsymbol{\sigma}$ represents the stress tensor. At the fiber surface $(r = R(z))$, there is no stress normal to the surface:

$$\boldsymbol{n} \cdot \boldsymbol{\sigma}(R, z) = \boldsymbol{0} \tag{A.3}$$

where $\boldsymbol{n} = \frac{e_r - R' e_z}{\sqrt{1 + R'^2}}$ is the vector normal to the fiber surface. Developing this condition provides:

$$\sigma_{rr}(R) = R' \sigma_{rz}(R) \tag{A.4}$$

$$\sigma_{rz}(R) = R' \sigma_{zz}(R) \tag{A.5}$$

We now specify the equations above in cylindrical coordinates, assuming axial symmetry. We consider a purely extensional flow ($\sigma_{rz} = 0$; $\partial_r v = 0$), with a velocity field of the form:

$$V(r, z) = u(r)\boldsymbol{e_r} + v(z)\boldsymbol{e_z} \tag{A.6}$$

Continuity equation:

$$\frac{1}{r} \partial_r(ru) + \partial_z v = 0 \tag{A.7}$$

Momentum equations:

$$\frac{1}{r} \partial_r(r\sigma_{rr}) + \partial_z \sigma_{rz} - \frac{\sigma_{\theta\theta}}{r} = 0 \tag{A.8}$$

$$\partial_z \sigma_{zz} = 0 \tag{A.9}$$

Development of the stress tensor:

$$\sigma_{rr} = 2\eta\partial_r u - p \tag{A.10}$$

$$\sigma_{\theta\theta} = \frac{2\eta u}{r} - p \tag{A.11}$$

$$\sigma_{zz} = 2\eta\partial_z v - p \tag{A.12}$$

$$\sigma_{rz} = 0 \tag{A.13}$$

The kinematic boundary condition at the fibre surface reads:

$$R' = \frac{u(R,z)}{v(R,z)} \tag{A.14}$$

$$u(0,z) = 0 \tag{A.15}$$

$$v(r,0) = v_0 \tag{A.16}$$

$$v(r,L) = D^2 v_0 \tag{A.17}$$

Integrating equation (A.7) over r and using the condition $u(0,z) = 0$ yields:

$$\int_0^r (\partial_r(ru) + r\partial_z v)\, dr = 0 \tag{A.18}$$

$$u(r,z) = -\frac{r}{2}v'(z) \tag{A.19}$$

Rewriting equations (A.10) and (A.11) provides:

$$\sigma_{rr} = \sigma_{\theta\theta} = -\eta v' - p \tag{20}$$

From (A.8), we obtain:

$$\partial_r(r\sigma_{rr}) = 0 \tag{A.21}$$

With the condition (A.4) one can show that:

$$\sigma_{rr} = \sigma_{\theta\theta} = 0 \tag{A.22}$$

Consequently:

$$p = -\eta v' \tag{A.23}$$

$$\sigma_{zz} = 3\eta v' \tag{A.24}$$

Considering volume conservation along an elementary unit slice during the draw, one can write:

$$\left(R^2(z)v(z)\right)' = 0 \tag{A.25}$$

Moreover, equation (A.9) provides the following relation:

$$\partial_z\left(R^2\sigma_{zz}\right) = 0 \tag{A.26}$$

Using equations (A.25) and (A.26) above, we obtain:

$$\partial_z\left(\eta\frac{v'}{v}\right) = 0 \tag{A.27}$$

Integrating (A.27) along z provides:

$$v(z) = \exp\left(\frac{\int_0^z \frac{dz}{\eta(z)}}{\int_0^1 \frac{dz}{\eta(z)}}\ln D^2\right) \tag{A.28}$$

We now turn to the modelling of the temperature field. In the steady state, the thermal energy equation reduces to:

$$\rho c_p \boldsymbol{v} \cdot \boldsymbol{\nabla} T = k\nabla^2 T \tag{A.29}$$

with c_p the specific heat capacity and k the thermal conductivity, assumed independent of temperature. In cylindrical coordinates, under axial symmetry condition, we get:

$$\rho c_p(u\partial_r T + v\partial_z T) = k\left(\frac{1}{r}\partial_r(r\partial_r T) + \partial_{zz}T\right) \tag{A.30}$$

At the fiber surface, we use the boundary condition

$$-k\boldsymbol{n}\cdot\boldsymbol{\nabla}T|_R = h\cdot(T(R) - T_{ext}(z)) \tag{A.31}$$

with h the heat transfer coefficient. At the first order, the equations become

$$\frac{\rho c_p}{k}(u\partial_r T + v\,\partial_z T) = \frac{1}{r}\partial_r(r\partial_r T) \tag{A.32}$$

$$-\partial_r T|_R = \frac{hL}{k}\left(T(R,z) - T_{air}(z)\right) \tag{A.33}$$

At this stage, we introduce the average temperature along the radial axis:

$$\langle T\rangle(z) = \frac{1}{\pi R(z)^2}\int_0^{R(z)} 2\pi r T(r,z)\mathrm{d}r \tag{A.34}$$

We only have a single partial differential equation for $T(r,z)$, along with boundary conditions. To simplify the resolution to a single differential equation in z, we assume a parabolic profile for T in the radial direction fulfilling condition (A.33):

$$\mathrm{T}(r,z) = \langle\mathrm{T}\rangle(z) + \frac{hL}{k}\frac{(\langle T\rangle(z) - T_{air}(z))R(z)}{4 + \frac{hL}{k}.R(z)}\left(1 - 2\frac{r^2}{R(z)^2}\right) \tag{A.35}$$

The thermal energy equation (A.32) becomes, using $u(r,z) = -\frac{r}{2}v'(z)$ and integrating from 0 to $R(z)$,

$$v(z)\langle \mathrm{T}\rangle'(z) = -\frac{2hL}{\rho c_p}\frac{\langle \mathrm{T}\rangle(z) - T_{air}(z)}{R(z)(1 + \frac{hL}{k}.R(z)/4)} \tag{A.36}$$

This is a partial differential equation over z only, that we can solve numerically to find $T(z)$, $R(z)$ being known through the velocity profile (c.f. equation (A.25)).

Appendix B – Body force from a reconstructed Van der Waals potential for a corrugated free film

Utilization of the Hamaker procedure to obtain the body force potential has two advantages: (i) in contrast to the disjoining pressure approach it can easily be formulated for any interfacially corrugated state of the film's interfaces and is therefore applicable to both short and long wavelength disturbance regimes. (ii) it is computationally easier to formulate the Hamaker potential for an unsymmetrical film system than it is to calculate the disjoining pressure of such a system. Details on how to implement the body force for Van Der Waals interactions based in the general case of a corrugated interface are provided below. The final result for the Van der Waals potential depends on the region of study. The body force is simply the opposite of the gradient of this potential. This derivation is derived from References 178, 179, and 180.

The change in potential energy is derived by first computing the potential energy of interaction (due to the van der Waals force) of molecules in an infinitesimal volume of continuum with respect to (i) the rest of the molecules in the film system and (ii) the rest of the molecules in the infinite system. The subtraction between these two energies is termed the excess van der Waals potential; the negative gradient of this potential is the body force which is introduced into the equation of motion.
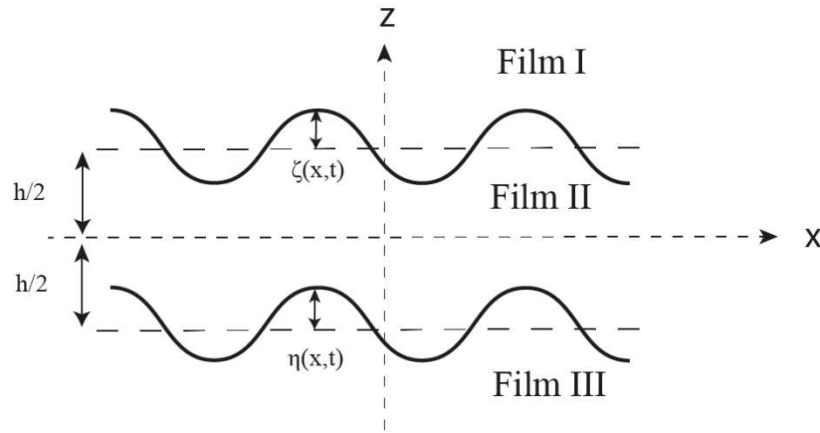
Figure B.1 – Schematic of the film system. The origin of the system is taken as the midplane of the unperturbed film. Adapted from Ref. 180.

The Van der Waals Potential $w_{i,j}$ between two molecules i and j can be written in the far field approximation as :

$$w_{i,j}(r) \sim \frac{C_{i,j}}{r^6} \tag{B.1}$$

$$A_{i,j} = \pi^2 \rho^i \rho^j C_{i,j} \tag{B.2}$$

$F_{i,j}(s)$ represents the potential energy (per unit volume) at a point r in phase i due to an infinite plane of phase j that is located a perpendicular distance s from r (valid in 3D):

$$F_{i,j}(s) = \rho^i \rho^j \int\limits_{s}^{\infty} 2\pi r w_{i,j}(r) dr = \frac{\rho^i \rho^j}{4} \frac{C_{i,j}}{s^4} \frac{2\pi}{} = \frac{1}{2\pi} \frac{A_{i,j}}{s^4}$$

(B.3)

The function $H^{\mathbf{1}}{}_{i,j}(x, y, z, t)$ (resp. $H^{\mathbf{2}}{}_{i,j}(x, y, z, t)$) is the perturbation in the potential energy (per unit volume) at a point in phase i, with coordinate x and located a distance |z| from the unperturbed upper (resp. lower) interface, caused by the displacement of phase j with the corrugation of the interface.

$$H^{\mathbf{1}}{}_{i,j}(x, z, t) = \rho^i \rho^j \int\limits_{\beta=-\infty}^{\infty} \int\limits_{\alpha=-\infty}^{\infty} \int\limits_{\gamma=0}^{\xi(\alpha,t)} w_{i,j}\left(((z-\gamma)^2 + (x-\alpha)^2 + (y-\beta)^2)^{1/2}\right) d\beta d\alpha d\gamma$$

(B.4)

$$H^{\mathbf{2}}{}_{i,j}(x, z, t) = \rho^i \rho^j \int\limits_{\alpha=-\infty}^{\infty} \int\limits_{\beta=-\infty}^{\infty} \int\limits_{\gamma=0}^{\eta(\alpha,t)} w_{i,j}\left(((z-\gamma)^2 + (x-\alpha)^2 + (y-\beta)^2)^{1/2}\right) d\beta d\alpha d\gamma$$

(B.5)

Developing these terms using the potential yields (in 2D):

$$H^{\mathbf{1}}{}_{i,j}(x, z, t) = \rho^i \rho^j \int\limits_{\beta=-\infty}^{\infty} \int\limits_{\alpha=-\infty}^{\infty} \int\limits_{\gamma=0}^{\xi(\alpha,t)} \frac{C_{i,j}}{((z-\gamma)^2 + (x-\alpha)^2 + (y-\beta)^2)^3} d\alpha d\beta d\gamma$$

(B.6)

$$H^{\mathbf{2}}{}_{i,j}(x, z, t) = \rho^i \rho^j \int\limits_{\beta=-\infty}^{\infty} \int\limits_{\alpha=-\infty}^{\infty} \int\limits_{\gamma=0}^{\eta(\alpha,t)} \frac{C_{i,j}}{((z-\gamma)^2 + (x-\alpha)^2 + (y-\beta)^2)^3} d\alpha d\beta d\gamma$$

(B.7)

Development of the flat film contribution

For any point in Film I (top layer):

$$\rho^I W^I{}_{NP}(x, z, t) = \int\limits_{z-h/2}^{\frac{h}{2}+z} F_{I,II}(u)\, du + \int\limits_{\frac{h}{2}+z}^{\infty} F_{I,I}(u)\, du + \int\limits_{0}^{\infty} F_{I,I}(u)\, du + \int\limits_{z-\frac{h}{2}}^{0} F_{I,I}(u)\, du$$

$$- \left(\int\limits_{z-\frac{h}{2}}^{\infty} F_{I,II}(u)\, du + \int\limits_{0}^{\infty} F_{I,I}(u)\, du + \int\limits_{z-\frac{h}{2}}^{0} F_{I,I}(u)\, du \right)$$

$$- \left(\int\limits_{z+\frac{h}{2}}^{\infty} F_{I,II}(u)\, du + \int\limits_{0}^{\infty} F_{I,I}(u)\, du + \int\limits_{z+\frac{h}{2}}^{0} F_{I,I}(u)\, du \right)$$

(B.8)

$$\rho^I W^I{}_{NP}(x, z, t) = \int\limits_{z+h/2}^{\infty} (F_{I,I}(u) + F_{II,II}(u) - 2F_{I,II}(u))\, du$$

(B.9)

$$\rho^I W^I{}_{NP}(x, z, t) = \frac{1}{2\pi} \int\limits_{\frac{h}{2}+z}^{\infty} \frac{A_{I,I} + A_{II,II} - 2A_{I,II}}{s^4}\, du$$

(B.10)

$$\rho^I W^I{}_{NP}(x,z,t) = \frac{1}{2\pi}(A_{I,I} + A_{II,II} - 2A_{I,II})\left[\frac{-1}{3s^3}\right]_{\frac{h}{2}+z}^{\infty} \tag{B.11}$$

$$\boldsymbol{\rho^I W^I{}_{NP}(x,z,t) = \frac{1}{2\pi}\left(A_{I,I} + A_{II,II} - 2A_{I,II}\right)\frac{1}{3\left(\frac{h}{2}+z\right)^3}} \tag{B.12}$$

For any point in Film II :

$$\rho^{II} W^{II}{}_{NP}(x,z,t) = \left(\int_{\frac{h}{2}-z}^{\infty} F_{II,I}(u)\,du + \int_{-\infty}^{z+\frac{h}{2}} F_{II,I}(u)\,du + \int_{0}^{\frac{h}{2}-z} F_{II,II}(u)\,du + \int_{z+\frac{h}{2}}^{0} F_{II,II}(u)\,du\right)$$

$$-\left(\int_{-\infty}^{\frac{h}{2}+z} F_{II,I}(u)\,du + \int_{\frac{h}{2}+z}^{0} F_{II,II}(u)\,du + \int_{0}^{\infty} F_{II,II}(u)\,du\right)$$

$$-\left(\int_{0}^{\frac{h}{2}-z} F_{II,II}(u)\,du + \int_{-\infty}^{0} F_{II,II}(u)\,du + \int_{\frac{h}{2}-z}^{\infty} F_{II,I}(u)\,du\right) \tag{B.13}$$

$$\boldsymbol{\rho^{II} W^{II}{}_{NP}(x,z,t) = -\int_{-\infty}^{\infty} (F_{II,II}(u))\,du} \tag{B.14}$$

For any point in Film III (bottom layer):

$$\rho^{III} W^{III}{}_{NP}(x,z,t) = \int_{0}^{\infty} F_{I,I}(u)\,du + \int_{0}^{-\frac{h}{2}-z} F_{I,I}(u)\,du + \int_{-\frac{h}{2}-z}^{\frac{h}{2}-z} F_{I,II}(u)\,du + \int_{\frac{h}{2}-z}^{\infty} F_{I,I}(u)\,du$$

$$-\left(\int_{0}^{\infty} F_{I,I}(u)\,du + \int_{0}^{-\frac{h}{2}-z} F_{I,I}(u)\,du + \int_{-\frac{h}{2}-z}^{\infty} F_{III,III}(u)\,du\right)$$

$$-\left(\int_{0}^{\infty} F_{II,II}(u)\,du + \int_{0}^{\frac{h}{2}-z} F_{II,II}(u)\,du + \int_{\frac{h}{2}-z}^{\infty} F_{I,II}(u)\,du\right) \tag{B.15}$$

$$\rho^{III} W^{III}{}_{NP}(x,z,t) = \int_{h/2-z}^{\infty} (F_{I,I}(u) + F_{II,II}(u) - 2F_{I,II}(u))\,du \tag{B.16}$$

$$\rho^{III} W^{III}{}_{NP}(x,z,t) = \frac{1}{2\pi}\int_{\frac{h}{2}-z}^{\infty} \frac{A_{I,I} + A_{II,II} - 2A_{I,II}}{s^4}\,du \tag{B.17}$$

$$\rho^{III} W^{III}{}_{NP}(x,z,t) = (A_{I,I} + A_{II,II} - 2A_{I,II})\left[\frac{-1}{3s^3}\right]_{\frac{h}{2}-z}^{\infty} \tag{B.18}$$

$$\boldsymbol{\rho^{III} W^{III}{}_{NP}(x,z,t) = \left(A_{I,I} + A_{II,II} - 2A_{I,II}\right)\frac{1}{3\left(\frac{h}{2}-z\right)^3}} \tag{B.19}$$

To obtain the volumic force, we can derivate along relevant directions:

- Derivative along x

$$-\frac{\partial \rho^I W^I_{NP}(x,z,t)}{\partial x} = 0 \tag{B.20}$$

$$-\frac{\partial \rho^{II} W^{II}_{NP}(x,z,t)}{\partial x} = 0 \tag{B.21}$$

$$-\frac{\partial \rho^{III} W^{III}_{NP}(x,z,t)}{\partial x} = 0 \tag{B.22}$$

- Derivative along z

$$-\frac{\partial \rho^I W^I_{NP}(x,z,t)}{\partial z} = \frac{1}{2\pi}\left(A_{I,I} + A_{II,II} - 2A_{I,II}\right)\frac{1}{\left(\frac{h}{2}+z\right)^4} \tag{B.23}$$

$$-\frac{\partial \rho^{II} W^{II}_{NP}(x,z,t)}{\partial z} = 0 \tag{B.24}$$

$$-\frac{\partial \rho^{III} W^{III}_{NP}(x,z,t)}{\partial z} = -\frac{1}{2\pi}\left(A_{I,I} + A_{II,II} - 2A_{I,II}\right)\frac{1}{\left(\frac{h}{2}-z\right)^4} \tag{B.25}$$

Development of the corrugation contribution

Let us calculate the film I excess VdW potential considering that the reference system is the corrugated interface I,II situated with interface II, III at infinity. The function $H^1_{i,j}(x,y,v,t)$ (resp. $H^2_{i,j}(x,y,v,t)$) is the perturbation in the potential energy (per unit volume) at a point in phase i, with coordinates x, y and located a distance $|v|$ from the unperturbed upper (lower) interface, caused by the displacement of phase j with the corrugation of the interface

$$\rho^I W^I_P(x,z,t) = H^1_{I,II}(x,-z+h/2,t) - H^1_{I,I}(x,-z+h/2,t) + H^2_{I,I}(x,z+h/2,t) - H^2_{I,II}(x,z+h/2,t) \tag{B.26}$$
$$-\left(H^1_{II,II}\left(x,-z+\frac{h}{2},t\right) - H^1_{I,I}\left(x,-z+\frac{h}{2},t\right)\right) - \left(H^2_{II,I}\left(x,z+\frac{h}{2},t\right) - H^2_{II,II}\left(x,z+\frac{h}{2},t\right)\right)$$

$$\boldsymbol{\rho^I W^I_P(x,z,t) = H^2_{I,I}\left(x,-z+\frac{h}{2},t\right) + H^2_{II,II}\left(x,-z+\frac{h}{2},t\right) - 2H^2_{I,II}\left(x,-z+\frac{h}{2},t\right)} \tag{B.27}$$

$$\boldsymbol{\rho^{II} W^{II}_P(x,z,t) = -H^1_{I,II}\left(x,-z+\frac{h}{2},t\right) + H^1_{II,II}\left(x,-z+\frac{h}{2},t\right) - H^2_{II,II}\left(x,z+\frac{h}{2},t\right) + H^2_{I,II}\left(x,z+\frac{h}{2},t\right)} \tag{B.28}$$
$$-\left(-H^1_{I,II}\left(x,-z+\frac{h}{2},t\right) + H^1_{II,II}\left(x,-z+\frac{h}{2},t\right)\right) - \left(-H^2_{II,II}\left(x,z+\frac{h}{2},t\right) + H^2_{I,II}\left(x,z+\frac{h}{2},t\right)\right)$$

$$\boldsymbol{\rho^{II} W^{II}_P(x,z,t) = 0} \tag{B.29}$$

$$\rho^I W^{III}_P(x,z,t) = H^1_{I,II}\left(x,-z+\frac{h}{2},t\right) - H^1_{I,I}\left(x,-z+\frac{h}{2},t\right) + H^2_{I,I}(x,z+h/2,t) - H^2_{I,II}(x,z+h/2,t) \tag{B.30}$$
$$-\left(H^1_{II,II}\left(x,-z+\frac{h}{2},t\right) - H^1_{II,I}\left(x,-z+\frac{h}{2},t\right)\right) - \left(H^2_{I,I}\left(x,z+\frac{h}{2},t\right) - H^2_{I,II}\left(x,z+\frac{h}{2},t\right)\right)$$

$$\rho^{J}W^{III}_{\ P}(x,z,t) = 2H^{1}_{\ I,II}\left(x,-z+\frac{h}{2},t\right) - H^{1}_{\ I,I}\left(x,-z+\frac{h}{2},t\right) - H^{1}_{\ II,II}\left(x,-z+\frac{h}{2},t\right) \tag{B.31}$$

Let us develop the integral terms:

$$H^{1}_{\ i,j}(x,y,v,t) = \rho^{j}\rho^{j} \int_{\alpha=-\infty}^{\infty}\int_{\beta=-\infty}^{\infty}\int_{\gamma=0}^{\zeta\,(x,t)} \frac{C_{i,j}}{((v-\gamma)^{2}+(x-\alpha)^{2}+(y-\beta)^{2})^{3}}\,dXdYd\gamma \tag{B.32}$$

Considering that $\alpha - x = X\ and\ dX = d\alpha$ as well as $Y = y - \beta$ and $dY = d\beta$

$$H^{1}_{\ i,j}(x,y,v,t) = \rho^{j}\rho^{j} \int_{Y=-\infty}^{\infty}\int_{X=-\infty}^{\infty}\int_{\gamma=0}^{\zeta\,(x,t)} \frac{C_{i,j}}{((v-\gamma)^{2}+(X)^{2}+(Y)^{2})^{3}}\,dXdYd\gamma \tag{B.33}$$

Considering that $\gamma - z = Z\ and\ dZ = d\gamma$

$$H^{1}_{\ i,j}(x,y,v,t) = \rho^{i}\rho^{j} \int_{Y=-\infty}^{\infty}\int_{X=-\infty}^{\infty}\int_{Z=+v}^{\zeta\,(x,t)+v} \frac{C_{i,j}}{((Z)^{2}+(X)^{2}+(Y)^{2})^{3}}\,dXdYdZ \tag{B.34}$$

Let us integrate along Y first given that $\zeta\,(x,t)$ is not dependent on Y :

$$H^{1}_{\ i,j}(x,v,t) = \rho^{i}\rho^{j} \int_{X=-\infty}^{\infty}\int_{Z=+v}^{\zeta\,(x,t)+v}\int_{Y=-\infty}^{\infty} \frac{C_{i,j}}{((Z)^{2}+(X)^{2}+(Y)^{2})^{3}}\,dXdYdZ \tag{B.35}$$

For that, we consider $C = \sqrt{X^{2}+Z^{2}}$ and do a variable change considering $Y = C.tan(u)$ and $dY = \frac{C}{cos^{2}(u)}\,du$:

$$H^{1}_{\ i,j}(x,v,t) = \rho^{i}\rho^{j}C_{i,j} \int_{X=-\infty}^{\infty}\int_{Z=+v}^{\zeta\,(x,t)+v}\int_{u=-\pi/2}^{\pi/2} \frac{1}{(C)^{6}(1+tan^{2}(u))^{3}}\frac{C}{cos^{2}(u)}\,dXdudZ \tag{B.36}$$

$$H^{1}_{\ i,j}(x,v,t) = \rho^{i}\rho^{j}C_{i,j} \int_{X=-\infty}^{\infty}\int_{Z=+v}^{\zeta\,(x,t)+v}\frac{1}{C^{5}}\int_{u=-\pi/2}^{\pi/2} cos^{4}(u)\,dXdudZ \tag{B.37}$$

$$H^{1}_{\ i,j}(x,v,t) = \rho^{i}\rho^{j}C_{i,j} \int_{X=-\infty}^{\infty}\int_{Z=+v}^{\zeta\,(x,t)+v}\frac{1}{4C^{5}}\int_{u=-\pi/2}^{\pi/2}\left[\frac{3}{2}+2\,cos(2u)+\frac{1}{2}cos(4u)\right]dXdudZ \tag{B.38}$$

$$H^{1}_{\ i,j}(x,v,t) = \rho^{i}\rho^{j}C_{i,j} \int_{X=-\infty}^{\infty}\int_{Z=+v}^{\zeta\,(x,t)+v}\frac{1}{4C^{5}}\left[\frac{3}{2}u+sin(2u)+\frac{1}{8}sin(4u)\right]_{u=-\pi/2}^{\pi/2}dXdZ \tag{B.39}$$

$$H^{1}_{\ i,j}(x,v,t) = \frac{3\pi}{8}\rho^{i}\rho^{j}C_{i,j} \int_{X=-\infty}^{\infty}\int_{Z=+v}^{\zeta\,(x,t)+v} \frac{1}{((Z)^{2}+(X)^{2})^{5/2}}\,dXdZ \tag{B.40}$$

$$\boldsymbol{H^{1}_{\ i,j}(x,v,t) = \frac{3}{8\pi}A_{i,j} \int_{\alpha=-\infty}^{\infty}\int_{\beta=0}^{\zeta\,(x,t)} \frac{1}{((v-\beta)^{2}+(x-\alpha)^{2})^{5/2}}\,d\alpha d\beta} \tag{B.41}$$

To obtain the volumic force, we can derivate along relevant directions:

- o Derivative along x

$$\frac{\partial H^1{}_{i,j}}{\partial x} = \frac{3}{8\pi} A_{i,j} \left[\int\limits_{\alpha=-\infty}^{\infty} \frac{\partial \zeta}{\partial x} \frac{1}{((v - \zeta(x,t))^2 + (x-\alpha)^2)^{5/2}} \, d\alpha d\beta \ + \int\limits_{\alpha=-\infty}^{\infty} \int\limits_{\beta=0}^{\zeta(x,t)} -\frac{5}{2}2(x-\alpha)\left(\frac{1}{((v-\beta)^2 + (x-\alpha)^2)^{7/2}} \right) d\alpha d\beta \right] \tag{B.42}$$

$$-\frac{\partial H^1{}_{i,j}}{\partial x} = \frac{3}{8\pi} A_{i,j} \left[-\frac{\partial \zeta}{\partial x} \int\limits_{\alpha=-\infty}^{\infty} \frac{1}{((v - \zeta(x,t))^2 + (x-\alpha)^2)^{5/2}} \, d\alpha d\beta \ + 5 \int\limits_{\alpha=-\infty}^{\infty} \int\limits_{\beta=0}^{\zeta(x,t)} \frac{(x-\alpha)}{((v-\beta)^2 + (x-\alpha)^2)^{7/2}} \, d\alpha d\beta \right] \tag{B.43}$$

o Derivative along z

$$\frac{\partial H^1{}_{i,j}}{\partial z} = \frac{3}{8\pi} A_{i,j} \left[\int\limits_{\alpha=-\infty}^{\infty} \int\limits_{\beta=0}^{\zeta(x,t)} -5 \frac{\partial v}{\partial z} \frac{(v-\beta)}{((v-\beta)^2 + (x-\alpha)^2)^{7/2}} \, d\alpha d\beta \right] \tag{B.44}$$

$$-\frac{\partial H^1{}_{i,j}}{\partial z} = \frac{15}{8\pi} A_{i,j} \left[\int\limits_{\alpha=-\infty}^{\infty} \int\limits_{\beta=0}^{\zeta(x,t)} \frac{\partial v}{\partial z} \frac{(v-\beta)}{((v-\beta)^2 + (x-\alpha)^2)^{7/2}} \, d\alpha d\beta \right] \tag{B.45}$$

- Considering that $v = -z + \frac{h}{2}$ for film III:

$$\rho^I W^{III}{}_P(x,z,t) = 2H^1{}_{I,II}\left(x, -z + \frac{h}{2}, t\right) - H^1{}_{I,I}\left(x, -z + \frac{h}{2}, t\right) - H^1{}_{II,II}\left(x, -z + \frac{h}{2}, t\right) \tag{B.46}$$

o Along z-axis:

$$-\frac{\partial \rho^{III} W^{III}{}_P(x,z,t)}{\partial z} = -\frac{15}{8\pi}\left(A_{I,I} + A_{II,II} - 2A_{I,II}\right)\left[\int\limits_{\alpha=-\infty}^{\infty} \int\limits_{\beta=0}^{\zeta(x,t)} \frac{\left(-z + \frac{h}{2} - \beta\right)}{\left(\left(-z + \frac{h}{2} - \beta\right)^2 + (x-\alpha)^2\right)^{7/2}} \, d\alpha d\beta \right] \tag{B.47}$$

$$-\frac{\partial \rho^{III} W^{III}{}_P(x,z,t)}{\partial z} = -\frac{15}{8\pi}\left(A_{I,I} + A_{II,II} - 2A_{I,II}\right)\left[\left(\frac{1}{5}\right)\int\limits_{\alpha=-\infty}^{\infty} \int\limits_{\beta=0}^{\zeta(\alpha,t)} \left(-\frac{5}{2}\right)(-2)\frac{\left(-z + \frac{h}{2} - \beta\right)}{\left(\left(-z + \frac{h}{2} - \beta\right)^2 + (x-\alpha)^2\right)^{7/2}} \, d\alpha d\beta \right] \tag{B.48}$$

$$-\frac{\partial \rho^{III} W^{III}{}_P(x,z,t)}{\partial z} = -\frac{15}{8\pi}\left(A_{I,I} + A_{II,II} - 2A_{I,II}\right)\left[\left(\frac{1}{5}\right)\int\limits_{\alpha=-\infty}^{\infty} \left[\frac{1}{\left(\left(-z + \frac{h}{2} - \beta\right)^2 + (x-\alpha)^2\right)^{5/2}} \right]_{0}^{\zeta(x,t)} \right] \tag{B.49}$$

$$-\frac{\partial \rho^{III} W^{III}{}_P(x,z,t)}{\partial z} = -\frac{3}{8\pi}\left(A_{I,I} + A_{II,II} - 2A_{I,II}\right) \int\limits_{\alpha=-\infty}^{\infty} \left[\frac{1}{\left(\left(-z + \frac{h}{2} - \zeta(\alpha,t)\right)^2 + (x-\alpha)^2\right)^{5/2}} - \frac{1}{\left(\left(-z + \frac{h}{2}\right)^2 + (x-\alpha)^2\right)^{5/2}} \right] \tag{B.50}$$

o Along x-axis:

$$-\frac{\partial \rho^{III} W^{III}{}_P(x,z,t)}{\partial x} = \frac{3}{8\pi}\left(A_{I,I} + A_{II,II} - 2A_{I,II}\right)\left[\frac{\partial \zeta}{\partial x}\int\limits_{\alpha=-\infty}^{\infty} \frac{1}{\left(\left(-z + \frac{h}{2} - \zeta(\alpha,t)\right)^2 + (x-\alpha)^2\right)^{5/2}} \, d\alpha - 5\int\limits_{\alpha=-\infty}^{\infty}\int\limits_{\beta=0}^{\zeta(x,t)} \frac{(x-\alpha)}{\left(\left(-z + \frac{h}{2} - \beta\right)^2 + (x-\alpha)^2\right)^{7/2}} \, d\alpha d\beta \right] \tag{B.51}$$

$$-\frac{\partial \rho^{III} W^{III}{}_P(x,z,t)}{\partial x} = \frac{3}{8\pi}\left(A_{I,I} + A_{II,II} - 2A_{I,II}\right)\left[\frac{\partial \zeta}{\partial x}\int\limits_{\alpha=-\infty}^{\infty} \frac{1}{\left(\left(-z + \frac{h}{2} - \zeta(x,t)\right)^2 + (x-\alpha)^2\right)^{5/2}} \, d\alpha - 5\int\limits_{\alpha=-\infty}^{\infty}\int\limits_{\beta=0}^{\zeta(x,t)} \frac{(x-\alpha)}{\left(\left(-z + \frac{h}{2} - \beta\right)^2 + (x-\alpha)^2\right)^{7/2}} \, d\alpha d\beta \right] \tag{B.52}$$

$$-\frac{\partial \rho^{III} W^{III}{}_P(x,z,t)}{\partial x} = \frac{3}{8\pi}\left(A_{I,I} + A_{II,II} - 2A_{I,II}\right)\left[\frac{\partial \zeta}{\partial x}\int\limits_{\alpha=-\infty}^{\infty} \frac{1}{\left(-z + \frac{h}{2} - \zeta(\alpha,t)\right)^2 + (x-\alpha)^2)^{5/2}} \, d\alpha d\beta - 5\int\limits_{\alpha=-\infty}^{\infty}\int\limits_{\beta=0}^{\zeta(x,t)} \frac{(x-\alpha)}{\left(\left(-z + \frac{h}{2} - \beta\right)^2 + (x-\alpha)^2\right)^{7/2}} \, d\alpha d\beta \right] \tag{B.53}$$

- Considering that $v = z + \frac{h}{2}$ for I:

$$\rho^I W^I{}_P(x,z,t) = H^2{}_{I,I}\left(x, z + \frac{h}{2}, t\right) + H^2{}_{II,II}\left(x, z + \frac{h}{2}, t\right) - 2H^2{}_{I,II}\left(x, z + \frac{h}{2}, t\right) \tag{B.54}$$

Appendix B

   o   Along z-axis

$$-\frac{\partial \rho^I W^I{}_P(x,z,t)}{\partial z} = -\frac{15}{8\pi}\big(A_{I,I} + A_{II,II} - 2A_{I,II}\big)\left[\int\limits_{\alpha=-\infty}^{\infty}\int\limits_{\beta=0}^{\eta\,(x,t)} \frac{\left(z+\frac{h}{2}-\beta\right)}{\left(\left(z+\frac{h}{2}-\beta\right)^2 + (x-\alpha)^2\right)^{7/2}}\,d\alpha d\beta\right] \tag{B.55}$$

$$-\frac{\partial \rho^I W^I{}_P(x,z,t)}{\partial z} = -\frac{15}{8\pi}\big(A_{I,I} + A_{II,II} - 2A_{I,II}\big)\left[(\tfrac{1}{5})\int\limits_{\alpha=-\infty}^{\infty}\int\limits_{\beta=0}^{\eta\,(x,t)} (-\tfrac{5}{2})(-2)\frac{\left(z+\frac{h}{2}-\beta\right)}{\left(\left(z+\frac{h}{2}-\beta\right)^2 + (x-\alpha)^2\right)^{7/2}}\,d\alpha d\beta\right] \tag{B.56}$$

$$-\frac{\partial \rho^I W^I{}_P(x,z,t)}{\partial z} = -\frac{3}{8\pi}\big(A_{I,I} + A_{II,II} - 2A_{I,II}\big)\left[\int\limits_{\alpha=-\infty}^{\infty}\left[\frac{1}{\left(\left(z+\frac{h}{2}-\beta\right)^2 + (x-\alpha)^2\right)^{5/2}}\right]_{0}^{\eta\,(x,t)}\right] \tag{B.57}$$

$$-\frac{\partial \rho^I W^I{}_P(x,z,t)}{\partial z} = -\frac{3}{8\pi}\big(A_{I,I} + A_{II,II} - 2A_{I,II}\big)\left[\int\limits_{\alpha=-\infty}^{\infty}\left(\frac{1}{\left(\left(z+\frac{h}{2}-\eta\,(x,t)\right)^2 + (x-\alpha)^2\right)^{5/2}} - \frac{1}{\left(\left(z+\frac{h}{2}\right)^2 + (x-\alpha)^2\right)^{5/2}}\right)d\alpha\right] \tag{B.58}$$

   o   Along x-axis:

$$-\frac{\partial \rho^I W^I{}_P(x,z,t)}{\partial x} = -\frac{3}{8\pi}\big(A_{I,I} + A_{II,II} - 2A_{I,II}\big)\left[\frac{\partial \eta}{\partial x}\int\limits_{\alpha=-\infty}^{\infty} \frac{1}{\left(\left(z+\frac{h}{2}-\eta(x,t)\right)^2 + (x-\alpha)^2\right)^{5/2}}\,d\alpha - 5\int\limits_{\alpha=-\infty}^{\infty}\int\limits_{\beta=0}^{\eta\,(x,t)} \frac{(x-\alpha)}{\left(\left(z+\frac{h}{2}-\beta\right)^2 + (x-\alpha)^2\right)^{7/2}}\,d\alpha d\beta\right] \tag{B.59}$$

$$-\frac{\partial \rho^I W^I{}_P(x,z,t)}{\partial x} = -\frac{3}{8\pi}\big(A_{I,I} + A_{II,II} - 2A_{I,II}\big)\left[\frac{\partial \eta}{\partial x}\int\limits_{\alpha=-\infty}^{\infty} \frac{1}{\left(\left(z+\frac{h}{2}-\eta(x,t)\right)^2 + (x-\alpha)^2\right)^{5/2}}\,d\alpha - 5\int\limits_{\alpha=-\infty}^{\infty}\int\limits_{\beta=0}^{\eta\,(x,t)} \frac{(x-\alpha)}{\left(\left(z+\frac{h}{2}-\beta\right)^2 + (x-\alpha)^2\right)^{7/2}}\,d\alpha d\beta\right] \tag{B.60}$$

$$-\frac{\partial \rho^I W^I{}_P(x,z,t)}{\partial x} = -\frac{3}{8\pi}\big(A_{I,I} + A_{II,II} - 2A_{I,II}\big)\left[\frac{\partial \eta}{\partial x}\int\limits_{\alpha=-\infty}^{\infty} \frac{1}{\left(z+\frac{h}{2}-\eta(x,t)\right)^2 + (x-\alpha)^2)^{5/2}}\,d\alpha - 5\int\limits_{\alpha=-\infty}^{\infty}\int\limits_{\beta=0}^{\eta\,(x,t)} \frac{(x-\alpha)}{\left(\left(z+\frac{h}{2}-\beta\right)^2 + (x-\alpha)^2\right)^{7/2}}\,d\alpha d\beta\right] \tag{B.61}$$

Total contributions

For any point in film I (top layer):

$$\rho^I W^I{}_{total}(x,z,t) = \rho^I W^I{}_{NP}(x,z,t) + \rho^I W^I{}_P(x,z,t) \tag{B.62}$$

For any point in Film II:

$$\rho^{II} W^{II}{}_{total}(x,z,t) = \rho^{II} W^{II}{}_{NP}(x,z,t) + \rho^{II} W^{II}{}_P(x,z,t) \tag{B.63}$$

For any point in Film III (bottom layer):

$$\rho^I W^{III}{}_{total}(x,z,t) = \rho^I W^{III}{}_{NP}(x,z,t) + \rho^I W^{III}{}_P(x,z,t) \tag{B.64}$$

Curriculum Vitae

Louis MARTIN-MONIER

Address : Avenue Marc Dufour 44, 1007 Lausanne
Email : louis.martin-monier@epfl.ch
Phone : +41 78 659 9036

Education

Since 2016
Lausanne, Switzerland

- **PhD – Department of Materials Science, École Polytechnique Fédérale de Lausanne (EPFL)**
  - Supervisor: Prof. Fabien SORIN
  - Studied the rearrangement process of thin films in various systems using fluid mechanics modeling. Designed and fabricated various chalcogenide and liquid metal based- metasurfaces and photonic circuits that enable large scale yet efficient nanoscale photonics.

2013-2016
Paris,
France

- **M.Sc – École des Mines de Paris - Physics and applications**
  - Core competencies: Physics of condensed matter and Nano objects, Quantum physics, Statistical Physics, Analytical and Numerical methods, Thermodynamics, Semiconductor Physics, Electronics, Materials Science

2010-2013
Paris,
France

- **B.Sc – Collège Stanislas**
  - Intensive program preparing for entrance exam to top French scientific universities
  - Core competencies: Theoretical and Applied Mathematics, Programming, Optics & Electromagnetism, Thermodynamics, Mechanics, Inorganic and organic chemistry

Professional experiences

Since Nov. 2016
Lausanne, Switzerland

- **Research Supervisor**
  - Supervised 6 Master student projects

Since Nov. 2016
Lausanne, Switzerland

- **Teaching Assistant**
  - Introduction to Materials Science

April-Sept. 2016
Stuttgart, Germany

- **DLR (German Aerospace Agency) – Research Intern**
  - Awarded Erasmus Scholarship
  - Optimization of transport properties in metal foam anodes for Solid Oxide Fuel Cells – R&D in the framework of EU project EVOLVE

June-Sept. 2015
Renningen, Germany

- **BOSCH – Research Intern**
  - Thermodynamic simulation of a micro-Combined Heat and Power (CHP) system based on a Commercial Solid Oxide Fuel Cell (SOFC)

Feb.-June 2015
Paris, France

- **Software Developer – Shell Eco-Marathon**
  - Development of a consumption optimizing algorithm for solar electrical vehicle prototypes
  - Winner of the Technical Innovation Award at Shell Eco Marathon (Rotterdam) out of 200+ participating teams

November 2013
Le Creusot, France

- **AREVA NP**
  - Investigation of Ni-Cr superalloys fatigue in primary cycle of nuclear reactors

Conferences and Publications

<u>Conference Proceedings and oral presentations</u>

L. Martin-Monier, T. Das Gupta, W. Yan, T. D. Nguyen, A. Page, and F. Sorin, "Self-assembled glass-based Fano resonant metasurfaces", Proc. SPIE 11292, Advanced Fabrication Technologies for Micro/Nano Optics and Photonics XIII, 112920D (28 February 2020), presented at SPIE Photonics West, San Fransisco 2020

L.Martin-Monier, T.Das Gupta, F.Sorin, Large-area all-dielectric metasurfaces via templated fluid instabilities, Oral presentation, 25th International Congress on Glass, Boston, USA, 2019.

T. Das Gupta, **L. Martin-Monier**, A. Le Bris, W. Yan, T.D. Nguyen, A. Page, Y. Qu, F. Sorin, "Flexible, large area all chalcogenide metasurfaces fabricated via template fluid instabilities", SPIE Photonics West, San Francisco, USA, 2019.

T. Das Gupta, **L. Martin-Monier**, A. Le Bris, W. Yan, T.D. Nguyen, A. Page, Y. Qu, Fabien Sorin, Template assisted dewetting of optical glasses for large area, flexible and stretchable all dielectric metasurfaces, Advanced Photonic Congress, Zürich, Switzerland, 2-5 July 2018.

T. Das Gupta, **L. Martin-Monier**, A. Le Bris, W. Yan, T.D. Nguyen, A. Page, Y. Qu, F. Sorin, Template assisted dewetting of optical glasses for large area, flexible and stretchable all dielectric metasurfaces, CLEOS, San Jose, USA, 2018.

T. Das Gupta, **L. Martin-Monier**, A. Le Bris, W. Yan, T.D. Nguyen, A. Page, Y. Qu, Fabien Sorin, Template assisted dewetting of chalcogenide materials for large area, flexible and stretchable all dielectric metasurfaces, EMRS Spring 2018

<u>Publications</u>

T. Das Gupta, **L. Martin-Monier**, A. Le Bris, W. Yan, T. Dang Nguyen, A. Page, Y. Qu, F. Sorin, Self-assembly of nanostructured glass metasurfaces via templated fluid instabilities; **Nature Nanotechnology,** 14: 320–327 (2019)

L.Martin-Monier, T.Das Gupta, W. Yan, S. Lacour, F.Sorin, "Controlled Oxidation of Liquid Metals for Stretchable Electronics and Photonics", **Advanced Functional Materials**, Accepted

L.Martin-Monier, P-L Piveteau, F.Sorin, "Novel insights into the design of stretchable electrical systems", **Science Advances**, Under Review

T. Das Gupta, **L. Martin-Monier**, J. Butet, K.-Y. Yang, A. Leber, C. Dong, W. Yan, T. Nguyen-Dang, O. J.F. Martin, F. Sorin, "Second harmonic generation in glass-based metasurfaces using tailored surface lattice resonances", **Nanoscale**, Under Review

L.Martin-Monier, P-G. Ledda**,** P-L. Piveteau, F. Gallaire, F.Sorin, "Atomistic scale-ordered dewetting captured through continuum mechanics framework", Manuscript in preparation.

W.Esposito, **L.Martin-Monier**, B. Xu, P-L. Piveteau, D.Daosheng, F.Sorin, "Templated fluid instabilities in Thermal drawing: a novel approach to 2D metamaterials", Manuscript in preparation

P-L. Piveteau, **L.Martin-Monier,** T. Das Gupta, B. Schyrr, F.Sorin, "Scalable large area chalcogenide based metasurface as highly sensitive index sensors", Manuscript in preparation.

L.Martin-Monier, P-L. Piveteau, F.Sorin, "Wide-angle meta-reflectors based on resonant gap Kerker effect", Manuscript in preparation

Patents

- Fabrication of glass-based nanostructures on large area rigid and soft planar substrates, fibers and textiles: US Patent App. 62/802,725

Scientific Expertise

- **Fabrication and processing:** E-beam lithography, Photolithography, Wet and Dry etching methods, Vaccum deposition systems (evaporation, sputtering), sol-gel processes, nanoimprinting processes

- **Materials characterization:** Environmental SEM, AFM, Energy Dispersive Spectroscopy

- **Optical characterization:** Reflectometry, Ellipsometry, FT-IR, Two Photon Spectroscopy

- **Programming skills:** Mathematica, Matlab, Lumerical (FDTD)**,** COMSOL Multiphysics, Python, Java, PHP, MySQL, C++, LabView

- **Language skills**: French: (Fluent), English (Fluent), German (Fluent), Mandarin (Notions)

References

1. P.G. De Gennes, F. Brochart-Wyart, D. Quere, Capillarity and Wetting Phenomenon : Drops, Bubbles, Pearls, Waves. Springer, 2004.

2. H.C. Hamaker, The London-van der Waals attraction between spherical particles. *Physica* **4**, 1058 (1937).

3. E.M. Lifshitz, The Theory of Molecular Attractive Forces between Solids. *Journal of Experimental Theoretical Physics USSR.* **29**, 94 (1954).

4. B.W. Ninham & V.A. Parsegian, Van der Waals Forces: Special Characteristics in Lipid-Water Systems and a General Method of Calculation Based on the Lifshitz Theory. *Biophys. Journal* **10**, 646 (1970).

5. McLachlan, Retarded dispersion forces between molecules. *Proc. R. Soc. A* **271**, 387 (1963).

6. J. Vissier, On Hamaker constants: A comparison between Hamaker constants and Lifshitz-van der Waals constants. *Adv. Colloid Interface Sci.* **3**, 331 (1972).

7. I.E. Dzyaloshinskii, E.M. Lifshitz, L.P. Pitaevskii, Van der Waals Forces In Liquid Films. *Sov. Phys. JETP* **37**, 161 (1960).

8. J.N. Israelichvili, Intermolecular and Surface Forces. Elsevier, Third Edition (2011).

9. D. Longbein, Van Der Waals Attraction Between Macroscopic Bodies. *J. Adhes* **1**, 237 (1969).

10. Seemann, R., S. Herminghaus, K. Jacobs, Gaining control of pattern formation of dewetting liquid films. J. Phys.: Condens. Matter 13 (2001) 4925–4938

11. Becker, Jürgen, Günther Grün, Ralf Seemann, Hubert Mantz, Karin Jacobs, Klaus R. Mecke, et Ralf Blossey. « Complex Dewetting Scenarios Captured by Thin-Film Models ». *Nat. Mater.* 2, 788 (2002).

12. L.E. Stillwagon, R.G. Larson, Fundamentals of topographic substrate leveling. *J. Appl. Phys.* **63**, 5251 (1988).

13. M. Backholm, M. Benzaquen, T. Salez, E. Raphaël, K. Dalnoki-Veress, Capillary Levelling of a Cylindrical Hole in a Viscous Film. *Soft Matter* **10**, 2550-2558 (2014).

14. A. Oron, S.H. Davis, S.G. Bankoff, Long-scale evolution of thin liquid films. *Rev. Mod. Phys.* **69**, 931-980 (1997).

15. Volodin, P., and Kondyurin, A. Dewetting of Thin Polymer Film on Rough Substrate: I. Theory. *J. Phys. D: Appl. Phys.* **41**, 065306 (2008).

16. A. Sharma and A.T. Jameel, Nonlinear Stability, Rupture, and Morphological Phase Separation of Thin Fluid Films on Apolar and Polar Substrates. *J. Colloid Interface Sci.* **161**, 190(1993).

17. R. Seemann, S. Herminghaus, K. Jacobs, Dewetting Patterns and Molecular Forces: A Reconciliation. *Phys. Rev. Lett.* **86**, 5534 (2001).

18. R. Seemann, S. Herminghaus, K. Jacobs, Dewetting Patterns and Molecular Forces: A Reconciliation. *Phys. Rev. Lett.* **86**, 5534 (2001).

19. C.V.Thompson, Solid-State Dewetting of Thin Films. *Annu. Rev. Mater. Res.* **42***, 399 (2012).

20. R. Zucker, Capillary-driven shape evolution in solid-state micro- and nano-scale systems. PhD Thesis, MIT, 2015.

21. Y. Jongpil, Solid-state dewetting of continuous and patterned single crystal Ni thin films. PhD Thesis, MIT, 2011.

22. M. Naffouti, R. Backofen, M. Salvalaglio, T. Bottein, M. Lodari, A. Voigt, T. David, A. Benkouider, I. Fraj, L. Favre, A. Ronda, I. Berbezier, D. Grosso, M. Abbarchi, M. Bollani, Complex dewetting scenarios of ultrathin silicon films for large-scale nanoarchitectures. *Sci. Adv.* 3, 1472 (2017).

23. Y. Almadori, Ł. Borowik, N. Chevalier, W. Hourani, F. Glowacki, J-C. Barbé, From Solid-State Dewetting of Ultrathin, Compressively Strained Silicon–Germanium-on-Insulator Films to Mastering the Stoichiometry of Si1–xGex Nanocrystals. *J. Phys. Chem. C* **120**, 7412 (2016).

24. J. Ye & C.V. Thompson, Templated solid-state dewetting to controllably produce. complex patterns. *Adv. Mater.* **23**, 1567 (2011).

25. D. Amram, L. Klinger, E. Rabkin, Anisotropic hole growth during solid-state dewetting of single-crystal Au–Fe thin films. *Acta Materialia* **60**, 3047 (2012).

26. E. Jiran & C. V. Thompson, Capillary Instabilities in Thin, Continuous Films. *Thin Solid Films* **208**, 23 (1992).

27. D. Kim, A.L. Giermann, C.V. Thompson, Solid-state dewetting of patterned thin films. *App. Phys. Lett.* **95**, 251903 (2009).

28. A.L. Giermann, C.V. Thompson, Solid state dewetting for ordered arrays of crystallographically oriented metal particles. *Appl. Phys. Lett.* **86**, 121903 (2005).

29. D. Peschka, S. Haefner, L. Marquant, K. Jacobs, A. Münch, B. Wagner, Signatures of slip in dewetting polymer films. *Proc. Natl. Ac. Sci. U.S.A* **116**, 9275 (2019).

30. U.Thiele & M.G.Velarde, Dewetting: film rupture by nucleation in the spinodal regime. *Phys, Rev. Lett.* **87**, 016104 (2001).

31. R. Seemann, S. Herminghaus, K. Jacobs, Gaining Control of Pattern Formation of Dewetting Liquid Films. *J. Phys. Condens. Matter* **13**, 4925 (2001).

32. E. Schäffer, Instabilities in Thin Polymer Films: Structure Formation and Pattern Transfer. PhD Thesis, Universität Konstanz (2001).

33. G. Reiter, Dewetting of thin polymer films. *Phys. Rev. Lett.* **68**, 75 (1992).

34. J. Bischof, D. Scherer, S. Herminghaus, P. Leiderer, Dewetting Modes of Thin Metallic Films: Nucleation of Holes and Spinodal Dewetting. *Phys. Rev. Lett.* **77**, 1536 (1996).

35. S. Herminghaus, K. Jacobs, K. Mecke, J. Bischof, A. Fery, M. Ibn-Elhaj, S. Schlagowski, Spinodal Dewetting in Liquid Crystal and Liquid Metal Films. *Science* **282**, 916 (1998).

36. J.N. Israelachvili, Intermolecular and surface forces. Elsevier Inc. **3** (2011).

37. S. John, Strong Localization of photons in certain disordered dielectric superlattices. *Phys. Rev, Lett* **58**, 2486 (1987).

38. E. Yablonovitch, Inhibited Spontaneous Emission in Solid State Physics and Electronics, *Phys. Rev, Lett* **58**, 2059 (1987).

39. A.F. Abouraddy, M. Bayindir, G. Benoit, S.D. Hart, K. Kuriki, N. Orf, O. Shapira, F. Sorin, B. Temelkuran, Y. Fink, Towards mulitmaterial multifunctional fibers that see, hear, sense and communicate. *Nat. Mater.* **6**, 336 (2007).

40. P. Russell, Photonic Crystal Fibers. *Science* **299**, 358 (2003).

41. E. Yablonovitch, T.J Gmitter, K.M. Leung, Photonic Band Structure: the Face Centered Cubic Case Emèploying Non-Spherical Atoms. *Phy. Rev. Lett.* **67**, 2295 (1991).

42. K.M. Ho, C.T. Chan, C.M. Soulkis, *Phys. Rev. Lett.* **65**, 3152 (1990).

43. V.G. Veselago The Electrodynamics of Substances with Simultaneously Negative Values of ε and μ. *Sov. Phys. Uspekhi* **10**, 509 (1968).

44. J.B. Pendry, Negative refraction Makes a Perfect Lens. *Phys. Rev. Lett.* **85**, 3966 (2000).

45. J.B. Pendry, D. Schurig, D.R. Smith, Controlling Electromagnitc Fields. *Science* **312**, 1780 (2006).

46. J. Valentine, S. Zhang, T. Zentgraf, E. Ulin-Avila, D.A. Genov, G. Bartal, X. Zhang, Three-dimensional optical metamaterials with a negative refractive index. *Nature* **455**, 376 (2008).

47. M.V. Rybin, D.S. Filonov, K.B. Samusev, P.A. Belov, Y.S. Kivshar, M.F. Limonov, Phase Diagram for the Transition from Photonic Crystals to Dielectric Metamaterials. *Nat. Commun.* 6, 10102 (2015).

48. P. Lalanne & P. Chavel, *Laser Photonics Rev.* **11**, 1600295 (2017).

49. N. Yu & F. Capasso, Flat Optics with Designer Metasurfaces. *Nat. Mater.* **13**, 139 (2014).

50. S. Sun, K.-Y. Yang, C.-M. Wang, T.-K. Juan, W.T. Chen, C.Y. Liao, Q. He, S. Xiao, W.-T. Kung, G.-Y. Guo, L. Zhou, D.P. Tsai, High-efficiency broadband anomalous reflection by gradient metasurfaces. *Nano Lett.* **12**, 6223 (2012)

51. S. Sun, Q. He, S. Xiao, Q. Xu, X. Li, L. Zhou, Gradient index metasurfaces as bridge linking propagating waves and surface waves. *Nat. Mater.* **11**, 426 (2012).

52. N. Yu, P. Genevet, F. Aieta, M.A. Kats, R. Blanchard, G. Aoust, J-P. Tetienne, Z. Gaburro, F. Capasso, Flat optics: Controlling wavefronts with optical antenna metasurfaces. *IEEE J. Sel. Top. Quant. Electron.* **19**, 4700423 (2013).

53. F. Aieta, P. Genevet, M.A. Kats, N. Yu, R. Blanchard, Z. Gaburro, F. Capasso, Aberration-free ultrat-thinflat lensesand axicons at telecom wavelengths based on plasmonic metasurfaces. *Nano lett.* **12**, 4932 (2012).

54. P. Genevet, N. Yu, F. Aieta, J. Lin, M.A. Kats, R. Blanchard, M.O. Scully, Z. Gaburro, F. Capasso, Ultra-thin Plasmonic Optical Vortex plates based on phase discontinuities. *Appl. Phys. Lett.* **100**, 013101 (2012)

55. Y.M. Yang, W.Y. Wang, P. Moitra, II. Kravchenko, DP. Briggs, J. Valentine, Dielectric Meta-reflectarray for broadband linear polarization conversion and optical vortex generation. *Nano Lett.* **14**, 1394 (2014).

56. N. Yu, F. Aieta, P. Genevet, MA. Kats, Z. Gaburro, F. Capasso, A broadband, background-free quarter waveplate based on plasmonic metasurfaces. *Nano Lett.* **12**, 6328 (2012).

57. Y. Zheng, Y. Zhou, J. Gao, X .Cao, H. Yang, S. Li, L. Xu, J. Lan, L. Jidi, Ultra-wideband polarization conversion metasurface and its application cases for antenna radiation enhancement and scattering suppression. *Sci. Rep.* **7**, 16137 (2017).

58. L. Zhang, J. Ding, H. Zheng, S. An, H. Lin, B. Zheng, Q. Du, G. Yin, J. Michon, Y. Zhang, Z. Fang, L. Deng, T. Gu, H. Zhang, J. Hu, Ultra-Thin High-Efficiency Mid-Infrared Transmissive Huygens Meta-Optics. *Nat Commun.* **9**, 1481 (2018).

59. M. Decker, I. Staude, M. Falkner, J. Dominguez, D.N. Neshev, I. Brener, T. Pertsch, Y.S. Kivshar, High-fficiency Dielectric Huygens' Surfaces. *Adv. Opt. Mater.* **3**, 813 (2015).

60. S. Pancharatnam, Generalized theory of interference, and its applications. Part I: Coherent pencils. *Proc. Indian Acad. Sci. Sect.A* **44**, 247 (1956).

61. M. Berry, Quantal phase factors accompanying adiabatic phase changes. *Proc. R. Soc. London A* **392**, 45 (1984).

62. L. Huang, X. Chen, H. Mühlenbernd, G. Li, B. Bai, Q. Tan, G. Jin, T. Zentgraf, S. Zhang, Dispersionless phase continuites for controlling light propagation. *Nano lett.* **12**, 5750 (2012).

63. X. Chen, L. Huang, H. Muhlenbernd, G. Li, B. Bai, Q. Tan, G. Jin, C-W. Qiu, S. Zhang, T. Zentgraf, Dual polarity plasmonic metalens for visible light. *Nature Commun.* **3**, 1198 (2012).

64. M. Kang, T. Feng, H.-T. Wang, J. Li, Wave front enginerring from an array of thin aperture antennas. *Opt. Express* **14**, 15882 (2012).

65. M. Shioi, H. Jans, K. Lodewijks, P.V. Dorpe, L. Lage, T. Kawamura, Tuning the interaction between propagating and localized surface plasmons for surface enhanced Raman scattering in water for biomedical and environmental applications. *Appl. Phys. Lett.* **104**, 243102 (2014).

66. Y. Chu, M.G. Banaee, K.B. Crozier, Double-resonance plasmon substrates for surface-enhanced raman scattering with enhancedment at excitation and stokes frequencies. *ACS Nano* **4**, 2804 (2010).

67. X. Zhang, Y. Zheng, X. Liu, W. Lu, J. Dai, D.Y. Lei, D.R. MacFarlane, Hierarchical porous plasmonic metamaterials for reproducible ultrasensitive surface-enhanced Raman spectroscopy. *Adv. Mater.* **27**,1090 (2015).

68. A. E. Cetin; C. Yilmaz; B. C. Galarreta; G. Yilmaz; H. Altug, A. Busnaina, Fabrication of Sub-10-nm Plasmonic Gaps for Ultra-Sensitive Raman Spectroscopy. Plasmonics. (2020).

69. Y. Lee, S-J Kim, H. Park, B. Lee, Metamaterials and Metasurfaces for Sensor Applications. *Sensors* **17**, 1726 (2017).

70. N. Bontempi, K.E. Chong, H.W. Orton, I. Staude, D.-Y. Choi, I. Alessandri, Y.S. Kivshar, D.N. Neshev, Highly sensitive biosensors based on all-dielectric nanoresonators. *Nanoscale* **9**, 4972 (2017).

71. A. Belushkin, F. Yesilkoy, J.J. Gonzalez-Lopez, J.C. Ruiz-Rodriguez; R. Ferrer, A. Fabrega, H.Altug, Rapid and Digital Detection of Inflammatory Biomarkers Enabled by a Novel Portable Nanoplasmonic Imager. *Small* **16**, 1906108 (2019).

72. F. Yesilkoy, E. R. Arvelo, Y. Jahani, M. Liu, A. Tittl, V. Cevher, Y. Kivshar, H.Altug, Ultrasensitive hyperspectral imaging and biodetection enabled by dielectric metasurfaces. *Nat. Photonics* **13**, 390 (2019).

73. A. Tittl, A. Leitis, M. Liu, F. Yesilkoy, D-Y. Choi, D.N. Neshev, Y. Kivshar, H. Altug, Imaging-based molecular barcoding with pixelated dielectric metasurfaces. *Science* **360**, 1105 (2018).

74. D. Ray, T. V. Raziman, C. Santschi, A. Tittl, D. Etezadi, H. Altug, O. J. F. Martin, Hybrid metal-dielectric metasurfaces for refractive index sensing. Conference on Lasers and Electro-Optics, JTh2A.74, Optical Society of America, (2018).

75. J.L. Gervais, C. Flytzanis, S. Haroche, G. Laval, Cours de Physique III-A : Matière et Rayonnement, Ecole Polytechnique, Edition1984.

76. G. Li, S. Zhang, T. Zentgraf, Nonlinear photonic metasurfaces. *Nat. Rev. Mater.* **1**, 17010 (2017).

77. E. Almeida, G. Shalem, Y. Prior, Subwavelength nonlinear phase control and anomalous phase matching in plasmonic metasurfaces. *Nat. Commun.* **7**, 10367 (2016)

78. T. Ellenbogen, N. Voloch-Bloch, A. Ganany-Padowicz, A. Arie, Nonlinear generation and manipulation of Airy beams. *Nat. Photonics* **3**, 395–398 (2009).

79. G. Li, S. Chen, Y. Cai, S. Zhang, K.W. Cheah, Third harmonic generation of optical vortices using holography based gold-fork microstructure. *Adv. Opt. Mater.* **2**, 389–393 (2014).

80. E. Almeida, O. Bitton, Y. Prior, Nonlinear metamaterials for holography. *Nat. Commun.* **7**, 12533 (2016).

81. W.Ye, F. Zeuner, X. Li, B. Reineke, S. He, C-W. Qiu, J. Liu, Y. Wang, S. Zhang, T. Zentgraf, Spin and wavelength multiplexed nonlinear metasurface holography. *Nat. Commun.* **7**, 11930 (2016).

82. P. Del'Haye, A. Schliesser, O. Arcizet, T. Wilken, R. Holzwarth, T.J. Kippenberg, Optical frequency comb generation from a monolithic microresonator. *Nature* **450**, 1214 (2007).

83. V.R. Almeida, C.A. Barrios, R.R. Panepucci, M. Lipson, All-optical control of light on a silicon chip. *Nature* **431**, 1081 (2004).

84. K. Nozaki, A. Shinya, S. Matsuo, Y. Suzaki, T. Segawa, T. Sato, Y. Kawaguchi, R. Takahashi, M. Notomi, Ultralow-power all-optical RAM based on nanocavities. *Nat. Photonics* **6**, 248 (2012).

85. L. Martin-Monier, T. Das Gupta, W. Yan, S. Lacour, F. Sorin, Nanoscale Controlled Oxidation of Liquid Metals for Stretchable Electronics and Photonics. *Adv. Funct. Mater.,* 2006711 (2020).

86. H-S. Ee, R. Agarwal, Tunable Metasurface and Flat Optical Zoom Lens on a Stretchable Substrate. *Nano Lett.* **16**, 2818-2823 (2016).

87. F. Lütolf, D. Casari, B. Gallinet, Low-Cost and Large-Area Strain Sensors Based on Plasmonic Fano Resonances. *Adv. Opt. Mater.* **4**, 715-721 (2016).

88. T. Lewi, H.A. Evans, N.A. Butakov, J.A. Schuller, Ultrawide Thermo-optic Tuning of PbTe Meta-Atoms. *Nano Lett.* **17**, 3940-3945 (2017).

89. M. Rahmani, L. Xu, A.E. Miroshnichenko, A. Komar, R. Camacho-Morales, H. Chen, Y. Zárate, S. Kruk, G. Zhang, D.N. Neshev, Y.S. Kivshar, Reversible Thermal Tuning of All-Dielectric Metasurfaces. *Adv. Funct. Mater.* **27**, 1700580 (2017).

90. L. Cong, Y. Kumar Srivastava, H. Zhang, X. Zhang, J. Han, R. Singh, All-Optical Active THz Metasurfaces for Ultrafast Polarization Switching and Dynamic Beam Splitting. *Light Sci. App.* **7**, 28 (2018).

91. M.R. Shcherbakov, P.P. Vabishchevich, A.S. Shorokhov, K.E. Chong, D-Y. Choi, I. Staude, A.E. Miroshnichenko, D.N. Neshev, A.A. Fedyanin, Y.S. Kivshar, Ultrafast All-Optical Switching with Magnetic Resonances in Nonlinear Dielectric Nanostructures. *Nano Lett.* **15**, 6985 (2015).

92. M. Decker, C. Kremers, A. Minovich, I. Staude, A.E. Miroshnichenko, D. Chigrin, D.N. Neshev, C. Jagadish, Y.S. Kivshar, Electro-Optical Switching by Liquid-Crystal Controlled Metasurfaces. *Opt. Express* **21**, 8879 (2013).

93. P.C. Wu, R.A. Pala, G.K. Shirmanesh, W-H. Cheng, R. Sokhoyan, M. Grajower, M.Z. Alam, D. Lee, H.A. Atwater, Dynamic Beam Steering with All-Dielectric Electro-Optic III–V Multiple-Quantum-Well Metasurfaces. *Nat. Commun.* **10**, 3654 (2019).

94. P.P Iyer, M. Pendharkar, J.A. Schuller, Electrically Reconfigurable Metasurfaces Using Heterojunction Resonators. *Adv. Opt. Mater.* **4**, 1582 (2016).

95. S. Abdollahramezani, O. Hemmatyar, H. Taghinejad, A. Krasnok, Y. Kiarashinejad, M. Zandehshahvar, A. Alù, A. Adibi, Tunable Nanophotonics Enabled by Chalcogenide Phase-Change Materials. *Nanophotonics* **9**, 1189 (2020).

96. Y. Zhang, J.B. Chou, J. Li, H. Li, Q. Du, A. Yadav, S. Zhou, M.Y. Shalaginov, Z. Fang, H. Zhong, C. Roberts, P. Robinson, B. Bohlin, C. Rios, H. Lin, M. Kang, T. Gu, J. Warner, V. Liberman, K. Richardson, J. Hu, Broadband Transparent Optical Phase Change Materials for High-Performance Nonvolatile Photonics. *Nat. Commun.* **10**, 4279 (2019).

97. Q. Wang, E. Rogers, B. Gholipour, C-M. Wang, G. Yuan, J. Teng, N.I. Zheludev, Optically reconfigurable metasurfaces and photonic devices based on phase change materials. *Nat. Photonics* **10**, 60–65 (2016).

98. X. Yin, T. Steinle, L. Huang, T. Taubner, M. Wuttig, T. Zentgraf, H. Giessen, Beam switching and bifocal zoom lensing using active plasmonic metasurfaces. Light Sci. Appl. **6**, 17016 (2017).

99. K. Dong, S. Hong, Y. Deng, H. Ma, J. Li, X. Wang, J. Yeo, L. Wang, S. Lou, K.B. Tom, K. Liu, Z. You, Y. Wei, C.P. Grigoropoulos, J. Yao, J. Wu, A Lithography-Free and Field-Programmable Photonic Metacanvas. *Adv. Mater.* **30**, 1703878 (2018).

100. C.R. De Galarreta, A.M. Alexeev, Y-Y. Au, M. Lopez-Garcia, M. Klemm, M. Cryan, J. Bertolotti, C.D. Wright, Nonvolatile Reconfigurable Phase-Change Metadevices for Beam Steering in the Near Infrared. *Adv. Funct. Mater.* **28**, 1704993 (2018).

101. A. Leitis, A. Heßler, S. Wahl, M. Wuttig, T. Taubner, A. Tittl, H. Altug, All-Dielectric Programmable Huygens' Metasurfaces. *Adv. Funct. Mater.* **30**, 1910259 (2020).

102. H. Chen, W-B. Lu, Z-G. Liu, M-Y. Geng, Microwave programmable Graphene Metasurface. *ACS Photonics* **6**, 1425 (2020).

103. L. Li, H. Lin, S. Qiao, Y-Z. Huang, J-Y. Li, J. Michon, T. Gu, C. Alosno-Ramos, L. Vivien, A. Yadav, K. Richardson, N. Lu, J. Hu, Monolithically integrated stretchable photonics. *Light. Sci. Appl.* **7**, 17138 (2018).

104. A. Leber, C. Dong, R. Chandran, T. Das Gupta, N. Bartolomei, F. Sorin., *Nat. Electron.* **3**, 316 (2020).

105. Y. Qu, T. Nguyen-Dang, A. G. Page, W. Yan, T. Das Gupta, G. M. Rotaru, R. M. Rossi, V. D. Favrod, N. Bartolomei, F. Sorin, *Adv. Mater.* **30**, 1707251 (2018).

106. T.Yamada, Y. Hayamizu, Y. Yamamoto, Y. Yomogida, A. Izadi-Najafabadi, D. N. Futaba, K. Hata, *Nat. Nanotech.,* **6**, 296 (2011).

107. V. Cacucciolo, J. Shintake, Y. Kuwajima, S. Maeda, D. Floreano, H. Shea, Stretchable pumps for soft machines. *Nature* **572**, 516 (2019).

108. J. Shintake, V. Cacucciolo, H. Shea, D. Floreano, Soft biomimetic fish robot made of dielectric elastomer actuators. *Soft Robotics* **5**, 466 (2018).

109. G. Agarwal, N. Besuchet, B. Audergon, J. Paik, Stretchable materials for robust soft actuators towards assistive wearable devices. *Sci. Rep.* **6**, 34224 (2016).

110. W. Luheng, D. Tianhuai, W. Peng, Influence of carbon black concentration on piezoresistivity for carbon-black-filled silicone rubber composite. *Carbon* **47**, 3151 (2009).

111. N. Hu, Y. Karube, M. Arai, T. Watanabe, C. Yan, Y. Li, Y. Liu, H. Fukunaga, Investigation on sensitivity of a polymer/carbon nanotube composite strain sensor. *Carbon* **48**, 680 (2010).

112. F. Xu, Y. Zhu, Highly conductive and stretchable silver nanowire conductors. *Adv. Mat.* **24**, 5117 (2012).

113. P. Lee, J. Lee, H. Lee, J. Yeo, S. Hong, K. H. Nam, D. Lee, S. S. Lee, S. H. Ko, Highly stretchable and highly conductive metal electrode by very long metal nanowire percolation network. *Adv. Mater.* **24**, 3326 (2012).

114. L. Jin, A. Chortos, F. Lian, E. Pop, C. Linder, Z. Bao, W. Cai, Microstructural origin of resistance–strain hysteresis in carbon nanotube thin film conductors. *Proc. Natl. Ac. Sci.* **115**, 1986 (2018).

115. L. Martin-Monier, T. Das Gupta, W. Yan, S. Lacour, F. Sorin, Nanoscale Controlled Oxidation of Liquid Metals for Stretchable Electronics and Photonics. *Adv. Funct. Mater.,* 2006711 (2020).

116. C. Thrasher, Z. Farrell, N. Morris, C. Willey, C. Tabor, Mechanoresponsive polymerized liquid metal networks. *Adv. Mat.* **20**, 1903864 (2019).

117. J. A. Fan, W.-H. Yeo, Y. Su, Y. Hattori, W. Lee, S.-Y. Jung, Y. Zhang, Z. Liu, H. Cheng, L. Falgout, M. Bajema, T. Colema, D. Gregoire, R.J. Larsen, Y. Huang, J. A. Rogers, Fractal design concepts for stretchable electronics. *Nat. Comm.* **5**, 3266 (2014).

118. O.A. Araromi, A. Oluwaseun, A.Moritz, A. Graule, K, L. Dorsey, S. Castellanos, J. R. Foster, W.-H. Hsu, A.E. Passy, J.J. Vlassak, J.C.Weaver, C.J.Walsh, R.J.Wood, Novel design strategies for modulating conductive stretchable system response based on periodic assemblies. *Nature* **587**, 219 (2020).

119. D. G. Baranov, D. A. Zuev, S. I. Lepeshov, O. V. Kotov, A. E. Krasnok, A. B. Evlyukhin, B. N. Chichkov, All-dielectric nanophotonics: the quest for better materials and fabrication techniques. *Optica* **4**, 814 (2017).

120. V. R. Manfrinato, L. Zhang, D. Su, H. Duan, R. G. Hobbs, E. A. Stach, K. K. Berggren, Resolution limits of electron-beam lithography toward the atomic scale. *Nano Lett.* **13**, 1555 (2013).

121. S. Hara, H. Wada, A. Shimojima, K. Kuroda, Formation of nanogrooves with sub-5 nm periodicity using local silicification at the interspace between a si substrate and lyotropic liquid crystals. *ACS Nano* **11**, 5160 (2017).

122. V. R. Manfrinato, A. Stein, L. Zhang, C.-Y. Nam, K. G. Yager, E. A. Stach, C. T. Black, Aberration-corrected electron beam lithography at the one nanometer length scale. *Nano Lett.* **17**, 4562–4567.

123. S. Okamoto, K. Inaba, T. Iida, H. Ishihara, S. Ichikawa, M. Ashida, Fabrication of singlecrystalline microspheres with high sphericity from anisotropic materials. *Sci. Rep.* **4**, 5186 (2014).

124. L. Shi, J. T. Harris, R. Fenollosa, I. Rodriguez, X. Lu, B. A. Korgel, F. Meseguer, "Monodisperse silicon nanocavities and photonic crystals with magnetic response in the optical region. *Nat. Commun.* **4**, 1904 (2013).

125. M. R. Beaulieu, N. R. Hendricks, J. J. Watkins, Large-area printing of optical gratings and 3d photonic crystals using solution-processable nanoparticle/polymer composites. *ACS Photonics* **1**, 799 (2014).

126. E. Miele, S. Raj, Z. Baraissov, P. Král, and U. Mirsaidov, "Dynamics of templated assembly of nanoparticle filaments within nanochannels. *Adv. Mater.* **29**, 1702682 (2017).

127. X. Ji, H.Y. Cheng, A.J. Grede, A. Molina, D. Talreja, S.E. Mohney, N.C. Giebink, J.V. Badding, V. Gopalan, Conformal coating of amorphous silicon and germanium by high pressure chemical vapor deposition for photovoltaic fabrics. *APL Materials* **6**, 046105 (2018): 046105.

128. A.B. Evlyukhin, S. M. Novikov, U. Zywietz, R. L. Eriksen, C. Reinhardt, S. I. Bozhevolnyi, B. N. Chichkov, Demonstration of magnetic dipole resonances of dielectric nanospheres in the visible region. Nano Lett. **12**, 3749 (2012).

129. J. Bohandy, B. F. Kim, F. J. Adrian, A. N. Jette, Metal deposition at 532 nm using a laser transfer technique. *J. Appl. Phys.* **63**, 1158 (1988).

130. A. Verma & A. Sharma, Self-organized nano-lens arrays by intensified dewetting of electron beam modified polymer thin-films. *Soft Matter* **7**, 11119 (2011).

131. J. Z. Wang, Z. H. Zheng, H. W. Li, W. T. S. Huck, H. Sirringhaus, Dewetting of conducting polymer inkjet droplets on patterned surfaces. *Nat. Mater.* **3**, 171 (2004).

132. D. Gentili, G. Foschi, F. Valle, M. Cavallini, and F. Biscarini, "Applications of dewetting in micro and nanotechnology. *Chem. Soc. Rev.* **41**, 4430 (2012).

133. Deng, D. S., Nave, J.-C., Liang, X., Johnson, S. G. and Fink, Y. Exploration of in-fiber nanostructures from capillary instability. *Opt. Exp.* **19,** 16273 (2011)

134. Yan, W. et al. Advanced multimaterial electronic and optoelectronic fibers and textiles. *Adv. Mat.* 1802348 (2018).

135. Y. Zha & C.B. Arnold, Solution-processing of thick chalcogenide-chalcogenide and metal-chalcogenide structures by spin-coating and multilayer lamination. *Opt. Mat. Exp.* **3,** 309 (2013).

136. Kohoutek, T., Orava, J., Lindsay Greer, A., and Fudouzi,H. Sub-micrometer soft lithography of a bulk chalcogenide glass. *Opt Exp*. **21,** 9584 (2013).

137. B.J. Eggleton, B. Luther-Davies, K.Richardson. Chalcogenide photonics. *Nat. Phot.* **5,** 141 (2011).

138. H. Peiman, C.D. Wright, H. Bhaskaran, An optoelectronic framework enabled by low-dimensional phase-change films. *Nature.* **511,** 206 (2014).

139. W. Yan, Y. Qu, T.D. Gupta, A. Darga, T. Nguyen-Dang, A.G. Page, M. Rossi, M. Ceriotti, F. Sorin, Semiconducting nanowire-based optoelectronic fibers. *Adv. Mat.* **29,** 1700681 (2017).

140. T.D. Gupta, L. Martin-Monier, W. Yan, A. Le Bris, T. Nguyen-Dang, A.G. Page, K-T. Ho, F. Yesilkoy, H. Altug, F. Sorin. Self-Assembly of Nanostructured Glass Metasurfaces via Templated Fluid Instabilities ». *Nat. Nanotech.* **14**, 320 (2019).

141. Y. Zou, L. Moreel, H. Lin, J. Zhou, L. Li, S. Danto, J. David-Musgraves, E. Koontz, K. Richardson, K.D. Dobson, R. Birkmire, J. Hu, Solution Processing and Resist-Free Nanoimprint fabrication of thin film chalcogenide glass devices: Inorganic–organic hybrid photonic integration. *Adv. Opt. Mat.* **2,** 759 (2014).

142. W. Yan, I. Richard, G. Kurtuldu, N.D. James, G. Schiavone, J.W. Squair, T. Nguyen-Dang, T. Das Gupta, Y. Qu, J.D. Cao, R. Ignatans, S.P. Lacour, V. Tileli, G. Courtine, J.F. Löffler, F. Sorin, Structured Nanoscale Metallic Glass Fibres with Extreme Aspect Ratios. *Nature Nanotechnology* **15**, 875 (2020).

143. Wang, Q. et al. Optically Reconfigurable metasurfaces and photonic devices based on phase change materials. *Nat. Phot.* **10,** 60 (2016).

144. R.W. Style, C. Hyland, R. Boltyanskiy, J.S. Wettlaufer, E.R. Dufresne, Surface tension and contact with soft elastic solids. *Nat. Commun.* **4,** 2728 (2013).

145. J-G. Liu & U. Mitsuru, High refractive index polymers: fundamental research and practical applications. *J. Mater. Chem.* **19**, 8907-8919 (2009).

146. T.D. Gupta, I. Maurin, A.C.H. Rowe, T. Gacoin, Ultrafine Tuning of the Metal Volume Fraction in Silver/Silicate Nano-composites near the Percolation Threshold. *Nanoscale.* **9,** 3504-3511 (2017).

147. B. Brudieu, A. Le Bris, J. Teisseire, F. Guillemot, G. Dantelle, S. Misra, P. Roca i Cabarrocas, F. Sorin, T. Gacoin, Sol–Gel Route Toward Efficient and Robust Distributed Bragg Reflectors for Light Management Applications. *Adv. Opt. Mat.* **2,** 1105 (2014).

148. M. Yaman, T. Khudiyev, E. Ozgur, M. Kanik, O. Aktas, E.O. Ozgur, H. Deniz, E. Korkut, M. Bayindir, Arrays of indefinitely long uniform nanowires and nanotubes. *Nat. Mater.* **10,** 494–501 (2011)

149. A.F. Abouraddy, M. Bayindir, G. Benoit, S. D. Hart, K. Kuriki, N. Orf, O. Shapira, F. Sorin, B. Temelkuran, Y. Fink. Towards Multimaterial Multifunctional Fibres That See, Hear, Sense and Communicate. *Nat. Mater* **6**, 336 (2007).

150. D.S. Deng, J.-C. Nave, X. Liang, S. G. Johnson, Y. Fink, Exploration of In-Fiber Nanostructures from Capillary Instability. *Opt. Express* **19**, 16273 (2011).

151. T. Nguyen-Dang, A.C. de Luca, W. Yan, Y. Qu, A.G. Page, M. Volpi, T. Das Gupta, S.P. Lacour, F. Sorin. Controlled Sub-Micrometer Hierarchical Textures Engineered in Polymeric Fibers and Microchannels via Thermal Drawing . *Advanced Funct. Mater.* **27**, (2017).

152. A.S. Tverjanovich, Temperature dependence of the viscosity of chalcogenide glass-forming melts. *Glass Phys. Chem.* **29**, 532 (2003)

153. A. Sharma and R. Khanna, Pattern Formation in Unstable Thin Liquid Films. *Phys. Rev. Lett.* **81**, 3463 (1998).

154. J. Bischof, D. Scherer, S. Herminghaus, P. Leiderer, Dewetting Modes of Thin Metallic Films: Nucleation of Holes and Spinodal Dewetting. *Phys. Rev. Lett.* **77**, 1536-39 (1996).

155. R. Xie, A. Karim, J.F. Douglas, C.C. Han, R.A. Weiss, Spinodal Dewetting of Thin Polymer Films. *Phys. Rev. Lett.* **81**, 1251-1254 (1998).

156. U. Thiele, M. Mertig, W. Pompe, Dewetting of an Evaporating Thin Liquid Film: Heterogeneous Nucleation and Surface Instability. *Phys. Rev. Lett.* **80**, 2869-2872 (1998).

157. U. Thiele, M.G. Verlarde, Dewetting: film rupture by nucleation in the spinodal regime. *Phys. Rev. Lett* **87**, 016104 (2001).

158. L. Rayleigh, On the Instability of a Cylinder of Viscous Fluid Under Capillary Force. *Phil. Mag.* **34,** 145-54 (1892).

159. S. Chandrasekhar, Hydrodynamic and Hydromagnetic Stability. New York, Dover (1961).

160. G. Boussinot & A. Efim, Brener. Inhibition of Rayleigh-Plateau instability on a unidirectionally patterned substrate. *Physical Review E* **92**, 032408 (2015).

161. K. Khare, S. Herminghaus, J.-C. Baret, B.M. Law, M. Brinkmann, R. Seemann, Switching Liquid Morphologies on Linear Grooves. *Langmuir* **23**, 12997 (2007).

162. A. Oron, S.H. Davis, S.G. Bankoff, Long-scale evolution of thin liquid films. *Rev. Mod. Phys.* **69**, 931 (1997).

163. J. Becker, G. Grün, R. Seemann, H. Mantz, K. Jacobs, K. R. Mecke, R. Blossey, Complex Dewetting Scenarios Captured by Thin-Film Models. *Nat. Mater.* **2**, 59 (2002).

164. V. S. Mitlin, Dewetting of Solid Surface: Analogy with Spinodal Decomposition, *J. Colloid Interface Sci.* **156**, 491 (1993).

165. A. Sharma & R. Khanna, Pattern Formation in Unstable Thin Liquid Films. *Phys. Rev. Lett.* **81**, 3463 (1998).

166. C. Maldarelli, R.K. Jain, I.B. Ivanov, Stability of Symmetric and Unsymmetric Thin Liquid Films to Short and Long Wavelength Perturbations, *J. Colloid Interf. Sci.* **78**, 118 (1980).

167. I.B. Ivanov, Thin Liqui Films, Ed., Marcel Dekker, Inc., New York, 1988

168. E.M. Lifschitz , The Theory of Molecular Attractive Forces between Solids. *Exper. Theoret. Phys. USSR* **29**, 94 (1955).

169. J. Israelichvili, Intermolecular and Surface Forces, Third Edition 2011

170. S.D.R. Wilson, The drag-out problem in film coating theory. *J. Eng. Math.* **16**, 209 (1982).

171. G. Lerisson, P. G. Ledda, G. Balestra, F. Gallaire, Instability of a thin viscous film flowing under an inclined substrate: steady patterns. *J. Fluid. Mech.* **898**, A6 (2020).

172. P.G. Ledda, G. Lerisson, G. Balestra, F. Gallaire, Instability of a thin viscous film flowing under an inclined substrate: the emergence and stability of rivulets. *J. Fluid Mech.* **904** (2020).

173. E. Jambon-Puillet, P.G. Ledda, F. Gallaire, P.T. Brun, Too fast to grow: Dynamics of pendant drops sliding on a thin film, arXiv preprint arXiv:2012.05941 (2020).

174. P.G. Ledda, G. Balestra, G. Lerisson, B. Scheid, M. Wyart, F Gallaire, Hydrodynamic-driven morphogenesis of karst draperies: spatio-temporal analysis of the two-dimensional impulse response, *J. Fluid Mech.* **910** (2021)

175. B. Xu, M. Li, F. Wang, S.G. Johnson, Y. Fink, D. Deng, Filament formation via the instability of a stretching viscous sheet: Physical mechanism, linear theory, and fiber applications. *Phys. Rev. Fluids* **4**, 073902 (2019).

176. X. Liang, Modeling of fluids and waves with analytics and numerics, Ph.D. thesis, Massachusetts Institute of Technology, 2013

177. B. Scheid, S. Quiligotti, B. Tran, H. A. Stone, Lateral shaping and stability of a stretching viscous sheet, *Eur. Phys. J. B* **68**, 487 (2009).

178. I.B. Ivanov, *Thin Liquid Films: Fundamentals and Applications*. Surfactant Science Series, **29**, Marcel Dekker Inc, New York, U.S.A. (1998).

179. R.K. Jain, C. Maldarelli, Stability of Thin Viscoelastic Films with Applications to Biological Membrane Deformation. *Annals of the New York Academy of Sciences* **404**, 89 (1983).

180. C. Maldarelli, R.K. Jain, I.B. Ivanov, Stability of Smmetric and Unsymmetric Thin Liquid Films to Short and Long Wavelength Perturbations. *J. Colloid Interf. Sci.* **78**, 118 (1980).

181. A.G. Page, M. Bechert, F. Gallaire, F. Sorin, Unraveling radial dependency effects in fiber thermal drawing. *Appl. Phys. Lett.* **115**, 044102 (2019).

182. F.M. Fowkes, Dispersion Force Contributions to Surface and Interfacial Tensions, Contact Angles, and Heats of Immersion. *Contact Angle, Wettability, and Adhesion* **43**, 99(1964).

183. T. Nguyen-Dang, A.C. de Luca, W. Yan, Y. Qu, A.G. Page, M. Volpi, T. Das Gupta, S.P. Lacour, F. Sorin, Controlled Sub-Micrometer Hierarchical Textures Engineered in Polymeric Fibers and Microchannels via Thermal Drawing. *Advanced Functional Materials* **27**, 1605935 (2017).

184. O. Yavas, M. Svedendahl, P. Dobosz, V. Sanz, R. Quidant. "On-a-Chip Biosensing Based on All-Dielectric Nanoresonators." *Nano Lett.* **17**, 4421 (2017).

185. N. Bontempi, K. E. Chong, H. W. Orton, I. Staude, D.-Y. Choi, I. Alessandri, Y. S. Kivshar, D. N. Neshev, Highly Sensitive Biosensors Based on All-Dielectric Nanoresonators. *Nanoscale* **9**, 4972 (2017).

186. A. Tittl, A. Leitis, M. Liu, F. Yesilkoy, D.-Y. Choi, D. N. Neshev, Y. S. Kivshar, H. Altug. Imaging-Based Molecular Barcoding with Pixelated Dielectric Metasurfaces. *Science* **360**, 1105 (2018).

187. A.A. Yanik,A. E. Cetin, M. Huang, A. Artar, S. H. Mousavi, A. Khanikaev, J. H. Connor, G. Shvets, H. Altug, Seeing Protein Monolayers with Naked Eye through Plasmonic Fano Resonances. *Proc. Natl. Ac. Sci. U.S.A* **108**, 11784 (2011).

188. J. Anker, P. Hall, O. Lyandres, N. Shah, J. Zhao, R. Van Duyne. Biosensing with Plasmonic Nanosensors. *Nat. Materials* **7**, 442 (2008).

189. Y. Yang, I.I. Kravchenko, D.P. Briggs, J. Valentine, All-Dielectric Metasurface Analogue of Electromagnetically Induced Transparency. *Nat. Communications* **5**, 5753 (2014).

190. M. Decker, I. Staude. Resonant Dielectric Nanostructures: A Low-Loss Platform for Functional Nanophotonics. *J. Optics* **18**, 103001 (2016).

191. F. Yesilkoy, R.A Terborg, J. Pello, A.A Belushkin, Y. Jahani, V. Pruneri, H. Altug, Phase-sensitive plasmonic biosensor using a portable and large field-of-view interferometric microarray imager. *Light Sci. App.* **7,** 17152 (2018).

192. Bohren, Craig F., and Donald R. Huffman, Absorption and Scattering of Light by Small Particles. Weinheim: Wiley-VCH, 2004.

193. S. Cai, Y. Zhang, H. Zhang, H. Yan, H. Lv, B Jiang, Sol−Gel Preparation of Hydrophobic Silica Antireflective Coatings with Low Refractive Index by Base/Acid Two-Step Catalysis. *ACS Appl. Mater. Interfaces* 6, 11470 (2014).

194. S.V. Makarov, M.I. Petrov, U. Zywietz, V. Milichko, D. Zuev, N. Lopanitsyna, A. Kuksin, I. Mukhin, G. Zograf, E. Ubyivovk, D.A. Smirnova, S. Starikov, B.N. Chichkov, Y.S. Kivshar, *Nano Lett.* **17**, 3047 (2017).

195. K. Y. Yang, J. Butet, C. Yan, G. D. Bernasconi, O. J. F. Martin, *ACS Photonics*, 2017, **4**, 1522–1530.

196. V.E. Babicheva, A.B. Evlyukhin, Resonant lattice Kerker effect in metasurfaces with electric and magnetic optical responses. *Laser Phot. Rev.*. **11,** 1700132 (2017).

197. J. Han & A. Lakhtakia, Semiconductor split-ring resonators for thermally tunable terahertz metamaterials. *J. Modern Optics* **56**, 554 (2009).

198. Li, Guixin, Shuang Zhang, et Thomas Zentgraf. « Nonlinear Photonic Metasurfaces ». *Nat. Rev. Mater.* **2**, 17010 (2017).

199. R. Paniagua-Domínguez, Y.F. Yu, A.E. Miroshnichenko, L.A. Krivitsky, Y.H. Fu, V. Valuckas, L. Gonzaga, Y.T. Toh, A.Y. Kay, B. Luk'yanchuk, A. Kuznetsov, Generalized Brewster Effect in Dielectric Metasurfaces. *Nat. Commun.* **7**, 10362 (2016).

200. M.S. Wheeler, J. Stewart Aitchison, M. Mojahedi, Coupled Magnetic Dipole Resonances in Sub-Wavelength Dielectric Particle Clusters. *JOSA B* 27, 1083 (2010).

201. F. Zhang, L. Kang, Q. Zhao, J. Zhou, D. Lippens, Magnetic and Electric Coupling Effects of Dielectric Metamaterial ». *New Journal of Physics* **14**, 033031 (2012).

202. A.E. Miroshnichenko, A.B. Evlyukhin, Y.F. Yu, R.M. Bakker, A. Chipouline, A.I. Kuznetsov, B. Luk'yanchuk, B.N. Chichkov, Y.S. Kivshar, Nonradiating Anapole Modes in Dielectric Nanoparticles, *Nat. Commun* **6**, 8069 (2015).

203. H-T. Chen, A.J. Taylor, N. Yu., A Review of Metasurfaces: Physics and Applications. *Rep. Prog. Phys.* **79**, 076401 (2016).

204. M.D. Dickey, Stretchable and Soft Electronics using Liquid Metals. *Adv. Mater.* **29**, 1606425 (2017).

205. M. Cianchetti, C. Laschi, A. Menciassi, P. Dario, Biomedical applications of soft robotics. *Nat. Rev. Mater.* **3**, 143 (2018).

206. S. Palagi, P. Fischer, Bioinspired microrobots. *Nat. Rev. Materials* **3**, 113 (2018).

207. J.A. Rogers, Z. Bao, K. Baldwin, A. Dodabalapur, B. Crone, V.R. Raju, V. Kuck, H. Katz, K. Amundson, J. Ewing, P. Drzaic, Paper-like electronic displays: Large-area rubber-stamped plastic sheets of electronics and microencapsulated electrophoretic inks. *Proc. Natl. Acad. Sci.* **98**, 4835 (2001).

208. T. Sekitani, T. Someya, Stretchable, large-area organic electronics. *Adv. Mater.* **22**, 2228 (2010).

209. S.C. Malek, H-S. Ee, R. Agarwal, Strain multiplexed metasurface holograms on a stretchable substrate. *Nano Lett.*. **17**, 3641 (2017).

210. I.M. Pryce, K. Aydin, Y.A. Kelaita, R.M. Briggs, H.A. Atwater, Highly strained compliant optical metamaterials with large frequency tunability. *Nano Letters* **10**, 4222 (2010).

211. S.C. Ambhire, S. Palkhivala, A. Agrawal, A. Gupta, G. Rana, R. Mehta, D. Ghindani, A. Bhattacharya, V.G. Achanta, S.S. Prabhu, "Pattern and Peel" method for fabricating mechanically tunable terahertz metasurface on an elastomeric substrate. *Opt. Mat. Express* **8**, 3382 (2018).

212. P.C. Wu, R.A. Pala, G.K. Shirmanesh, W-H. Cheng, R. Sokhoyan, M. Grajower, M.Z. Alam, D. Lee, H.A. Atwater, Dynamic beam steering with all-dielectric electro-optic III–V multiple-quantum-well metasurfaces. *Nat. Commun.* **10**, 1 (2019).

213. M. Decker, C. Kremers, A. Minovich, I. Staude, A.E. Miroshnichenko, D. Chigrin, D.N. Neshev, C. Jagadish, Y.S. Kivshar, Electro-optical switching by liquid-crystal controlled metasurfaces. *Opt. Express* **21**, 8879 (2013).

214. S. Makarov, S. Kudryashov, I. Mukhin, A. Mozharov, V. Milichko, A. Krasnok, P. Belov, Tuning of magnetic optical response in a dielectric nanoparticle by ultrafast photoexcitation of dense electron–hole plasma. *Nano Lett.* **15**, 6187 (2015).

215. M.J. Dicken, K. Aydin, I.M. Pryce, L.A. Sweatlock, E.M. Boyd, S. Walavalkar, J. Ma, H.A. Atwater, Frequency tunable near-infrared metamaterials based on VO2 phase transition. *Opt. Express* **17**, 18330 (2009).

216. J. Sautter, I. Staude, M. Decker, E. Rusak, D.N. Neshev, I. Brener, Y.S. Kivshar, Active tuning of all-dielectric metasurfaces. *ACS Nano* **9**, 4308 (2015).

217. H. Tao, A.C. Strikwerda, K. Fan, W.J. Padilla, X. Zhang, R.D. Averitt, Reconfigurable terahertz metamaterials. *Phys. Rev. Lett.* **103**, 147401 (2009).

218. K.E. Spells, The determination of the viscosity of liquid gallium over an extended range of temperature. *Proc. Phys. Soc.* **48**, 299 (1936).

219. R.N. Lyon, *Liquid Metals Handbook*, Washington D.C, Office of Naval Research, US Dept. of Navy (1952).

220. W.M. Haynes, *CRC Handbook of Chemistry and Physics. 92nd Edition.*, Boca Raton, FL, USA 2012.

221. F.Geiger, C.A. Busse, R.I. Loehrke, The vapor pressure of indium, silver, gallium, copper, tin, and gold between 0.1 and 3.0 bar. *Int. J. of Thermophys.* **8**, 425 (1987).

222. S.C. Hardy, The surface tension of liquid gallium. *J. Crystal Growth* **71**, 602 (1985).

223. U. König, W. Keck, Measurement of the surface tension of gallium and indium in a hydrogen atmosphere by the sessile drop method. *J. Less Common Met.* **90**, 299 (1983).

224. T. Liu, P. Sen, C. Kim, Characterization of liquid-metal Galinstan® for droplet applications. *2010 IEEE 23rd International Conference on Micro Electro Mechanical Systems*, Wanchai, Hong Kong, 2010, p. 560.

225. B.A. Gozen, A. Tabatabai, O.B. Ozdoganlar, C. Majidi, High-density soft-matter electronics with micron-scale line width. *Adv. Mater.* **26**, 5211 (2014).

226. R.K. Kramer, C. Majidi, R.J. Wood, Masked deposition of gallium-indium alloys for liquid-embedded elastomer conductors. *Adv. Funct. Mater.* **23**, 5292 (2013).

227. J.W. Boley, E.L. White, R.K. Kramer, Mechanically sintered gallium–indium nanoparticles. *Adv. Mater.* **27**, 2355 (2015).

228. G. Li, X. Wu, D-W. Lee, A galinstan-based inkjet printing system for highly stretchable electronics with self-healing capability. *Lab on a Chip* **16**, 1366 (2016).

229. J-H. So, M.D. Dickey, Inherently aligned microfluidic electrodes composed of liquid metal. *Lab on a Chip* **11**, 905 (2011).

230. C.W. Park, Y.G. Moon, H. Seong, S.W. Jung, J.Y. Oh, B.S. Na, N.M. Park, S.S. Lee, S.G., Im, J.B. Koo, Photolithography-based patterning of liquid metal interconnects for monolithically integrated stretchable circuits. *ACS Appl. Mat. Inter.* **8**, 15459 (2016).

231. A. Tabatabai, A. Fassler, C. Usiak, C. Majidi, Liquid-phase gallium–indium alloy electronics with microcontact printing. *Langmuir* **29**, 6194 (2013).

232. A. Hirsch, H.O. Michaud, A.P. Gerratt, S. De Mulatier, S.P. Lacour, Intrinsically stretchable biphasic (solid–liquid) thin metal films. *Adv. Mater.* **28**, 4507 (2016).

233. A. Hirsch, S.P. Lacour, A method to form smooth films of liquid metal supported by elastomeric substrate. *Adv. Sci.* **5**, 1800256 (2018).

234. A. Hourlier-Fargette, A. Antkowiak, A. Chateauminois, S. Neukirch, Role of uncrosslinked chains in droplets dynamics on silicone elastomers. *Soft Matter* **13**, 3484 (2017).

235. K. Doudrick, S. Liu, E.M. Mutunga, K.L. Klein, V. Damle, K.K. Varanasi, K. Rykaczewski, Different shades of oxide: From nanoscale wetting mechanisms to contact printing of gallium-based liquid metals. *Langmuir* **30**, 6867 (2014).

236. M.J. Regan, H. Tostmann, P.S. Pershan, O.M. Magnussen, E. Dimasi, B.M. Ocko, X-ray study of the oxidation of liquid-gallium surfaces. *Phys. Rev. B* **55**, 10786 (1997).

237. A. Le Bris, F. Maloum, J. Teisseire, F. Sorin, Self-organized ordered silver nanoparticle arrays obtained by solid state dewetting. *Appl. Phys. Lett.* **105**, 203102 (2014).

238. D. Stauffer, A. Aharony, *Introduction To Percolation Theory*. CRC Press, Boca Raton FL, U.S.A. 1994.

239. M.E. Levinshtein, B.I. Shklovskii, M.S. Shur, A.L. Efros, Nonlinear effects in the emission of interstellar molecules. *Zh. Eksp. Teor. Fiz* **69**, 386 (1975).

240. N.I. Lebovka, S. S. Manna, S. Tarafdar, N. Teslenko, Percolation in models of thin film depositions. *Phys. Rev. E* **66**, 066134 (2002).

241. J.A. Räty, K-E. Peiponen, T. Asakura, *UV-Visible Reflection Spectroscopy of Liquids*, Springer 2013.

242. A.B. Kuzmenko, Kramers–Kronig constrained variational analysis of optical spectra. *Review of Scientific Instruments* **76**, 083108 (2005).

243. P. Volodin, A. Kondyurin, Dewetting of thin polymer film on rough substrate. *J. Phys D Appl. Phys.* **41**, 065306 (2008).

244. T.D. Gupta, L. Martin-Monier, W. Yan, A. Le Bris, T. Nguyen-Dang, A.G. Page, K-T. Ho, F. Yesilköy, H. Altug, Y. Qu, F. Sorin, Self-assembly of nanostructured glass metasurfaces via templated fluid instabilities. *Nat. Nanotech.* **14**, 320 (2019).

245. J.M. Chabala, Oxide-growth kinetics and fractal-like patterning across liquid gallium surfaces. *Phys. Rev. B*, **46**, 11346 (1992).

246. A. Roth. *Vacuum Technology*, Elsevier, Amsterdam 1990.

247. T.G Beckwith, N. L. Buck, R.D. Marangoni, *Mechanical Measurements*. Third Edition. Addison-Wesley Publishing Co., 1982.

248. R.H. Pritchard, P. Lava, D. Debruyne, E. M. Terentjev, Precise determination of the Poisson ratio in soft materials with 2D digital image correlation. *Soft Matter* **9**, 6037 (2013).

249. C.S. Smith, Piezoresistance effect in germanium and silicon *Phys. Rev.* **94**, 42 (1954).

250. S. Middlehoek. *Silicon Sensors*. Delft, The Netherlands: Delft University Press, 1994.

251. R. He, P. Yang, Giant piezoresistance effect in silicon nanowires. *Nat. Nanotech.* **1**, 42 (2006).

252. A.C.H. Rowe, A. Donoso-Barrera, C. Renner, S. Arscott, Giant room-temperature piezoresistance in a metal-silicon hybrid structure. *Phys. Rev. Lett.* 100, 145501 (2008).

253. J.Y. Yen, Finding the K Shortest Loopless Paths in a Network. *Manag. Sci.* **17**, 712 (1971).

254. W. Li, S. Yang, A. Shamim, Screen printing of silver nanowires: balancing conductivity with transparency while maintaining flexibility and stretchability. *npj Flex Electron* **3,** 13 (2019).

255. S. Zhang, H. Zhang, G. Yao, F. Liao, M. Gao, Z. Huang, K. Li, Y. Lin, Highly stretchable, sensitive, and flexible strain sensors based on silver nanoparticles/carbon nanotubes composites. *J. Alloys Compd.* **652**, 48 (2015).

256. J. Shintake, E. Piskarev, S. H. Jeong, D. Floreano, Ultrastretchable strain sensors using carbon black-filled elastomer composites and comparison of capacitive versus resistive sensors *Adv. Mat. Tech.* **3**, 1700284 (2018).

257. S. Shajari, M. Mahmoodi, M. Rajabian, K. Karan, U. Sundararaj, L.J. Sudak, Highly Sensitive and Stretchable Carbon Nanotube/Fluoroelastomer Nanocomposite with a Double-Percolated Network for Wearable Electronics. *Adv. Elec. Mater.* **6**, 1901067 (2020).

258. C. Thrasher, Z. Farrell, N. Morris, C. Willey, C. Tabor, Mechanoresponsive Polymerized Liquid Metal Networks. *Adv. Mater.* **31**, 1903864 (2019).

259. E. Pone, C. Dubois, N. Gu, Y. Gao, A. Dupuis, F. Boismenu, S. Lacroix, M. Skorobogatiy, Drawing of the hollow all-polymer Bragg fibers. *Opt Express* **14**, 5838 (2006).

260. T. Nguyen-Dang, A.C. de Luca, W. Yan, Y. Qu, A.G. Page, M. Volpi, T. Das Gupta, S. Lacour, F. Sorin, Controlled Sub-Micrometer Hierarchical Textures Engineered in Polymeric Fibers and Microchannels via Thermal Drawing, *Adv. Funct. Mater.* **27**, 1605935 (2017).

261. S. C. Xue, R. I. Tanner, G. W. Barton, R. Lwin, M. C. J. Large, and L. Poladian, Fabrication of Microstructured Optical Fibers-Part I: Problem Formulation and Numerical Modeling of Transient Draw Process. *J. Light. Technol.* **23**, 2245 (2005).

262. S. Xue, G. Barton, S. Fleming, and A. Argyros, Heat Transfer Modeling of the Capillary Fiber Drawing Process. *J. Heat Transf.* **139**, 072001 (2017).